

# A Model Study of Airborne Trace Gas Observations in the Troposphere

by

Stephen Robert Arnold

Submitted in accordance with the requirements for the degree of Doctor of  
Philosophy.

University of Leeds

School of the Environment

May 2004.

The candidate confirms that the work submitted is his own and that appropriate credit has been given where reference has been made to the work of others.

This copy has been supplied on the understanding that it is copyright material and that no quotation from the thesis may be published without proper acknowledgement.

## Acknowledgements

I express my sincere thanks to my supervisor, Martyn Chipperfield, for his guidance, support and patience, without which this thesis would not have been possible.

I would like to thank my colleagues Mathew Evans, Dominick Spracklen, Stewart Davies, Richard Ellis, Rita Cardoso, and Doug Parker for their advice and assistance on all matters atmospheric. I also thank Jason Lander and James Groves for assistance with computing issues.

There are many others from the wider community who I would like to thank. I extend special thanks to Fiona O'Connor and John Methven with whom I have shared a very rewarding working relationship and good friendship during the past four years. Special thanks also go to Prof. John Pyle and Kathy Law for much encouragement, fresh ideas and enthusiasm with regard to my work. I also thank Peter Good for assistance with the EDGAR emissions code.

I express my thanks to Ruth Purvis, Ally Lewis and Jim McQuaid for assistance and discussions regarding the analysis of NMHC observations.

My sincere gratitude is extended to Mark Blitz, Dwayne Heard and Prof. Mike Pilling for supplying their new laboratory measurements of acetone quantum yields, and assistance in their parameterisation for modelling. I also thank Sue Gray, University of Reading for supplying me with mesoscale model output used in Chapter 6.

I would like to thank the rest of the EXPORT science team for making the EXPORT project such a success.

Many others have played their part in preserving my sanity throughout these studies: Foxy, Damo, Mags, Alex, Bob, Neil, Matt, Paul, Sal, Mike T, Dave T, Rup, Moules.

I would also like to acknowledge the financial assistance I have received from the UK Natural Environment Research Council.

Finally, I extend special thanks to my family, in particular my parents, for their continued support over the past 4 years.

## Abstract

This thesis is concerned with the composition of the troposphere over Central Europe. In particular, transport and chemistry processes important in controlling ozone concentrations have been investigated using aircraft data and chemistry-transport models.

Model simulations using a Lagrangian chemistry transport model have been performed, and analysed alongside output from an Eulerian global chemistry transport model, and aircraft observations obtained in the Central European troposphere during Summer 2000, as part of the EU EXPORT aircraft campaign.

Analysis of observed non-methane hydrocarbon (NMHC) concentrations show that quantitative estimates of air mass age from NMHC ratios are complicated by mixing effects. The relative importance of mixing and chemistry in changing a given NMHC ratio are shown to be dependent on both season (due to the abundance of OH) and the synoptic situation (due to the strength of vertical mixing). Isoprene is shown to be the dominant OH sink in the Romania-Hungary border region. In Poland and the Czech Republic short-lived alkenes played a more important role in photochemistry. The greater number of NMHC species in the Lagrangian model compared to the computationally-expensive Eulerian model was shown to increase PBL ozone production rates by up to  $\sim 30\%$ .

The importance of acetone for chemistry in the UT is re-evaluated, in light of new laboratory measurements of its photolysis quantum yields. A 30% contribution by acetone to the total OH concentration in the tropics is reduced to 18%, and from 25% to 8% at mid-latitudes. Contributions from acetone to  $\text{HO}_x$  in the regions of the highest altitude EXPORT observations are seen to be relatively small ( $< 5\%$  for the updated quantum yield photolysis rates).

The implications of the use of Lagrangian or Eulerian model formulations for chemistry in the troposphere are also examined. Vertical exchange between the boundary layer and the free troposphere, facilitated by frontal systems is better treated using an Eulerian approach where sub-grid mixing processes play a key role. Forcing the Lagrangian model with output from a mesoscale meteorological model gives the best

simulation, as some of the larger regions of convection are explicitly resolved.

In domains dominated by fine-scale layering of air masses, a novel Lagrangian reverse-domain-filling technique with chemistry simulates the positions of air mass gradients and characteristics remarkably well. The Eulerian model mixes down fine-scale layers too quickly, with important consequences for domain-average ozone photochemistry, producing an underestimate of a factor 4 in ozone production from the reaction  $\text{NO} + \text{HO}_2$ .



# Contents

<b>1</b>	<b>Motivation and background</b>	<b>1</b>
1.1	Introduction . . . . .	1
1.2	Motivation . . . . .	1
1.2.1	Tropospheric ozone . . . . .	2
1.2.2	Aims of this thesis . . . . .	3
1.3	Physical characteristics of the troposphere . . . . .	5
1.3.1	Vertical stability and the tropopause . . . . .	5
1.3.2	Large-scale Dynamics . . . . .	7
1.3.3	Planetary Boundary Layer (PBL) . . . . .	9
1.4	Chemical processes . . . . .	11
1.4.1	Ozone ( $\text{O}_3$ ) . . . . .	12
1.4.2	The OH radical and $\text{HO}_x$ . . . . .	12
1.4.3	Nitrogen oxides ( $\text{NO}_x$ ) . . . . .	14
1.4.4	Methane Oxidation . . . . .	16
1.4.5	Sinks and reservoirs of $\text{HO}_x$ and $\text{NO}_x$ . . . . .	17

1.4.6	Night time chemistry . . . . .	19
<b>2</b>	<b>Modelling atmospheric chemistry and transport</b>	<b>21</b>
2.1	Introduction . . . . .	21
2.2	The Role of Models . . . . .	21
2.3	Model Formulation . . . . .	24
2.3.1	Eulerian Models . . . . .	24
2.3.2	Lagrangian Models . . . . .	28
2.4	The TOMCAT Global CTM . . . . .	31
2.5	The CiTTyCAT Lagrangian model . . . . .	33
2.5.1	Advection and mixing . . . . .	33
2.5.2	Chemistry scheme . . . . .	34
2.5.3	Photolysis . . . . .	34
2.5.4	Boundary layer and surface deposition . . . . .	35
2.5.5	Surface emissions . . . . .	36
2.5.6	Initialisation . . . . .	36
<b>3</b>	<b>The EXPORT Campaign: Data and interpretation</b>	<b>38</b>
3.1	Introduction . . . . .	38
3.2	C130 Instrumentation . . . . .	39
3.2.1	Temperature, Humidity and Position . . . . .	39
3.2.2	Tropospheric trace gases . . . . .	40

3.3	Air mass back-trajectories . . . . .	40
3.4	EXPORT flights: location and synoptic conditions . . . . .	41
3.5	EXPORT data: O <sub>3</sub> , CO, NO <sub>y</sub> , HCHO, H <sub>2</sub> O <sub>2</sub> and thermodynamic variables. . . . .	43
3.5.1	Flight A772 (31/07/2000) . . . . .	46
3.5.2	Flight A773 (02/08/2000) . . . . .	49
3.5.3	Flight A774 (03/08/2000) . . . . .	55
3.5.4	Flight A775 (09/08/2000) . . . . .	61
3.5.5	Flight A776 (10/08/2000) . . . . .	64
3.6	Conclusions . . . . .	69
<b>4</b>	<b>Interpretation of non-methane hydrocarbon observations</b>	<b>71</b>
4.1	Introduction . . . . .	71
4.2	NMHC sources and sinks . . . . .	72
4.3	NMHCs used to diagnose atmospheric processing . . . . .	73
4.4	Mixing and chemistry . . . . .	76
4.4.1	TOPSE data: evidence for combined dilution and chemistry .	78
4.4.2	Application to EXPORT NMHC data . . . . .	81
4.5	NMHCs in the Central European PBL . . . . .	86
4.6	Relative contributions of NMHCs to regional photochemistry . . . .	90
4.7	Evidence for halogen chemistry from EXPORT Flight A775 . . . . .	94
4.8	Conclusions . . . . .	100

<b>5</b>	<b>Comparisons of aircraft observations with the CiTTyCAT model</b>	<b>103</b>
5.1	Introduction . . . . .	103
5.2	Basic model comparison . . . . .	104
5.2.1	Ozone . . . . .	104
5.2.2	NO <sub>y</sub> . . . . .	111
5.2.3	CO and NMHCs . . . . .	112
5.3	Ozone budget over Central Europe . . . . .	113
5.3.1	Instantaneous rates . . . . .	113
5.3.2	Net change in ozone over 4 days . . . . .	119
5.4	Ozone budget in individual air masses . . . . .	121
5.4.1	Type A . . . . .	121
5.4.2	Type B . . . . .	123
5.4.3	Type C . . . . .	123
5.4.4	Type D . . . . .	124
5.5	Contributions of NMHCs to PBL photochemistry . . . . .	124
5.6	Conclusions . . . . .	125
<b>6</b>	<b>Chemistry and transport in a cold frontal region</b>	<b>132</b>
6.1	Introduction . . . . .	132
6.2	Mid-latitude cyclones . . . . .	133
6.3	WCB structure . . . . .	136
6.3.1	RDF trajectories and satellite data . . . . .	136

6.3.2	CTM output . . . . .	139
6.4	Vertical mixing in the frontal region . . . . .	144
6.4.1	Uniform mixed layer . . . . .	144
6.4.2	Decaying emissions profile . . . . .	147
6.5	Resolving vertical transport: Mesoscale trajectories . . . . .	150
6.5.1	Mesoscale Unified Model . . . . .	151
6.5.2	Model comparison . . . . .	153
6.5.3	UM trajectories with chemistry . . . . .	156
6.6	Conclusions . . . . .	156
<b>7</b>	<b>Long-range transport to Europe observed during EXPORT</b>	<b>159</b>
7.1	Introduction . . . . .	159
7.2	Long-range pollution transport . . . . .	160
7.3	Observed air mass structure . . . . .	161
7.3.1	August 9th 2000 (A775) . . . . .	161
7.3.2	August 10th 2000 (A776) . . . . .	163
7.4	Transport pathways . . . . .	170
7.5	Modelling LRT using the CiTTyCAT model . . . . .	172
7.5.1	Basic model along 10-day back trajectories . . . . .	173
7.5.2	Introduction of mixing . . . . .	175
7.6	Chemistry and mixing in observed air mass types . . . . .	176
7.6.1	E.Am Air Mass . . . . .	176

7.6.2	Mid US Air Mass . . . . .	177
7.6.3	S.E. US Coast Air Mass . . . . .	178
7.6.4	W.Am Air Mass . . . . .	179
7.7	Modelled ozone production in LRT layers . . . . .	181
7.7.1	RDF with full chemistry . . . . .	181
7.7.2	LRT ozone budget . . . . .	182
7.8	Conclusions . . . . .	184
<b>8</b>	<b>Photodissociation of acetone in the troposphere</b>	<b>200</b>
8.1	Introduction . . . . .	200
8.2	Atmospheric Chemistry of Acetone . . . . .	200
8.3	Temperature-dependent quantum yields for acetone photolysis . . .	203
8.3.1	Determination of quantum yields . . . . .	203
8.3.2	Parameterisation of quantum yields as a function of wave- length, pressure and temperature . . . . .	204
8.4	Atmospheric implications of temperature-dependence . . . . .	207
8.4.1	Altitude dependence of photolysis rates . . . . .	207
8.4.2	Chemical implications . . . . .	209
8.5	Acetone during EXPORT . . . . .	216
8.6	Conclusions . . . . .	219
<b>9</b>	<b>Conclusions</b>	<b>221</b>
9.1	Summary of results . . . . .	221

9.2	Future work . . . . .	224
-----	-----------------------	-----

## List of figures

1.1	Factors responsible for climate forcing . . . . .	3
1.2	Observations of tropospheric ozone concentrations . . . . .	4
1.3	Temperature profile of the atmosphere . . . . .	6
1.4	Instability in the troposphere . . . . .	7
1.5	Global mean circulation . . . . .	8
1.6	Diurnal PBL evolution . . . . .	10
1.7	Ozone production as function of $\text{NO}_x$ . . . . .	15
2.1	Eulerian and Lagrangian advection . . . . .	25
2.2	RDF Surface $\text{NO}_2$ over the UK . . . . .	32
2.3	CO emissions from the EDGAR inventory . . . . .	37
3.1	EXPORT Flight tracks . . . . .	42
3.2	Met Office synoptic charts for periods of EXPORT flights. . . . .	43
3.3	Vertical profiles of EXPORT data . . . . .	45
3.4	RDF -4 day $q$ and change in pressure . . . . .	47



3.5	A772 Time series . . . . .	48
3.6	RDF 4 day back trajectory $q$ . . . . .	50
3.7	A773 Time series . . . . .	51
3.8	RDF -2 day $q$ and change in pressure . . . . .	53
3.9	A773 RDF -2 day $\theta_e$ . . . . .	54
3.10	A774 Time series . . . . .	56
3.11	A774 RDF change in pressure. . . . .	57
3.12	RDF -1.5 day $\theta_e$ and $q$ . . . . .	58
3.13	Section RDF $\theta_e$ and $q$ . . . . .	59
3.14	A774 tracer-tracer correlations. . . . .	60
3.15	A775 Time series . . . . .	63
3.16	RDF origin longitude . . . . .	64
3.17	A775 tracer-tracer correlations. . . . .	65
3.18	A776 Time series . . . . .	66
3.19	RDF -5 day longitude. . . . .	68
4.1	Benzene-toluene relationship . . . . .	74
4.2	NMHC scatter plot . . . . .	75
4.3	NMHC scatter plot . . . . .	77
4.4	TOPSE flight tracks . . . . .	79
4.5	TOPSE NMHC correlations . . . . .	80
4.6	NMHC scatter plot . . . . .	82

4.7	NMHC scatter plot . . . . .	85
4.8	Near surface NMHC observations 1 . . . . .	87
4.9	Near surface NMHC observations 2 . . . . .	88
4.10	Map of power facilities in Eastern Europe . . . . .	89
4.11	Map of gas facilities in Eastern Europe . . . . .	91
4.12	NMHC / CO correlation plots . . . . .	92
4.13	OH loss rates for PBL NMHCs . . . . .	93
4.14	Speciated NMHC OH loss rates . . . . .	94
4.15	Vertical profile of NMHC OH loss rates . . . . .	95
4.16	NMHC scatter plot . . . . .	96
4.17	Relationship between NMHC loss rates due to OH and Cl . . . . .	98
4.18	Unusual NMHC ratios . . . . .	98
4.19	Back trajectories arriving on flight A775 . . . . .	101
5.1	Model vs data (A772) . . . . .	105
5.2	Model vs data (A773) . . . . .	106
5.3	Model vs data (A774) . . . . .	107
5.4	Model vs data (A775) . . . . .	108
5.5	Model vs data (A776) . . . . .	109
5.6	Initial concentrations . . . . .	114
5.7	MeOO + NO rate comparison . . . . .	115
5.8	Total Net P(O <sub>3</sub> ) for EXPORT flights . . . . .	117

5.9	Ozone production rates for simple and complex NMHC schemes . . .	118
5.10	Individual ozone production and loss terms . . . . .	119
5.11	Net change in ozone over 4 days . . . . .	120
5.12	Trajectories for individual air mass types . . . . .	122
5.13	Along trajectory output Type A . . . . .	127
5.14	Along trajectory output Type B . . . . .	128
5.15	Along trajectory output Type C . . . . .	129
5.16	Along trajectory output Type D . . . . .	130
5.17	OH loss rates from model NMHCs . . . . .	131
6.1	Norwegian model of cyclogenesis . . . . .	134
6.2	Airstreams in the Browning-type mid latitude cyclone model . . . .	136
6.3	A773 RDF -2 day $\theta_e$ . . . . .	138
6.4	RDF -2 day change in $q$ and $\theta_e$ . . . . .	140
6.5	Meteosat satellite image of IR brightness temperature . . . . .	141
6.6	CiTTyCAT and TOMCAT model output along A773 flight track . .	142
6.7	Sections of interpolated and RDF TOMCAT CO . . . . .	143
6.8	CiTTyCAT model output for 5km mixed layer . . . . .	146
6.9	Dependence of emission rates on mixing layer treatment . . . . .	147
6.10	CiTTyCAT model output for exponentially decayed emissions profile	149
6.11	Arrival grids for UM and ECMWF trajectories . . . . .	152
6.12	UM and ECMWF trajectories . . . . .	154

6.13	UM and ECMWF trajectories arriving near the flight track . . . . .	155
6.14	CiTTyCAT output for UM and ECMWF trajectories . . . . .	157
7.1	RDF change in pressure in region of Flight A775 . . . . .	162
7.2	RDF change in pressure on vertical sections . . . . .	164
7.3	Observed CO, ozone, $q$ , $\theta_e$ for Flight A775 . . . . .	165
7.4	Back trajectories arriving on Flight A775 . . . . .	166
7.5	RDF vertical section in region of Flight A776 . . . . .	167
7.6	$q$ comparisons for flight track shift . . . . .	168
7.7	Observed CO, ozone, $q$ , $\theta_e$ for latter part of A776 . . . . .	169
7.8	Back trajectories arriving on Flight A776 . . . . .	186
7.9	NCEP surface analyses from August 2000 . . . . .	187
7.10	TOMCAT CO field over North West Atlantic . . . . .	188
7.11	Comparisons of model output with observations for A776 . . . . .	189
7.12	Trajectories for individual air mass types . . . . .	190
7.13	Along trajectory output: E. Am air mass . . . . .	191
7.14	Along trajectory output: Mid US air mass . . . . .	192
7.15	Along trajectory output: S.E. US Coast air mass . . . . .	193
7.16	Along trajectory output: S.E. US Coast air mass with background and emissions shift . . . . .	194
7.17	Along trajectory output: W.Am. air mass . . . . .	195
7.18	Along trajectory output: W.Am. air mass with PHOBEA initialisation	196

7.19	Ozone on RDF sections from TOMCAT and CiTTyCAT . . . . .	197
7.20	$P(O_3)$ on RDF sections from TOMCAT and CiTTyCAT . . . . .	198
7.21	Vertical profile of MeOO, NO and $P(O_3)$ for A776 . . . . .	199
7.22	Correlations of ozone budget terms . . . . .	199
8.1	Photo-oxidation scheme for acetone . . . . .	202
8.2	Observations of acetone quantum yields . . . . .	205
8.3	Parameterised quantum yields . . . . .	208
8.4	Vertical profiles of acetone J-rates . . . . .	210
8.5	Convective initialised air parcel . . . . .	214
8.6	Convective inflow of acetone to UT . . . . .	216
8.7	Acetone concentrations from EXPORT . . . . .	218

# List of tables

3.1	Trace gas instrumentation on board the C130 during the EXPORT campaign. . . . .	40
3.2	Summary of the five science flights flown by the C130 aircraft. . . .	44
4.1	NMHC second-order OH reaction rates and lifetimes . . . . .	72
4.2	NMHC second-order OH and Cl reaction rates . . . . .	96
5.1	Details of trajectory types used for individual air mass budget studies.	121
8.1	Global atmospheric budget of acetone. Data from <i>Jacob et al.</i> , [2002].	201
8.2	Prescribed chemistry and conditions for UT model experiments. . . .	211
8.3	Steady-state day averages from box model constrained by mid-latitude UT observations (Experiment 1a). . . . .	212
8.4	Steady-state day averages from box model constrained by tropical UT observations (Experiment 1b). . . . .	212
8.5	Steady-state day average concentrations from box model constrained with EXPORT UT observations. . . . .	219

# 1. Motivation and background

## 1.1 Introduction

This Chapter discusses the motivation for the research in this thesis, as well as an overview of the physics and chemistry of the troposphere, which form the basis of the study. In Section 1.2, the need for an understanding of tropospheric photochemical processes is highlighted, and a number of research questions are posed, which this thesis will address. In Section 1.3 the basic physical characteristics of the troposphere are discussed. The chemical processing of trace gases in the troposphere is then described in Section 1.4.

## 1.2 Motivation

In recent years, there has been increasing concern that the technical and industrial development of the human race has led to a significant and unprecedented perturbation to the Earth's climate system. This is mainly through enhanced atmospheric concentrations of radiatively active gases, such as carbon dioxide ( $\text{CO}_2$ ) and methane ( $\text{CH}_4$ ), resulting from fossil fuel combustion, the growth in the human population and agriculture. These gases are believed to enhance the warming of the lower atmosphere, through absorption of outgoing long-wave radiation from the Earth. *Harries et al.*, [2001] showed that satellite observations of differences in the Earth's outgoing long-wave radiation over a 27 year period from 1970 to 1997, were consistent with the estimated changes in the atmospheric burdens of these gases.

The extent of the growth in these anthropogenic environmental influences, since

the industrial revolution, has been so enormous that it has been argued that we are in a time-period during which these factors dominate the Earth's climate, in some ways more than any natural variability. This concept has led to the label 'the *anthropocene* period' [Crutzen, 2002]. Evidence suggests that the current state of the Earth system lies outside the range of natural variability exhibited over the past 500 thousand years [Crutzen and Steffen, 2003]. If we are to realistically predict the impact that these influences may have on the future of the Earth, the complex set of processes and feedbacks in the Earth system need to be understood and quantified.

### 1.2.1 Tropospheric ozone

Ozone ( $O_3$ ) is made *in situ* in the troposphere, through the degradation of hydrocarbon compounds, and this production is catalysed by nitrogen oxides (see Section 1.4). In terms of climate forcing, it is the third most important greenhouse gas, after  $CO_2$  and  $CH_4$  (see Fig. 1.1). However, due to its shorter lifetime and complex dependence on its precursors, the atmospheric budget of ozone is much less well understood than the well-mixed, longer-lived  $CO_2$  and  $CH_4$ . Ozone also plays an indirect role in the climate system, as it is the chief source for the OH radical in the troposphere. This is responsible for almost all of the oxidation of  $CH_4$ , and so determines its atmospheric lifetime. OH is also responsible for the oxidation of ozone precursors.

As well as playing a central role in the climate-composition question, ozone has a more direct impact on human life. At the surface, it can be harmful to both animal and plant life, resulting in respiratory complaints [Dockery, 1993] and damage to crop yields [PORG, 1997]. Downwind of heavily populated regions of the globe, where emissions of its precursors are large, surface ozone concentrations frequently exceed the stipulated safe health limit imposed by the World Health Organisation of an averaged concentration of 61ppbv over 8 hours of exposure [WHO, 2000]. Observations suggest that during the rapid industrial growth of the last century, ozone concentrations in the troposphere may have increased by as much as two-fold (see Fig. 1.2). Increased emissions of ozone precursors, particularly from developing regions such as Asia, are expected to lead to further increases in tropospheric ozone



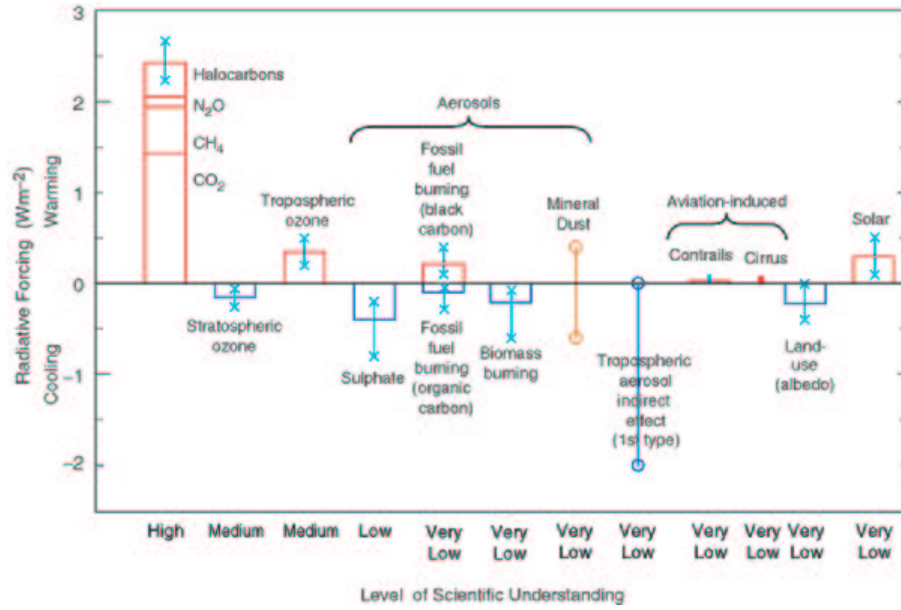


Figure 1.1: *Estimates of global mean radiative forcing of the climate system for 2000 relative to 1750. Thin lines indicate the uncertainties in the magnitudes of the processes. Ozone is the third most active radiative gas, contributing approximately 70-80% of the forcing from methane. The role of ozone is less well understood than the well mixed greenhouse gases. (Based on Figure 6.6 from IPCC Third Annual Report [2001])*

in future years (e.g Brasseur *et al.*, [1998]).

### 1.2.2 Aims of this thesis

In this thesis, aircraft observations are used in conjunction with atmospheric chemistry-transport models to investigate processes controlling the tropospheric ozone distribution over Central Europe. Issues to be addressed include:

- Does a photochemical model reproduce the ozone concentrations and photochemistry associated with the heavily polluted environment of Central Europe?
- How does the treatment of transport processes in the model impact the export of this pollution from near the European surface into the large-scale atmosphere?

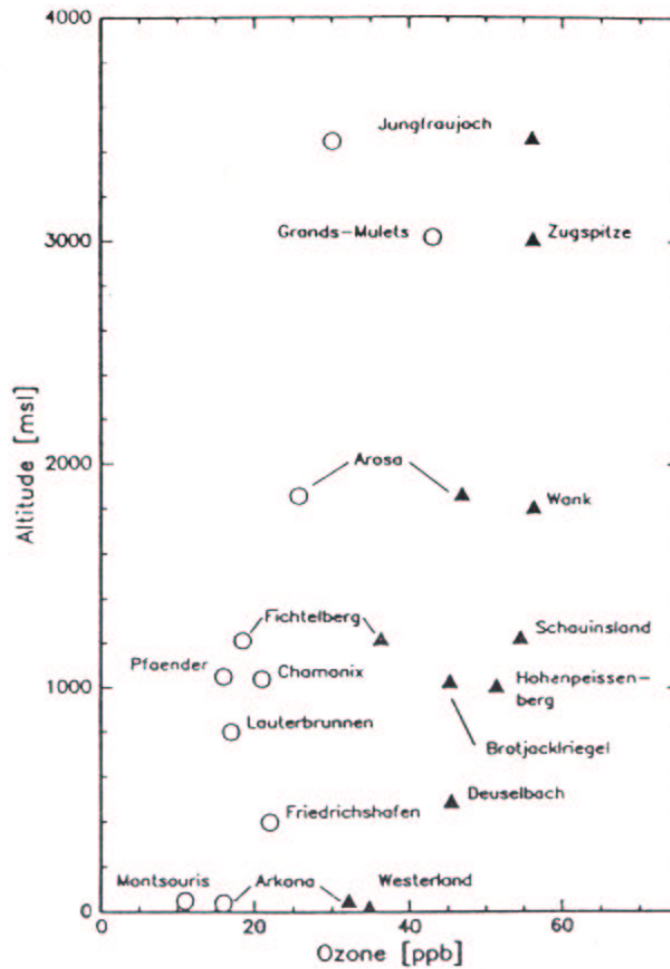


Figure 1.2: *Observations of ozone in the European troposphere at non-urban locations. Circles denote measurements taken prior to 1956, and triangles denote measurements made post 1988. Adapted from Staehelin et al., [1994].*

- How important is long-range transport in determining the ozone concentrations over Central Europe?
- How critical is our understanding of chemistry of oxygenated hydrocarbon compounds for predicting ozone production?
- How do different modelling approaches affect conclusions regarding the photochemistry of ozone in the troposphere?

All of these issues are ultimately important in our understanding of the distributions of ozone in the troposphere.

## 1.3 Physical characteristics of the troposphere

The troposphere is the lower-most layer of the Earth's atmosphere, extending from the surface of the Earth to an altitude of between about 8km at the poles and 16km in the tropics. The tropopause is the boundary between the troposphere below and the stratosphere above. The density of the atmosphere decreases exponentially with altitude, with the atmospheric pressure at the tropopause being approximately one tenth of the surface pressure. Consequently, approximately 90% of the atmosphere's mass lies in the troposphere.

Temperature in the troposphere generally decreases with altitude, while absorption of solar UV radiation in the ozone-rich stratosphere results in temperature increasing with altitude (Fig. 1.3).

### 1.3.1 Vertical stability and the tropopause

The dynamic behaviour of the troposphere is determined by the temperature lapse rate with altitude. The temperature generally decreases with height at a rate which exceeds the moist adiabatic lapse rate, due to radiative heating of the lower atmosphere. Adiabatic expansion of an air parcel as it is displaced from lower altitudes to a cooler higher altitude would therefore result in the air parcel cooling to a temperature which remains warmer than its new surroundings (see Fig. 1.4). The air parcel therefore remains buoyant with respect to the surroundings, and the atmospheric column remains vertically unstable. The result is that convective instability vertically mixes the troposphere throughout its depth; indeed the word 'troposphere' comes from the Greek *tropos*, literally meaning 'turning'. Trace gases can be transported throughout the depth of the troposphere on timescales of days, or even as little as hours, in deep convective events in the tropics.

The World Meteorological Organisation define the position of the tropopause as the

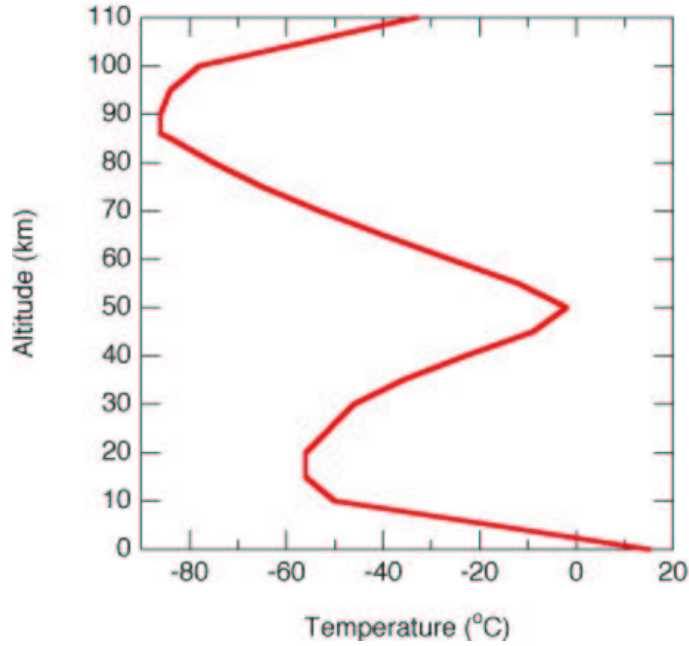


Figure 1.3: *The profile of the atmosphere's temperature with altitude. Temperature decreases with height in the troposphere, before increasing with altitude in the stratosphere due to heating by UV absorption in the ozone layer.*

lowest altitude point at which the lapse rate decreases to  $2\text{K km}^{-1}$  or less, provided the average lapse rate over the two kilometres above this point does not exceed this value. Through the layers of the atmosphere in the region of the tropopause, the temperature profile reaches a turning point, with the lapse rate becoming positive in the stratosphere. The stratosphere is therefore very stable with respect to vertical displacement, with trace gas transport timescales of many years over its depth. The tropopause region effectively forms a barrier to transport between the well-mixed troposphere and the stable stratosphere. The position of the tropopause can also be characterised by gradients in atmospheric chemical constituents. The stratosphere is found to be very dry, and also rich in ozone compared to the troposphere. Sharp discontinuities in vertical profiles of the concentrations of such constituents occur as the upper troposphere meets the lower stratosphere. Potential vorticity (PV) provides a third, dynamic tropopause definition. This quantity is defined as the product of the static stability and the absolute vorticity for a given isentropic surface. PV values are generally up to an order of magnitude greater in the stratosphere,

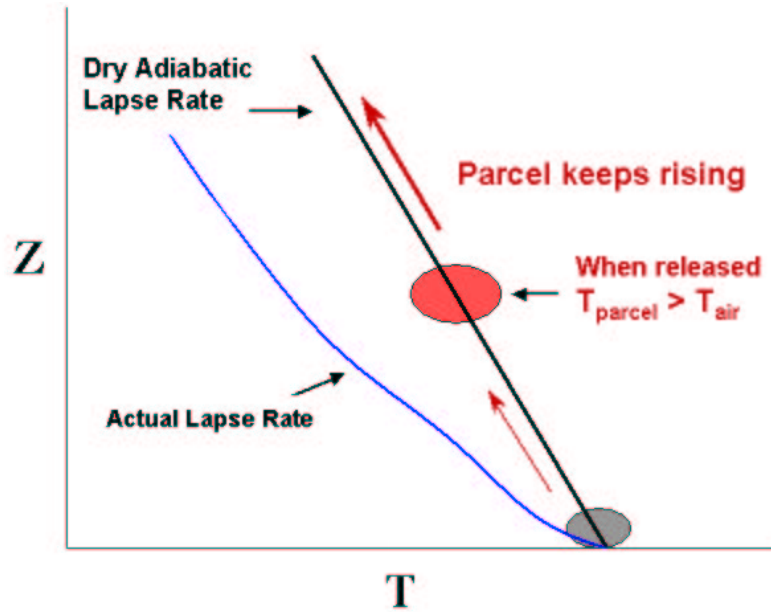


Figure 1.4: Decrease in temperature ( $T$ ) with altitude ( $z$ ) in the troposphere, for dry adiabatic ascent (black) and as found in the environment (blue). Instability in the troposphere arises through the environmental lapse rate exceeding the adiabatic lapse rate. Adiabatic displacement of an air parcel vertically results in maintained buoyancy, causing the air parcel to continue to move. This instability is characteristic of the troposphere. Based on figure taken from [<http://psb.usu.edu/courses/bmet2000/stability.html>]

and the 1.5-2.0 PVU ( $1 \text{ PVU} = 10^{-6} \text{ m}^2 \text{ s}^{-1} \text{ K kg}^{-1}$ ) surface is generally seen to be coincident with the tropopause position, outside of the tropics.

### 1.3.2 Large-scale Dynamics

The large-scale motion of air in the troposphere can be described by a number of characteristic circulations resulting from the variation in solar heating of the atmosphere around the globe and the Earth's rotation. Such circulations are useful for describing the mean state of the atmospheric flow on a hemispheric scale, however at any one time observed winds are also influenced by smaller scale mechanisms such as orographic forcing, convective transport and weather systems.

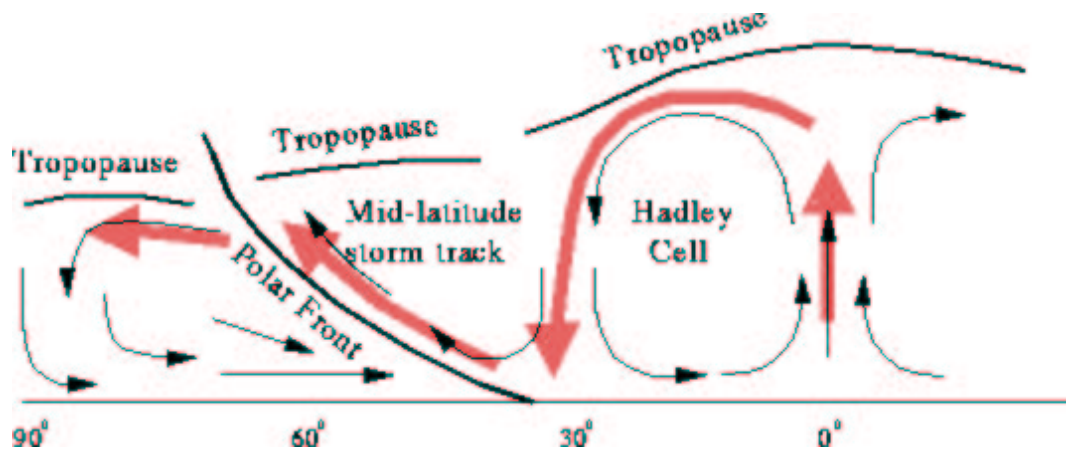


Figure 1.5: The mean global tropospheric circulation can be represented by three main cells operating through the depth of the troposphere at tropical, mid and polar latitudes. The circulations are driven by the variation in solar heating with latitude. Image taken from Lecture Notes for Course ENVI2150, School of Environment, University of Leeds. Module Leader: Ken Carslaw.

The Earth's rotation means that an airflow in the atmosphere is subjected to displacement due to conservation of angular momentum. The observed apparent force which acts in this way is known as the Coriolis force. For an observer on the Earth's surface, this causes flows in the northern hemisphere to be deflected to the right, and flows in the southern hemisphere to be deflected to the left. The Coriolis force combined with heat transport between the more intensely solar-heated Equator and the relatively cold polar regions results in three circulation-type patterns spread over the latitudes (Fig. 1.5). Deflection of the flows by the Coriolis force determines the east-west component of the winds at each latitude.

At the Equator, intense solar heating forces warm air to rise to the tropopause, where it then spreads polewards. The air subsides in the sub-tropics and at the surface a return flow takes the air back to the equator. This return flow is deflected by the Coriolis force to the west. At mid-latitudes, flow is dominated by large-scale eddy motions. These are set up due to a strong north-south temperature gradient at what is known as the polar front. Baroclinic instabilities arise as a result of the temperature gradient and result in baroclinic waves of high and low pressure regions travelling around the globe. The Coriolis force encourages rotation

to set up around the low pressure regions, warm air from the south being uplifted pole-wards around the circulation. This drives westerly flow in the mid-latitudes, with the maximum seen in the strong jet-streams in the upper troposphere. The formation of mid-latitude cyclones is discussed in depth in Chapter 6. Equator-wards descent of colder air is also facilitated by the baroclinic eddies, but the flow is not a closed mid-latitude circulation, although it is often labelled the Ferrel cell. A weaker Hadley-type cell also exists in the polar regions, driven by descent of air over the poles and outflow of cold air at the surface away from the pole.

Despite forming a barrier to transport, the tropopause is not completely impermeable. In the tropics, there is transition layer which allows slow transport across the tropopause, known as the tropical tropopause layer (TTL). It is believed that ascending tropospheric air in the tropics can enter the stratosphere *via* this layer, with exchange along isentropic surfaces between the lower-most stratosphere and the tropical upper troposphere (UT). This transport forms a key part of the large-scale wave-driven Brewer-Dobson circulation. The details of the role of the TTL in such transport and its role in the dehydration of air entering the stratosphere are not currently well understood. Exchange across the tropopause also occurs at mid-latitudes, facilitated by tropopause folding. In such stratosphere-troposphere exchange (STE) events, thin layers of air from the stratosphere penetrate the troposphere parallel to the tropospheric jet-stream. Turbulent mixing then dilutes these intrusions into the troposphere. Such transport events are important in determining the ozone budget of the troposphere [e.g. *Langford, 1999*].

### 1.3.3 Planetary Boundary Layer (PBL)

The layer of the troposphere adjacent to the surface is known as the planetary boundary layer (PBL). This is a highly turbulent, well-mixed layer, which extends to between a few hundred metres and  $\sim 2$  kilometres altitude. It is the boundary layer which interacts directly with the Earth's surface, and so it is important for the transfer of surface emissions into the troposphere. Emitted species become mixed into the boundary layer and are then vented out into the free troposphere. Such venting can be facilitated by detrainment from convective cells into the free

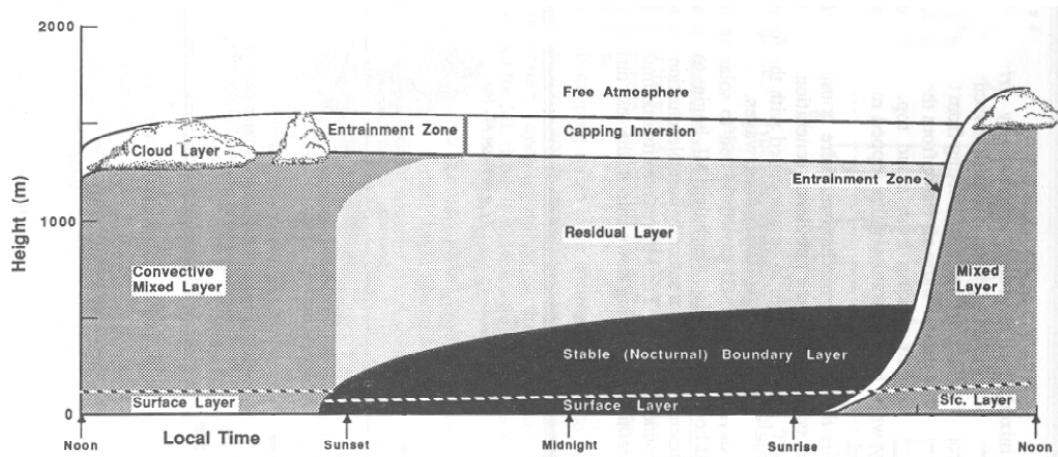


Figure 1.6: *The diurnal cycle of the planetary boundary layer (PBL). Solar heating of the Earth's surface during the day forces convective mixing to entrain air from the free troposphere, and the height of the mixed layer steadily grows. At dusk, the mixed layer collapses, leaving a residual layer behind, and a much shallower stable boundary layer. Taken from Stull, [1991].*

troposphere, and also the action of frontal systems which are efficient in setting up large-scale lifting of surface air to free-tropospheric altitudes (see Chapter 6).

On a daily basis, the height of the turbulent PBL layer rises and falls due to solar heating of the Earth's surface (Fig. 1.6). At dusk, the top of the PBL layer falls, leaving some of the pollutants which have accumulated in the PBL during the day behind in a residual layer above the descending PBL top. Large-scale advection in the free-troposphere can then erode this residual layer, releasing fresh pollutants into the free troposphere. As sunlight returns, increasing solar heating of the surface causes the PBL height to rise. As it rises through the morning, air from the residual layer, which has now been mixed with free-tropospheric air is re-incorporated into the PBL. This diurnal mechanism allows a limited amount of venting of polluted air from the PBL.

As well as mixing out surface emissions into the troposphere, air in the PBL can lose trace gases to the surface through deposition. As air passes over the surface exchange of trace species out of the air is facilitated primarily by absorption onto plant stomata or onto water surfaces. Some gases are very efficiently removed by



this process from the surface layer.

## 1.4 Chemical processes

Chemical processes play a central role in determining the behaviour and composition of the Earth's troposphere. The chemical transformations that occur in the atmosphere contribute to the changes in the distributions of trace gases, and so can affect other atmospheric systems. Changes in the distribution of radiatively active gases, such as methane ( $\text{CH}_4$ ) and ozone ( $\text{O}_3$ ) will have consequences for the temperatures in the troposphere, and therefore the dynamics [e.g. *Stevenson et al.*, 1998]. The formation of aerosols in the atmosphere from e.g. sulfur compounds will also have an effect on the radiative budget of the atmosphere. There are feedback mechanisms between these systems, as dynamic mechanisms will play a role in determining the spatial distribution of chemical species. An understanding of tropospheric chemical processes is therefore vital, in order to gain a better understanding of global issues such as climate change, down to regional-scale air quality and weather prediction.

Much of the chemistry in the troposphere is driven by emissions of species from the Earth's surface, either from anthropogenic activities such as transport and industry, or from natural sources such as vegetation. Species emitted into the atmosphere are then generally oxidised, or removed by deposition at the surface or washed out. Each species has a characteristic lifetime in the atmosphere, dependent on rates of chemical reaction with oxidants such as the OH radical, ozone and  $\text{NO}_3$ , its affinity for removal by cloud droplets or rain, and its susceptibility to deposition.

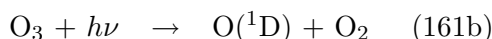
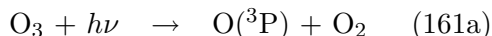
The gas-phase chemical system of the atmosphere is very complex, especially in the troposphere where surface emissions of thousands of different species occur. However, the basic processes are now relatively well understood, and what follows is a summary of these processes.

### 1.4.1 Ozone (O<sub>3</sub>)

For many years, it was assumed that the ozone in the troposphere was controlled by input from the stratosphere, where ozone concentrations are much larger, and loss by deposition to the Earth's surface. In the 1970s, *Crutzen*, [1973] and *Chameides and Walker*, [1973] proposed mechanisms for the *in situ* production of ozone in the troposphere. These mechanisms are discussed later in this Section. It is now understood that STE events, surface deposition, and *in situ* production all play a role in determining the tropospheric ozone distribution.

### 1.4.2 The OH radical and HO<sub>x</sub>

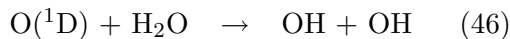
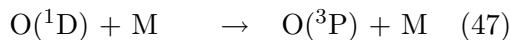
Gas-phase chemistry in the atmosphere is driven by the action of ultra-violet radiation on stable molecules (photolysis) and the formation of radical species. The most important of these radical species is the OH (hydroxyl) radical. This species is responsible for almost all the oxidation of species in the troposphere, and so is important for the removal of pollutants such as volatile organic compounds (VOCs) and nitrogen oxides. Species which are not oxidised by OH are generally considered to be inert in the troposphere. The OH radical is most commonly formed by the photolysis of ozone in the presence of water vapour.



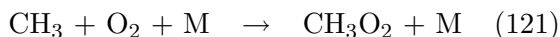
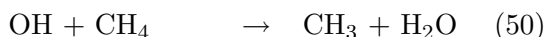
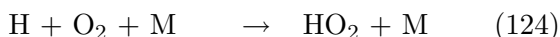
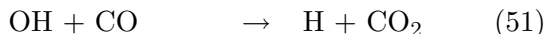
(Reaction numbers given are consistent with those in Appendix A).

Photolysis of ozone yields an oxygen molecule mostly accompanied by a ground-state oxygen atom (O(<sup>3</sup>P)) (R161a). However, if the wavelength of the radiation is sufficiently short (<330nm), then an oxygen atom in an excited electronic state (O(<sup>1</sup>D)) may be produced. This excited oxygen atom may then be collisionally deactivated to its ground-state (R47), or in the presence of water vapour can react to yield two OH radicals (R46).

In an atmosphere free from pollution by non-methane hydrocarbons (NMHCs) and



nitrogen oxides, the main reaction routes for OH are with CO and CH<sub>4</sub>.



The HO<sub>2</sub> radical is produced via the oxidation of CO to CO<sub>2</sub>. In the presence of nitrogen oxides, OH and HO<sub>2</sub> are rapidly interconverted through oxidation of NO, and the time-scale which determines their relative partitioning (typically < 1-10 s) is far shorter than the time-scale which determines their combined abundance. Consequently, they are often referred to together as HO<sub>x</sub> (=OH+HO<sub>2</sub>).

In the clean troposphere, loss of HO<sub>x</sub> is mainly via the self-reaction of HO<sub>2</sub> or the formation of methyl hydrogen peroxide.



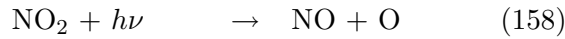
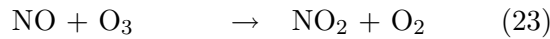
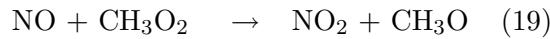
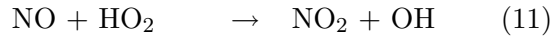
Both H<sub>2</sub>O<sub>2</sub> and CH<sub>3</sub>OOH are water soluble, and can therefore be lost from the gas-phase reaction system by rainout.

In the upper troposphere, it has been noted from aircraft measurements (e.g. *Brune et al.*, [1999]) that HO<sub>x</sub> concentrations are far larger than those predicted by R46 alone. It has been suggested that convective pumping of oxygenated hydrocarbon compounds, such as acetone, peroxides, and aldehydes from the boundary layer into the UT may account for this discrepancy [*Jaeglé et al.*, 1997; *Jaeglé et al.*, 2001]. The photolysis of these precursors provide extra primary production of HO<sub>x</sub> (see Chapter 8).

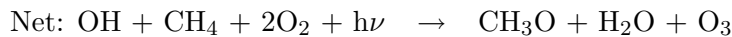
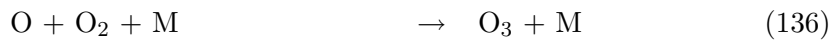
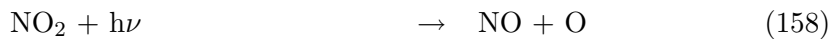
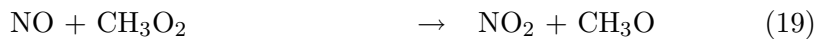
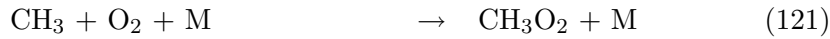
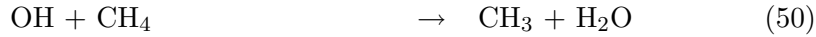
### 1.4.3 Nitrogen oxides ( $\text{NO}_x$ )

The presence of nitrogen oxides ( $\text{NO} + \text{NO}_2 = \text{NO}_x$ ) has important consequences for  $\text{HO}_x$  and the chemistry of the troposphere.  $\text{NO}_x$  is produced in large quantities by the combustion of petrochemicals at the surface, or by aircraft [*Kohler et al.*, 1997], and in biomass burning events [*Singh et al.*, 1996, *Jaeglé et al.*, 1998]. Lightning is also responsible for the production of large quantities of  $\text{NO}_x$  in the upper troposphere [*Stockwell et al.*, 1999a].

$\text{NO}$  reacts with a methyl-peroxy radical, ozone or  $\text{HO}_2$  to produce  $\text{NO}_2$ , which is then rapidly photolysed to yield  $\text{NO}$  and an oxygen atom.



These reactions provide a catalytic cycle for the production of ozone in the troposphere:



The conversion of  $\text{NO}$  to  $\text{NO}_2$  without the consumption of an ozone molecule leads to net ozone production.

In regions where  $\text{NO}$  concentrations are very small, ozone loss can dominate through the reaction with  $\text{HO}_2$ .

The net rate of ozone production shows a non-linear response to  $\text{NO}_x$  concentration,

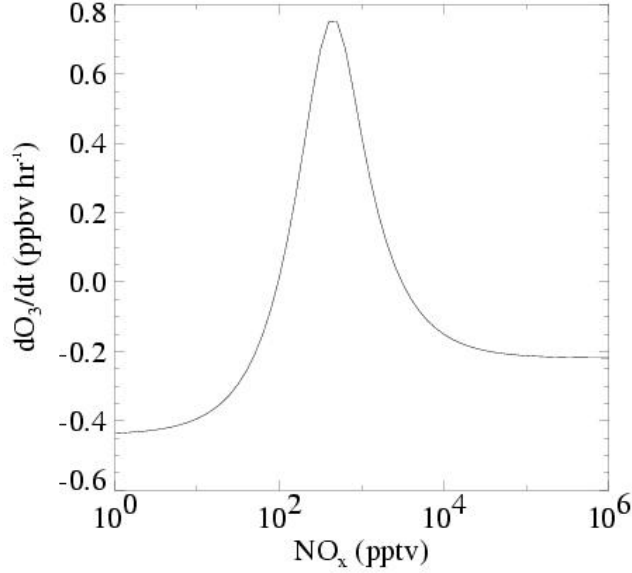
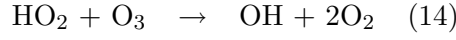
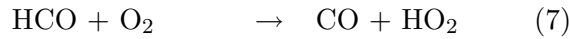
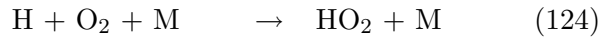
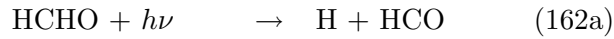
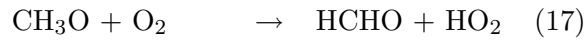
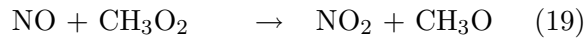
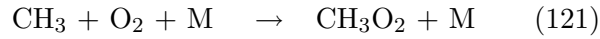
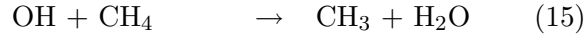


Figure 1.7: Ozone production rate as a function of ambient  $\text{NO}_x$  concentration. Ozone production is optimised where  $\text{NO}_x$  concentrations are large enough to allow efficient use of the available peroxy radicals for conversion of  $\text{NO}$  to  $\text{NO}_2$ . At high  $\text{NO}_x$ , diminished radical concentrations reduce ozone production efficiency. Image from Evans, [1999].

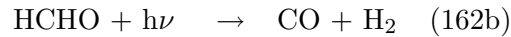
due to the combined influences of the above processes. Figure 1.7 shows that there is an optimum level of  $\text{NO}_x$  at which ozone production is maximised. Ozone production initially increases with  $\text{NO}_x$ , as more  $\text{NO}$  is oxidised to  $\text{NO}_2$  (R11 and R19) which then photolyses to yield  $\text{O}$ . (R158). At higher levels of  $\text{NO}_x$ , ozone production begins to decrease. This is due to a repartitioning of  $\text{HO}_x$  and the reaction of  $\text{OH}$  with  $\text{NO}_2$  to produce  $\text{HONO}_2$  (see Section 1.4.5). As  $\text{NO}$  increases, R11 converts more  $\text{HO}_2$  to  $\text{OH}$ , which is then removed by reaction with  $\text{NO}_2$ . These effects decrease the amount of  $\text{HO}_2$  available for ozone production. It should also be noted that a result of this sequence of events is the overall decrease in  $\text{HO}_x$  at high levels of  $\text{NO}_x$ . Surface observations described by Eisele *et al.*, [1997] support a similar dependence of  $\text{HO}_x$  on  $\text{NO}_x$  concentrations.

#### 1.4.4 Methane Oxidation

Removal of methane by OH has already been discussed, but the oxidation sequence of methane continues to form products which are themselves important for HO<sub>x</sub> chemistry.



Assuming the photolysis of formaldehyde (HCHO) occurs exclusively by R162a, it can be seen that two molecules of HO<sub>2</sub> are produced. In this way, the oxidation of methane by OH leads to a net production of an extra HO<sub>x</sub> radical. However, there are two photolysis routes for HCHO, and so the net production of HO<sub>x</sub> is less. The second channel R162b contributes ~ 40% of the photolysis sink, and so an average of 0.6 extra HO<sub>x</sub> are yielded through photolysis of HCHO.



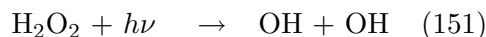
Methane oxidation can also lead to a loss of HO<sub>x</sub>. For clean areas, low in NO<sub>x</sub>, the formation of methyl hydrogen peroxide has already been discussed. This can react with OH *via* two channels, to form water, either destroying or conserving a HO<sub>x</sub> molecule.



The result of these mechanisms, is that the secondary production of HO<sub>x</sub> from methane oxidation is very dependent on local NO<sub>x</sub> concentrations. *Jaeglé et al.*, [2001] discuss secondary HO<sub>x</sub> production from methane as a function of NO<sub>x</sub>, and

show that the  $\text{HO}_x$  yield from methane oxidation increases with increasing  $\text{NO}_x$  and decreasing  $\text{HO}_x$  production from primary sources.

As already mentioned, other important primary sources of  $\text{HO}_x$ , especially in the upper troposphere, are thought to be the photolysis of acetone, aldehydes and peroxides. These are photolysed to initiate sequences which produce  $\text{HO}_x$ . Hydrogen peroxide ( $\text{H}_2\text{O}_2$ ) photolyses to produce two OH radicals directly.

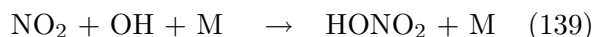


Aldehydes, which can be formed from  $\text{RO}_2$  radicals in reactions analogous to the production of HCHO, and acetone which is a product of the oxidation of higher organics, are also photolysed to produce  $\text{HO}_x$  radicals. Acetone photochemistry in the UT is discussed in detail in Chapter 8.

In the polluted troposphere, in the presence of significant levels of NO and a variety of volatile organic compounds (VOCs), ozone production generally dominates. Non-methane hydrocarbons (NMHCs) are oxidised by OH in an analogous manner to methane, providing an extra source of peroxy radicals ( $\text{RO}_2$ ) to fuel the ozone production cycle. The importance of NMHCs is highlighted in Chapter 4.

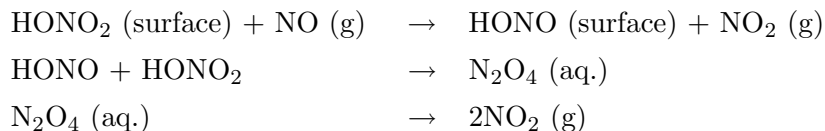
#### 1.4.5 Sinks and reservoirs of $\text{HO}_x$ and $\text{NO}_x$

$\text{NO}_x$  and  $\text{HO}_x$  are removed from the troposphere *via* the formation of sink species, which are either inert to regeneration of the reactive species or are removed due to their solubility in rain. The formation of nitric acid ( $\text{HONO}_2$ ) is an important sink for  $\text{NO}_x$ .  $\text{HONO}_2$  is highly water soluble and so is efficiently removed in precipitation.



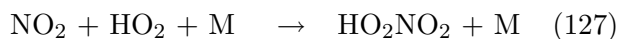
Nitric acid can be photolysed relatively slowly to release  $\text{NO}_2$ , and some authors have discussed the existence of a heterogeneous conversion of nitric acid to  $\text{NO}_x$  (e.g.

*Saliba et al.*, [2001]). This mechanism occurs in the presence of water and existing gas-phase  $\text{NO}_x$ , with  $\text{HONO}_2$  adsorbed onto aerosol surfaces.



Such mechanisms have been suggested in order to explain the persistence of  $\text{NO}_x$  and ozone production observed in the troposphere, and gas-phase models' overestimation of  $\text{HONO}_2$  abundances.

$\text{NO}_2$  also reacts with  $\text{HO}_2$  to form peroxy nitric acid ( $\text{HO}_2\text{NO}_2$ ).



Unlike  $\text{HONO}_2$ ,  $\text{HO}_2\text{NO}_2$  can undergo thermal decomposition to return its precursors. It is also photolysed to yield a nitrate radical.



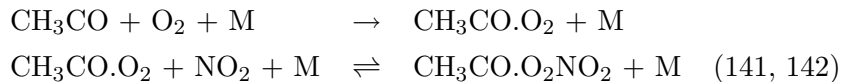
Recently, a photolysis channel for  $\text{HO}_2\text{NO}_2$  in the near-infra-red has been discovered [*Roehl et al.*, 2002]. This has been shown to affect the coupling between  $\text{HO}_x$  and  $\text{NO}_x$ , effectively reducing the amount of  $\text{HO}_2\text{NO}_2$  reacting with OH (R55), and so increasing ambient  $\text{HO}_x$  [*Salawitch et al.*, 2002]. However, this is estimated to be significant in the troposphere only at high latitudes in springtime.

$\text{NO}$  and  $\text{OH}$  can also react to form the species  $\text{HONO}$ , which is photolysed back to its precursors. The reaction of any of these reservoir species with  $\text{OH}$  to form  $\text{H}_2\text{O}$  is a sink for  $\text{HO}_x$  (discussed by *Jaeglé et al.*, [2001]).

An important species which is formed via the oxidation of hydrocarbons in the presence of nitrogen oxides is peroxy acetyl nitrate (PAN). PAN exists in thermal



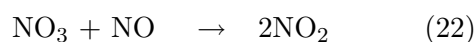
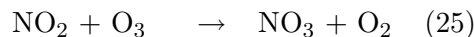
equilibrium with its precursors.



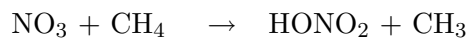
The thermal equilibrium means that in relatively cold air masses, PAN formed can be transported away to regions remote from pollution sources. If the PAN then thermally decomposes, it will release  $\text{NO}_2$ . In this way PAN can act as a source of  $\text{NO}_x$  in relatively clean regions of the atmosphere.

#### 1.4.6 Night time chemistry

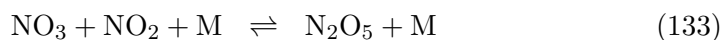
During the night there is no source of photons to initiate the photochemistry which drives most of the chemistry of the troposphere. At night, the nitrate radical ( $\text{NO}_3$ ) takes over from OH as the chief oxidant in the troposphere. During the day,  $\text{NO}_3$  concentrations are small mainly due to photolysis but also due to reaction with NO.



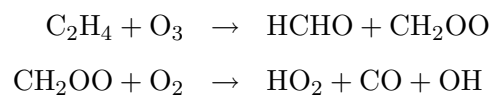
$\text{NO}_3$  acts as an oxidant with hydrocarbons in a similar manner to OH, but reacts far more slowly.



The nitrate radical can also form  $\text{N}_2\text{O}_5$ , which is a night time reservoir for  $\text{NO}_2$ .  $\text{N}_2\text{O}_5$  can thermally decompose to return its precursors, and can also react with water heterogeneously (i.e. on clouds) to form nitric acid.



Mechanisms for  $\text{HO}_x$  production at night from alkenes have been suggested [*Paulson and Orlando*, 1996; *Ariya et al.*, 2000]. These mechanisms involve the reaction of an alkene with ozone, forming formaldehyde and  $\text{HO}_x$  products.



## **2. Modelling atmospheric chemistry and transport**

### **2.1 Introduction**

This Chapter summarises the development of numerical models which are now routinely used to investigate chemistry and transport in the atmosphere. A hierarchy of models exist, each type designed for application to different aspects of the atmospheric system. The philosophy behind the development and structure of different model types is discussed, before describing the models used to obtain results in this thesis.

The role of models in assisting our understanding of the atmospheric system is discussed in Section 2.2. Different formulations for the treatment of transport and chemistry are presented in Section 2.3, including a discussion of the novel reverse domain filling approach. The TOMCAT CTM is described in Section 2.4 and the CiTTyCAT model is described in detail in Section 2.5.

### **2.2 The Role of Models**

Numerical models of the atmosphere play a central role in understanding the past and present atmosphere, and predicting the possible future states of the atmosphere. Such models are involved in a sequence of steps necessary in advancing our understanding of these states.

Our understanding of the current atmospheric state is advanced through model val-

validation using observations from the real atmosphere. Models are a mathematical description of how we understand different processes in the atmosphere to interact and their impacts on parameters that we can observe. Using best knowledge of how these parameters should evolve, the model can be compared directly with observations made in the real atmosphere. Such comparisons allow validation of our understanding of what controls the processes governing the current state of the atmosphere. Such comparisons can also identify missing processes in the model, i.e. deficiencies in our understanding.

A validated model, which is well understood and represents our best understanding of the atmosphere can then be used to test hypotheses. The model allows an investigation into the atmospheric impact of a change in the rate of a process or the introduction of a new process which is believed to be important. An example of such a study is described in Chapter 8, where the atmospheric implications of a modified photodissociation reaction rate are investigated.

Such studies are also useful for testing the evolution of the atmosphere following predicted future changes in factors controlling its state. Both future air quality and climate can be simulated through use of atmospheric models forced by our best estimates of how influencing factors such as surface emissions will evolve into the future. Such simulations allow policy makers to investigate the impacts of any proposed changes in human influence on the atmosphere system (e.g. curbing of emissions).

Chemical transport models (CTMs) are used to investigate the atmospheric processes responsible for the spatial and temporal concentration distributions of trace gases in the atmosphere. These distributions depend on source strength of the trace gases, dynamic processes which transport air around the atmosphere, and chemical processes which create and destroy the gases.

CTMs are ‘off-line’ models; the model winds used being calculated separately from the chemistry-advection simulation itself. They use winds and temperatures output from more complex general circulation models (GCMs) or operational weather forecast models to advect air in their model atmospheres. This approach is useful, since the simulation is linked to real meteorology, with operational analysed

winds incorporating assimilated global observations from radiosondes, surface sites and satellites. This also means that sensitivities to the chemical treatment can be investigated, with an invariable ‘best estimate’ of the atmosphere dynamics for the time period of study, linked to real meteorology. CTMs are also cheaper to run than more complex GCMs, since expensive dynamical calculations do not need to be performed.

The advection in CTMs is driven by off-line winds, which represent the atmospheric motion at the scale of the resolution of output from the dynamic model. For operational analyses, this is typically of the order of  $1^\circ \times 1^\circ$ . In CTMs, it is therefore necessary to account for processes which transport air on smaller scales. Examples include PBL turbulence and convective transport. In a CTM it is not possible to account for these explicitly, and they must be parameterised. Such parameterisations simplify the processes, so that relationships between large-scale dynamic variables available in the analyses are used to diagnose the magnitudes of the process. Parameterisations can be problematic, leading to erroneous results, as they are crude compared to the detailed mechanisms driving the process in the real atmosphere. A certain amount of ‘tuning’ is therefore often required.

In recent years, with increased computing power, it has become possible to carry out model studies of feedbacks between atmospheric chemistry and dynamics. Such feedbacks exist through atmospheric composition effects on radiation, which in turn drives dynamics, which distributes trace gases. The inclusion of a detailed treatment for trace gas chemistry in a GCM allows these feedbacks to be investigated. GCMs calculate their own dynamics, forced by their own radiation schemes, including feedbacks from the composition of the model atmosphere. Such simulations are far more computationally intensive than CTM simulations, since the chemistry and dynamic calculations must be carried out together explicitly. These studies are especially relevant over long-term climatic timescales, where changes in atmospheric composition may affect the atmosphere’s mean radiation balance, which in turn has significant consequences for atmospheric dynamics. Long-term temperature changes may also affect the kinetics of chemical reactions in the atmosphere. This highlights another use of models, allowing the simulation of the global atmosphere hundreds of years into the future. Such studies have revealed some important possibilities concerning

the future evolution of the Earth’s atmosphere [e.g. *Shindell et al.*, 2003].

## 2.3 Model Formulation

CTMs can generally be grouped into two different types, depending on how the advection of air in the atmosphere is treated.

- Eulerian models divide the atmosphere into a fixed grid of boxes, and the advection of air through the atmosphere is considered as a flux across the boundaries between the boxes.
- Lagrangian models consider the advection of air as non-stationary, isolated air parcels which move through the model atmosphere along paths known as trajectories.

Figure 2.1 demonstrates the conceptual frameworks of the two different model types.

### 2.3.1 Eulerian Models

The majority of CTMs consider advection in an Eulerian framework. The model domain is divided into a fixed grid of cells. Typical grid sizes may range from metres in micro-scale street-canyon type models up to hundreds of kilometres in global CTMs, the number of cells used being limited by computing costs. The models calculate the rate of change of a tracer concentration,  $C$ , in each grid cell according to the wind velocity advecting air across each face of the box and the chemical loss and production rates:

$$\frac{dC}{dt} + \nabla \cdot (C \underline{V}) = P - LC \quad (2.1)$$

This is the ‘continuity equation’, which forms the basis of all models.  $\underline{V}$  represents the velocity vector across the box in all spatial dimensions being modelled and  $P$  and  $L$  are the chemical production and loss rates respectively.

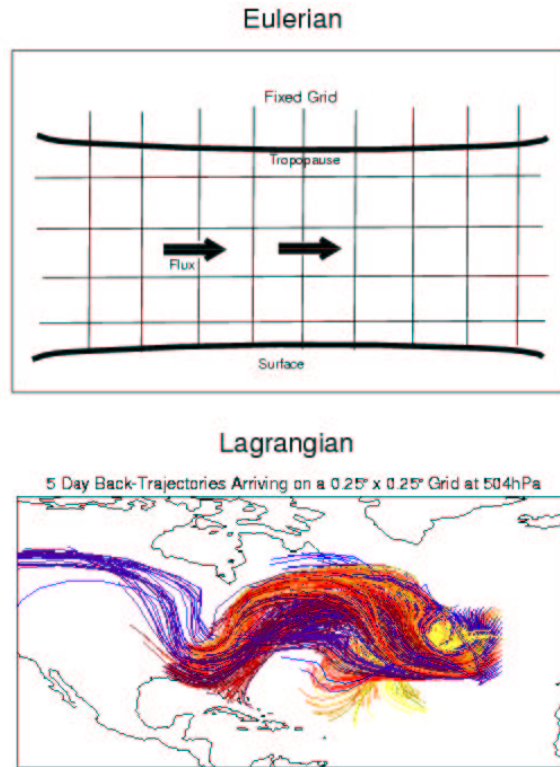


Figure 2.1: *Illustration of the concepts of Eulerian and Lagrangian advection schemes. The Eulerian scheme considers advection as a flux across interfaces between boxes on a fixed grid over the model domain. Lagrangian schemes treat transport as a movement of air parcels through the domain along air mass trajectory paths.*

Eulerian models have been applied to a problems across the range of 0 to 3 spatial dimensions, on a range of scales. A hierarchy of model complexities exists, which is described below in terms of the spatial dimensions considered.

### 0D (box) models

Zero-dimensional (box) models treat a single, isolated parcel of air without a consideration of transport processes. For this reason they are computationally cheap,

and far more detailed chemistry can be included. These models are generally used to investigate detailed chemical mechanisms before they are reduced to be included in large-scale CTMs. They are also useful for examining sensitivities of the chemical system to a particular process under a fixed set of physical conditions [e.g. *Arnold, et al.*, 2004]. Box models are also sometimes constrained by observations of long-lived species to infer concentrations of shorter lived radical species which are assumed to be in steady state in the chemical system [e.g. *Carslaw et al.*, 1999]. Such models are limited in their application to the real atmosphere by their lack of transport.

### 1D models

1D models utilise a single vertical column of grid boxes to simulate the variation of tracers across the depth of the atmosphere. Such models are useful for examining boundary layer mixing processes, and exchange of tracer from the surface across the PBL and into the free troposphere. Since fluxes need only be considered across box interfaces in one dimension, such models have the advantage of being computationally cheap. These models have been used in the past to compute globally average conditions, where advection between the boxes is neglected, each box boundary representing a global average of a pressure surface with a parameterised diffusive transport between layers. This is a gross approximation, and since advances in computing power this modelling approach has been superceded.

### 2D models

Two-dimensional models are generally used to simulate tracer distributions over a latitude-height domain. In the early days of global chemistry-transport modelling, 2D models were used to simulate zonal-mean global tracer distributions over such a domain [e.g. *Law and Pyle*, 1993a,b] since computing power limitations made full 3D simulations infeasible. The 2D simulation allows the use of variations in dynamics, temperature and insolation with latitude in the atmosphere. Any variability with longitude is ignored, meaning that comparisons with location-specific observed datasets are not possible. The use of zonally averaged tracers in global



tropospheric calculations can lead to erroneous results, due to the non-linearity of the photochemical system [*Kanakidou and Crutzen, 1993*].

In the stratosphere, 2D models have been more useful, as variations with longitude are less significant than in the troposphere. Source strengths of tracers in the troposphere will show variations with longitude due to the positions of continents, and air and sea transport routes. In the stratosphere, sources of trace gases from the troposphere are dependent on troposphere-stratosphere exchange mechanisms which show dependence on latitude, but are little affected by longitude. This approach has also now been largely superseded, since 3D simulations of the atmosphere are now possible.

### 3D models

With advances in computing power, 3D CTMs are now widely used over a range of scales. Fluxes across the six interfaces of each grid cell must be considered at each model time step. Three-dimensional chemistry-transport modelling of the global troposphere [e.g. *Stockwell and Chipperfield, 1999*; *Lawrence et al., 1999* ; *Wang et al., 1998*] and the global stratosphere [e.g. *Chipperfield, 1999*] are now routine. Global models vary in horizontal resolution, with grid sizes ranging from several hundreds of kilometres down to less than 100 km. Such models allow detailed investigation of global budgets and burdens of trace gases. 3D global CTMs generally include parameterised treatments for mixing processes occurring on scales finer than the model grid resolution. The 3D framework also allows a full treatment of emissions on a latitude-longitude surface grid.

Mesoscale 3D models [e.g. *Tulet et al., 1999*, *Flatoy and Hov, 1996*] can be employed to study smaller-scale structures, having grid-sizes on the order of 1-20 km. These models are generally driven by on-line calculated dynamics, rather than using off-line winds. Analysed winds are generally used as the boundary conditions at the domain edges. Such models have been used to study the processes affecting venting of polluted PBL air into the free troposphere [*Donnel et al., 2001*] and the complex dynamics associated with frontal systems [*Esler et al., 2003*]. Mesoscale models have the resolution to provide treatments for complex terrain, and detailed schemes for

PBL dynamics and convective systems.

### 2.3.2 Lagrangian Models

The Lagrangian advection framework treats the movement of individual, isolated air parcels through the atmospheric domain. Lagrangian CTMs model an individual air parcels as it travels through the atmosphere along a single air mass trajectory, the path of which is generally calculated off-line from meteorological analyses. The position  $\underline{P}$  of the air parcel is calculated in time according to:

$$\frac{d}{dt}\underline{P}(x, y, z) = \underline{V}(x, y, z) \quad (2.2)$$

The CTM then separately performs calculations on the concentrations of tracers in the advected air mass according to production and loss terms due to chemical processes. This so-called ‘operator split’ approach is common to most Lagrangian CTMs.

The CiTTyCAT model, used in this thesis, is an example of such a model. It is described in detail in Section 2.5. Such models are cheap to operate, since no advection calculation is required. Consequently, it is generally possible to include more detailed photochemistry in this type of CTM than in an Eulerian model. However, single parcel Lagrangian models cannot be integrated for more than a few days, due to the isolation of the modelled air parcel. It is possible to account for emission and surface deposition fluxes in and out of the box, but the lack of diffusive exchange across the boundaries of the air mass with the surrounding air through which it is travelling, means that after a few days the chemistry within the box can become unrepresentative of the region containing the air parcel. Initialisation of the chemistry in the parcel is often taken from grid-point fields output from an Eulerian CTM. The use of a simple, single parcel Lagrangian model over back-trajectories of a few days in length has shown success in simulating the variability in observed tracer concentrations at a surface site [Evans *et al.*, 2000].

As will be discussed in detail in subsequent chapters, treatment of mixing processes,

which may be due to the turbulent PBL, convective transport, or diffusive mixing across air mass boundaries as they are stretched by advection, is difficult and generally highly simplified, or ignored, in the Lagrangian treatment. In this thesis, examples will be given of where the lack of mixing in the Lagrangian framework results in deviations of the modelled tracer values from those observed. It will also be shown that in some cases, the inherent mixing in a global Eulerian model due to the large grid size, means that observed fine-scale structure is smeared out in the simulation. The exploitation of lack of such mixing in Lagrangian models to simulate fine-scale structure is also discussed.

Global CTMs have also been developed using a Lagrangian framework in both the troposphere (e.g. the STOCHEM model [Collins *et al.*, 2000]) and stratosphere (e.g. the CLAMS model [McKenna *et al.*, 2003]). These models employ a sufficiently large number of separate air parcels to cover the global atmosphere. Advection of each parcel and chemistry within each parcel is carried out separately. As discussed above, chemistry-transport modelling of an isolated Lagrangian air parcel for more than a few days leads to unrealistic model output. Global Lagrangian models therefore require a treatment of mixing if they are to be useful over timescales generally modelled by global 3D models. This can be achieved by imposing a fixed Eulerian grid over the model domain. At each STOCHEM timestep, tracer concentrations in Lagrangian air parcels which find themselves within a given Eulerian grid cell are relaxed to the average of the tracer values from that group of parcels. In this way, Eulerian mixing processes are artificially imposed on the Lagrangian parcels to simulate the effects of diffusion in the atmosphere. Similar treatments are used to account for convective and PBL mixing in the model. An alternative treatment to imposing the fixed grid, is to use averaging according to a ‘nearest neighbours’ type approach [e.g. the CLAMS model]. Here, air parcels which find themselves within a given proximity of each other are used to calculate the relaxation parameters used to impose mixing on the set of parcels.

## The Reverse Domain Filling Method

The diverse range of origins of air arriving at a fixed site can explain the observed temporal tracer variability there. Similarly, fine-scale spatial structure of a given parameter within a domain of the atmosphere can also be explained by air masses from differing origins being advected into close proximity. This is the basis of the reverse domain filling (RDF) method [Sutton *et al.*, 1994].

By calculating the back-trajectory origins of a grid of finely spaced points within a given volume, points within the arrival grid can be labelled with the values of a parameter at the air mass origins. This has been shown to successfully simulate the high resolution structure observed in the parameter, on the scale of the finely-spaced arrival grid (e.g. Methven *et al.*, [2003]). In practice, a limit is placed on the scale of the structure that can be simulated by the length of the trajectories used. Without a treatment for mixing, diverse trajectory origins will create a ‘noisy’ field on the arrival grid, with unrealistically strong gradients. Using purely Lagrangian parcels, the RDF advection onto the arrival grid is therefore limited to a few days. As well as limits imposed by the creation of noise, for the RDF method to be valid it must be assumed that the advected quantity is conserved over the length of advection along the back-trajectories. This is a good approximation over a few days for many long-lived atmospheric tracers. It must also be assumed that advection of the air parcels onto the grid by winds of a coarser spatial scale is capable of producing structure on a finer scale which is realistic [Methven and Hoskins, 1999].

Using a Lagrangian CTM, the RDF method has been refined in this thesis to include chemistry, emissions and surface deposition along each back-trajectory. A method of introducing mixing processes along longer back-trajectories will also be discussed in Chapter 7. The use of a Lagrangian CTM along the RDF trajectories means that the evolution of chemical species can be treated in air masses as they are advected onto the high resolution arrival grid. This is an improvement on traditional RDF simulations, where chemical tracers involved in a complex system, which includes species of lifetimes much shorter than the advection period, had to be assumed to remain constant. The method retains the RDF assumptions in that it uses lower resolution gridpoint wind fields to calculate the origins of air masses arriving on

a finer spaced arrival grid. Initial chemical values taken at the origins are then modified according to the detailed photochemistry of the Lagrangian CTM.

Figure 2.2 shows  $\text{NO}_2$  distributions over the south of the UK for 10/04/99, calculated using the RDF technique with Lagrangian advection from ECMWF wind fields of approximately  $1.125^\circ$  horizontal resolution. The arrival grid is isobaric at 980hPa, and air parcels arrive with a spacing of  $0.25^\circ$  in longitude and  $0.25^\circ$  in latitude. The top panel shows the  $\text{NO}_2$  field given by passive advection of  $\text{NO}_2$  from a 3D global Eulerian CTM onto the high resolution grid over 5-day backward trajectories. Addition of a Lagrangian CTM integration along each trajectory produces the field shown in the lower panel. This is the RDF method with chemistry, discussed above. Without chemistry and emissions, the RDF simulation shows fine-scale structure, however 5-day back-trajectory origins of a species as short-lived as  $\text{NO}_2$  result in structure which bears no resemblance to that expected from a surface pollutant at 980hPa over the UK. The addition of emissions and chemistry gives a more realistic fine-scale structure, as fresh emissions are picked up by trajectories passing over conurbations and  $\text{NO}_2$  concentrations are decayed chemically as air parcels are advected away from emission regions. The resulting distribution in this case shows  $\text{NO}_2$  concentrations highest over cities and decaying as the large-scale westerly flow advects air out to the east over the North Sea. The RDF approach with chemistry is a relatively cheap way to generate high-resolution spatial tracer structure.

## 2.4 The TOMCAT Global CTM

The TOMCAT 3D CTM [Chipperfield *et al.*, 1993; O'Connor *et al.*, 2003] is an Eulerian global model, driven by analysed winds from the ECMWF. 3D advection is carried out using the scheme of Prather, [1986] which considers conservation second-order tracer moments. As discussed above, like most 3D CTMs, the model includes parameterisations for sub grid-scale transport processes. Moist convective transport is parameterised according to Tiedtke, [1989] and is described by Stockwell and Chipperfield, [1999]. This includes shallow and deep convective updraughts, and large-scale subsidence. This scheme also includes lightning emissions of  $\text{NO}_x$ , coupled to the convection scheme throughout the depth of the troposphere. A turbulent

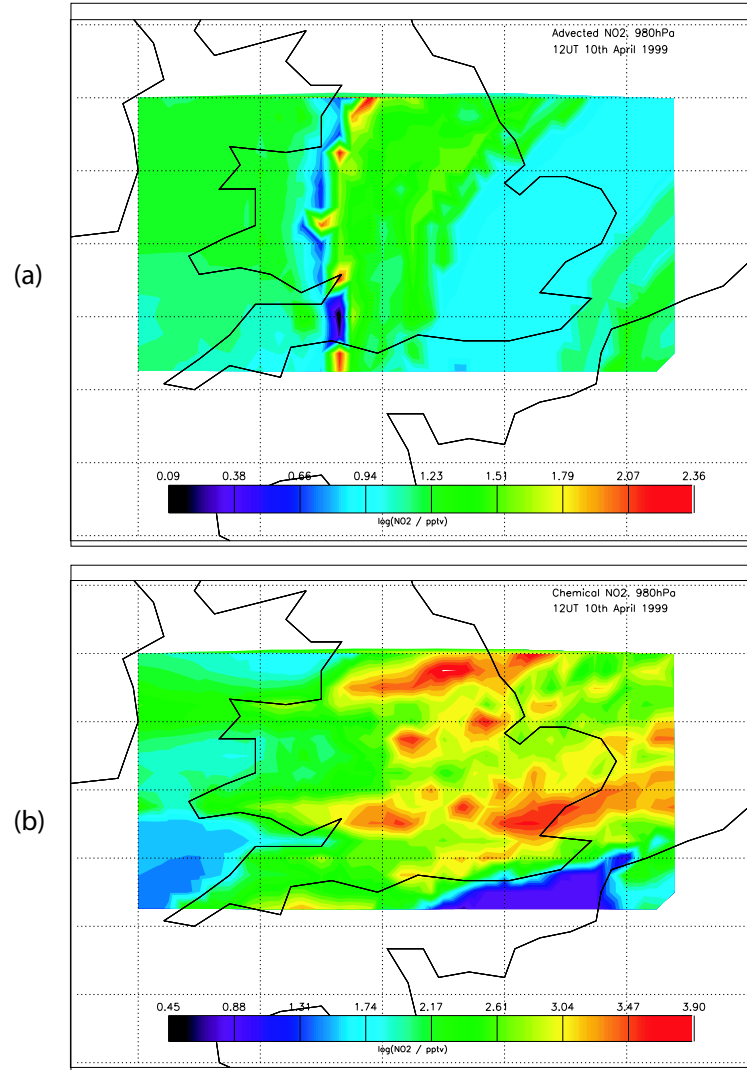


Figure 2.2: Reverse domain filling simulation of surface  $\text{NO}_2$  concentrations (pptv) over the UK. 5-day back trajectories are used, arriving on a high resolution grid at 980hPa. (a) Initial  $\text{NO}_2$  advected from TOMCAT model. (b) As (a) but including full chemistry and emissions from the CiTTYCAT model.

PBL is represented using the non-local diffusion scheme from the NCAR Community Climate Model Version 2 [Holstag and Boville, 1993], implemented by Wang *et al.*, [1999].

Integration of the chemical rates of change is carried out using the IMPACT algorithm [Carver and Stott, 2000]. Gas phase rate coefficients are taken from Atkinson *et al.*, [1997] and DeMore *et al.*, [1997]. Photolysis rates are pre-computed and taken from an offline integration of the Cambridge 2D model [Law and Pyle, 1993a]. Both wet and dry deposition of species are considered. These schemes are described in detail by Giannakopoulos *et al.*, [1999].

The model runs discussed in this thesis use a horizontal resolution of approximately  $2.8^\circ$  (128 grid boxes in longitude  $\times$  64 grid boxes in latitude) with 31 levels from the surface to 10hPa. The tropospheric chemistry scheme used comprises 48 gas phase species, and considers over 130 reactions, and is treated using the ASAD package [Carver *et al.*, 1997]. As well as basic  $\text{HO}_x$ - $\text{NO}_x$ - $\text{CH}_4$  tropospheric chemistry, two non-methane hydrocarbons are included ( $\text{C}_2\text{H}_6$ ,  $\text{C}_3\text{H}_8$ ), as well as acetone and PAN. Emissions are taken from the Third Annual Assessment of the IPCC [2001].

## 2.5 The CiTTyCAT Lagrangian model

The basic version of the Cambridge Tropospheric Trajectory model of Chemistry and Transport (CiTTyCAT) [Evans *et al.*, 2000] is an off-line Lagrangian CTM, which models gas-phase tropospheric photochemistry along a single 3D air parcel trajectory. Temperature, pressure and specific humidity are interpolated from the atmospheric analyses used to calculate the air parcel trajectory and used in the model chemistry scheme. Surface emission and deposition processes act on the air parcel as it enters the PBL.

### 2.5.1 Advection and mixing

The air parcel follows a 3 dimensional trajectory through the atmosphere which is calculated offline from the resolved wind field of a GCM or atmospheric analyses.

The standard model uses trajectories calculated from ECMWF analysed winds at a horizontal resolution of T106 ( $1.125^\circ \times 1.125^\circ$ ) with 60 vertical levels [Methven, 1997]. Surface pressure is taken from the analyses and used to calculate the height of the air parcel above the surface. In Chapter 6, trajectories output from a mesoscale GCM are also used to force the model.

Advection by trajectories derived from large-scale winds means that there is no inclusion of sub-grid transport processes due to convection or turbulent mixing. Concentration changes in air parcels can only result from chemical reaction, or deposition and emission in the model boundary layer. In Chapter 7 a method of introducing mixing into the model will be discussed and its effects assessed.

## 2.5.2 Chemistry scheme

Ninety tropospheric trace gases are considered by CiTTyCAT, including basic tropospheric photochemistry ( $\text{HO}_x$ ,  $\text{NO}_x$ , CO,  $\text{CH}_4$ , ozone, HCHO etc), as well as the oxidation of ten non-methane hydrocarbons ( $\text{C}_2\text{H}_2$ ,  $\text{C}_2\text{H}_4$ ,  $\text{C}_2\text{H}_6$ ,  $\text{C}_3\text{H}_6$ ,  $\text{C}_3\text{H}_8$ ,  $\text{C}_4\text{H}_{10}$ ,  $\text{C}_5\text{H}_{12}$ ,  $\text{C}_6\text{H}_{14}$ ,  $\text{C}_6\text{H}_6$ ,  $\text{C}_7\text{H}_8$ ) in a parameterised scheme [Hough, 1991]. Oxidation of isoprene ( $\text{C}_5\text{H}_8$ ) and acetone ( $\text{CH}_3\text{COCH}_3$ ) are explicitly included with reduced mechanisms. Gas-phase kinetic data are taken from IUPAC, 2002 [[http : //www.iupac – kinetic.ch.cam.ac.uk/](http://www.iupac-kinetic.ch.cam.ac.uk/)] where available, with additional information from JPL, [2003] and the Leeds Master Chemical Mechanism [[http : //www.chem.leeds.ac.uk/Atmospheric/MCM/mcmproj.html](http://www.chem.leeds.ac.uk/Atmospheric/MCM/mcmproj.html)]. The scheme comprises over 200 gas-phase bimolecular and termolecular reactions.

## 2.5.3 Photolysis

Photodissociation of photolabile species is treated according to the 2-stream isotropic approach adapted from the scheme of Hough [1988]. The model atmosphere is split into 35 levels between the surface and the top of the atmosphere at 32km, and scattering and absorption is considered at each of these levels, to calculate the actinic flux over 171 wavelength intervals [WMO, 1985] at each level centre. Scattering of light by molecules and aerosols is isotropic, meaning that half is scattered downward



and half upwards. Six successive orders of scattering and molecular absorption of the direct beam are calculated at each level. Scattering and absorption of diffuse light produced by scattering the direct beam is treated separately, with an increased path length of a factor  $2\cos\theta$  [Madronich, 1987]. Absorption due to  $O_2$  and  $O_3$  is considered, with the vertical profile of  $O_3$  taken from the US Standard Atmosphere, which is representative of mid latitudes with a total ozone column of approximately 350 Dobson Units. Rayleigh molecular scattering is considered, calculated as a function of wavelength. Scattering by aerosol is also included using a simple aerosol profile from *Braslau and Dave* (1973) with a total optical depth of 0.1.

#### 2.5.4 Boundary layer and surface deposition

CiTTyCAT uses a very crude parameterisation for boundary layer treatment, employing a climatology of monthly mean daily maximum boundary layer heights from an assimilation of global meteorological data with a resolution of  $2^\circ$  latitude  $\times$   $2.5^\circ$  longitude [Schubert *et al.*, 1993]. The use of the maximum daily boundary layer heights is to allow adequate dispersal of emitted pollutants across the PBL height and gives a crude approximation to the formation and re-incorporation of a residual layer as the PBL height falls and again rises over a diurnal cycle. While this treatment grossly over-simplifies the behaviour of the boundary layer, a more rigorous treatment would require detailed information regarding turbulence and convective fluxes in the PBL region. In addition, using a diurnally varying PBL height would require some parameterisation of the mixing between the rising PBL and the residual layer, and between the residual layer and the free troposphere. Although crude, the simple treatment used is seen to provide an adequate treatment of the effects of PBL processes on the air parcel and of the dispersal of emissions.

Dry deposition of trace gases is considered when the air parcel is within the model boundary layer. The ‘deposition velocity’ approach is used, which parameterises the rate of loss of a species according to the thickness of the depositing atmospheric layer (here the PBL) and a characteristic velocity dependent on the species and the land surface type. Deposition velocities in CiTTyCAT are supplied for species based on five land surface types: water, forest, grass, tundra/desert and ice/snow, at 1m

above the surface. The velocities at the centre of the depositing layer are calculated from the 1m velocities and advection speed of the air parcel in the PBL using the method of *Isaksen et al.*, [1985]. Land surface data is taken from a high resolution land-sea mask of  $1/12^\circ$  resolution, in conjunction with data from a global land-use archive [*Matthews*, 1983 and *Wilson and Hendershon-Sellers*, 1985].

### 2.5.5 Surface emissions

Surface emissions are incorporated into a CiTTyCAT box when it passes into the model boundary layer. The emission of a species is considered by assuming that the emitted mass is well mixed across the height of the planetary boundary layer. This converts the surface mass flux to a rate of concentration increase in the PBL, and so the emission is added to the box in the PBL at a rate determined by the PBL height. This approach is commonly used in Lagrangian CTMs [e.g. *Collins et al.*, 2000].

Emission data for anthropogenic species are taken from the EDGAR v3 inventory [<http://www.rivm.nl/env/int/coredata/edgar/index.html>], which provides emissions data for CO, NO<sub>x</sub> and VOCs on a  $1^\circ \times 1^\circ$  global grid (see Fig. 2.3). Speciation of VOC is taken from the CORINAIR inventory [*European Environment Agency*, 1994], in the absence of adequate information from EDGAR. These emissions are now commonly used in global CTMs, providing an up-to-date comprehensive global coverage of natural and man-made gas sources at relatively high resolution. Emissions of isoprene are taken from the global inventory of *Guenther et al.*, [1995].

### 2.5.6 Initialisation

Chemistry in CiTTyCAT is initialised by interpolation of 2D concentration fields from the Cambridge 2D model [*Law and Pyle*, 1993a,b; *Law and Nisbet*, 1996] or 3D global fields from a  $2.8^\circ \times 2.8^\circ$  full chemistry integration of the TOMCAT model [*F.M. O'Connor*, *Personal communication*, 2001], interpolated to the trajectory start time and position. The 2D model output provides initialisation for ozone, CO, HCHO, NO, NO<sub>2</sub>, CH<sub>4</sub>, PAN, H<sub>2</sub>O<sub>2</sub>, CH<sub>3</sub>OOH, C<sub>2</sub>H<sub>6</sub> and C<sub>3</sub>H<sub>8</sub>. The TOMCAT

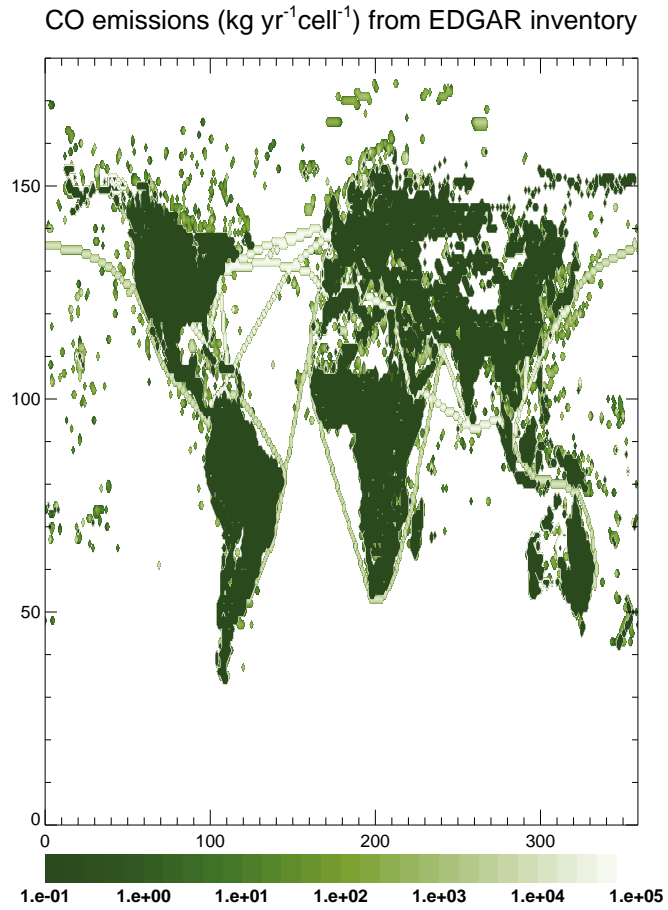


Figure 2.3: *Global CO emissions from  $1^\circ \times 1^\circ$  surface grid cells from the EDGAR v3 inventory, which accounts for a comprehensive suite of anthropogenic sources including land and sea transport.*

model provides global output of 48 tropospheric trace gases, any of which can be used to initialise the CiTTyCAT model.

## 3. The EXPORT Campaign: Data and interpretation

### 3.1 Introduction

In summer 2000 the EXPORT (European eXport of Particulates and Ozone by long-Range Transport) experiment was conducted over central Europe. The scientific aims of the experiment were to evaluate the import and export of ozone and its precursors to and from the European region. Three aircraft were involved: the UK Met Office C130, the DLR Falcon and the French Mystère, all based at DLR in Oberpfaffenhofen, Germany. To complement the range of in-situ measurements of trace gases made by the C130 and Falcon, the Mystère was equipped with an upward looking ozone lidar. The Met Office C130 made a transfer flight from Boscombe Down, UK to Oberpfaffenhofen and a further 5 science flights.

In this Chapter, the observations from these flights are analysed in the context of the transport regimes encountered. Analysis is made based on the observations only, without assistance from atmospheric chemistry-transport models.

In Section 3.2, the data collection on board the C130 aircraft is described. Section 3.3 describes the calculation of back trajectories used to aid the analysis. The location of the flights and meteorological conditions are described in Section 3.4. Standard tropospheric trace gas measurements are described for each flight in Section 3.5, with reference to the three-dimensional air mass structure encountered by the aircraft, with the aid of a reverse domain filling trajectory method.

## 3.2 C130 Instrumentation

The C130 aircraft was equipped with standard instrumentation for meteorological measurements and additional instrumentation for the measurement of trace species relevant to tropospheric photochemistry.

### 3.2.1 Temperature, Humidity and Position

The position of the aircraft and thermodynamic quantities were measured by the Meteorological Research Flight (MRF) group of the UK Met Office. Temperature was measured using a Rosemount 102AL platinum resistance thermometer with accuracy  $\pm 0.3\text{K}$  [Inverarity, 1999]. Two humidity ( $q$ ) measurements were made. The first used Lyman- $\alpha$  fluorescence [Nicholls *et al.*, 1990] with an accuracy of  $\pm 15\text{ppmm}$ , and the second measured dew-point temperature with a General Eastern 1011B thermoelectric hygrometer. Static pressure was measured by a variable capacitance method (Rosemount 1201F) with an accuracy  $\pm 3\text{hPa}$ . Aircraft position was determined by a global positioning system (Navstar XR5) with an accuracy of  $\pm 50\text{m}$ .

Specific humidity is calculated from dew point temperature using the formula of Bolton [1980]. The accuracy of the hygrometer measurements at low dew-points decreases ( $\pm 0.3\text{K}$  at  $270\text{K}$ ,  $\pm 1\text{K}$  at  $200\text{K}$ ), and the response is slower, and so following Methven *et al.*, [2003], in this thesis Lyman- $\alpha$   $q$  is used for  $q < 0.0007\text{ kg kg}^{-1}$ , and dew-point  $q$  is used elsewhere. Equivalent potential temperature ( $\theta_e$ ) is calculated from temperature,  $q$  and pressure using the empirical formula of Bolton, [1980].  $\theta_e$  is the temperature attained by an air parcel after it has been lifted dry adiabatically to its lifting condensation level, and then pseudo-wet-adiabatically with respect to water saturation, losing all water to condensation as it is lifted, before being brought down dry adiabatically to  $1000\text{mb}$ . This quantity is conserved following pseudo-adiabatic processes, accounting for latent heating from water vapour. It is expected to be conserved following large-scale advection of air masses in the troposphere, in the absence of strong mixing (see Methven *et al.*, [2003]).

### 3.2.2 Tropospheric trace gases

A comprehensive suite of trace gas observations were made during the five EXPORT science flights. The range of measurements, their accuracies and techniques are summarised in Table 3.1. The data described in this chapter are averaged over 10 second windows along the flight. The C130 science speed is 180 knots, which is equivalent to  $92.5 \text{ ms}^{-1}$ . This gives a spatial resolution of less than 100m for a 1Hz measurement, and a spatial resolution of 925m over the 10 sec averaging window.

Table 3.1: Trace gas instrumentation on board the C130 during the EXPORT campaign.

Species	Technique	Freq.	Acc.	Instit.	Manufacturer / Ref.
Ozone	UV absorption	1 Hz	2%	MRF	Thermoenvironmental
CO	Resonance fluorescence	1 Hz	15%	MRF	<i>Gerbig et al.</i> , [1999]
NO	Chemiluminescence	10s	<21%	UEA	<i>Brough et al.</i> , [2003]
NO <sub>2</sub>	Photolysis and chemiluminescence	10s	<26%	UEA	<i>Brough et al.</i> , [2003]
NO <sub>y</sub>	Gold converter and chemiluminescence	10s	<21%	UEA	<i>Brough et al.</i> , [2003]
HONO <sub>2</sub>	Gold converter and chemiluminescence	10s	<21%	UEA	<i>Brough et al.</i> , [2003]
PAN	Gas Chromatograph	4min	20pptv	MRF	<i>Hov et al.</i> , [2000]
HCHO	Fluorometric	6min	23%	UEA	<i>Hov et al.</i> , [2000]
H <sub>2</sub> O <sub>2</sub>	Fluorometric	1Hz	20pptv	UEA	<i>Hov et al.</i> , [2000]
Organic peroxide	Fluorometric	1Hz	20pptv	UEA	<i>Hov et al.</i> , [2000]
NMHCs	Grab samples			U Leeds	<i>Purvis et al.</i> , [2003]

### 3.3 Air mass back-trajectories

Trajectories used in this thesis are calculated using the UGAMP off-line trajectory model [*Methven*, 1997]. Velocity fields from 6-hourly ECMWF operational analyses are used to integrate the trajectory position, using a fourth-order Runge-Kutta

method with a timestep of 36 mins. The trajectories are three dimensional; vertical advection is achieved using the ECMWF vertical wind component. Velocity, specific humidity, surface pressure, and temperature are interpolated to the particle positions linearly in time, and using a cubic Lagrange method in the vertical followed by bilinear interpolation in the horizontal.

The ECMWF model fields used are T106 spectral resolution (approximately  $1.25^\circ \times 1.25^\circ$ ), with 60 vertical levels from the surface to 0.1hPa. These trajectories do not account for transport which is on a ‘sub-grid’ scale, i.e. too small to be resolved on the grid from which the winds are taken. Processes such as convective transport and turbulence are parameterised in the ECMWF model, and their contributions are not included in the trajectories which are derived from the large-scale analysed winds.

### 3.4 EXPORT flights: location and synoptic conditions

With the exception of the first transit flight from the UK, all the flights operated from Oberpfaffenhofen, Germany ( $48^\circ 05'N$   $011^\circ 17'E$ ). Flight tracks are shown in Figure 3.1. The flights were flown over central Europe, mainly over Germany, Poland, Hungary, Austria, the Czech Republic and Slovakia. Boundary layer flight legs allowed the characterisation of freshly emitted polluted air over this region, and observations in the free troposphere enabled various air mass types to be sampled depending on the meteorology.

Figure 3.2 shows synoptic charts covering the EXPORT period. The five science flights took place under two types of regime. The flights on July 31, August 9 and August 10 sampled the troposphere under high pressure conditions. Under such conditions the troposphere would be expected to be relatively settled with a degree of vertical stability. During vertically stable conditions over Europe, where transfer of freshly polluted air masses to the free troposphere is limited, the large-scale westerly flow in the free troposphere will bring in air masses from diverse origins, which can lead to layers of chemically distinct air masses persisting throughout the depth of the free troposphere [e.g. *Newell et al.*, 1996]. Table 3.2 shows a summary of the

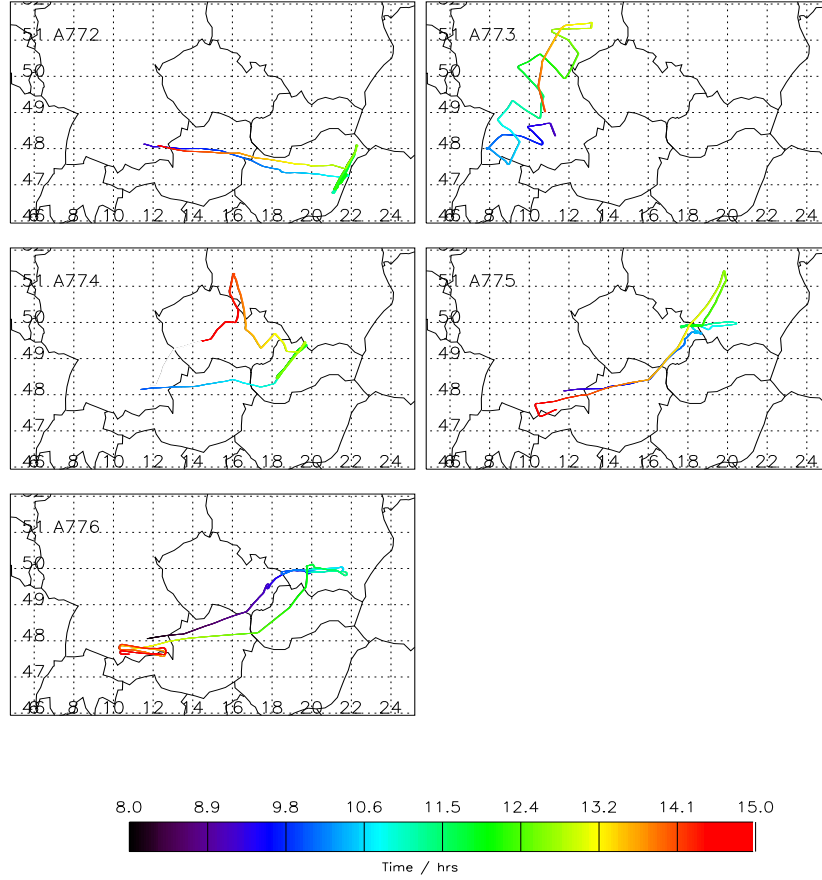


Figure 3.1: *Ground-relative flight tracks for the five EXPORT science flights. Colour indicates time in UT. For further details see Table 3.2.*

five flights.

On August 2 a cold front passed over central Europe, associated with a mid-latitude cyclone centred over the Baltic regions. The passage of such a system results in strong vertical mixing through the troposphere, facilitating the transfer of freshly polluted boundary layer air to the free troposphere. In particular, a strongly ascending airstream, known as the warm conveyor belt (WCB) and associated with the cyclone, lies in the region of the cold front. This is a band of warm, moist air which ascends from near the surface into the upper troposphere. WCBs have been



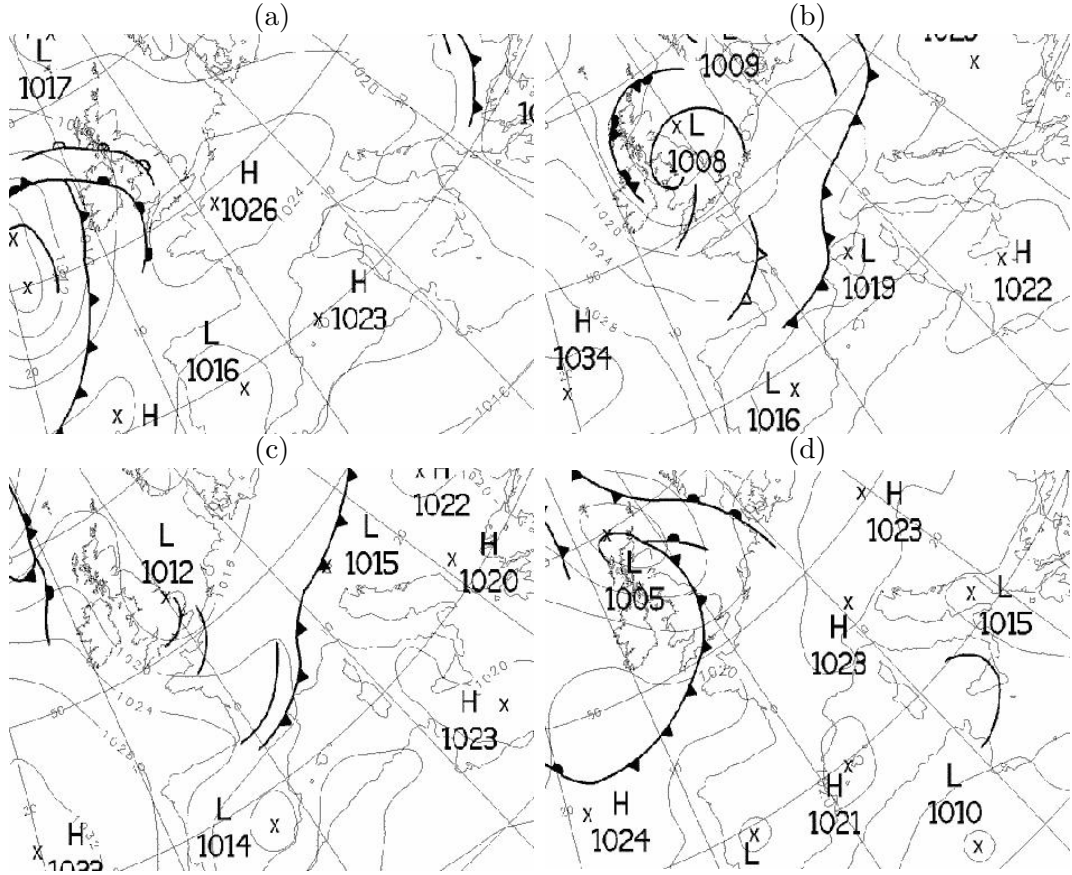


Figure 3.2: UK Met Office surface charts covering the location and period of the EXPORT campaign. (a) 00UT 31/07/00, (b) 00UT 03/08/00, (c) 12UT 03/08/00, (d) 00UT 10/08/00. Taken from: <http://www.wetterzentrale.de/topkarten>

shown to be highly efficient in the transfer of boundary layer pollutants to the upper troposphere [Cooper *et al.*, 2000]. The sampled WCB will be discussed in detail in Chapter 6.

### 3.5 EXPORT data: $O_3$ , CO, $NO_y$ , HCHO, $H_2O_2$ and thermodynamic variables.

In this section observations of chemical and thermodynamic variables are used in conjunction with air mass back-trajectories to estimate the roles of the transport

Table 3.2: Summary of the five science flights flown by the C130 aircraft.

Flight	Date	Location	Features sampled
A772	31/07/00	Austria, Hungary	Hungarian PBL, FT east of Germany.
A773	02/08/00	Germany	Cold frontal region, WCB.
A774	03/08/00	Austria, Slovakia, Czech Rep., Poland	WCB outflow, Czech PBL.
A775	09/08/00	Austria, Czech Rep., Poland	Poland PBL, LRT layers in UT.
A776	10/08/00	Austria, Slovakia, Czech Rep., Poland	PBL/FT Poland, LRT layers in UT.

processes discussed above in determining the composition of the troposphere over Europe.

Vertical profiles of CO, ozone, water vapour, and  $\theta_e$  for the six flights are shown in Figure 3.3. CO profiles for flights A775 and A776 demonstrate a strong decoupling between the polluted PBL and less polluted free troposphere, due to the limited vertical exchange between the PBL and free troposphere under the settled synoptic conditions. *Purvis et al.*, [2003] showed vertical profiles of VOC concentrations which confirmed the presence of a well-mixed freshly polluted PBL, and a more aged free troposphere. This can also be seen in the profiles of water vapour and  $\theta_e$ , which show a sharp discontinuity at the top of the PBL, at about 880hPa and 830hPa on August 9 and 10 respectively. The profiles also demonstrate a degree of layering in the free troposphere with air masses of diverse thermodynamic and chemical signatures observed in close vertical proximity.

By contrast, water vapour and  $\theta_e$  profiles for flight A773 and A774, show a more well-mixed troposphere with a weaker gradient between the PBL and free troposphere. CO concentrations observed in the free troposphere are significantly elevated compared with those observed on flights A775 and A776.

Next, each of the five science flights are examined in detail, with regard to different air mass types sampled. For each flight, a three dimensional picture of the path of the aircraft through air masses of different thermodynamic and physical properties

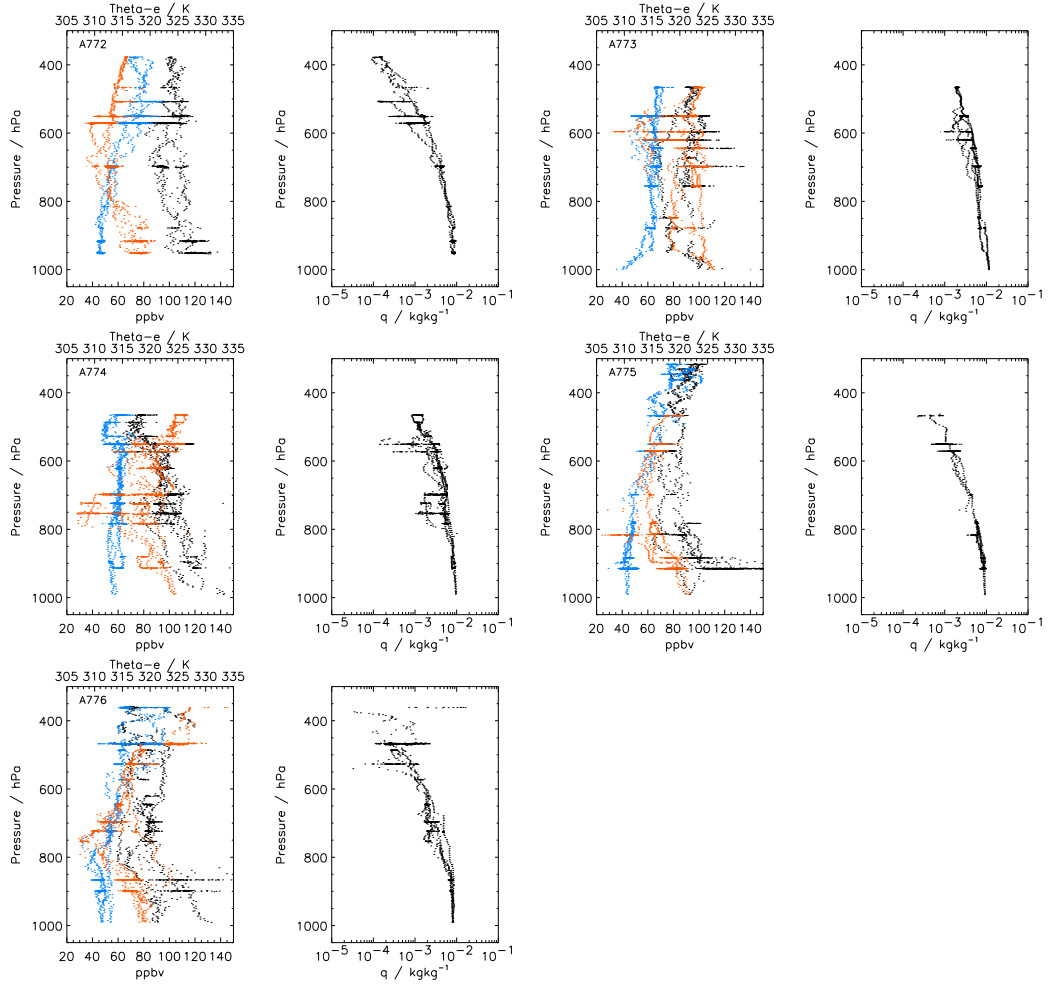


Figure 3.3: Vertical profiles of CO, ozone,  $\theta_e$  and  $q$  for the five EXPORT science flights. Data shown are ten second averages. Black: CO or  $q$ ; Blue: ozone; Red:  $\theta_e$

has been created by projecting the flight track onto a 3D simulation of air mass structure within the domain of the flight. This is achieved using the reverse domain filling (RDF) method described in Chapter 2. The 3D RDF reconstructions of air mass structure shown here are for 12UT on each flight day. Back trajectories are calculated from a finely spaced grid ( $0.25^\circ$  latitude  $\times$   $0.4^\circ$  longitude  $\times$  12-30 hPa in the vertical) in the region of each flight, with attributes  $q$ ,  $\theta_e$  and temperature interpolated from the ECMWF analyses. Following Methven *et al.*, [2003] ‘air mass-relative’ flight tracks are used to indicate the position of the aircraft relative to the 12UT position of the sampled air masses. This is to account for the change in position

of observed features between the 12UT reference time and the time of sampling. In practice, this means that short back and forward trajectories from ECMWF winds are used to shift the flight track to discover the aircraft's position relative to the air masses in the domain at 12UT. This approach is useful for visualising the path of the aircraft through the three-dimensional air mass structure of the atmosphere, which is more difficult with a simple time-series comparison.

### 3.5.1 Flight A772 (31/07/2000)

The first EXPORT science flight took place mainly over Austria and Hungary. Boundary layer observations were made over the Hungary-Romania border region, and higher altitude constant pressure legs were flown in the free troposphere.

Figure 3.4 shows the air mass relative flight track at 12UT overlaid on a RDF reconstruction of the 577hPa pressure surface, showing the change in pressure of the air on that surface over the previous 4 days. This diagnoses regions of ascent and descent from the 3D trajectories. The chosen surface altitude is approximately that of the longer horizontal flight legs between 9.43 - 10.83 and 12.97 - 14.02UT. Specific humidity at 4-day back-trajectory origins is shown to give an indication of the thermodynamic histories of air masses in the domain.

After an initial climb, the aircraft flew out to the east through a region of descent, where air masses of lower specific humidity had been brought down from higher in the troposphere. Here, observed  $q$  (Fig. 3.5) shows a significant amount of structure, with lower values consistent with those from the 4-day RDF simulation. Strong gradients between more moist, polluted air masses and drier, background air masses are evident in the data. The presence of sudden increases in CO,  $q$  and coincident decreases in ozone at between 9.5 and 10.0UT for example, may point to uplift in convective cells which were recorded by the flight crew in the southern regions of the flight. During the second part of this horizontal leg, the aircraft passed into a region of weak ascent, which shows more homogeneity in observed  $\theta_e$  and  $q$ , with values close to those obtained from the 4-day RDF field.  $\text{NO}_x$  becomes quite low, with PAN becoming the dominant component of  $\text{NO}_y$ . Air masses here have ascended weakly from above the PBL over Northern Europe. This air mass is sampled again

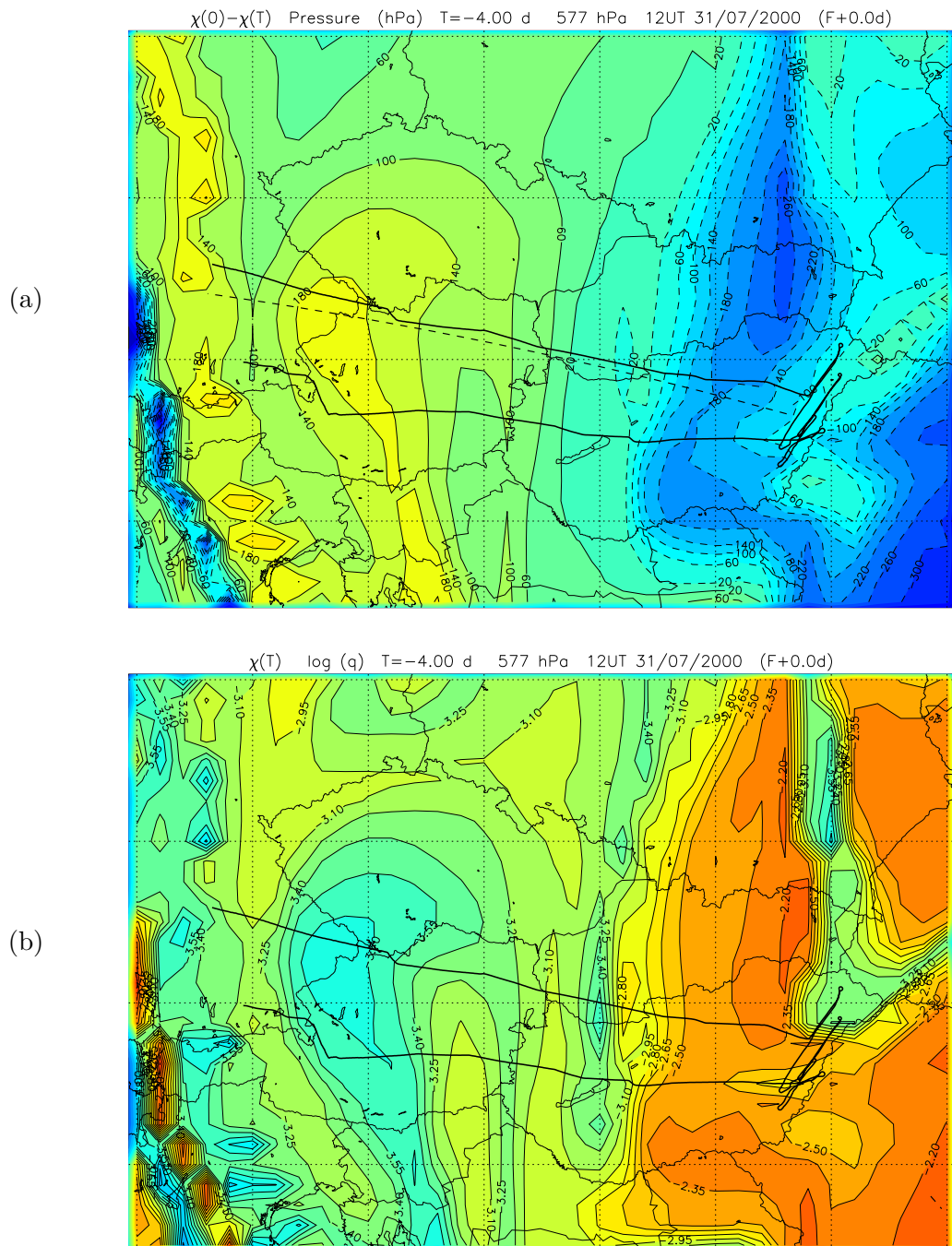


Figure 3.4: 577hPa surface of -4 day RDF simulation in region of flight A772. Air-mass-relative flight path is shown as a solid line. (a) Change in pressure over 4-day back trajectories. Blue regions with dotted contours denote ascent and green coloured solid contours denote descent. (b) Specific humidity at 4-day back trajectory origins.

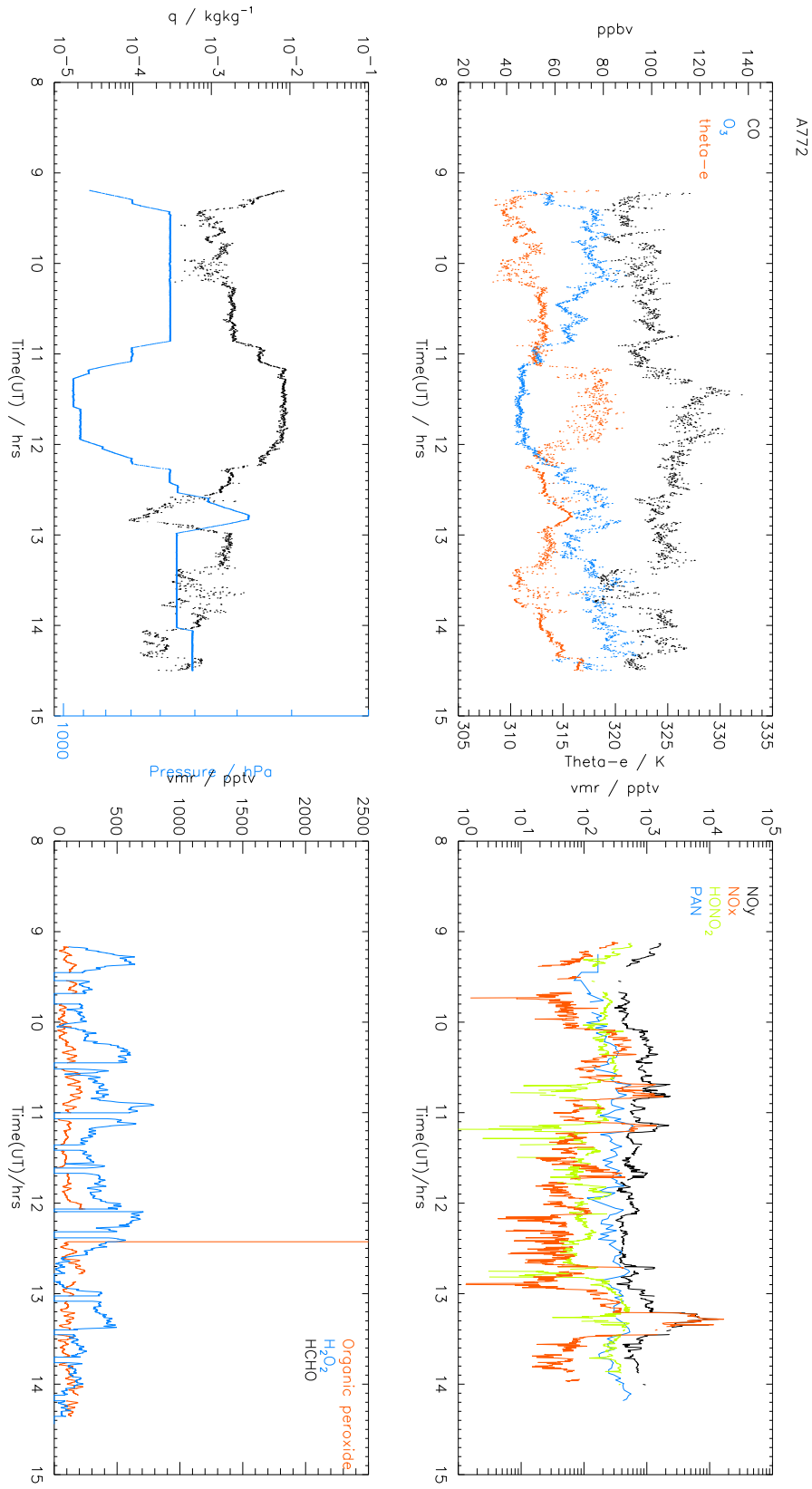


Figure 3.5: Time series observations for C130 flight A772 (31/07/00).

on the return leg, between 13.0 and 13.5UT.

Near the end of the return leg, sharp air mass gradients are seen between relatively dry air which has descended from the UT over the Atlantic and Northern Europe. Ozone is relatively enhanced at  $\sim 80$ ppbv, with CO at around 110ppbv. This may be indicative of aged pollution which has been transported in the UT in a long-range event, for example from the North American region. Immediately following this air mass, a thin filament of ascent from the West Atlantic mid-troposphere is sampled. This has correspondingly lower CO and ozone.

Descent of the aircraft into the Hungarian PBL ( $\sim 11$ UT) shows expected increases in  $q$ ,  $\theta_e$  and CO.  $\text{NO}_x$  and HCHO also show enhancements, as freshly polluted air is sampled. Ozone concentrations are quite low (40-50ppbv), and show an anti-correlation with ozone precursor species. A cross-section through the 3D RDF domain (Fig. 3.6) for the eastern extreme of the flight track, shows the path of the aircraft through the vertical structure of the troposphere during the profiles carried out in the northeast-southwest flight segment along the Hungary-Romania border. As the aircraft descends, it enters a layer which has undergone moderate descent from the north, just above the PBL, and which is low in ozone, with moderate CO. The boundary layer environment is moist and turbulent, as indicated by noisy  $\theta_e$  and CO observations.

### 3.5.2 Flight A773 (02/08/2000)

On August 2, a cold front passed over Germany, and the aim of flight A773 was to sample the associated WCB, in order to characterise its role as a transporter of pollution from the European PBL.

The warm conveyor belt can be seen as a prominent feature in a 3D RDF reconstruction as a region of recent strong ascent and a band of high  $\theta_e$  and elevated  $q$ . Large-scale slantwise ascent in a WCB lifts air from lower levels into the mid/upper troposphere over a timescale of 1.5 - 2 days (see Chapter 6 for a detailed discussion). Figure 3.8 shows the air mass relative flight track of the aircraft imposed on a plot of change in pressure over two day back trajectories in the region of the frontal system.

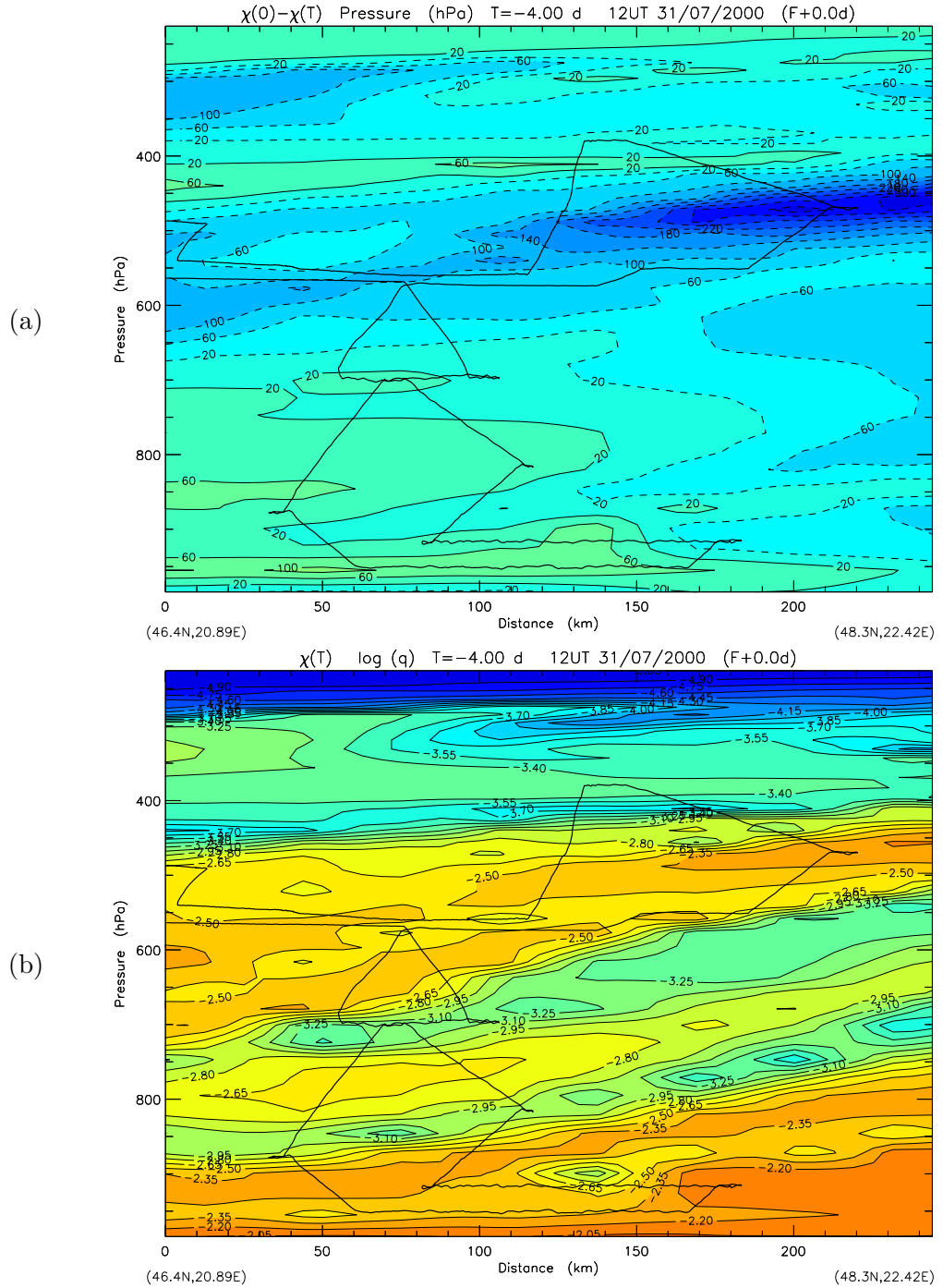


Figure 3.6: *RDF* section through the troposphere in the plane of the northeast-southwest A772 flight track segment at the eastern extreme of the flight path. Air mass relative flight path is shown as a solid line. (a) Pressure at 4 day back trajectory origins. (b) Specific humidity at 4 day back trajectory origins.



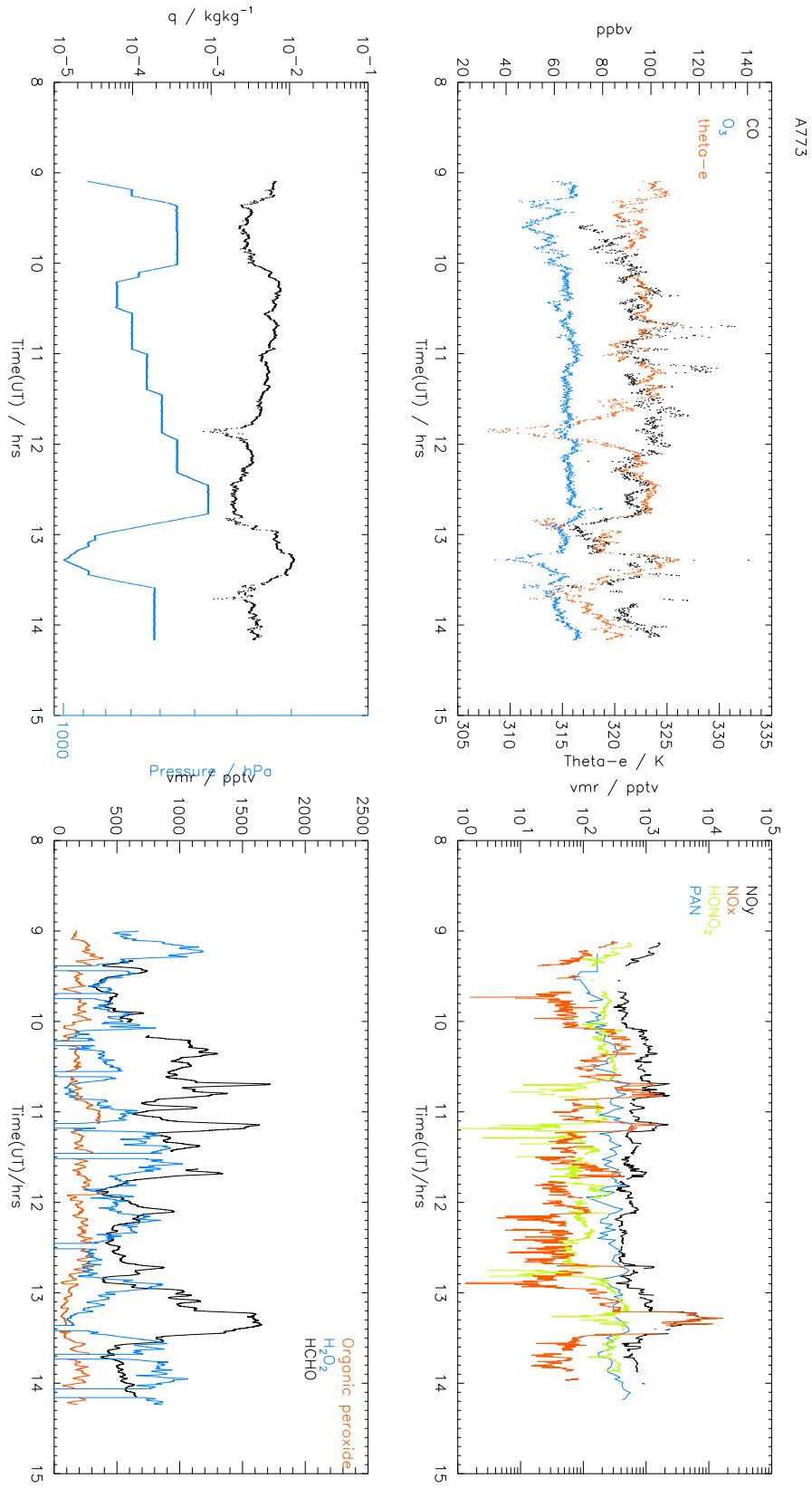


Figure 3.7: Time series observations for C130 flight A773 (02/08/00).

The aircraft flies back and forward across the WCB region, climbing to follow the ascending air stream in a series of six horizontal legs, shown as a series of steps in the altitude plot. Sections through the frontal system showing  $\theta_e$  can be used to visualise the position of the WCB airstream. PBL air with high  $\theta_e$  is dragged up from the surface by the WCB, and over the short timescale for ascent, the ascending air stream can be marked as a band of strongly elevated  $\theta_e$  from short back trajectory origins (Fig. 3.9).

Tracer concentrations (Fig. 3.7) are very well mixed along the ascent through the WCB region, with CO concentrations observed on the higher altitude transects elevated to levels characteristic of those observed in the PBL. The first two horizontal transects through the WCB (legs 1 and 2), are within the main band of strong ascent identified in the RDF reconstruction. The higher altitude transects (legs 3-6) are above this main band. The observed concentrations of CO, however remain typical of those observed in the PBL, indicating the presence of polluted air above the main region of strong ascent. The RDF trajectories however, indicate that the large-scale flow brings in air masses above the region of strong ascent which have not seen recent PBL influence.

*Purvis et al.*, [2003] made a detailed analysis of transport in this frontal system using NMHC compounds to deduce timescales for vertical transport. Their main conclusion was that from the significantly elevated concentrations of short-lived NMHC species in the higher altitude legs through the WCB, it is likely that convection embedded in the WCB system is a significant transporter of PBL mass to the upper levels, as well as the slantwise slow-ascent in the main band. In Chapter 6, the relative roles of slantwise ascent resolved in the meteorological wind fields and convection on a sub-grid scale for this vertical transport are examined in detail, with the help of chemical transport models.

The condensation and precipitation in clouds formed by the ascent of the moist air also has important implications for tracer distributions in the system. Some species are removed efficiently under such conditions, either by washout in rain droplets or by the condensation of gases onto cloud droplets. Acidic species such as  $\text{HONO}_2$  are directly water soluble, and gas-phase  $\text{NO}_y$  and  $\text{HO}_y$  species readily condense onto cloud droplets.  $\text{NO}_y$  data show sharp drops in  $\text{HONO}_2$  which are coincident

$\chi(0)-\chi(T)$  Pressure (hPa)  $T=-2.00$  d 679 hPa 12UT 02/08/2000 (F+0.0d)

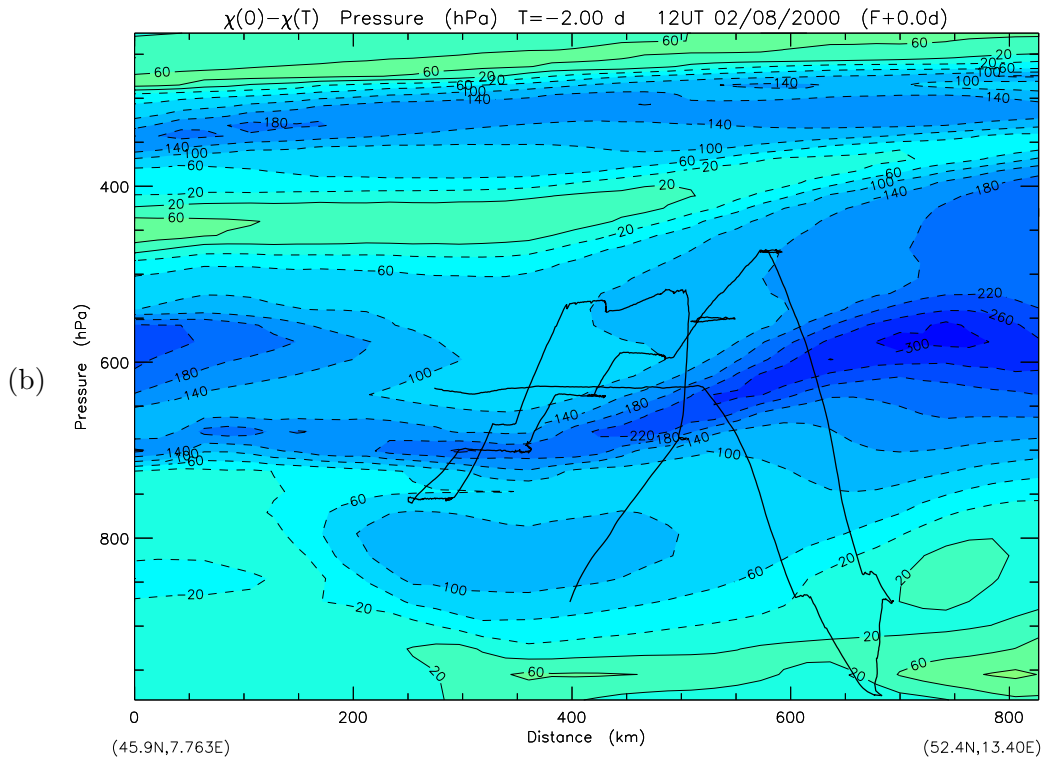
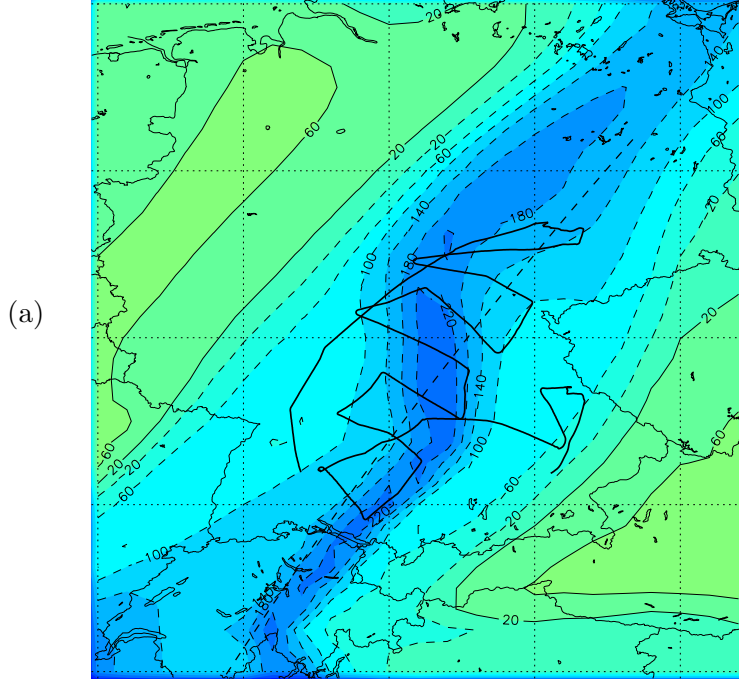


Figure 3.8: 679hPa surface of -2 day RDF simulation in region of flight A773. Air mass relative flight path is shown as a solid line. (a) Change in pressure over 2-day back trajectories. Blue regions with dotted contours denote ascent and green coloured solid contours denote descent. Dotted line shows position of vertical cross-section plotted in panel (b). (b) Vertical cross-section through RDF domain along dashed line in Panel (a), showing change in pressure over 2-day back trajectories.

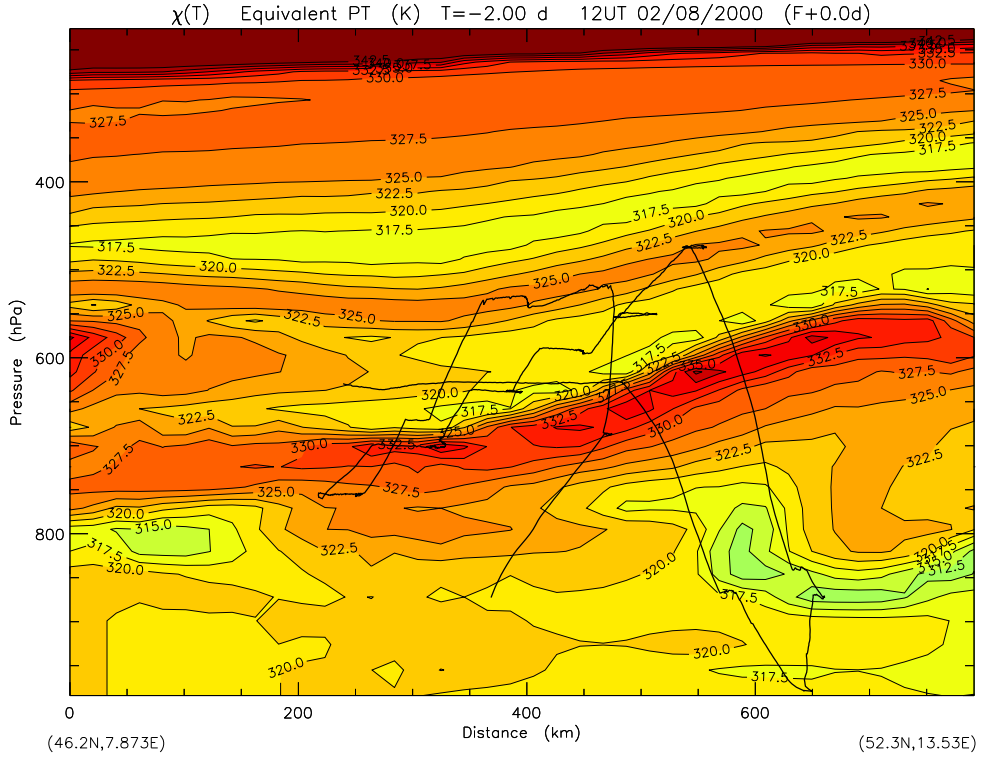


Figure 3.9:  $\theta_e$  at 2-day back trajectory origins arriving on the A773 RDF grid on a vertical cross-section approximately along the axis of the WCB. 12UT air mass relative flight track is shown as a solid line.

with sharp decreases in  $\text{H}_2\text{O}_2$ , suggesting washout of these species. The strongest examples of this occur at around 10.75UT, where the aircraft passes through the main band of ascent and at around 11.25UT when the aircraft is just above the main band of ascent resolved by the RDF simulation.

These sharp drops also coincide with strong enhancements to  $\text{NO}_x$ , HCHO and CO, confirming the position of the aircraft in the region of strong ascent of fresh polluted air from the PBL below. A drop in  $q$  and  $\theta_e$  occurs just before 12UT, as the aircraft is climbing from horizontal leg 4 to leg 5. The aircraft appears to be away from the influence of strong ascent here, and is sampling air which has ascended more slowly from the lower troposphere above the main band of ascent. At this time,  $\text{HONO}_2$  and PAN become the dominant  $\text{NO}_y$  species, with lower  $\text{NO}_x$ , and there is a drop in HCHO and the peroxide.

During leg 6, there is a narrow spike in  $\text{NO}_x$ , and increase in HCHO, and associated increases to both CO and ozone.  $\text{H}_2\text{O}_2$  and  $\text{HONO}_2$  also appear to be suppressed. This flight leg is well above the main band of ascent, and these observations seem to suggest the presence of a relatively deep convective event. Immediately after this event, free tropospheric air is sampled, with higher  $\text{HONO}_2$  and  $\text{H}_2\text{O}_2$ , and much lower  $\text{NO}_x$ .

### 3.5.3 Flight A774 (03/08/2000)

By August 3, the WCB stretches from the Pyrenees region, up into central Germany, and is still active in the vertical transport of moist surface air marked on the synoptic chart marked as a cold front. The cold front stretching between the active WCB region and the parent cyclone, marks a boundary between outflow of warm, moist air masses which have ascended the WCB over the previous 24 hours, and drier air masses which run in from further west in the mid troposphere on the cold side of the marked front. The aircraft flew from the north-east extreme of the active WCB, out to the east and then the north, passing between the warm, moist sector of air masses and the cold sector of air masses which are brought in behind the front from the mid troposphere.

Time series of observations (Fig. 3.10) and the RDF simulation (Figures 3.11 - 3.13) show the initial southern flight leg passing first through air which is strongly ascending as part of the remaining WCB, confirmed by observations of heavy rain and thick cloud. The aircraft then climbed out of the top of the cloud, through more weakly ascending flow above the main band of moist outflow, on the warm side of the front. A vertical profile of stacked horizontal legs was then flown over Slovakia, first through air which had ascended over the previous 1-1.5 days. During the fourth altitude leg of the stack the aircraft exits the ascending moist air, to enter drier air which had arrived from the Atlantic mid troposphere. The moist uplifted air was then sampled again as the aircraft descended to turn north into the colder side of the marked front. At approximately 13.5UT, the aircraft entered dry, cold air descending behind the front, which it again intercepted after a dip into the boundary layer at the northern extreme of the flight path. The aircraft then flew

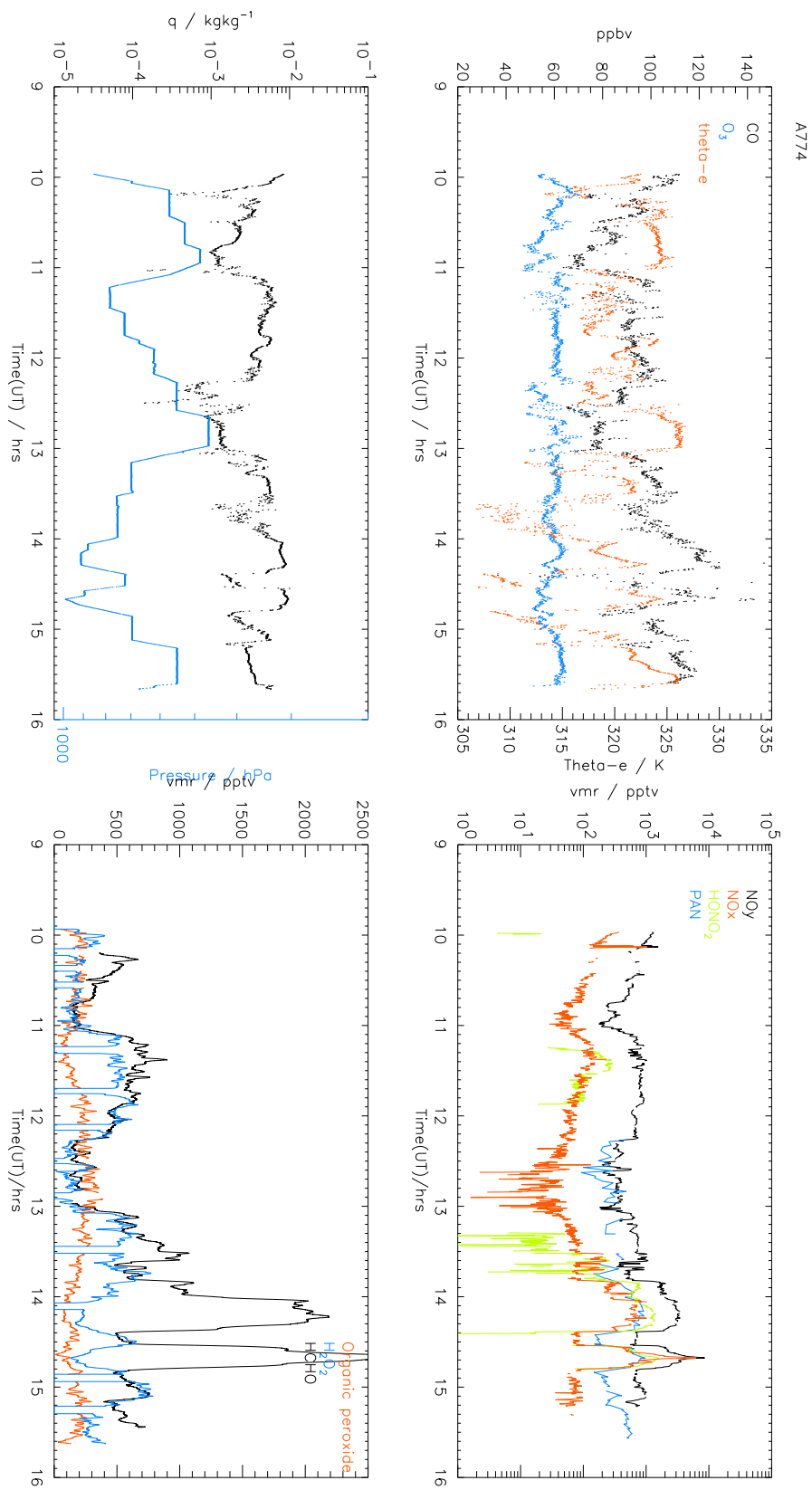


Figure 3.10: Time series observations for C130 flight A774 (03/08/00).

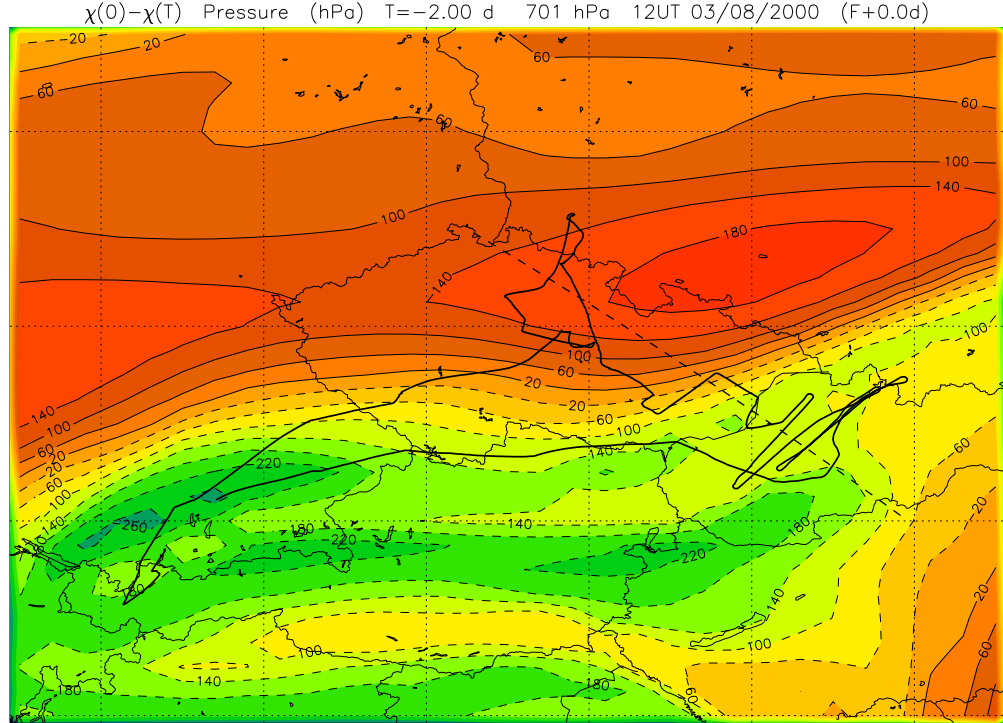
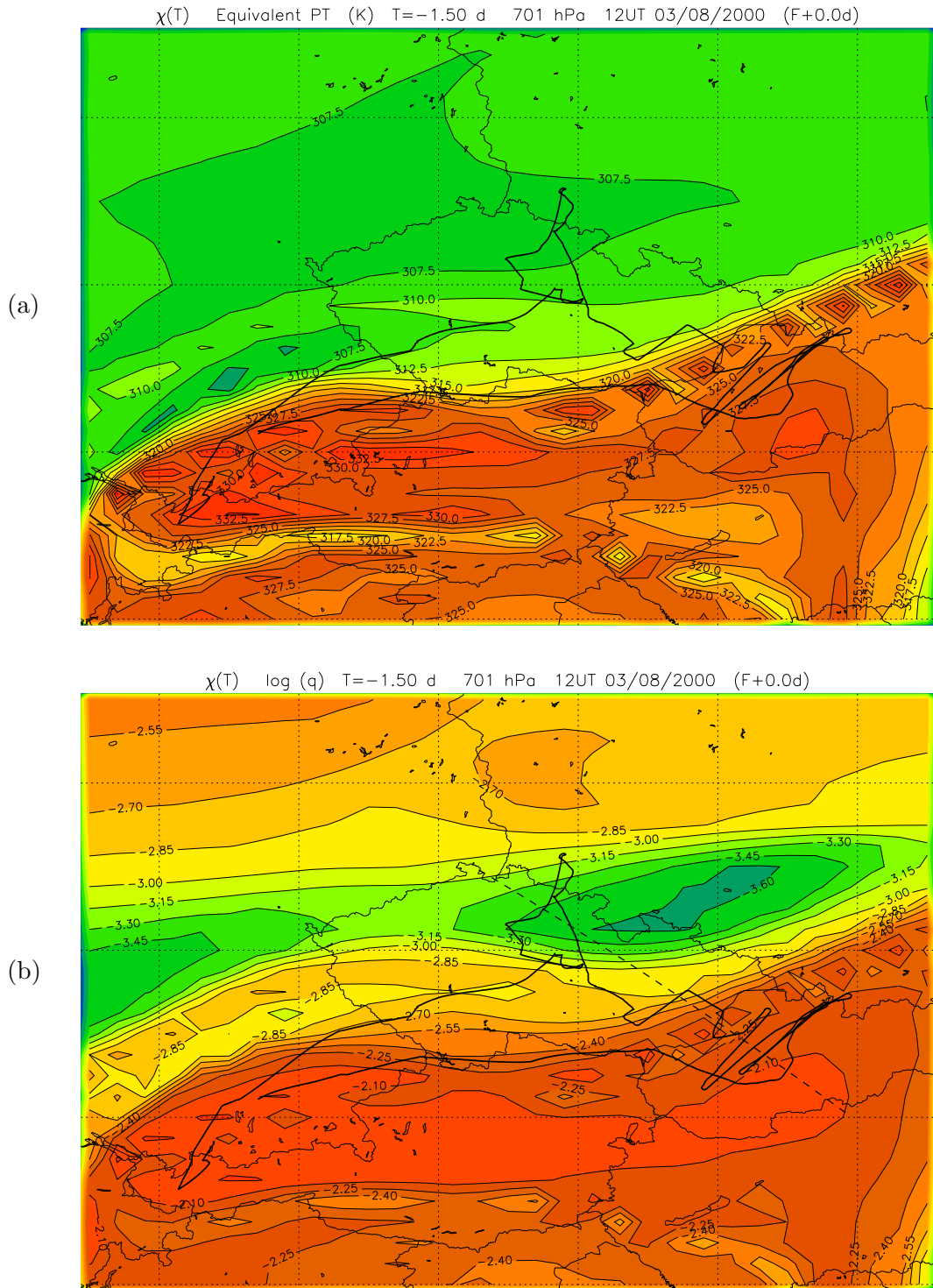


Figure 3.11: *Change in pressure along 2-day back trajectories arriving on a high resolution RDF grid in the region of flight A774. Ascent is denoted by dotted contours. Ascent over the previous two days is seen for air masses arriving on the warm side of the cold front, which are part of the outflow from the active WCB. Solid line shows 12UT air mass relative flight track.*

back towards the active WCB region first sampled, crossing from the cold sector to go back through the moist uplifted air on the warm side.

Observed vertical profiles of CO, ozone and water vapour (fig. 3.3) all show enhancements in the mid troposphere comparable with the vertical distribution of freshly polluted air sampled the previous day. Air masses sampled above the main band of moist outflow before 11.0UT, give a positive ozone/CO correlation with slope of approximately 0.25 (Fig. 3.14), with some showing a higher slope on the third upper leg. These air masses are a mixture of strong ascent over the Atlantic and flow from the North Atlantic mid troposphere. The drier air masses sampled above the moist outflow at the top of the Slovakia stack show reduced CO concentrations with





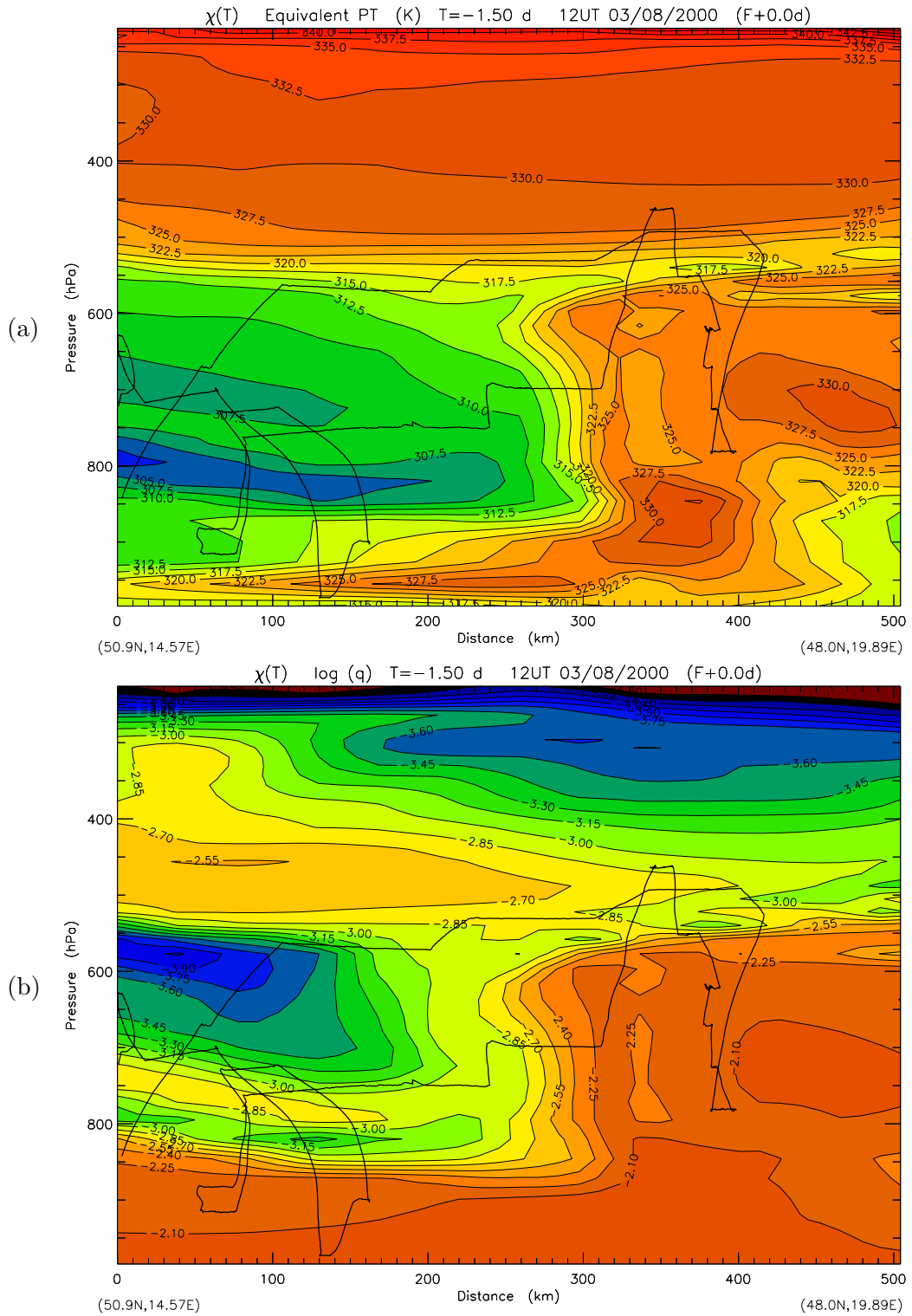


Figure 3.13: Vertical sections along dotted line shown in Figure 3.12 (b), showing boundary between warm, moist air in the outflow from the WCB and colder, drier air running in behind the marked cold front.

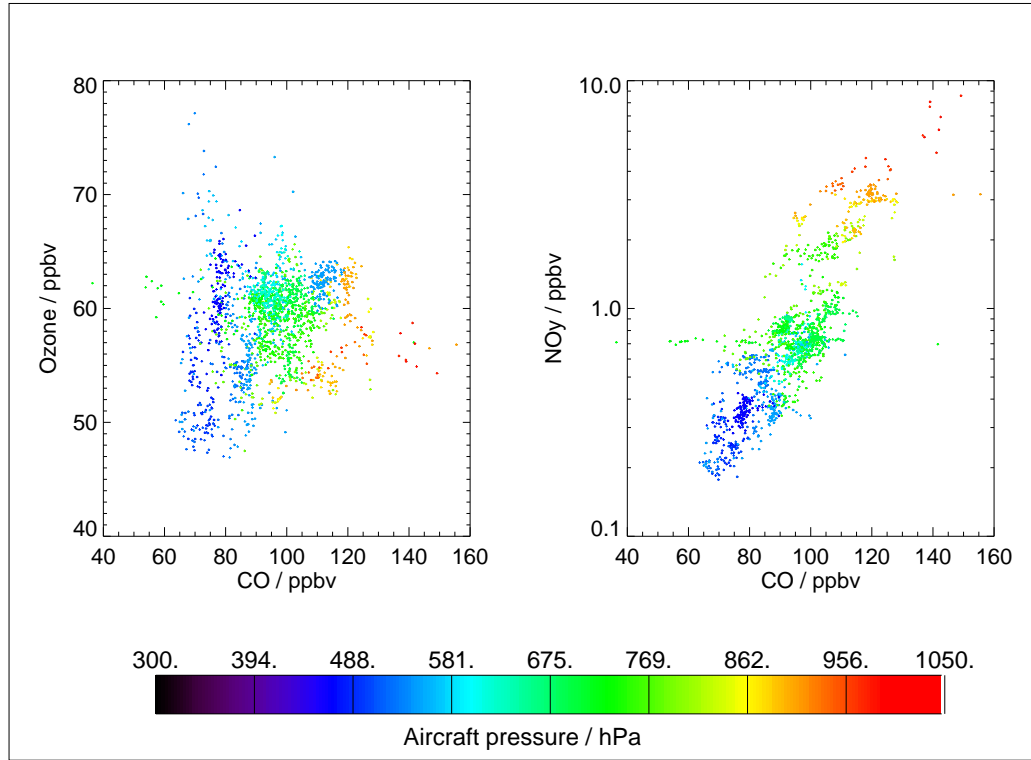


Figure 3.14: *Tracer-tracer correlations coloured by aircraft pressure for flight A774 (03/08/00). Left: ozone (ppbv) / CO (ppbv); Right: total NO<sub>y</sub> (ppbv) / CO (ppbv).*

an ozone/CO slope of about 0.5, indicating more aged polluted air, which has not seen recent uplift in the WCB region. This is confirmed by the low NO<sub>x</sub> concentrations and low NO<sub>x</sub>/NO<sub>y</sub> ratio, as well as low concentrations of HCHO. HCHO and peroxide concentrations are elevated in the WCB outflow region, indicating recent polluted photochemistry. Here, H<sub>2</sub>O<sub>2</sub> is significantly larger than organic peroxide, since little washout has occurred over the time period since uplift of precursors, and also due to the moderately elevated ambient NO concentrations which favour the conversion of organic peroxides to HO<sub>2</sub> via formaldehyde formation.

There is a positive NO<sub>y</sub>/CO relationship (Fig. 3.14) throughout the flight, indicating polluted tropospheric NO<sub>y</sub> sources, with little or no evidence of stratospheric NO<sub>y</sub>. The air at the top of the Slovakian stack has a large fraction of its NO<sub>y</sub> as PAN, with little NO<sub>x</sub>, indicating aged polluted air. It shows a shallow NO<sub>y</sub>/ozone slope of approximately 10-12 pptv/ppbv. This same relationship is seen for NO<sub>y</sub> and

O<sub>3</sub> observed on leg 3, early in the flight as the aircraft flew above the moist WCB outflow, with peroxide and NO<sub>y</sub> speciation as described at the top of the Slovakia stack. Back trajectories show air masses arriving during both of these periods from strong ascent from the PBL over the West Atlantic ocean. The region of the existing WCB, and moist WCB outflow is higher in NO<sub>y</sub> (400-1000pptv) with a steeper NO<sub>y</sub>/O<sub>3</sub> slope, demonstrating fresher polluted air with little NO<sub>y</sub> loss to physical removal such as washout. Similar slopes are seen for some of the air sampled above the main region of outflow.

Boundary layer segments of the flight show quite scattered NO<sub>y</sub>/CO and ozone/CO correlations, with CO concentrations of over 120ppbv. NO<sub>x</sub> concentrations are over 1ppbv, approaching 10ppbv near the surface. HCHO concentrations are over 2ppbv, indicating efficient, fast photochemistry. Peroxides are suppressed in the boundary layer, as removal by both wet and dry deposition is very efficient in the moist PBL environment.

### 3.5.4 Flight A775 (09/08/2000)

Flight A775 took place under settled synoptic conditions, with a high pressure ridge extending into central Europe. The aircraft made extensive boundary layer legs over Czech Republic and Poland, as well as samples of air masses in the upper troposphere which trajectory forecasts suggested had origins in the North American troposphere. Vertical profiles of CO and water vapour (Fig 3.3) reveal a strong PBL / free troposphere gradient, with the height of the top of the well mixed PBL at around 880hPa. Boundary layer CO concentrations range between 80 and over 150 ppbv, and ozone around 40-50ppbv with some very low values of around 25ppbv. Mean mid-tropospheric CO concentrations show less enhancement compared with the more freshly uplifted air sampled during the previous two flights. Layers of enhanced concentrations to both CO and ozone (80-100ppbv) are evident in the upper troposphere, which suggest the presence of filaments of aged pollution.

Boundary layer NO<sub>x</sub> concentrations vary between 1 and just over 10 ppbv, and are the largest component of NO<sub>y</sub>, with HONO<sub>2</sub> around 1 ppbv. Boundary layer HCHO concentrations range between 1500 and 2500pptv, again with suppressed H<sub>2</sub>O<sub>2</sub> due

to deposition. At around 11.66UT, CO levels drop to around 100ppbv, accompanied by a drop in  $\text{NO}_x$  to around 500pptv. At this point in the boundary layer segment,  $\text{HONO}_2$  is the largest  $\text{NO}_y$  component, and there is a reduction in HCHO to around 1100pptv.

The upper altitude flight legs sampled air masses which trajectories indicate have arrived from the west Atlantic and over the North American continent (Fig. 3.16). Initially, correlated CO and ozone concentrations between 80 and 100ppbv are observed on the upper flight leg, with  $\text{NO}_x$  between 20 and 80pptv, and total  $\text{NO}_y$  less than 1ppbv. PAN and  $\text{HONO}_2$  concentrations vary between 100-300pptv. These tracer profiles are indicative of aged photochemical pollution, correlating with back-trajectory origins which suggest import of North American tropospheric air. Larger ozone concentrations may indicate some mixing of air from the tropopause region into uplifted polluted air. Ozone / CO shows a steep, positive slope for pressure less than  $\sim 500\text{hPa}$ , consistent with aged pollution (Fig. 3.17). There is some evidence of a stratospheric signal at the highest altitudes with a steep negative slope for observations at pressure less than  $\sim 390\text{ hPa}$ . The  $\text{NO}_y$  / CO correlation does not show a robust slope at these altitudes, and may indicate a mixed tropospheric-stratospheric character.

Just before 13.0UT, ozone and CO appear to become anti-correlated, with CO concentrations ranging between 80-100ppbv, and ozone concentrations are somewhat lower than those described above (70-85ppbv). Such an anti-correlation may suggest relatively fresh sources of pollution, where photochemistry has had insufficient time to produce ozone from primary precursors. This is unlikely in this case, since ozone concentrations are somewhat higher than those observed in very fresh pollution.  $\text{NO}_y$  speciation also suggests an aged polluted signature, with  $\text{NO}_x$  concentrations ranging between 20 and 200pptv, and  $\text{HONO}_2$  and PAN at around 200-400pptv. Another explanation for the anti-correlation would be the presence of a species, which during its photochemistry in the atmosphere, acts to destroy any ozone produced photochemically from co-emitted precursors or mixed in from the tropopause region. Candidate species for such behaviour may be halogen-containing molecules that can release Cl or Br atoms, which are efficient in destroying ozone [e.g. *Barrie et al.*, 1988]. This possibility will be addressed further in Chapter 4, with reference to

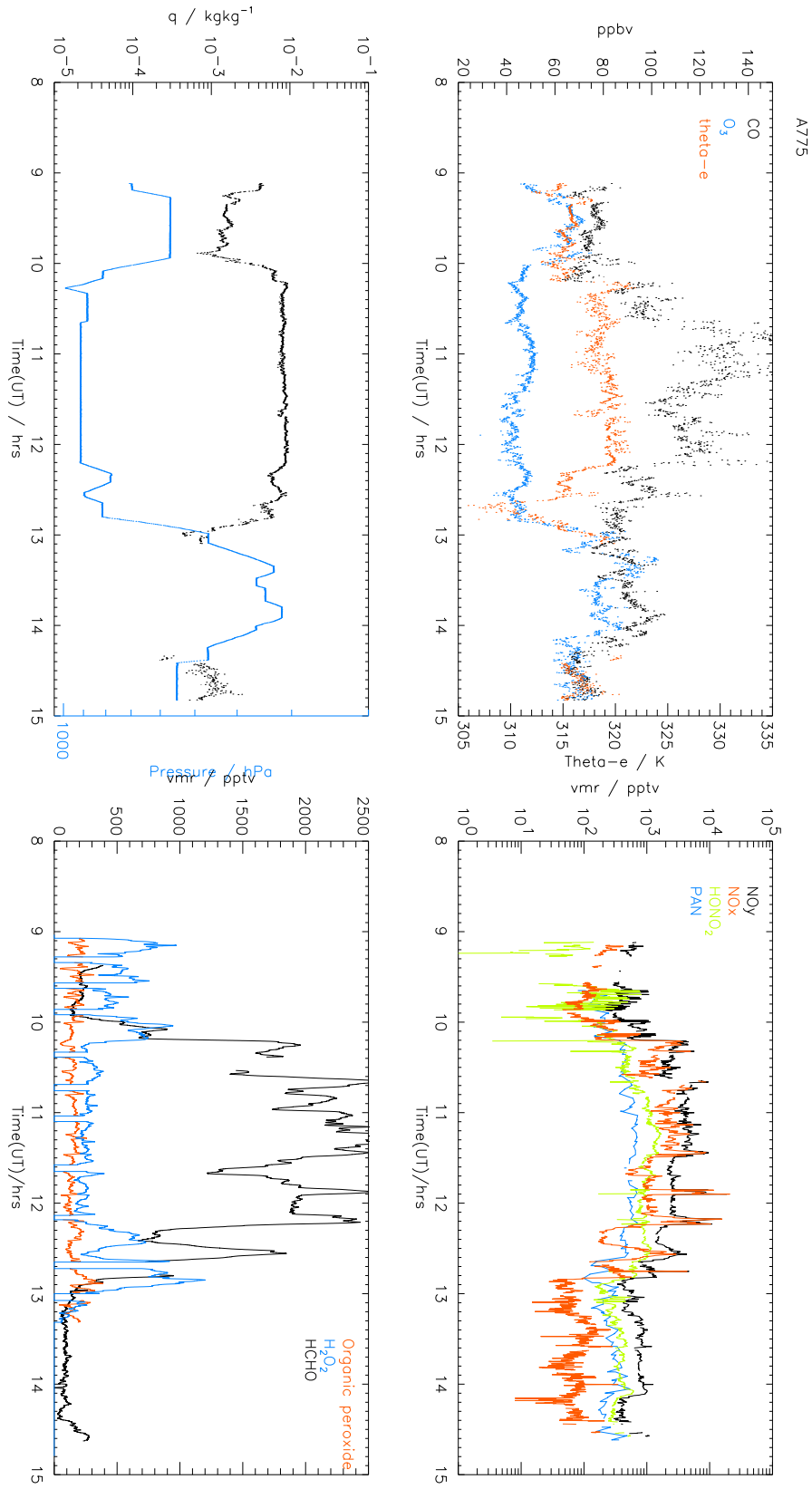


Figure 3.15: Time series observations for C130 flight A775 (09/08/00).

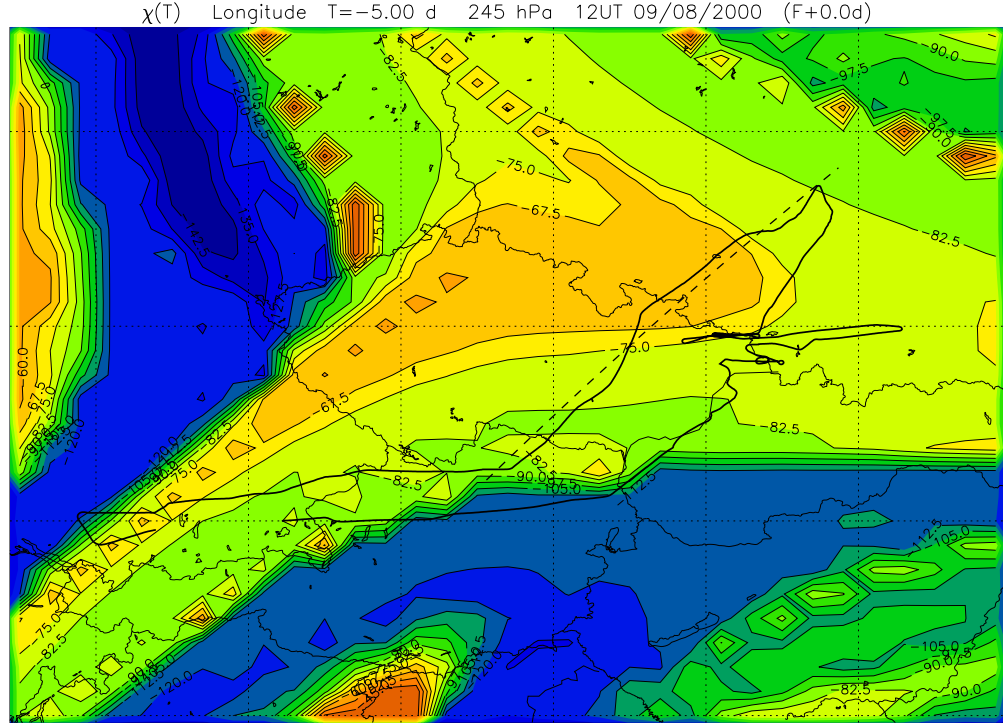


Figure 3.16: *Origin longitude at 5-day back trajectory origins arriving on a high resolution RDF grid in the region of flight A775. Solid line shows air mass relative flight track.*

observed non-methane hydrocarbon concentrations during this period of the flight.

### 3.5.5 Flight A776 (10/08/2000)

During this flight, the high pressure region remained over central Europe, with very similar conditions to the previous day. Boundary layer observations were made over the Czech Republic and Poland. Again, mid/upper tropospheric flight legs were made in air masses which appeared to have been imported from the far west, over the North American continent. The CO vertical profile (Fig. 3.3) again reveals a sharp PBL-free troposphere interface, with an approximate PBL height of 850hPa. Boundary layer CO concentrations range between 80 and over 150 ppbv, with ozone in the range 30-60ppbv. Mean mid-tropospheric CO remains lower than during

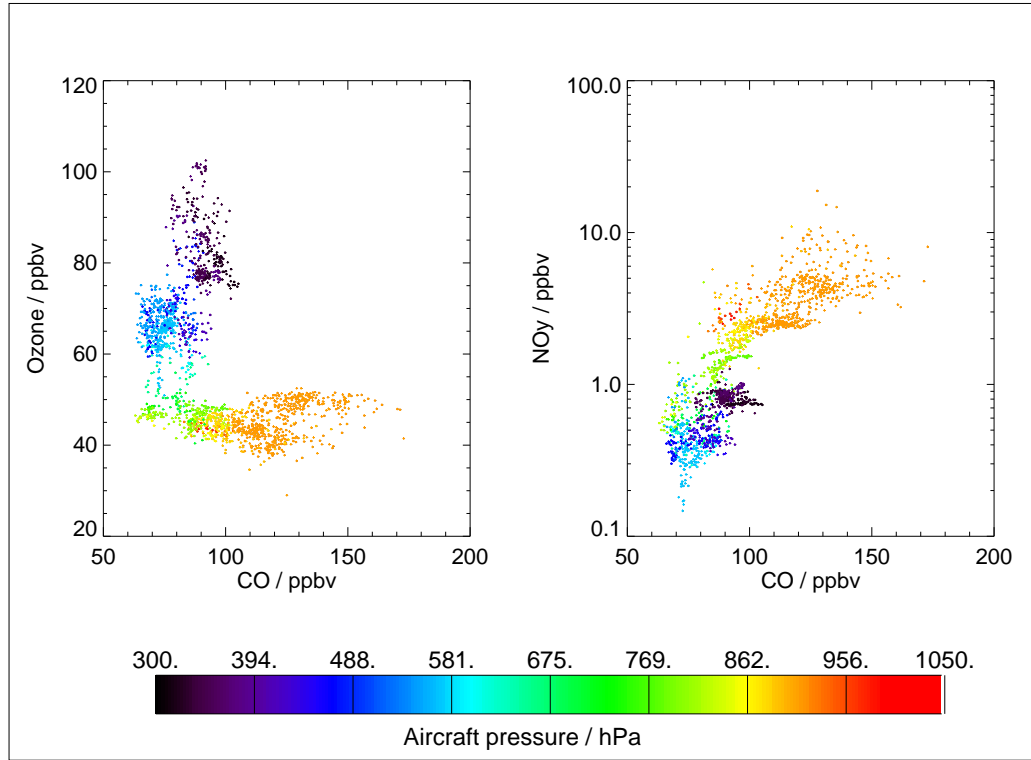


Figure 3.17: *Tracer-tracer correlations coloured by aircraft pressure for flight A775 (09/08/00). Left: ozone (ppbv) / CO (ppbv); Right: total NO<sub>y</sub> (ppbv) / CO (ppbv).*

the more vertically well-mixed conditions of A773 and A774, but distinct layers of enhanced CO and ozone are present, as in A775. Boundary layer concentrations of peroxides, HCHO and NO<sub>y</sub> are very similar to those observed the previous day.

A period of relatively well mixed CO and ozone concentrations between 10.5 and 11.5UT corresponds to ascent through air which has been uplifted from the boundary layer of north-east United States. CO concentrations between 80-90ppbv suggest anthropogenic influence. NO<sub>x</sub> concentrations are low (30-40ppbv), suggesting aged pollution and PAN is the major NO<sub>y</sub> component. This indicates outflow of large concentrations of NO<sub>x</sub> and NMHCs, forming PAN which is preserved during ascent to the cold UT. PAN increases and NO<sub>x</sub> decreases as the altitude of trans-Atlantic transport and the sampled air masses increases, where the colder temperatures favour PAN formation from the NO<sub>x</sub>. H<sub>2</sub>O<sub>2</sub> concentrations lie between 1 and 1.5 ppbv, with 300-400pptv HCHO. This indicates relatively active photochemistry,

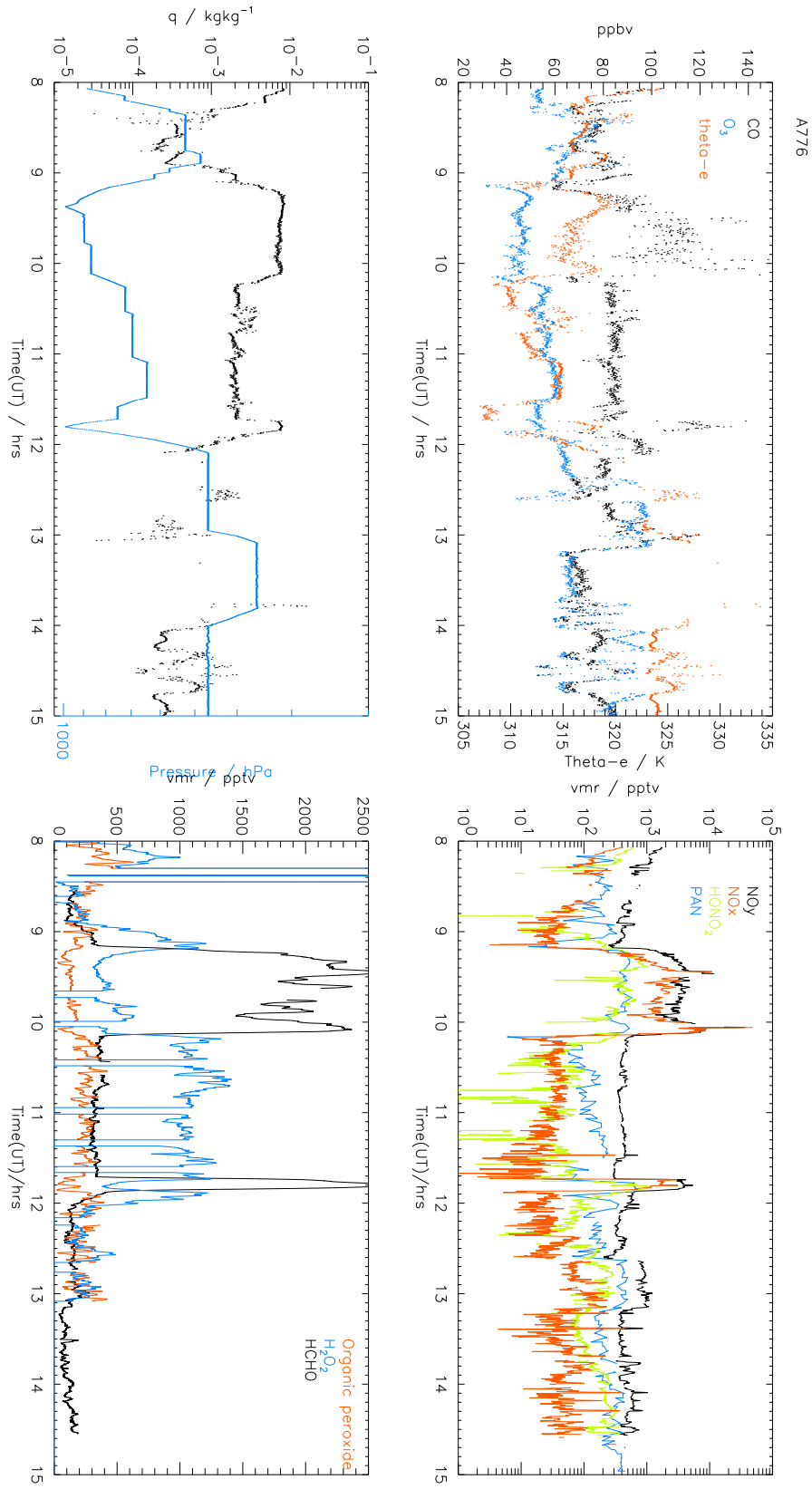


Figure 3.18: Time series observations for C130 flight A776 (10/08/00).



trajectories indicating uplift from the US boundary layer around 5 days prior to sampling.

Between 12.0 and 15.0UT, Fig 3.18 shows that the aircraft sampled air masses in the mid/upper troposphere between 500 and 200hPa. RDF trajectories near the flight path between these times also indicate extensive import of air from the North American region. Between 12.0 and 13.0 UT, much of the air appears to arrive from higher altitudes over the North American continent, with possible influence from the tropopause region. This is also suggested by larger ozone concentrations than those observed during the US PBL uplift earlier in the flight. Peroxide and HCHO concentrations are also much lower, indicating less recent polluted photochemistry. Just after 12.5UT, an air mass is intercepted with lower CO (60ppbv) and very low ozone (40ppbv). There is an associated enhancement to water vapour and  $\theta_e$ . This air appears to have ascended from the mid-Atlantic marine boundary layer. During the last section of the flight, the aircraft passes back and forth between air masses of a variety of distinct origins over the North American continent and in the upper troposphere over North America. This section of flight A776 is examined in detail with reference to chemistry and transport in Chapter 7.

The largest  $\text{NO}_y$  component during the periods of apparent long-range import from North America is seen to be PAN. The previous day,  $\text{HONO}_2$  and PAN concentrations were very similar during sampling of air imported from the Canadian lower troposphere.  $\text{HONO}_2$  concentrations are slightly lower during the later sections of flight A776, which may indicate a more aged signature, where  $\text{HONO}_2$  has been lost to washout, or a difference in  $\text{NO}_y$  partitioning brought about by a greater affinity for PAN production over  $\text{HONO}_2$  formation. This may be the case where air masses have been more rapidly uplifted to cold temperatures, where  $\text{NO}_2$  is efficiently trapped as PAN or where there are more organic species that are efficient in producing peroxyacetyl radicals. Both of these issues may affect  $\text{NO}_y$  partitioning here, since far stronger uplift is observed for air masses from the US PBL during A776 than A775, and A776 boundary layer air is more likely to contain urban anthropogenic NMHC signatures from the US PBL.

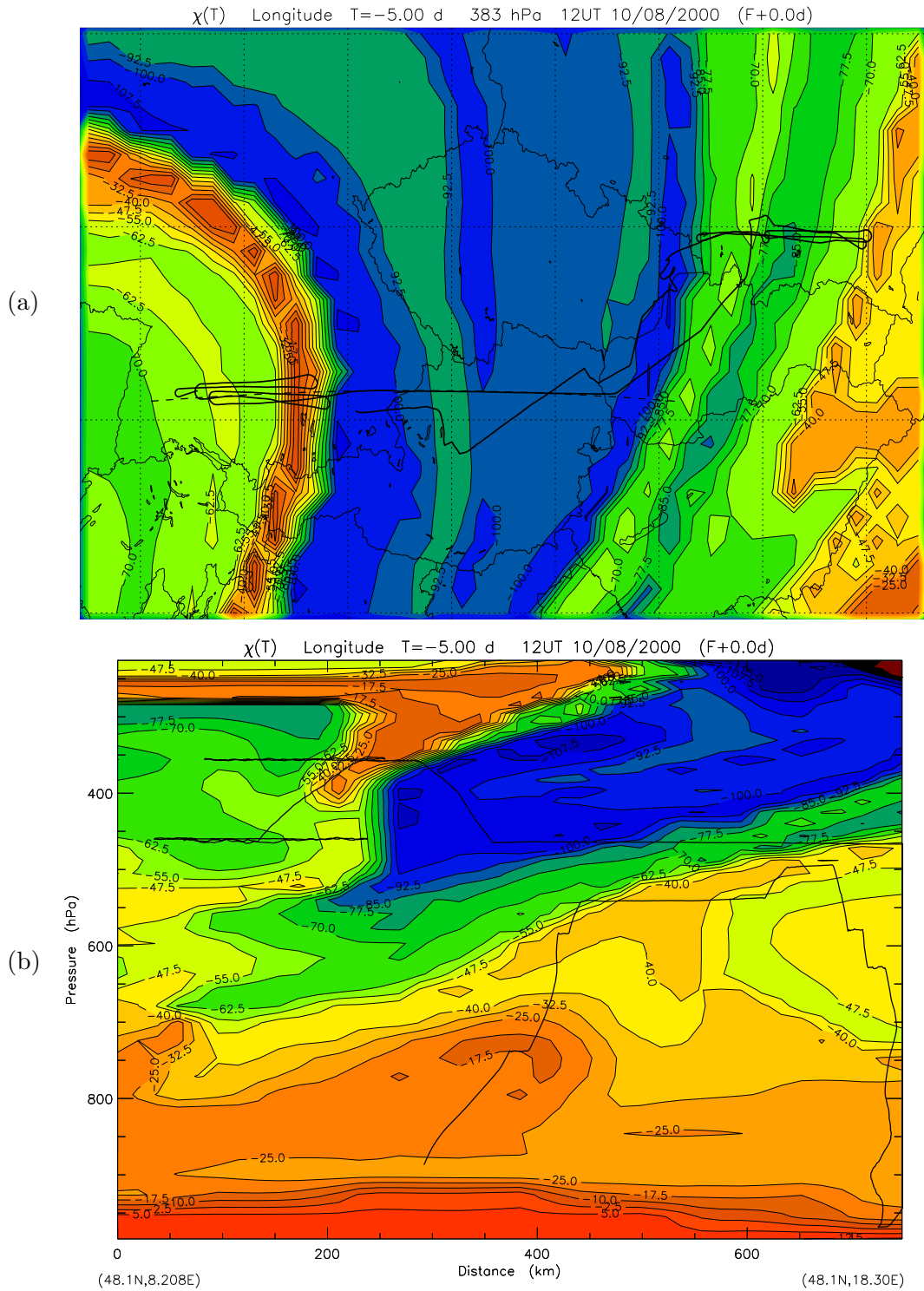


Figure 3.19: Longitude at 5-day back trajectory origins arriving on a high resolution RDF grid in the region of flight A776. Solid line shows 12UT air-mass-relative flight track. (a) Origin longitude on the 383hPa pressure surface. (b) Vertical cross-section along plane indicated by dotted line in panel (a).

### 3.6 Conclusions

The EXPORT aircraft observations have provided a unique dataset of detailed trace gas concentrations over Central Europe during contrasting synoptic conditions. The strong vertical mixing associated with the passage of a cold front and its associated warm conveyor belt airstream was successfully sampled on August 2 and 3. A high pressure system over the region allowed observations of a freshly polluted PBL and a more aged free troposphere to be sampled on August 9 and 10. During such settled conditions, import of North American pollution into the Central European free troposphere was identified.

Reverse domain filling (RDF) trajectory simulations have been used to construct 3D air mass structures in the region of the flights. These simulations have been shown to diagnose regions of ascent or descent and geographical or thermodynamic origins of air, which correspond well to the observed chemical characteristics in the sampled domain.

On August 2 and 3, elevated free-tropospheric observations of CO and NO<sub>x</sub> revealed strong ascent of polluted PBL air in the regions of ascent denoted by the RDF simulations. The WCB itself was resolved as a band of strongly elevated origin  $\theta_e$  on August 2. Transects through this band and in the region above showed the strongest pollutant elevations, coinciding with reductions in soluble species such as HONO<sub>2</sub> and H<sub>2</sub>O<sub>2</sub> due to wash out. The following day, flight A774 sampled air which had ascended the WCB over the previous 24-48 hours, as well as older free tropospheric air, descending behind the front. The observed chemical characteristics in these different transport regimes matched well the positions of gradients between the different air mass types derived from the RDF simulation.

The flights made on July 31 and August 9 & 10 sampled highly polluted PBL air in the Central European region. Tracer concentrations showed a sharp gradient at ~880-830 hPa, coincident with the top of the PBL. The free troposphere showed a strong contrast to the PBL, with more aged air mass characteristics. This is demonstrated by the sharp departure in ozone-CO slopes between the PBL and free troposphere. Layers of enhanced ozone and CO at the highest altitudes were

coincident with RDF trajectory origins west of the Atlantic Ocean, suggesting import of North American pollution.  $\text{NO}_y$ , CO and ozone correlations also suggest some stratospheric influence at these altitudes.

## 4. Interpretation of non-methane hydrocarbon observations

### 4.1 Introduction

As well as the suite of observations discussed in Chapter 3, during EXPORT ‘grab’ samples of air were taken on board the C130 aircraft. These were analysed post-flight for non-methane hydrocarbon (NMHC) compounds using a gas chromatograph (GC) by Ruth Purvis, University of Leeds. In this chapter the NMHC dataset is exploited to obtain information on the roles of transport, mixing and photochemistry in the central European troposphere. The contributions of the range of measured NMHCs to the local boundary-layer photochemistry of different regions of central Europe is also investigated.

In Section 4.2 sources and sinks of NMHCs are briefly discussed. In Section 4.3 the use of NMHC compounds as markers for atmospheric processing is introduced. Chemical and mixing effects on the observed relationships of NMHCs are discussed in Section 4.4. In Section 4.5 the PBL distributions of observed NMHCs are examined and in Section 4.6 the effects of this distribution on the regional photochemistry is discussed. Inferences of chemistry involving halogens are made in Section 4.7, diagnosed from NMHC observations. Conclusions are summarised in Section 4.8.

## 4.2 NMHC sources and sinks

Non-methane hydrocarbon (NMHC) compounds can be used to infer information on both dynamic and chemical processes in the atmosphere. Such compounds usually have well-known sources to the atmospheric system, and also have a very wide range of atmospheric lifetimes, from the order of minutes to months. In addition, the loss of such compounds in the atmosphere is usually dominated by oxidation by the OH radical, giving the compounds characteristic atmospheric lifetimes. Table 4.1 shows examples of NMHCs measured on the C130 aircraft, along with their OH reaction rate constants. Mean atmospheric lifetimes are also shown, assuming a diurnal average [OH] radical concentration of  $2 \times 10^6 \text{ molec cm}^{-3}$ . The characteristic sources and atmospheric lifetimes of these compounds makes them powerful as tracers of atmospheric transport processes, and more so when used together.

Table 4.1: *NMHC second-order rate constants for reaction with the OH radical ( $\text{cm}^3 \text{molec}^{-1} \text{s}^{-1}$ ) and atmospheric lifetimes resulting from oxidation by a constant OH field of  $2 \times 10^6 \text{ molec cm}^{-3}$  at 298K. Kinetic data taken from IUPAC 2002 Recommendation [<http://www.iupac-kinetic.ch.cam.ac.uk/>] and the Leeds Master Chemical Mechanism [<http://www.chem.leeds.ac.uk/Atmospheric/MCM/mcmproj.html>]*

	$k_{OH} / 10^{12} \text{cm}^3 \text{molec}^{-1} \text{s}^{-1}$	Lifetime
ethane	0.24	24.1 days
acetylene	0.90	6.4 days
propane	1.10	5.3 days
iso-butane	2.19	2.6 days
n-butane	2.44	2.4 days
ethene	8.52	16.3 hrs
propene	26.3	5.3 hrs
isoprene	101	1.4 hrs

Many NMHCs result from anthropogenic activities, and emissions from industrialised or heavily populated regions will contain a complex mixture of NMHCs with a variety of reactivities in the atmosphere. Within the general category of anthropogenic sources, many NMHC compounds have very specific sources that are well

characterised. For example, benzene ( $C_6H_6$ ) and toluene ( $C_7H_8$ ) are almost exclusively emitted from automotive activities. Propane ( $C_3H_8$ ) emissions are associated with the transport and use of natural gas and liquefied petroleum. Some NMHCs have large non-anthropogenic sources. Isoprene ( $C_5H_8$ ) is emitted in large quantities from vegetation. Emissions are highly dependent on leaf temperature and sunlight exposure [Guenther *et al.*, 1993]. Consequently, isoprene emissions show strong diurnal and seasonal cycles, but nevertheless contribute an estimated 503 Tg of reactive carbon per year to the troposphere [Guenther *et al.*, 1995]. Isoprene emissions are estimated to be three times greater than anthropogenic NMHC emissions over the US [Lamb *et al.*, 1987].

NMHCs are important as precursors of photochemically produced ozone in the troposphere, due to their ability to form peroxy radicals during their oxidation sequence. The efficiency with which NMHCs can form such reactive peroxy radicals determines their importance to ozone photochemistry. Isoprene has a very large ozone production efficiency due to the production of several intermediate peroxy radicals during its oxidation. Tropospheric ozone should not be considered solely a product of man-made precursor emissions, since the natural biosphere-atmosphere system is capable of contributing large quantities of ozone precursors.

### 4.3 NMHCs used to diagnose atmospheric processing

NMHCs with characteristic, correlated sources can be used to gain information on the atmospheric processing of an air mass since it was given a fresh signature of emissions. Two NMHC compounds emitted together, with a known concentration relationship, and sufficiently different lifetimes can be used to infer the ‘age’ of a given air mass; i.e. the time since it encountered fresh emissions. Benzene and toluene are routinely used in this way, since they have closely correlated emission sources [e.g. Gelencser *et al.*, 1997]. Their concentration ratio at emission is approximately 4:1 toluene:benzene, with atmospheric lifetimes of about 5 and 1 days respectively. The ratio toluene:benzene therefore reduces in a given air mass with time since emission in a predictable fashion (Fig. 4.1). In order for this method to be viable, it has to be assumed that an air mass containing fresh emissions dilutes

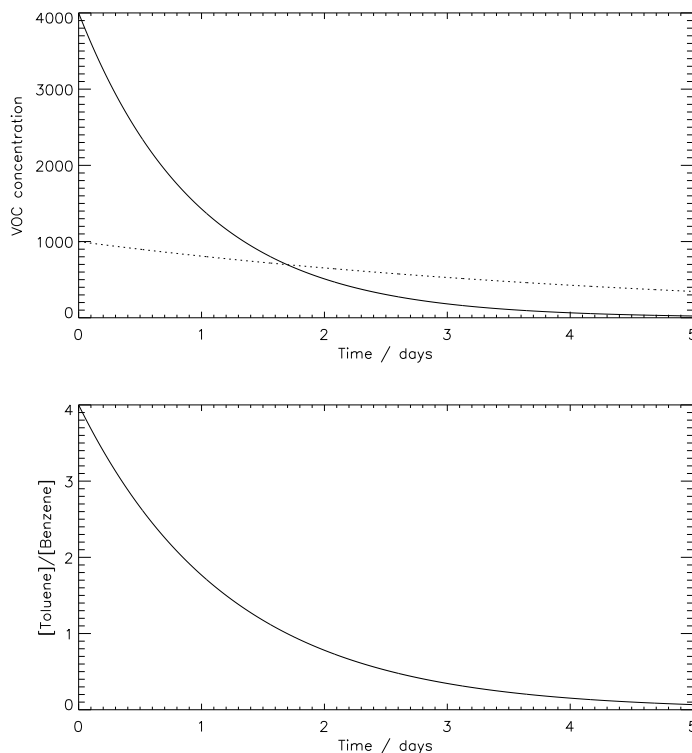


Figure 4.1: *The evolution of the concentrations of benzene (dashed) and toluene (solid) (top), and the ratio [toluene]/[benzene] with time since emission into an air mass (bottom).*

into a background of negligible concentrations of the two species (i.e. mixing does not change the concentration ratio), and that only OH oxidation is responsible for the chemical loss of both species. These assumptions are often accepted to be valid for NMHCs in a plume as it mixes into the background troposphere.

Figure 4.2 illustrates the use of NMHCs ratios as a proxy for air mass ‘age’. The observed concentrations of butane and propane are shown plotted against the ratios of their concentrations to that of ethane for all NMHC canisters from the five EXPORT science flights (with the exception of flight A775, for reasons explained in Section 4.7). Ethane has a long lifetime ( $\sim 20$  days) compared with propane ( $\sim 5$  days) and butane ( $\sim 2$  days), and so the ratios are expected to decrease with time since emission, with decreasing NMHC concentrations. This appears to be the case



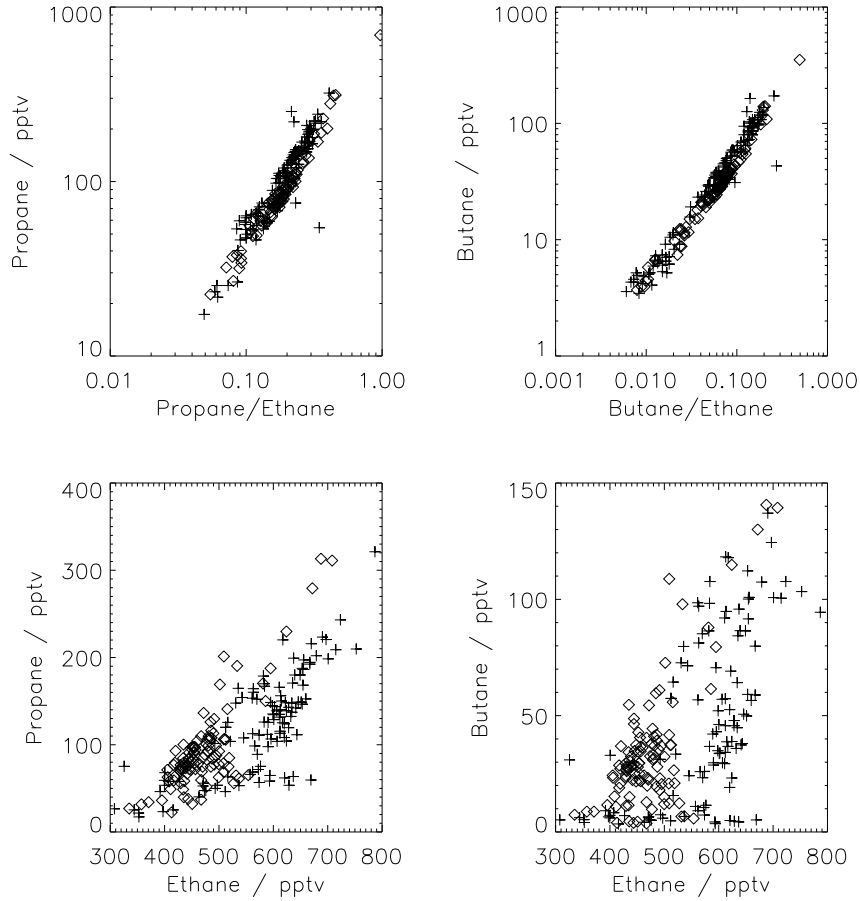


Figure 4.2: *Concentrations of propane and butane plotted against their respective ratios to ethane (top) and against the concentration of ethane (bottom). Compact correlations in the upper plots indicate the justification for the use of the NMHC ratios as a proxy for ‘air mass age’, as well as a linked source relationship for the three species. Crosses show A772/6 and diamonds A773/4.*

in the EXPORT dataset, where the highest concentrations of propane and butane coincide with the highest ratios to ethane ( $\sim 0.45$  and  $0.2$  respectively). Plots of propane and butane against ethane (Fig. 4.2) also support the assumption made that the three NMHCs have similar sources and show an approximate correlation in the atmosphere.

Vertical profiles of NMHCs for the EXPORT flights were discussed by *Purvis et*

*al.*, [2003]. The contrasting vertical distributions during flights A773/4 and flights A775/6 were noted, and attributed to the efficient vertical transport of fresh PBL air by the frontal system sampled during A773/4. Vertical profiles of propane and butane illustrate this (Fig. 4.3). Vertical profiles of the propane/ethane and butane/ethane ratios confirm the presence of much younger air in the mid troposphere during flights A773/4 than during A775/6, with ratios close to those observed in the PBL. *Purvis et al.*, [2003] showed the presence of very short-lived NMHC species in the mid troposphere during flight A773, due to rapid ascent of PBL air into the free troposphere.

## 4.4 Mixing and chemistry

While reactive NMHCs are useful for examining the rate of transport of air from fresh pollution source, more care must be taken when using ratios, such as that of benzene to toluene, in an attempt to infer quantitative estimates of such transport times, or ‘air mass age’. Mixing of a freshly polluted air mass with non-zero concentrations of the NMHCs in surrounding air complicates the simple view that NMHC ratio evolution can be attributed to chemistry only. The relative magnitudes of source and loss processes for most NMHCs mean that they have non-zero concentrations throughout the troposphere. Even in regions remote from sources, there will remain a ‘background’ concentration of an NMHC species. This invalidates the assumption of ‘ideal dilution’; i.e. that dilution of an air mass into the background atmosphere is to zero concentrations, and so does not alter the NMHC ratios in the air mass.

Despite the likely invalidity of this assumption, Figures 4.2 and 4.3 (above) demonstrate that there appears to be a relationship between the ratios of observed NMHCs and their observed concentration. However, it cannot be assumed that photochemistry alone is responsible for the evolution of an NMHC ratio. *Parrish et al.*, [1992] and *McKeen and Liu*, [1993] showed that although observed and modelled NMHC ratios show a characteristic relationship in the atmosphere, due to mixing between air masses, this relationship departs from that expected from chemical decay only.

The EXPORT dataset also suggests that both mixing and chemistry have a role in

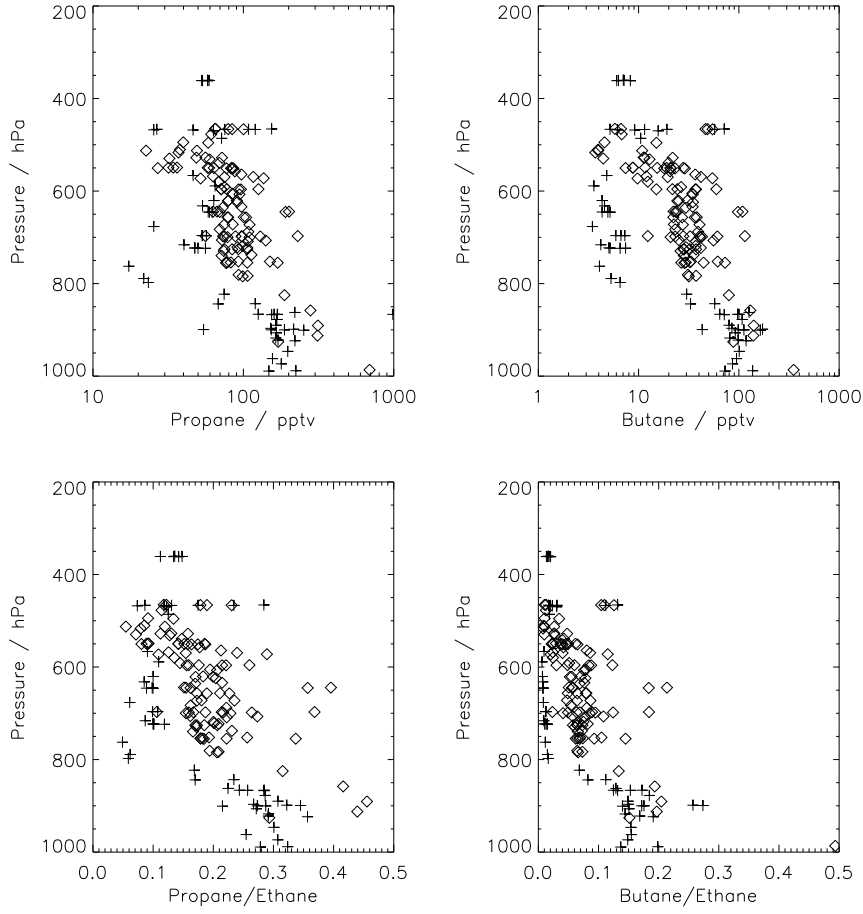


Figure 4.3: Vertical profiles of absolute concentrations (pptv) (also shown by Purvis *et al.*, [2003]) and NMHC ratios observed during the EXPORT campaign. Fresh PBL air has the highest ratios and concentrations, which diminish with altitude as more aged air is sampled. Crosses indicate A772/6 and diamonds A773/4.

determining the evolution of a given NMHC relationship in an air mass. Figure 4.2 shows slightly different slopes for the flights with vertically well mixed NMHC profiles (A773/4) and the more vertically settled conditions of the other flights (A772/6). For example, a given propane mixing ratio appears to correspond to a slightly larger propane/ethane concentration ratio for flights A773/4, where the rapid more vertical transport from the PBL is believed to be active. This means that ethane and propane are being removed at more similar rates in these flights, which leads to a larger concentration ratio for a given loss of propane than would be expected from

their different photochemical loss rates. This could be explained by mixing effects, where the loss rates of the species are affected by mass exchange between air masses, as well as photochemical decay. Idealised dilution, where the air mass mixes into a background of negligible concentrations, would remove ethane and propane at equal rates. In the EXPORT data, a combination of chemical removal and mixing results in a greater propane/ethane concentration ratio for a given processing time since emission compared with chemical removal only. This effect appears to be greater in flights A773/4 than in flights A772/6.

#### 4.4.1 TOPSE data: evidence for combined dilution and chemistry

Observations of NMHCs made over several months during the US-led TOPSE (Tropospheric Ozone Production about the Spring Equinox) experiment [Atlas *et al.*, 2003] provide good examples of the relative roles of chemical decay and mixing effects in determining the evolution of NMHC ratios. The experiment was aimed at examining the chemical and dynamical evolution of the troposphere over North America through the winter-spring transition. A total of 42 flights were made at mid-high latitudes over North America between February and May 2000 (Fig. 4.4). NMHC data were collected in canister samples, as during the EXPORT experiment. Observations of butane and propane are sparse; however other species can be used to illustrate the roles of mixing and chemistry in determining the evolution of the observed NMHC concentrations.

Figure 4.5 shows iso-butane (lifetime  $\sim 2.5$  days) versus acetylene (lifetime  $\sim 6.5$  days) for each month of TOPSE observations. The compact lines show that the two species are correlated in the atmosphere. The largest concentrations are observed during February in the boundary layer, and the compact correlation between the species through to lower concentrations suggests a systematic evolution of the concentration ratio with time in the atmosphere, as air masses are processed.

Plotting the two species in this manner effectively examines the ratio between the two species. If initial concentrations are assumed, it is possible to plot the expected evolution of the concentrations of the two NMHCs in the air mass due to only chemical reaction with the OH radical, and due to only idealised dilution to a negligible

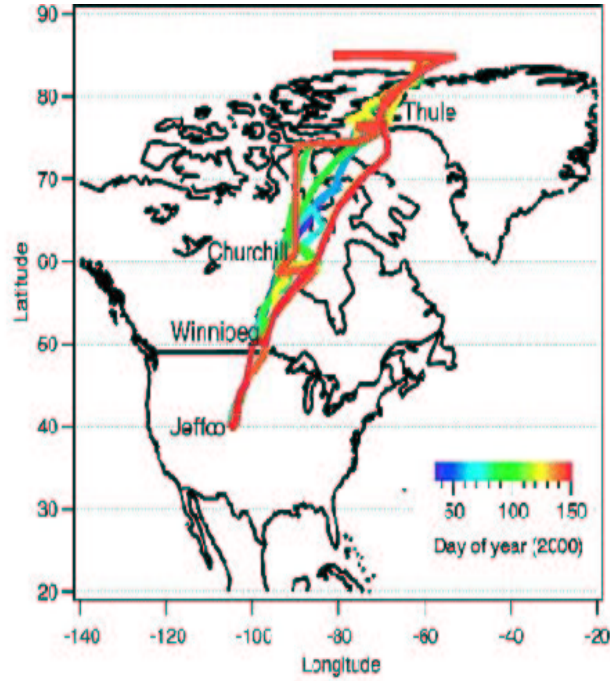


Figure 4.4: *Flight tracks of the TOPSE flights coloured by day of year. Taken from Atlas et al., [2003].*

background.

For chemical loss by some time averaged OH concentration,  $\overline{[OH]}$ , over a given time period,  $\Delta t$ , the concentration of species X will follow:

$$[X] = [X]_0 \cdot \exp(-k_X \overline{[OH]} \Delta t) \quad (4.1)$$

Where  $[X]_0$  is the initial concentration at emission,  $[X]$  is the concentration after time  $\Delta t$ , and  $k_X$  is the second-order rate constant for the reaction of X with OH. The decay of a second species, Y, can be related to that of X as:

$$\frac{\ln[X] - \ln[X]_0}{\ln[Y] - \ln[Y]_0} = \frac{k_X}{k_Y} \quad (4.2)$$

A log-log plot will therefore yield a slope given by the ratio of the two OH reaction

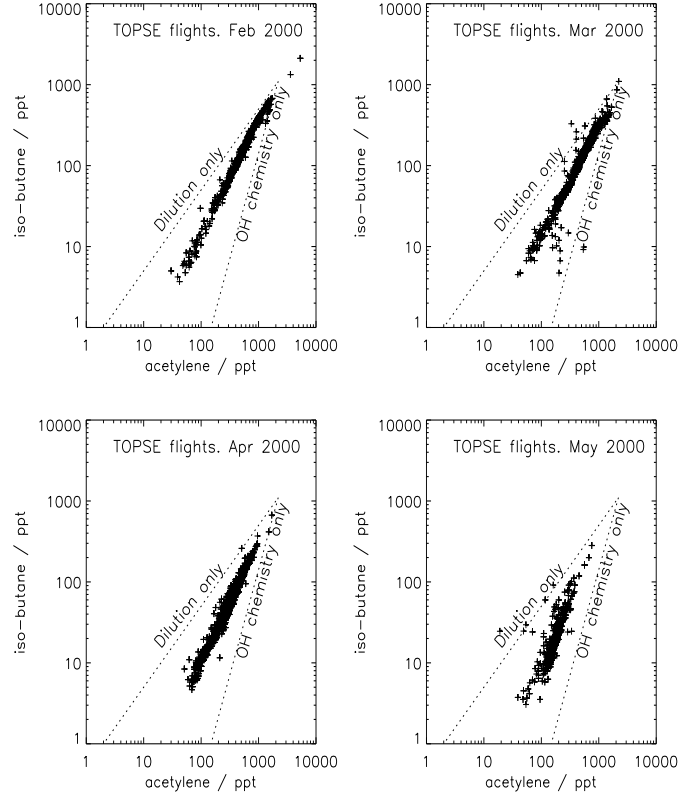


Figure 4.5: *Relationships between acetylene (pptv) and iso-butane (pptv) for four months of aircraft observations made during the TOPSE experiment between February and May 2000. OH chemistry line calculated at 298K.*

rate constants:

$$\ln[X] = \frac{k_X}{k_Y} \ln[Y] - \left( \frac{k_X}{k_Y} \ln[Y]_0 - \ln[X]_0 \right) \quad (4.3)$$

During ideal dilution by a zero-tracer background, both species will be removed at the same 1/e folding rate. This can be represented by a single constant  $K$ , which accounts for all processes mixing air between the considered air mass and the clean background:

$$[X] = [X]_0 \cdot \exp(-K\Delta t) \quad (4.4)$$

This yields the simple relationship:

$$\ln[X] = \ln[Y] - (\ln[Y]_0 + \ln[X]_0) \quad (4.5)$$

NMHC concentrations modified by dilution only should therefore follow a slope of unity.

Figure 4.5 shows that the TOPSE data points lie offset from the ‘OH chemistry only’ line. As discussed with reference to the EXPORT data, the slope of the data points suggests a more equal loss rate for the two species, than those implied by chemistry alone. A second line of slope unity corresponds to the evolution of the concentration ratio due to idealised dilution only (i.e. to a negligible tracer background). The data points are seen to lie between these two regimes, demonstrating the joint roles of mixing processes and chemistry in determining the concentration ratio of the NMHCs. This behaviour has been noted previously in relation to aircraft data and CTM output [*Parrish et al.*, 1992; *McKeen and Liu*, 1993]. However, the TOPSE data show that the relative roles of these processes also demonstrate some seasonality. During February, data points lie very close to the ‘dilution only’ line at high concentrations, demonstrating relatively slow chemical loss and a significant role for mixing effects. Through the following months, data points shift towards the bottom left of the plots, and lie nearer the ‘chemistry only’ line, demonstrating faster photochemical processing. As sunlight increases through winter into spring, the mean diurnal OH concentration is expected to increase, leading to more extensive chemical processing of the observed NMHCs.

#### 4.4.2 Application to EXPORT NMHC data

Plots analogous to Figure 4.5 for the EXPORT observations are shown in Figure 4.6. Both the relationship between observed iso-butane and acetylene and the relationship between observed n-butane and propane concentrations are shown. Lines

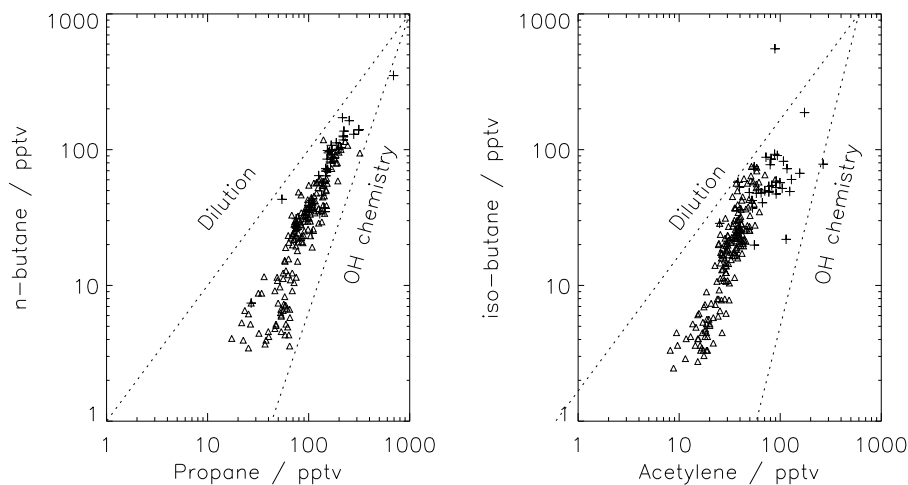


Figure 4.6: Analogous plots to Figure 4.5 for EXPORT observations of *n*-butane, propane and iso-butane, acetylene. Crosses indicate observations from flights A772/6 and diamonds A773/4. Dotted lines indicate the OH-loss-only slope calculated at 298K and the idealised dilution slope.

of 1:1 slope are plotted corresponding to the ‘dilution only’ regime, and ‘chemistry only’ slope are plotted. As with the TOPSE data, the range of observed concentrations falls between the two regimes. This relies on the selection of the initial concentrations of the species at emission i.e. the point where the dilution and chemistry slopes meet. These are based on the maximum observed concentrations during EXPORT. Ground-based NMHC observations made at urban sites, very close to emission sources suggest that these initial concentrations are underestimated. *Derwent et al.*, [2000] discussed NMHC observations from a number of urban sites in the UK. Urban surface observations of propane, *n*-butane, iso-butane and acetylene from this study were on the order of  $\sim 2$ -4 ppbv. Adopting these increased source concentrations would alter the proximity of the data points to the slopes representing the two regimes, and would suggest greater atmospheric chemical processing of the NMHC ratios than implied by Fig. 4.6. This reflects the uncertainties inherent in drawing any conclusions from this method regarding the relative roles of mixing and chemistry.

Using the ratios of propane and butane to ethane discussed in Section 4.3, an alter-



native analysis of the EXPORT dataset can be made. By using ratios rather than absolute concentrations, emission source ratios can be used rather than needing to assume absolute initial species concentrations. Emission ratios for many pairs of NMHCs with similar sources are often assumed to be characteristic and constant in different regions.

Consider three co-emitted NMHCs X, Y, and Z. The evolution of the concentration ratios  $[X]/[Z]$  and  $[Y]/[Z]$  with time due to OH chemistry only and dilution only can be derived as below, where  $k_X$ ,  $k_Y$  and  $k_Z$  are the reaction rate coefficients for reaction of OH with X, Y and Z respectively.

For OH chemistry only:

$$\begin{aligned}\frac{[X]}{[Z]} &= \frac{[X]_0}{[Z]_0} \exp[-(k_X - k_Z)\overline{[OH]}\Delta t] \\ \frac{[Y]}{[Z]} &= \frac{[Y]_0}{[Z]_0} \exp[-(k_Y - k_Z)\overline{[OH]}\Delta t]\end{aligned}\quad (4.6)$$

$$\frac{\ln\frac{[X]}{[Z]} - \ln\frac{[X]_0}{[Z]_0}}{\ln\frac{[Y]}{[Z]} - \ln\frac{[Y]_0}{[Z]_0}} = \frac{(k_X - k_Z)}{(k_Y - k_Z)} \quad (4.7)$$

$$\ln\frac{[X]}{[Z]} = \frac{(k_X - k_Z)}{(k_Y - k_Z)} \ln\frac{[Y]}{[Z]} - \left[ \frac{(k_X - k_Z)}{(k_Y - k_Z)} \ln\frac{[Y]_0}{[Z]_0} - \ln\frac{[X]_0}{[Z]_0} \right] \quad (4.8)$$

A plot of  $\ln\frac{[X]}{[Z]}$  vs  $\ln\frac{[Y]}{[Z]}$ , therefore yields a slope given by the ratio of the differences in the OH rate constants for each NMHC pair. Only the intercept is affected by the initial concentration ratios.

For ideal dilution to a negligible background, all three species will be removed at the same  $1/e$  folding rate. This would result in constant concentration ratios, unchanged with time.

Using ethane, the NMHC alkane with the longest photochemical lifetime, in the denominator of the NMHC ratios allows the derivation of another limiting case for the relationship between the concentration ratios. Due to its long lifetime in the

atmosphere, ethane is expected to show an appreciable background concentration with relatively low variability (see *Parrish et al*, [1992]). Background concentrations of more reactive species are therefore expected to be smaller with greater variability according to distance from source. A limiting case may be considered where very aged background air would contain a non-zero, but small, concentration of the longest-lived species and negligible concentrations of the two more reactive species. In this case, the concentration  $[Z]$  would not be modified in the same manner as  $[X]$  and  $[Y]$  during mixing with this background, however the denominators of both ratios would be modified in the same way.  $[X]$  and  $[Y]$  would be removed at the same  $1/e$  dilution rate,  $K$ .

$$\begin{aligned}\frac{[X]}{[Z]} &= \frac{[X]_0 \exp(-K\Delta t)}{[Z]_0 \gamma} \\ \frac{[Y]}{[Z]} &= \frac{[Y]_0 \exp(-K\Delta t)}{[Z]_0 \gamma}\end{aligned}\tag{4.9}$$

$\gamma$  represents the dependence of  $[Z]$  on the initial concentration at emission,  $[Z]_0$ . This expression can be reduced to:

$$\frac{\ln \frac{[X]}{[Z]} - \ln \frac{[X]_0}{[Z]_0}}{\ln \frac{[Y]}{[Z]} - \ln \frac{[Y]_0}{[Z]_0}} = 1\tag{4.10}$$

$$\ln \frac{[X]}{[Z]} = \ln \frac{[Y]}{[Z]} - \left[ \ln \frac{[Y]_0}{[Z]_0} - \ln \frac{[X]_0}{[Z]_0} \right]\tag{4.11}$$

This dilution scenario therefore should yield a slope of unity, on a log-log plot of the two NMHC ratios. This slope represents the limiting case of how the relationship between the concentration ratios would change with no chemical loss and ideal dilution to a background of very aged air. A non-zero background of  $[X]$  and  $[Y]$ , as well as  $[Z]$ , yields a distribution of points between the 1:1 and chemical slopes [*McKeen and Liu*, 1993].

In Section 4.3, it was shown that the EXPORT NMHC ratios appear to decay with time from emission, with PBL ratios showing the highest observed values. A scatter plot of n-butane/ethane vs propane/ethane shows a distribution of points decaying

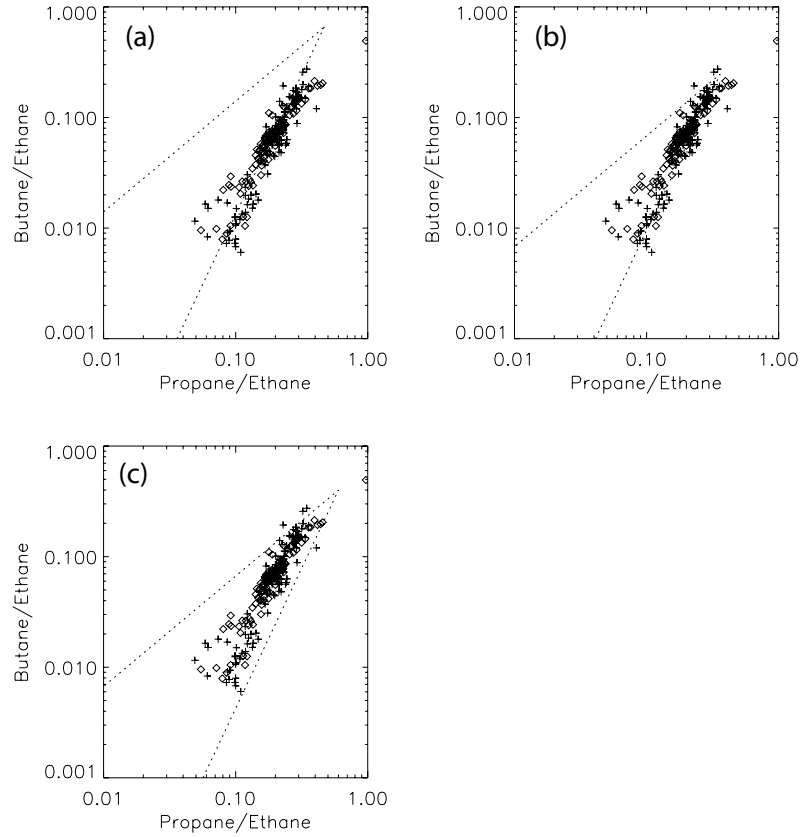


Figure 4.7: *NMHC ratio relationship for EXPORT data. Crosses show A772/6 and diamonds A773/4. (a) Initial ratios taken from Klemp et al., [2002]. (b) Initial ratios derived from near surface EXPORT observations. (c) Minimum initial ratios to give reasonable fit to data.*

from the PBL values to lower ratios as air masses are processed in the atmosphere (Fig. 4.7). From the expressions derived above, theoretical ‘chemistry only’ and ‘dilution only’ lines are plotted to show how the two ratios should change due to chemical decay by reaction with OH and due to idealised dilution to a negligible background respectively (from Equations 4.8 and 4.11). The chemistry and dilution lines meet at a point given by the specified values of the two concentration ratios at emission into the atmosphere.

*Klemp et al.*, [2002] compiled emission ratios for NMHCs by averaging 124 NMHC datasets measured throughout Germany. These emission ratios are used in Figure

4.7a to define the intersection of the two theoretical slopes. It is evident that the EXPORT dataset does not agree well with these emissions ratios. The data are expected to fall approximately between the chemistry and dilution regimes, however in this case the data points are apparently clustered around the chemistry only line. This suggests an underestimation in the emission ratio of propane:ethane.

An alternative pair of emission ratios (derived from correlations of near-ground EXPORT observations) are used in Figure 4.7b. Linear fits of NMHC observations made at pressures of over 900hPa are used to derive slopes of propane:ethane and n-butane:ethane. Since these observations are close to the ground, it is assumed that they are the nearest-to-source observations available from the dataset. A consequence of using these values is that some data points lie very close to the initial values. The distribution again suggests an underestimation in the initial ratios, which is likely, since mixing and chemistry will already have altered even the closest-to-surface observed ratios since the NMHCs were emitted. Figure 4.7c shows the minimum emission ratios which best fit the distribution of the EXPORT data. These are approximately 0.6 for propane:ethane and 0.4 for n-butane:ethane. These are comparable with ratios calculated by *Klemp et al.*, [2002] specific to the Augsburg urban region in Germany. Overall, the range of transport regimes and PBL regions sampled during the campaign mean that it is unlikely that a fixed set of emission ratios can be used for the entire dataset.

## 4.5 NMHCs in the Central European PBL

The five EXPORT science flights took extensive samples of the boundary layer. This yielded a unique dataset of NMHC concentration observations near the surface in Central Europe, along with coincident observations of species described in Chapter 3. Figure 4.8 shows the locations of canister samples taken at altitudes between the surface and 850hPa, coloured with the concentrations of various measured NMHCs.

The majority of boundary layer samples were taken in the north, over Czech Republic and Poland. A number of samples were also taken in the region of the Hungary-Romania border. Largest concentrations of ethane, propane, butane and

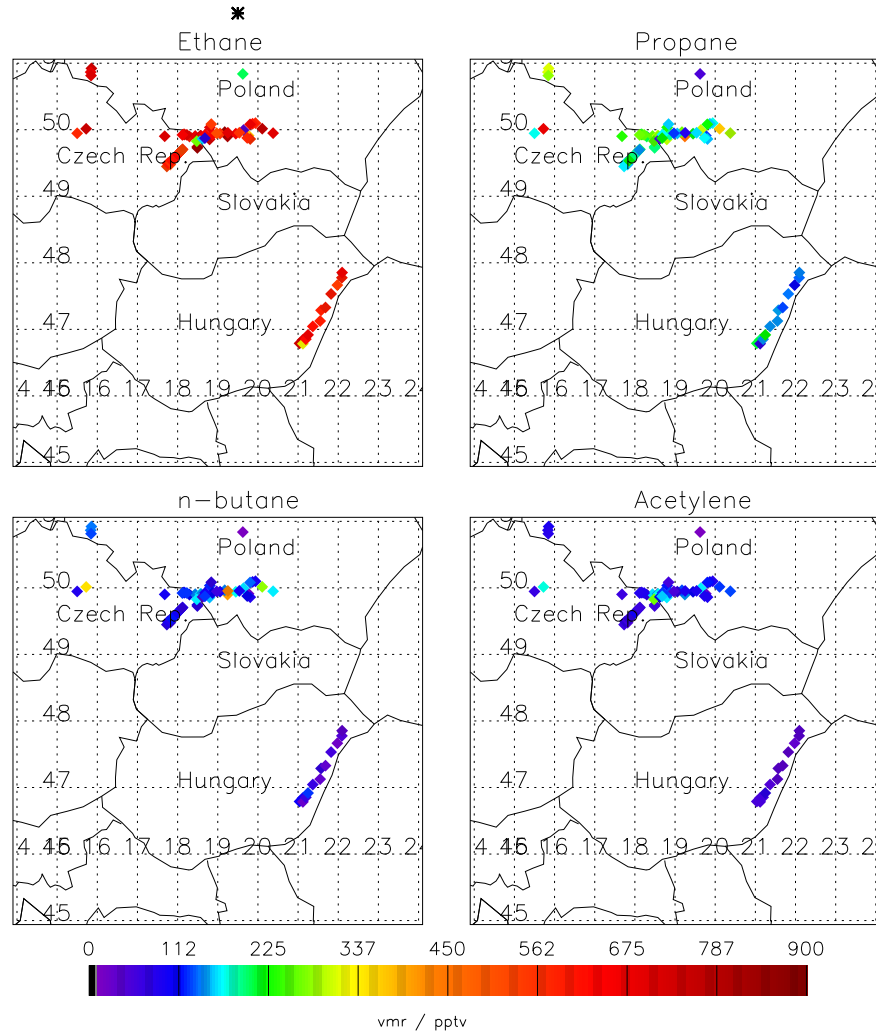


Figure 4.8: Near surface NMHC observations (pptv) made during the EXPORT campaign over central Europe at pressures greater than 850hPa.

acetylene are seen to the north, over Poland and the Czech Republic. The region to the south-west of the Polish city of Krakow was heavily sampled, and shows some of the highest concentrations of anthropogenic NMHCs. A plot of observed  $\text{NO}_x$  concentrations averaged over the bottle fill times (Fig. 4.9) confirms the largest levels of anthropogenic pollution in this region. The small number of samples taken in central Czech Republic show similarly large values, near the town of Hradec Kralove ( $\sim 50^\circ\text{N}$ ,  $\sim 15.5^\circ\text{E}$ ). Largest concentrations of shorter lived NMHCs, such as the alkenes were also observed in these regions.

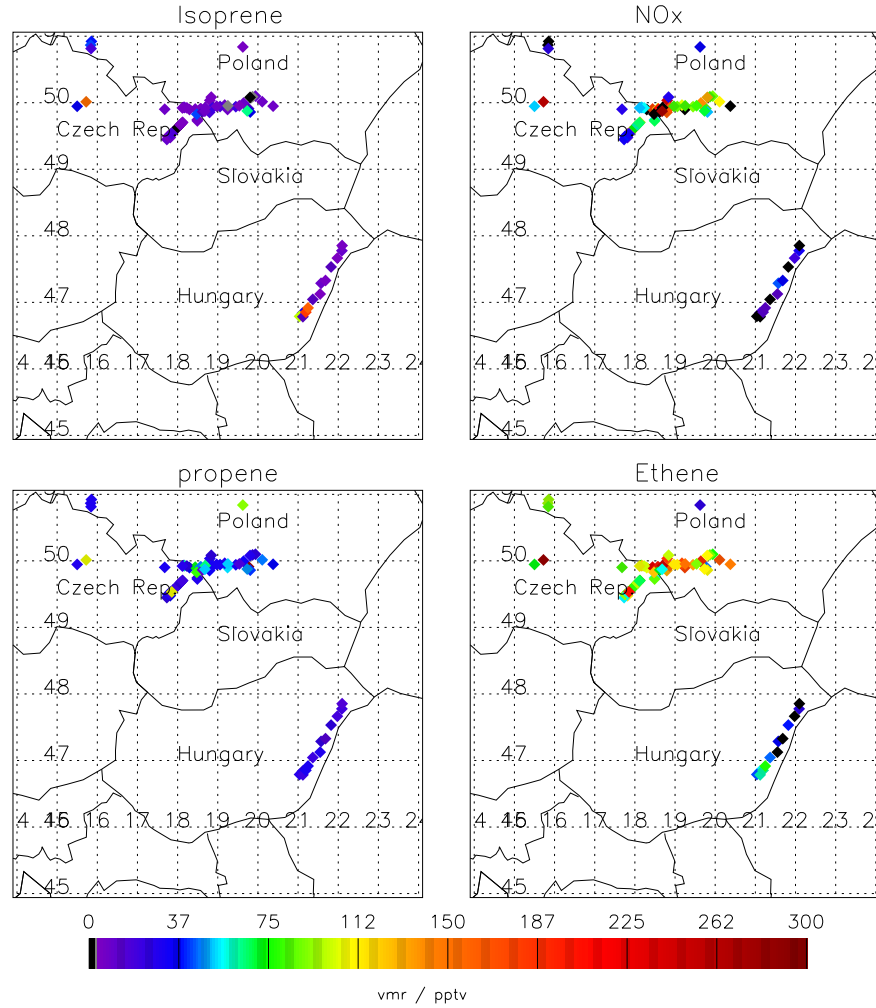


Figure 4.9: Near surface NMHC and  $\text{NO}_x$  observations (pptv) made during the EXPORT campaign over central Europe at pressures greater than 850hPa.  $\text{NO}_x$  scale is 20 times larger. i.e. Values 0 to 6000.

The region to the southwest of Krakow is bounded between the western edge of the Carpathian mountains to the southeast and mountains along the Czech-Poland border to the southwest. The area is heavily industrialised, and includes several major fossil fuel-burning power facilities (Fig. 4.10). This level of industry coupled with the presence of mountains to the south is likely to lead to the trapping of high levels of anthropogenic pollutants in the PBL.

The bottle samples filled in the PBL near the Hungary-Romania border show lower

### Eastern Europe: Major Power Facilities



Figure 4.10: *Locations and types of major power facilities in Eastern Europe. The region to the southwest of Krakow, near the Polish-Czech border is heavily industrialised by power plants. However, the power industry has no major facilities in the region of the Hungarian-Romanian border. Map produced by US Central Intelligence Agency, 1980. Source: University of Texas Online Library: [http://www.lib.utexas.edu/maps/europe.html]*

concentrations of anthropogenic NMHCs, and also lower averaged  $\text{NO}_x$  concentrations. However, propane concentrations are relatively enhanced to the south of this region. Propane has a large source from natural gas usage, and consequently shows a different distribution to acetylene, which has its major source from automotive combustion. Natural gas facilities are present in the south of this region (Fig. 4.11), however emissions associated with heavy industry and transport are likely to be lower than in the Poland samples, since the region is more sparsely populated. Both propane and acetylene show correlations with CO in the free tropospheric samples (Fig. 4.12), since they are all markers for PBL polluted air. In the PBL itself, correlations are not as well defined, highlighting the wide variety in the sources of CO, and the different predominant sources of propane and acetylene.

## 4.6 Relative contributions of NMHCs to regional photochemistry

The relatively complex mixture of NMHCs present in the central European PBL will play an active role in regional photochemistry. NMHCs are precursors to tropospheric ozone production through their ability to form peroxy radicals, which provide a route for conversion of NO to  $\text{NO}_2$  in the troposphere. The oxidation of NMHCs to produce peroxy radicals is initiated by reaction with the OH radical. The rate at which different NMHCs react with the OH radical to produce peroxy radicals, is therefore an indication of their relative contributions to the local photochemistry. This rate is determined by the rate constant for the reaction, which generally shows a temperature dependence and often a pressure dependence, and also the ambient concentration of the NMHC itself.

*Goldan et al.*, [2000] described NMHC data taken during the Southern Oxidant Studies of summer 1995 and 1996 over the southern US states, and calculated *in situ* OH loss rates for each NMHC. CO accounted for the greatest OH loss rate, followed by methane, reflecting their large abundances. NMHCs were found to contribute a small proportion, equivalent to approximately 1/15 of the CO loss rate in the PBL. Isoprene, however was seen to make a very large contribution in some regions, accounting for an OH loss rate several times larger than the CO rate. This



### Eastern Europe: Major Gas Facilities



Figure 4.11: Locations and types of major gas facilities in Eastern Europe. There are no major natural gas activities in the region to the south of Krakow. Gas storage facilities are present in the south of the Hungarian-Romanian border region. Map produced by US Central Intelligence Agency, 1980. Source: University of Texas Online Library: [<http://www.lib.utexas.edu/maps/europe.html>]

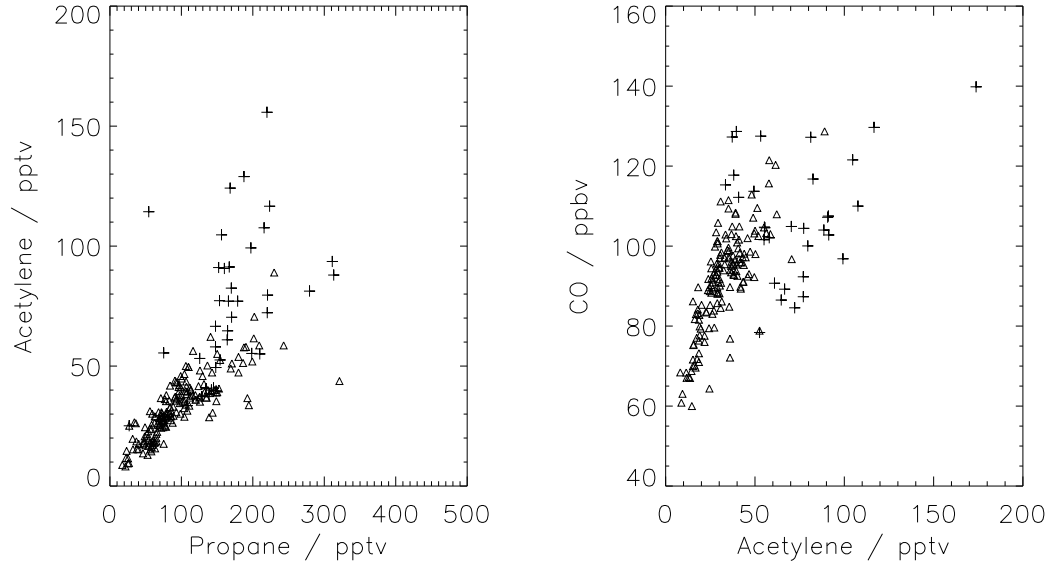


Figure 4.12: *Correlations between CO, propane and acetylene for free tropospheric samples (triangles) and PBL air (crosses) for the EXPORT observations.*

highlights the reactivity of isoprene and its large abundance in the South-East US [Guenther *et al.*, 1995]. A similar study was undertaken by Winkler *et al.*, [2002], using data from the BERLIOZ experiment, which was collected in the region of Berlin, Germany. Of the NMHCs, isoprene was seen to contribute up to 90% of the OH loss rate due to NMHCs.

The calculated OH loss rates using EXPORT NMHC data from pressures greater than 850hPa are plotted against latitude in Figure 4.13. Methane is shown as an approximate guide only, assuming a constant atmospheric concentration of 1.8ppmv, since it was not measured on the C130. CO is the dominant contributor to OH loss, as expected. Losses by methane and NMHCs are comparable in magnitude, however, the concentration of methane assumed is likely to be an underestimate of PBL methane concentrations, and so the contribution from methane is an underestimate. Isoprene does not contribute to as large an extent as observed over the Southern US. However, it does become as important as CO in the southern latitudes of the study. This demonstrates a possible important role for isoprene in photochemical ozone formation in the Hungarian-Romanian border region. Any ozone formation is

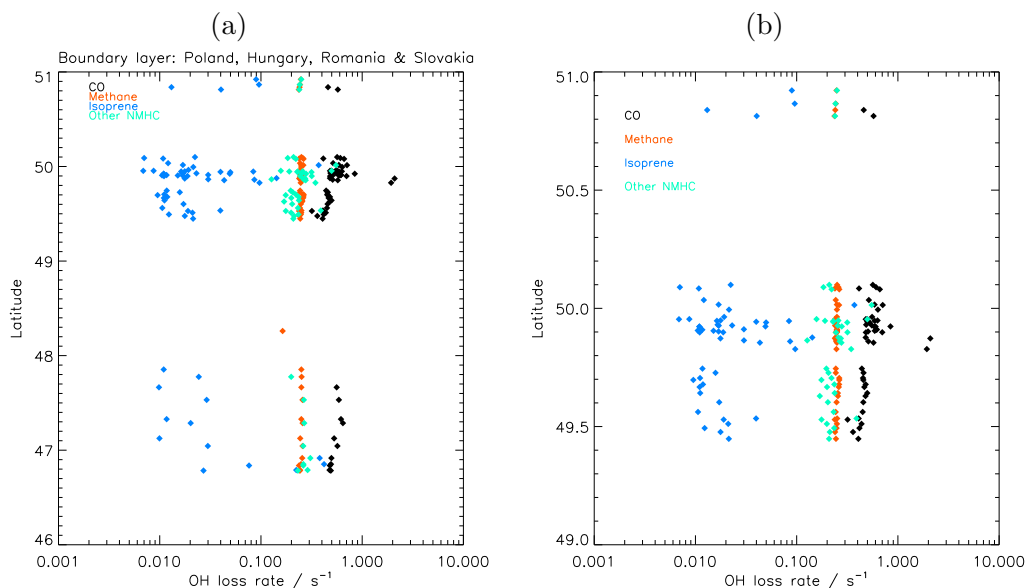


Figure 4.13:  $OH$  loss rates ( $s^{-1}$ ) calculated for PBL NMHC samples taken during the EXPORT campaign.  $OH$  rate constants at 298K and surface pressure are used.

likely to be  $NO_x$ -limited, however, since concentrations of  $NO$  are relatively small.

Speciation of the NMHC contributions (fig. 4.14) shows large contributions from the alkenes, in particular 1,3 butadiene. These species have fast rate constants with  $OH$ , and so are very efficient in producing peroxy radicals when present. The relative importance of isoprene becomes more marked in the southern regions away from strong sources of the anthropogenic NMHCs. In some cases, accounting for  $\sim 2$ -3 times the  $OH$  loss due to the other NMHCs.

Similar analyses have been made of two vertical profiles made by the C130. A stacked profile over Slovakia was made during flight A774 in the WCB outflow, and another was made during flight A772 over the Hungarian-Romanian border.  $OH$  loss rates were calculated from NMHC observations made during these profiles, but using rate constants calculated using the averaged temperature and pressure over the periods of the observations. Isoprene again shows a greater importance over the Hungarian-Romanian border region than in the polluted outflow sampled during A774. The total NMHC contributions at higher altitudes in the Slovakian stack also shows greater values than the  $CO$  contribution. This reflects the large concentrations

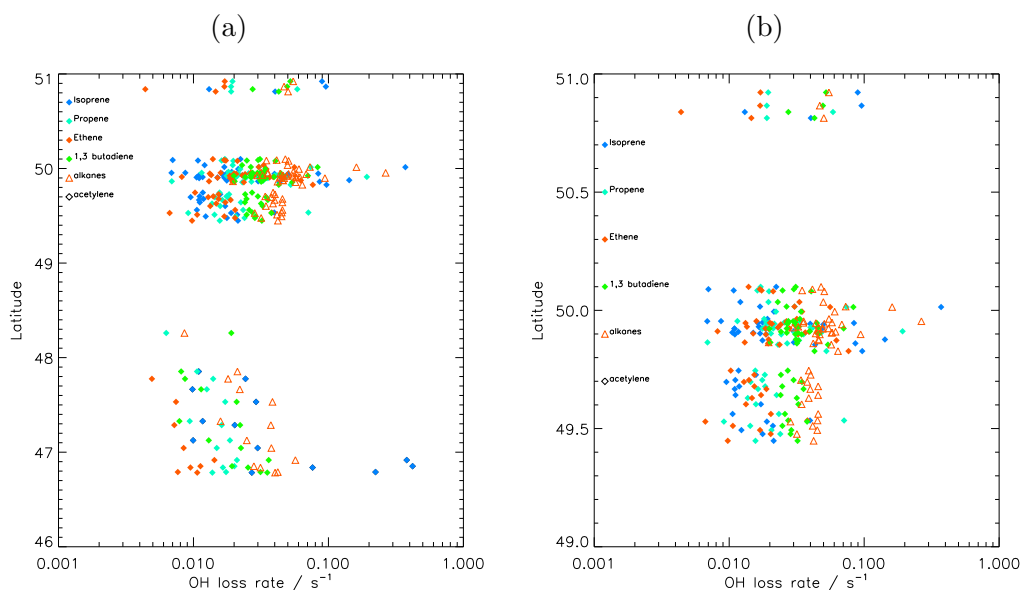


Figure 4.14:  $OH$  loss rates ( $s^{-1}$ ) calculated for PBL NMHC samples taken during the EXPORT campaign, for individual NMHC species types.

of fast-reacting alkenes present even at the higher altitudes in the freshly polluted outflow.

## 4.7 Evidence for halogen chemistry from EXPORT Flight A775

In the previous sections of this Chapter, NMHC data from flight A775 (August 9 2000) were omitted from the analysis. Data collected during the latter part of this flight showed unusual relationships between NMHC species, uncharacteristic of the rest of the flights. Figure 4.16 shows a number of NMHC correlations, with data collected after 12.40UT during this flight highlighted by diamond symbols. Observations of n-butane/iso-butane from the other flights (discussed in Section 4.4) showed a strong correlation, with an approximate 1:1 concentration ratio for all observations. This highlights the closely related sources of these isomers, and their almost equal  $OH$  oxidation rate constants. This observed relationship gives good support to the assumption that  $OH$  oxidation is mainly responsible for NMHC

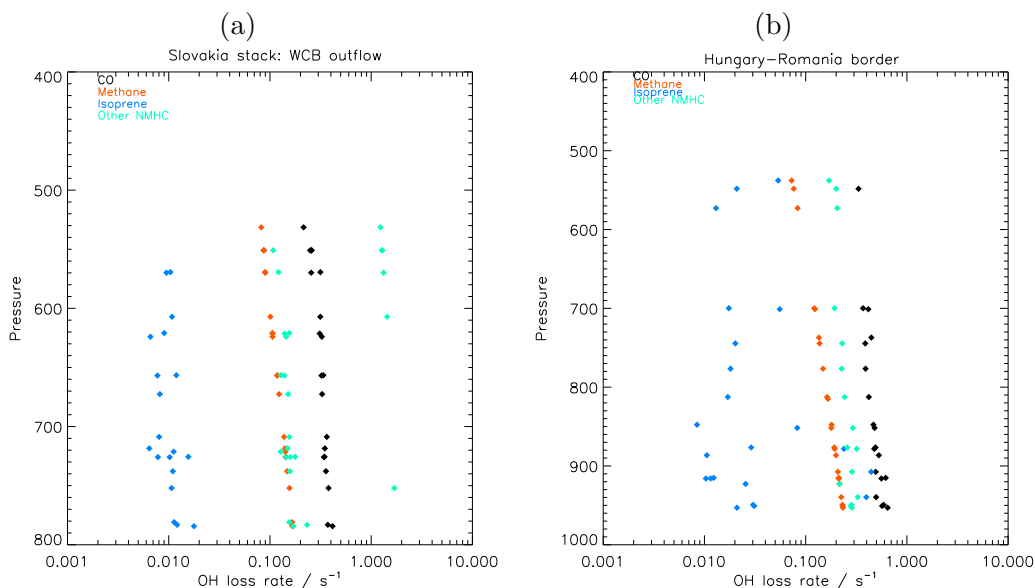


Figure 4.15: *OH loss rates ( $s^{-1}$ ) calculated for NMHC samples taken during (a) the stacked profile over Slovakia and (b) a stacked profile over the Hungarian-Romanian border.*

chemical removal. However, for observations made during the latter part of A775, this relationship breaks down. Larger iso-butane concentrations are observed for a given n-butane concentration, suggesting either a change in the source relationship of the two species, or that the chemical removal of n-butane is occurring at a faster rate than that of iso-butane. Plots of other pairs of NMHCs show similar deviations from the patterns observed during the rest of the flights.

The observations showing unusual NMHC relationships were made during the same period noted in Chapter 3 for an ozone/CO anti-correlation. A possible explanation for the unusual tracer relationships would be halogen chemistry. Cl and Br atoms are known to destroy ozone very efficiently and also react with NMHCs at rates very different from their OH oxidation rates (see Table 4.2). For example, n-butane is removed approximately 50% faster than iso-butane by Cl, whereas the OH removal rates are very similar, with the iso-butane rate only  $\sim 8\%$  faster. Br removes iso-butane twenty times faster than n-butane.

The ratios of n-butane and iso-butane to ethane from the EXPORT observations can

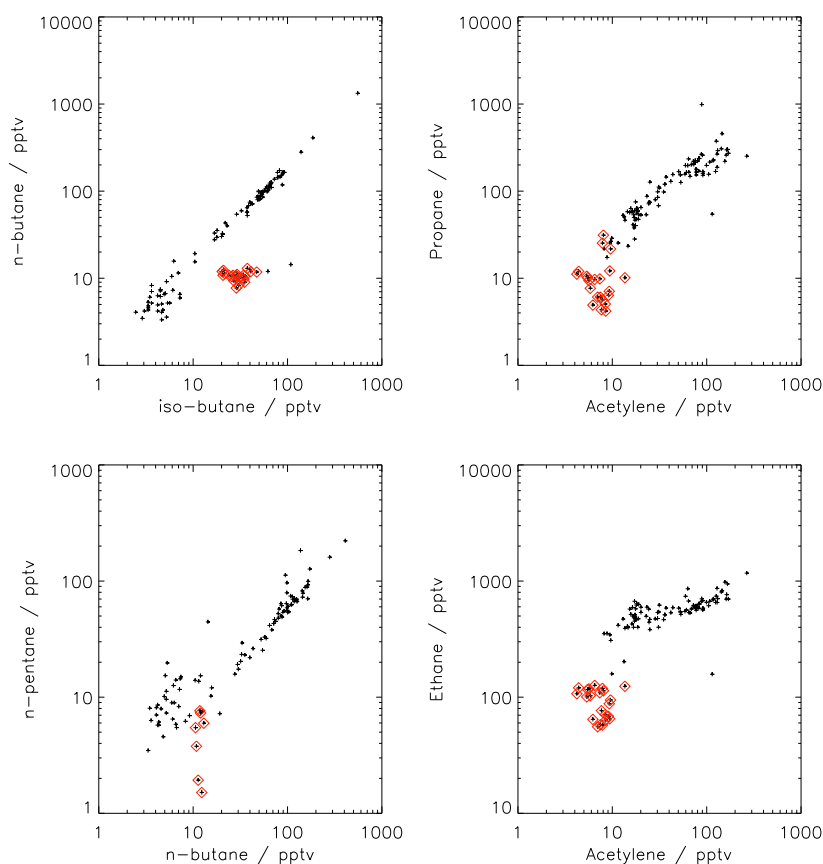


Figure 4.16: *NMHC ratio relationship for all EXPORT flights. Red diamonds highlight observations made after 12.40 UT during flight A775 (09/08/00).*

Table 4.2: *NMHC second-order rate constants for reaction with the OH radical and Cl atoms ( $\text{cm}^3 \text{molec}^{-1} \text{s}^{-1}$ ) at 298K. Kinetic data taken from IUPAC 2002 Recommendation [<http://www.iupac-kinetic.ch.cam.ac.uk/>] and the Leeds Master Chemical Mechanism [<http://www.chem.leeds.ac.uk/Atmospheric/MCM/mcmproj.html>]*

	$k_{\text{OH}} / 10^{12} \text{cm}^3 \text{molec}^{-1} \text{s}^{-1}$	$k_{\text{Cl}} / 10^{12} \text{cm}^3 \text{molec}^{-1} \text{s}^{-1}$
ethane	0.24	81.0
propane	1.10	120
iso-butane	2.19	218
n-butane	2.44	143

be used to infer a range of concentrations of halogen atoms, which would have to be present to produce the observed slope of [n-butane]/[ethane] vs [iso-butane]/[ethane]. Neglecting the effects of mixing, the slope of a plot of two pairs of NMHC ratios reduces to the ratio of the differences between the rate constants for oxidation for each pair (Equation 4.8). In the analysis of the NMHC data from flight A775, it is necessary to consider the reaction of the NMHCs with both OH and halogen atoms, since both of these processes will be competing for the removal of the NMHCs. For removal by both OH and Cl, the concentration of [X] will vary according to chemistry only as:

$$[X] = [X]_0 \cdot \exp(-(k_{X(Cl)}[\overline{Cl}] + k_{X(OH)}[\overline{OH}])\Delta t) \quad (4.12)$$

This yields

$$\frac{[X]}{[Y]} = \frac{[X]_0}{[Y]_0} \exp((k_{Y(Cl)} - k_{X(Cl)})[\overline{Cl}] + (k_{Y(OH)} - k_{X(OH)})[\overline{OH}])\Delta t) \quad (4.13)$$

For three co-emitted NMHCs, the analogous expression to Equation 4.8 becomes:

$$\ln \frac{[X]}{[Z]} = S \ln \frac{[Y]}{[Z]} - \left[ S \ln \frac{[Y]_0}{[Z]_0} - \ln \frac{[X]_0}{[Z]_0} \right] \quad (4.14)$$

where

$$S = \frac{(k_{Z(Cl)} - k_{X(Cl)})[\overline{Cl}] + (k_{Z(OH)} - k_{X(OH)})[\overline{OH}]}{(k_{Z(Cl)} - k_{Y(Cl)})[\overline{Cl}] + (k_{Z(OH)} - k_{Y(OH)})[\overline{OH}]}$$

A notable feature of this relationship is that the slope of a log-log plot of  $\frac{[X]}{[Z]}$  vs  $\frac{[Y]}{[Z]}$ , given by  $S$ , remains linear but has a dependence on the mean concentrations of the oxidants present,  $[\overline{OH}]$  and  $[\overline{Cl}]$ , as well as their reaction rate coefficients with the NMHCs. A range of slopes is therefore possible, depending on the relative amounts of the oxidants present, as well as the ambient temperature. Figure 4.17 shows the dependence of the calculated slopes on the mean concentrations of OH and Cl, for ambient temperatures of 230K and 298K.

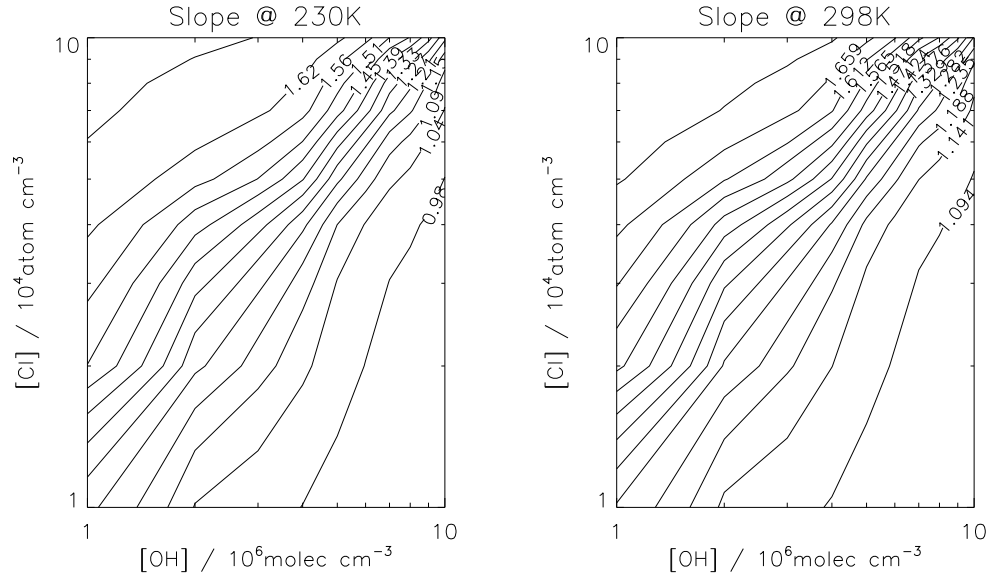


Figure 4.17: Slopes given by Equation 4.14 for a range of mean  $[OH]$  and  $[Cl]$  concentrations at temperatures of 230 and 298K.

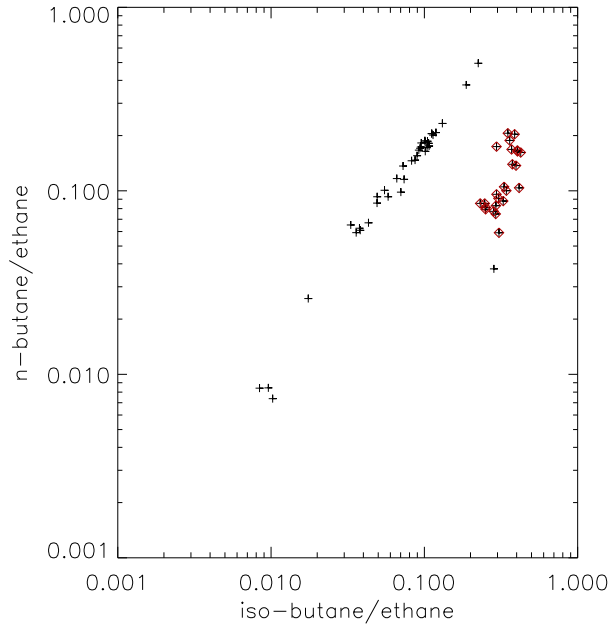


Figure 4.18:  $\frac{[n\text{-butane}]}{[ethane]}$  versus  $\frac{[iso\text{-butane}]}{[ethane]}$  ratios observed during EXPORT flight A775 (09/08/00). Red diamonds highlight observations made after 12:24 UT.



A plot of  $\ln \frac{n\text{-butane}}{\text{ethane}}$  vs  $\ln \frac{iso\text{-butane}}{\text{ethane}}$  for observations made during flight A775 is shown in Figure 4.18. Linear regressions of the plotted ratios yield gradients of 1.06 and 1.42 for data taken before and after 12:24 UT respectively. The slope expected from OH chemistry only, according to Equation 4.8 is given by

$$\frac{(k_{n\text{-butane}} - k_{\text{ethane}})}{(k_{iso\text{-butane}} - k_{\text{ethane}})}$$

Taking values for the OH rate constants of the NMHCs from Table 4.2, a value of 1.095 is obtained for the OH chemistry only slope. As discussed earlier, the rate constants for reaction of OH with n-butane and iso-butane are almost equal, and this yields a slope close to 1. The experimental slope of 1.06 is within 4% of the theoretical slope. The effect of temperature in changing the rate coefficients will give slight differences, since the calculated slope is for 298K. It should also be noted that the effects of mixing will draw data points away from the calculated slope towards a slope of unity, as discussed in Section 4.4. The experimental slope of 1.06, is therefore consistent with the influences of mixing and OH chemistry.

The slope of 1.42 obtained from data collected after 12:24UT suggests a role for Cl in the NMHC oxidation, rather than Br. Oxidation by Br would move the data points towards larger ratios of n-butane/ethane for a given iso-butane/ethane ratio, rather than vice-versa. The observed slope can be related to a mean concentration of Cl atoms by assuming a value for the mean OH concentration of the air masses during their advection from emission. Assuming a range of  $[\overline{OH}]$  of between  $1 \times 10^6$  and  $3 \times 10^6$  molec  $\text{cm}^{-3}$ , Figure 4.17 gives a value of between  $\sim 1.4 \times 10^4$  and  $4.0 \times 10^4$  atoms  $\text{cm}^{-3}$  for  $[\overline{Cl}]$ . It was noted above that mixing does very little to change the observed slope of the ratios under OH oxidation, since the OH reaction rate coefficients of n-butane and iso-butane are very similar. However, under Cl oxidation the observed slope is likely to be changed more markedly due to mixing, since as the points are drawn towards a slope of unity by mixing, they will be shifted over a greater range from the ideal chemical slope. Therefore in reality, the chemistry-only slope yielding this observed distribution of points is likely to be somewhat greater than 1.42. This would imply either a lower  $[\overline{OH}]$  value or a higher  $[\overline{Cl}]$  value than those derived above.

The magnitude of  $\overline{[Cl]}$  required in these air masses to produce the observed NMHC distributions is similar to that inferred in previous studies of NMHC oxidation by Cl atoms in the troposphere. *Rudolph et al.*, [1999] inferred Cl concentrations of a few  $10^4$  atoms  $\text{cm}^{-3}$  in the Arctic troposphere from NMHC observations. *Wingenter et al.*, [1996] inferred Cl concentrations between  $\sim 3$  and  $\sim 6 \times 10^4$  atoms  $\text{cm}^{-3}$  over the North Atlantic lower troposphere. *Lelieveld et al.*, [1999] inferred a diurnal mean Cl concentration of up to  $1 \times 10^4$  atoms  $\text{cm}^{-3}$  from NMHC observations in the lower-most stratosphere. They also inferred a Cl source from heterogeneous activation on ice crystals just above the tropopause.

As well as heterogeneous activation around the tropopause, chlorine atoms can be liberated in the marine PBL, through reaction of OH with HCl degassed from acidified NaCl aerosol [*Chameides and Stelson*, 1992]. Surface catalytic reactions involving HOBr and  $\text{Cl}^-$  may also yield marine Cl atoms *Andrae and Crutzen*, [1997].

The source of any Cl present in the case of EXPORT flight A775 is not clear. Back trajectories for the period of flight A775 during which the unusual NMHC ratios were observed, and for the periods during which observed NMHC ratios were similar to those observed during the rest of the flights are shown in Figure 4.19. There are no obvious differences between the transport paths for air masses arriving in these two time periods. However, the presence of the unusual NMHC ratios across the range of aircraft altitude levels in the latter half of the flight suggests a source of Cl which impacts some air masses transported at lower altitudes and those transported more rapidly in the UT. A marine Cl source in the north-west Atlantic PBL may provide an explanation, since frontal uplift from this region is brought into close proximity with air masses advected in the Atlantic UT. However, this is speculative.

## 4.8 Conclusions

The aims of this Chapter were to exploit the observations of NMHC species made during the EXPORT flights. Due to their characteristic sources and atmospheric lifetimes, NMHCs have been shown to provide useful insights into chemical and transport processes in the lower troposphere over Central Europe.

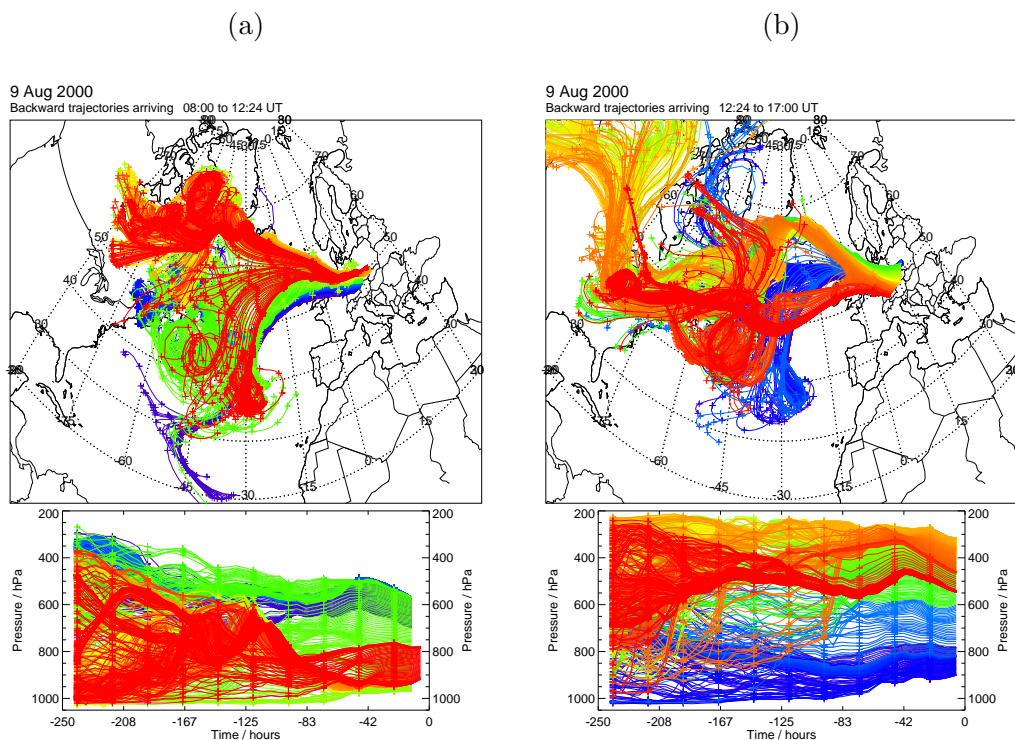


Figure 4.19: *Back trajectories arriving on the flight track of Flight A775 (Aug. 9 2000) (a) before 12.40 UT and (b) after 12.40 UT.*

Both chemistry and mixing have been shown to be important in determining the evolution of the ratio of two given NMHC species. Under such conditions, it is not possible to infer quantitative estimates of transport timescales for observed air masses since they encountered fresh emission. Despite this, correlations between absolute NMHC concentrations and their ratios have been observed, with largest concentrations and ratios observed near to the surface. Some qualitative comparison of the relative roles of mixing and chemistry in determining the evolution of air masses have also been inferred. During the TOPSE experiment, the relative roles of mixing and chemistry were seen to change through winter into spring, corresponding to increased abundances of the OH radical. Similarly, stronger mixing between air masses during the vertically unsettled EXPORT flights A773/4 than during the more stable conditions of flights A772/6 led to increased NMHC ratios relative to a given absolute NMHC concentration.

The Central European PBL was sampled extensively during the EXPORT campaign. NMHC observations reveal strong anthropogenic pollution over Poland and the Czech Republic, which correlates well to the regions of heavy industry to the south west of Krakow. Calculations of the OH loss rate due to the loading of different NMHC species suggest that in some cases, NMHCs contribute to a faster OH loss than CO in uplifted outflow from the sampled WCB. This is dominated by large concentrations of short-lived, highly reactive alkenes. To the south, observations were made over the Hungary-Romania border region. Isoprene was seen to be the dominant NMHC in the PBL, sometimes contributing an OH loss  $\sim 2$ -3 times that from the total of the other NMHCs. Industrial sourced NMHC concentrations were far lower in this region. However, propane concentrations were relatively high due to the presence of gas facilities in the region.

Unusual ratios of NMHCs observed during flight A775 (August 9 2000) suggest a role for Cl atoms in the removal of NMHCs. These observations correlate with observed ozone-CO anticorrelation, suggesting Cl removal of ozone. For a given range of reasonable OH concentrations, a diurnal mean Cl atom concentration of  $\sim 1.4 \times 10^4$  to  $4.0 \times 10^4$  atoms  $\text{cm}^{-3}$  was inferred. This is consistent with tropospheric Cl atom concentrations inferred in past studies. The source of the Cl atoms is unclear, however a marine PBL source in the North Atlantic is a possibility.

## 5. Comparisons of aircraft observations with the CiTTyCAT model

### 5.1 Introduction

Direct comparisons between atmospheric observations and numerical model simulations can be key for understanding processes important in controlling observed parameters. Here, the CiTTyCAT Lagrangian chemistry-transport model is used to simulate the concentrations of tropospheric trace gases observed during the EXPORT flights. The basic model data comparison allows identification of some of the chemical and transport processes responsible for the observed tracer signatures. The performance of the numerical model is assessed with reference to model initialisation and chemical processing. The model is also used to examine the chemical production and loss terms of the ozone budget in observed air masses.

In Section 5.2, the CiTTyCAT model is compared directly with observations made on the EXPORT flights. Production and loss processes for ozone are considered in Section 5.3, and results are compared with a TOMCAT model budget study carried out in the domain of the EXPORT flights. The evolution of chemistry and the ozone budget of individual air mass types are investigated in Section 5.4. In Section 5.5, the model is used to examine the contributions of different NMHCs to photochemistry in the PBL region. Section 5.6 summarises the conclusions of this Chapter.

## 5.2 Basic model comparison

The CiTTyCAT model was used to simulate the chemistry and transport of air masses along 4-day back trajectories arriving on each of the five EXPORT flights at a frequency of ten seconds. Deposition and global emissions from the EDGAR v3 inventory were included. Two sets of model runs were performed, first with initialisation taken from the Cambridge 2D model climatology [Law and Pyle, 1993a,b], and second with initial species concentrations taken from interpolated fields from a TOMCAT 3D model simulation covering summer 2000 [F.M. O'Connor, *personal communication*, 2001]. The TOMCAT simulation used the default tropospheric chemistry configuration described in Chapter 2, with a horizontal resolution of approximately  $2.8^\circ \times 2.8^\circ$ .

Output from the model for each flight is compared with the aircraft observations in Figures 5.1 - 5.5. There are obvious differences between the model runs using 2D and 3D initialisations. The amount of structure and variability produced by the 2D initialisation is reduced compared with the 3D initialisation, due to the use of zonal mean initial concentrations. Variability in the initial state of the trajectories is only derived from their initial latitudes and not from their initial longitudes. Output from the two model runs are discussed below with reference to the air mass types encountered.

### 5.2.1 Ozone

Ozone time series comparisons generally show a good qualitative agreement between model and observations; the model reproduces the magnitude of observed concentrations and the variations associated with sampling different air mass types. The 3D initialisation tends to give a better agreement in most cases in the free troposphere. Here, over 4-day trajectories that do not encounter emissions, the modelled net photochemical term for ozone is small, and the initial conditions are the dominant factor in controlling the ozone concentration (see Methven *et al.*, [2003]). The 3D initialisation is likely to be more reliable in these terms, since the TOMCAT model is forced using analysed meteorology, and contains 3D treatments for emis-

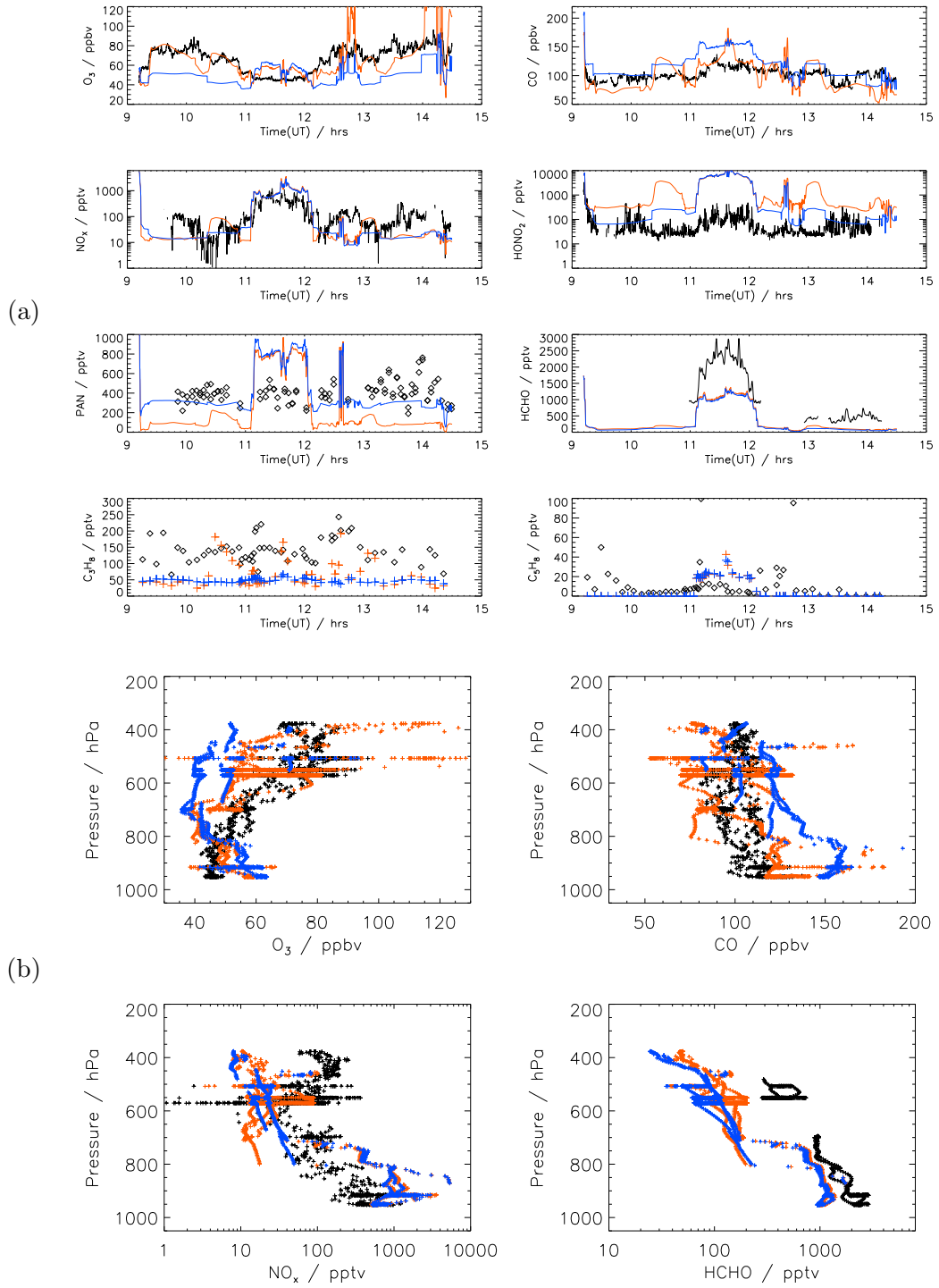


Figure 5.1: *CiTTyCAT* model/data comparisons for Flight A772 (31/07/00). (a) 10-second averaged time series and (b) vertical profiles. Black: obs.; Blue: 2D initialisation; Red: 3D initialisation.

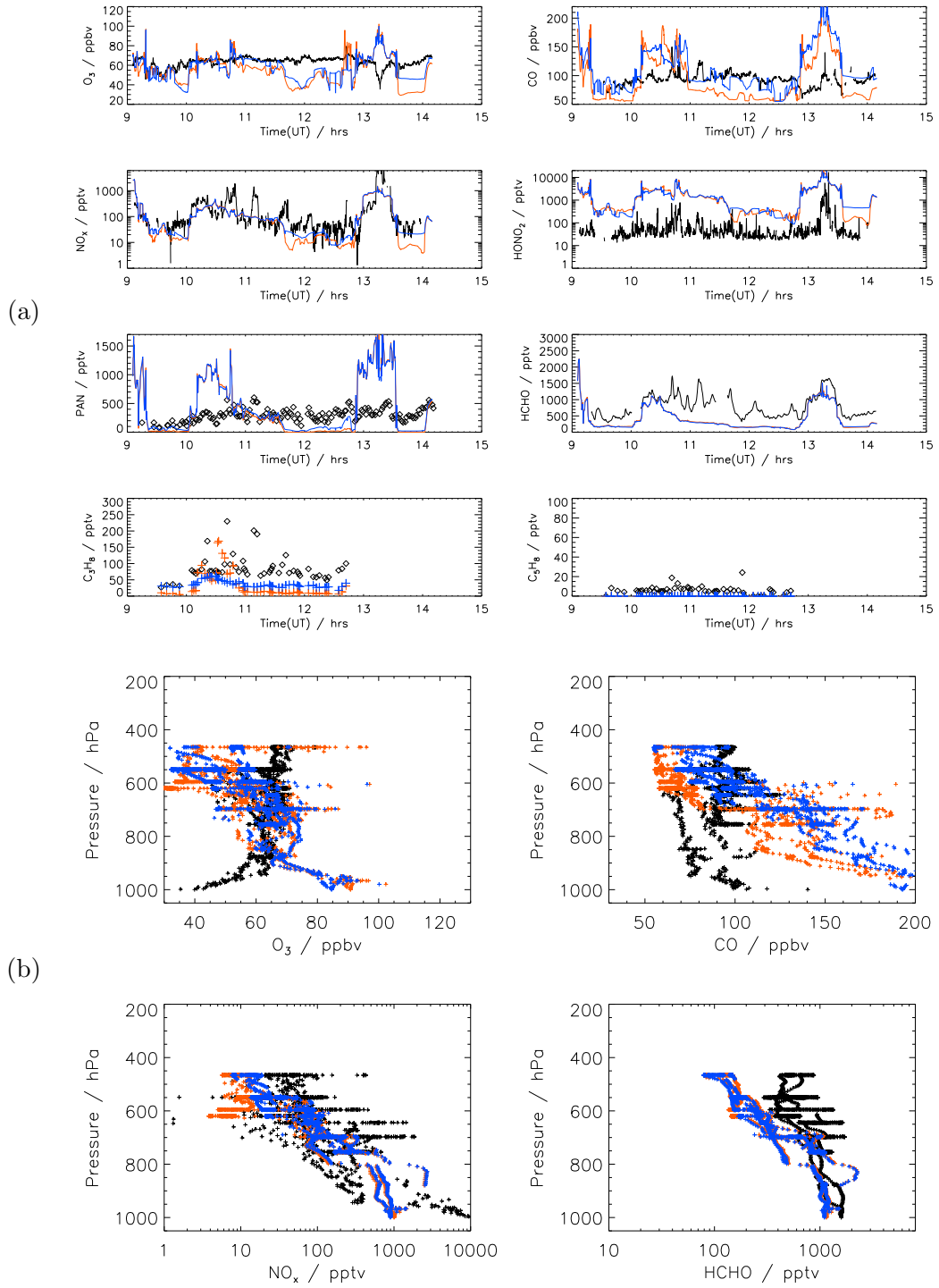


Figure 5.2: *CiTTyCAT* model/data comparisons for Flight A773 (02/08/00). (a) 10-second averaged time series and (b) vertical profiles. Black: obs.; Blue: 2D initialisation; Red: 3D initialisation.



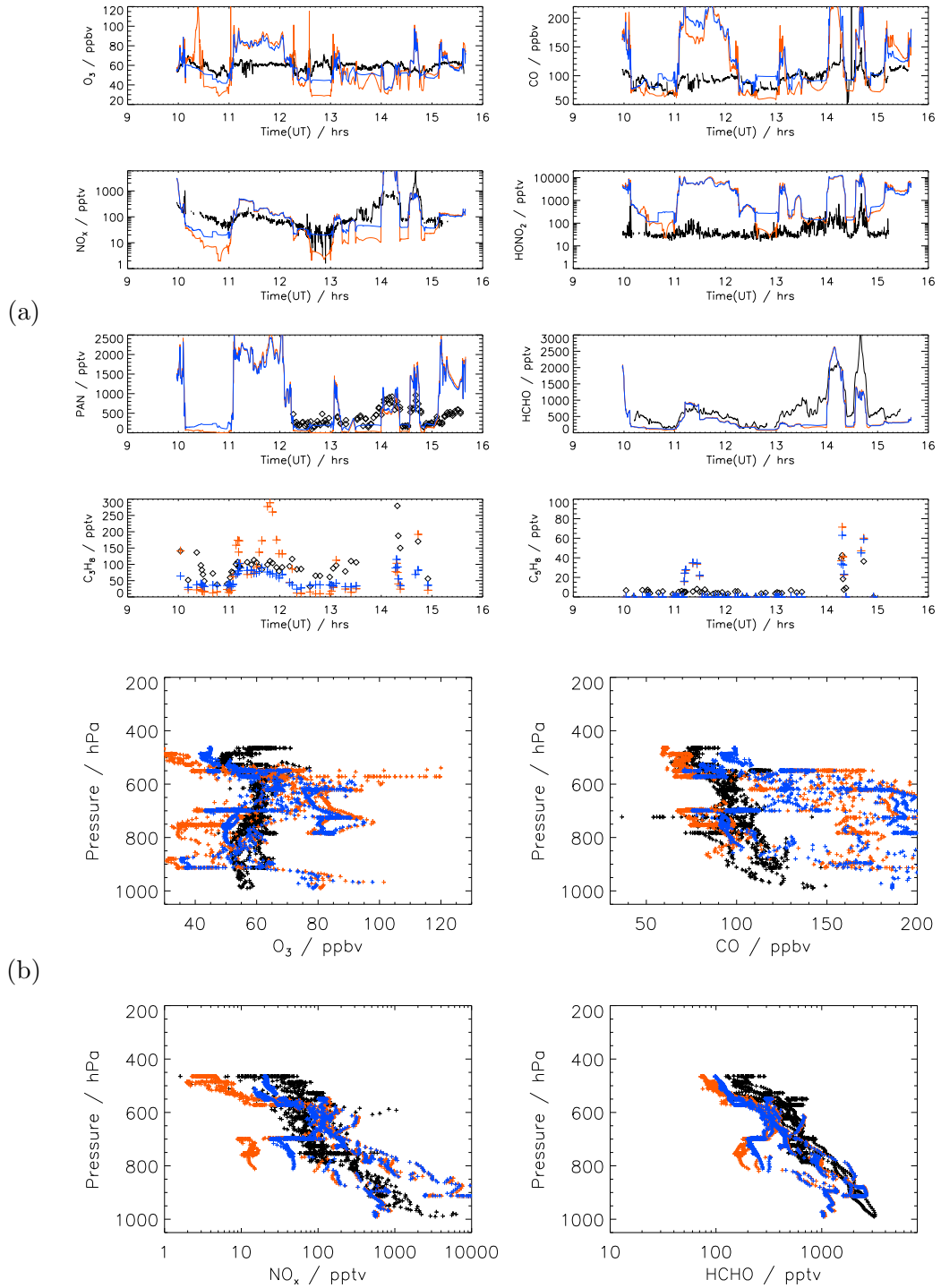


Figure 5.3: *CiTTyCAT* model/data comparisons for Flight A774 (03/08/00). (a) 10-second averaged time series and (b) vertical profiles. Black: obs.; Blue: 2D initialisation; Red: 3D initialisation.

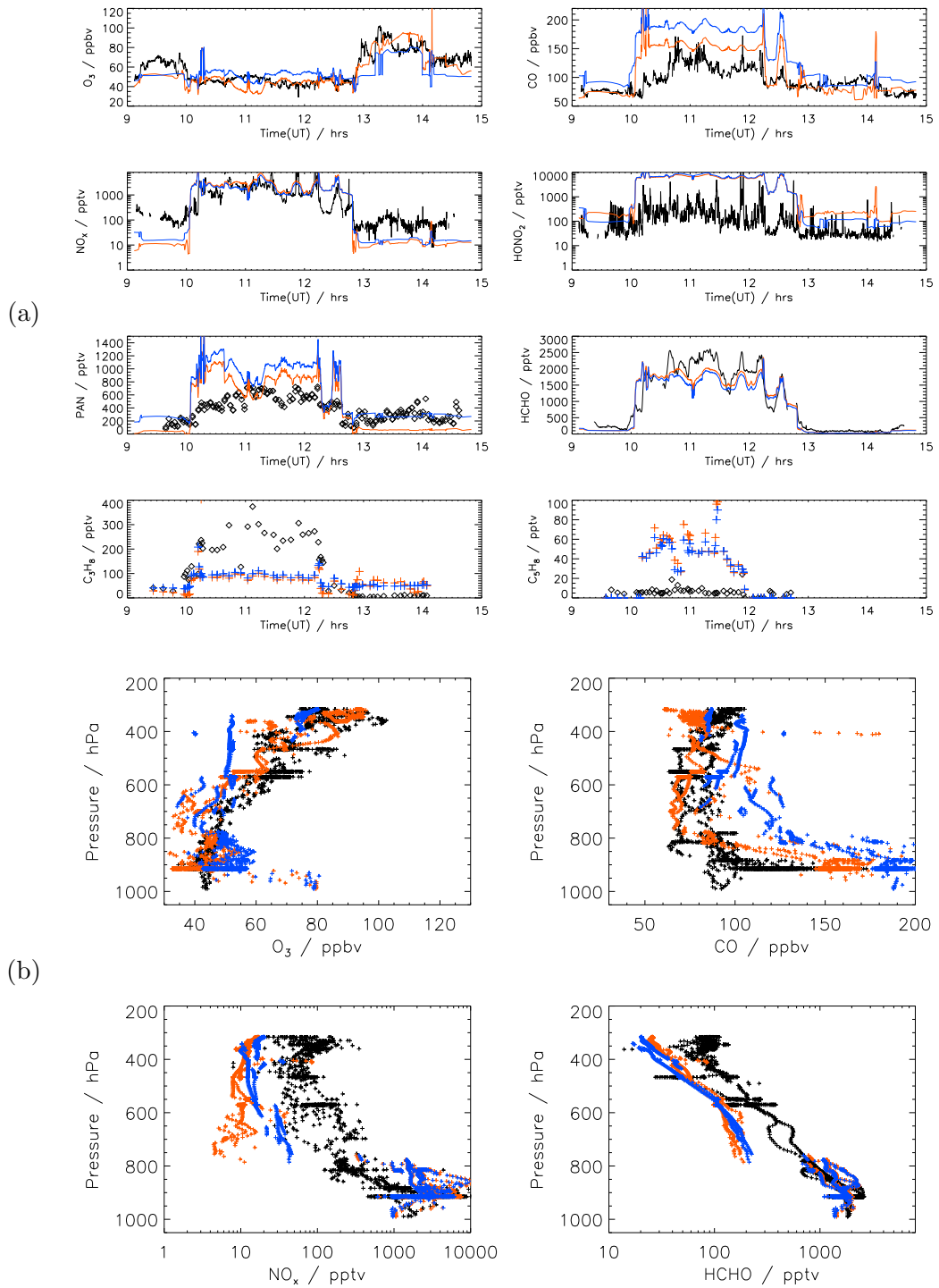


Figure 5.4: *CiTTyCAT* model/data comparisons for Flight A775 (09/08/00). (a) 10-second averaged time series and (b) vertical profiles. Black: obs.; Blue: 2D initialisation; Red: 3D initialisation.

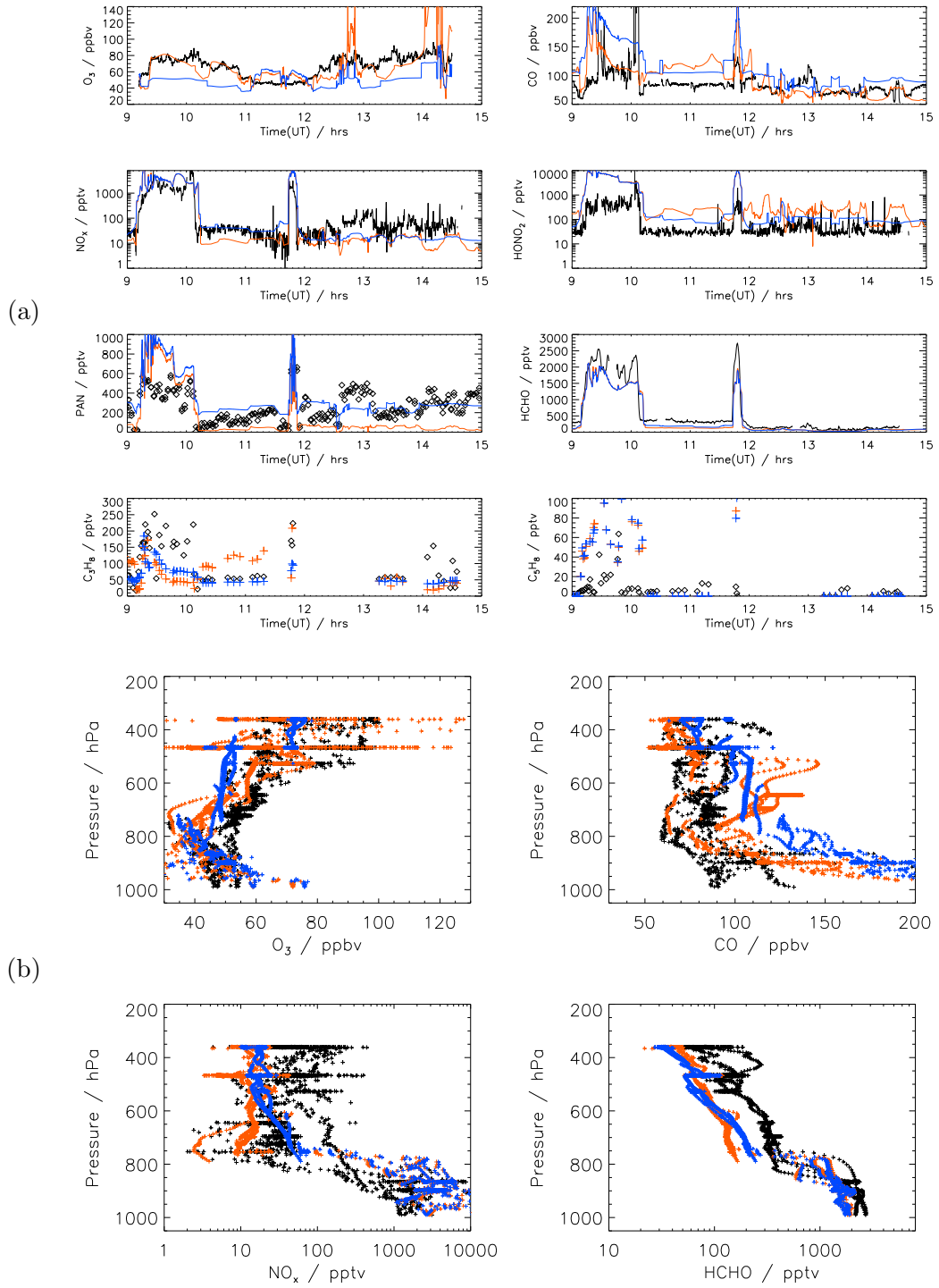


Figure 5.5: *CiTTyCAT* model/data comparisons for Flight A776 (10/08/00). (a) 10-second averaged time series and (b) vertical profiles. Black: obs.; Blue: 2D initialisation; Red: 3D initialisation.

sions, ozone deposition and stratosphere-troposphere exchange. TOMCAT also has a diurnal cycle, meaning initial conditions can be obtained at the correct time of day. The 2D initialisation is a climatology, not tied to specific dates. The model output is day-averaged, without a diurnal cycle. The 2D day-averaged, zonal mean chemistry and output cannot be expected to give a good representation of ozone concentrations at the air mass origin locations and times.

In the PBL, where the net photochemical term is larger, precursor emissions as well as the initial ozone concentrations become significant for the final ozone concentrations. Here, the CiTTyCAT model tends to overestimate ozone. This may be due to inadequate mixing from the PBL air masses into the free troposphere, allowing precursor concentrations to accumulate and over-produce ozone. This is evident in some cases, where PBL concentrations of  $\text{NO}_x$ , CO and NMHCs are very large in the model compared with observations (e.g. in the PBL during August 9 and August 10). On August 2, however, observed PBL ozone concentrations near the surface were as low as 40ppbv, compared with  $\sim 90$ ppbv from the model. The  $\text{NO}_x$  comparison suggests that large  $\text{NO}_x$  concentrations ( $\sim 10$ ppbv) observed near the surface may have resulted in titration of ozone by NO. The smaller  $\text{NO}_x$  concentrations in the model ( $\sim 1$ ppbv) mean that this titration is not as efficient.

In the UT, ozone concentrations produced by the 3D-initialised model are often large compared with observations. In these cases, back trajectories have transported air from near the tropopause over the Atlantic. The initial ozone concentrations given by TOMCAT are large, associated with the influence of stratospheric air in that model. The net photochemical term in this type of UT transport is very small, where the ozone lifetime is long and precursor concentrations small. The position of the tropopause and the stratospheric ozone concentrations from TOMCAT are therefore the major influences on the final model ozone concentration. As well as errors in these factors, the CiTTyCAT model also has no mixing of the ozone-rich air out into the UT. This may also lead to larger ozone concentrations being modelled than those observed.

### 5.2.2 $\text{NO}_y$

In the CiTTyCAT model, concentrations of  $\text{NO}_x$  are often small compared with observations. This is partly due to the isolated nature of the air parcels considered. Regardless of how good the initial concentrations of  $\text{NO}_x$  are, the lack of mixing in the model means that once the  $\text{NO}_x$  has been converted to longer lived reservoir  $\text{NO}_y$  species, such as  $\text{HONO}_2$  and PAN, the air parcel becomes permanently  $\text{NO}_x$ -depleted over its 4-day transport. In the PBL this is counteracted by emissions of fresh  $\text{NO}_x$  into the air parcels, allowing a better simulation of the observations. The so-called ‘persistence’ of  $\text{NO}_x$  concentrations in the UT is generally not captured well by CTMs (e.g. the TOMCAT model [O’Connor *et al.*, 2004]). This can lead to erroneous conclusions regarding the tropospheric ozone budget, since net ozone production/loss is very sensitive to the concentration of NO. The production/loss regime can reverse over a narrow range of NO concentrations, at the so-called compensation point (see e.g. Reeves *et al.*, [2002]). Realistic simulation of UT NO concentrations is therefore essential to allow realistic conclusions regarding the ozone budget.

Concentrations of  $\text{HONO}_2$  are generally large in the model compared with observations. This is due to efficient formation from  $\text{NO}_x$  mentioned previously, and also due to the lack of physical (non-chemical) loss processes for  $\text{HONO}_2$  in the model.  $\text{HONO}_2$  is highly soluble and is efficiently washed out of the atmosphere. Such loss is not included in CiTTyCAT.

Mid tropospheric  $\text{HONO}_2$  concentration are almost always smaller in the model when using the 2D initial fields. This appears to be due to different partitioning of  $\text{NO}_y$  in the initial chemical state. Figure 5.6 shows the initial concentrations picked up by the 4-day back trajectories from the TOMCAT 3D model and the 2D model climatology. In almost all cases, the  $[\text{PAN}]/[\text{HONO}_2]$  ratio in the 2D initialisation lies between 1 and 10, whereas it has a value of less than 1 in the 3D initialisation. The TOMCAT model partitions the majority of its  $\text{NO}_y$  in the free troposphere into  $\text{HONO}_2$ , and PAN concentrations are generally small compared with observations due to the lack of higher hydrocarbon chemistry. The 2D model however, often has concentrations of PAN many times those of  $\text{HONO}_2$ , despite also having limited hydrocarbon chemistry. This may be a consequence of the zonal-mean model

structure. Figure 5.6 demonstrates that for trajectories arriving in Central Europe the 2D initialisation gives a more homogeneous range of initial concentrations with longitude compared with the full 3D initialisation. In effect, the polluted signatures of air over the continental regions at mid-latitudes is smeared out zonally. Trajectories initialised over the Atlantic will therefore pick up a more polluted signature than is realistic. Likewise, air masses initialised over the continents will pick up a less strongly polluted signature, although in these regions emissions have the potential to mask the importance of the initial state. These effects are evident in the distributions of initial CO and NO<sub>2</sub> with longitude.

### 5.2.3 CO and NMHCs

Modelled CO concentrations from CiTTyCAT are very large in the PBL compared with observations, where they are dominated by emissions. This suggests that the lack of explicit mixing between the PBL and free troposphere allows large concentrations of emitted species to accumulate in PBL air parcels. In the free troposphere, 3D initialised model CO concentrations are generally similar in magnitude to observations. However, during flight A774 (August 3 2000), in the region of outflow from the WCB system (11.0-12.0 UT), the model produces quantities of CO, propane and isoprene far larger than observed. Emissions into air parcels which have followed the resolved flow from the lower troposphere into the middle troposphere have picked up large quantities of model emissions, which are not diluted into the surroundings by the model. HCHO, which is generally low in the free troposphere is well modelled here, due to the presence of freshly active photochemical pollutants in the in the model.

In contrast, during the ascent of the WCB itself (flight A773, Aug. 3 2000) CO and NMHC comparisons demonstrate that the model does not capture the enhancements of pollutants in the higher altitude regions of the WCB. This is due to the resolved flow of the trajectories not penetrating the PBL to pick up emissions. This supports the hypothesis of *Purvis et al.*, [2003], that the enhancements to pollutants in the upper levels of the WCB are largely due to smaller-scale convective transport from the PBL, rather than the large-scale slantwise ascent along the WCB. This is

discussed in detail in Chapter 6.

Under conditions where there is limited transfer between the PBL and free troposphere, CO concentrations show a strong gradient at the top of the model PBL. 2D initialisation tends to produce larger-than-observed CO concentrations, due to zonal averaging as discussed above. A strong gradient is also seen in HCHO, with the model predicting too much in the PBL and too little above, indicating that emissions are over-polluting the model PBL and that the 4-day trajectories in the free troposphere, without the influence of emissions, have become too photochemically inactive by the time they arrive. Enhancements to CO and propane seen at high altitudes are not captured by the model. This is since origins of these pollutants are likely to be over North America, and 4-day back trajectories are not long enough to capture the polluted initialisation.

## 5.3 Ozone budget over Central Europe

### 5.3.1 Instantaneous rates

Output from the CiTTyCAT model can be used to examine the relative importance of the photochemical production and destruction terms in determining the net ozone change in the domain of the EXPORT flights. A study of the ozone budget in this region during the EXPORT campaign has already been performed using the TOMCAT CTM [O'Connor *et al.*, 2004]. Here, the results from the CiTTyCAT model are compared with this study. For the remainder of the Chapter, all CiTTyCAT output discussed is from the 3D-initialised model.

Instantaneous reaction rates from the model are used to diagnose the individual photochemical production and loss terms for ozone on the EXPORT flight paths. It is difficult to validate such rates against observations, since they ultimately depend on the abundance of peroxy ( $\text{RO}_2$ ) radicals and  $\text{HO}_x$  concentrations, which are not widely measured. However, limited observations are available from the PERCA instrument on board the C130 [Green *et al.*, 2003], which measures the concentration of methyl peroxy radicals ( $\text{MeOO}$ ).

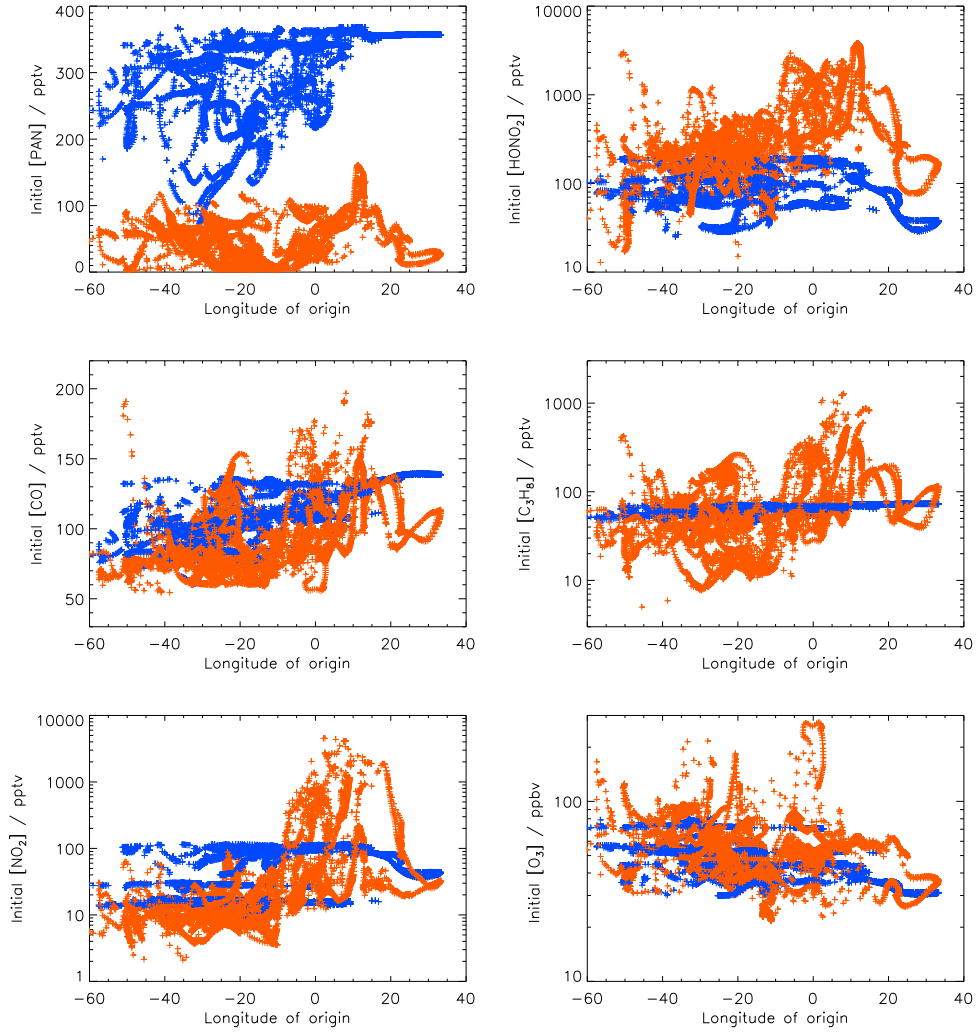


Figure 5.6: *Initial concentrations for 4-day trajectories arriving on all EXPORT flight tracks. Blue: taken from 2D model climatology; Red: taken from TOMCAT 3D model.*

Figure 5.7 compares model and observed rates for the formation of ozone from the reaction  $\text{NO} + \text{MeOO}$  on the EXPORT flight tracks. At all altitudes, the largest observed ozone production rates ( $\text{P}(\text{O}_3)$ ) are not captured by the model. In the mid-troposphere, this is due to the larger concentrations of NO and MeOO observed in the WCB during flight A773, than captured in the model. The lower range of  $\text{P}(\text{O}_3)$  from  $\text{MeOO} + \text{NO}$  is captured well in the mid-troposphere ( $0.01 - 0.30 \text{ ppbv hr}^{-1}$ ). In the UT, both model NO and MeOO concentrations are smaller



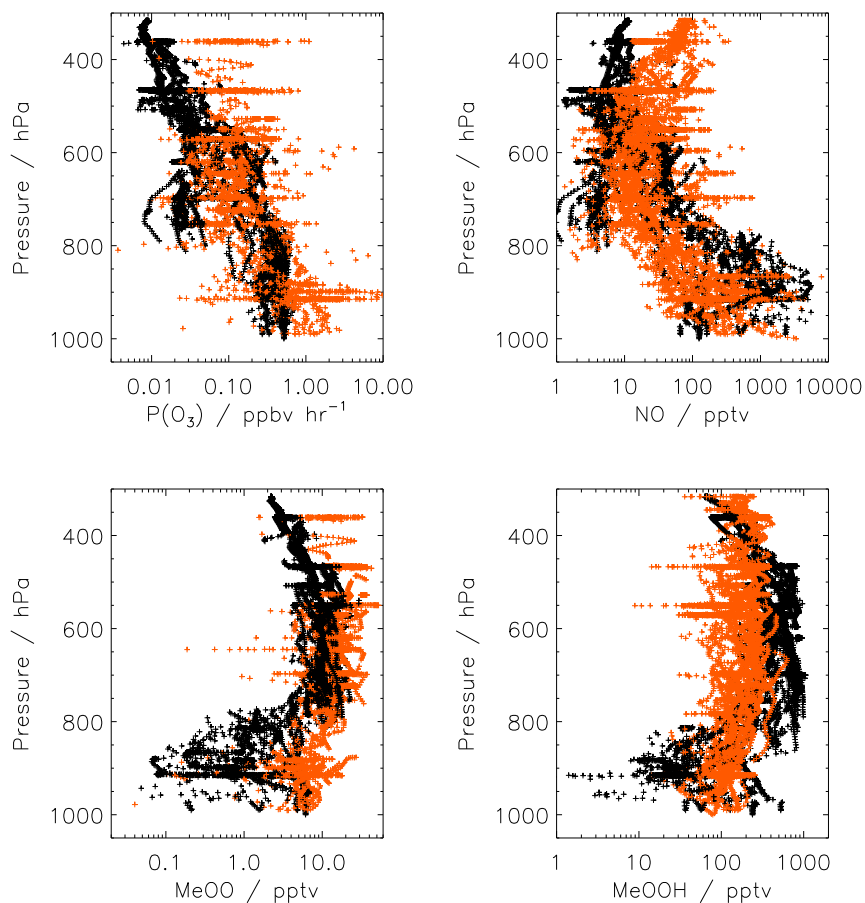


Figure 5.7: Comparison of CiTTyCAT modelled rate (black) and rate based on observed  $[MeOO]$  and  $[NO]$  (red) for the bimolecular reaction between  $NO + MeOO$  (i.e.  $k[NO][MeOO]/[M]$  in  $ppbv\ hr^{-1}$ ). Concentrations (pptv) of  $NO$ ,  $MeOO$  and  $MeOOH$  along EXPORT flight tracks as a function of aircraft pressure. Red: observations; Black: CiTTyCAT model.

than observed, leading to model  $P(O_3)$  in the range  $0.01-0.10\ ppbv\ hr^{-1}$ , with the observed rate being between  $0.02-1.00\ ppbv\ hr^{-1}$ . The model appears to be generally biased towards lower  $MeOO$  than observed at all altitudes. This may be a result of  $MeOO$  formation from higher hydrocarbons, which are not included in the model. This underestimation is especially apparent in the PBL, where observed  $MeOO$  concentrations are generally in the range  $3-30\ pptv$ , with the modelled concentration range between  $\sim 0.1$  and  $7\ pptv$ . O'Connor *et al.*, [2004] attributed small PBL

$P(O_3)$  in the TOMCAT model during the EXPORT flights to localised sources of high NO concentrations, not captured by the model. Results here however, suggest the discrepancy in the CiTTyCAT model is likely to be due to low PBL [MeOO], since the largest concentrations of NO in the European PBL are captured by the model.

Total net  $P(O_3)$  rates for the five EXPORT science flights are shown in Figure 5.8. These are model-calculated instantaneous net rates considering all odd-oxygen producing and destroying reactions included in the CiTTyCAT chemistry scheme (see Appendix A). The net rate is strongly positive in the model PBL, coincident with the highest concentrations of NO and peroxy radicals. Maximum  $P(O_3)$  rates are  $> 4.5$  ppbv  $hr^{-1}$ , occurring up to  $\sim 800$ hPa. This compares to maximum rates derived from the TOMCAT model of  $\sim 3.5$  ppbv  $hr^{-1}$ , near the surface [O'Connor *et al.*, 2004]. Larger ozone production in the CiTTyCAT PBL can be at least partly attributed to the increased number of NMHC species considered (i.e.  $C_4 - C_6$  and isoprene, in addition to ethane and propane also in TOMCAT). Figure 5.9 compares net  $P(O_3)$  calculated including peroxy radicals from all NMHC species considered by CiTTyCAT with net  $P(O_3)$  including only peroxy radicals from NMHCs considered in TOMCAT (ethane, propane). When considering this limited suite of organic peroxy radicals, the maximum modelled net  $P(O_3)$  reduces to less than 4 ppbv  $hr^{-1}$ , consistent with the TOMCAT model calculation. The contribution from extra NMHCs considered by CiTTyCAT is between less than  $\sim 0.1$  and  $0.7$  ppbv  $hr^{-1}$ .

Above the PBL, the values of CiTTyCAT net  $P(O_3)$  are far smaller, and often negative. The role of the extra CiTTyCAT NMHCs is also small here, as these are only present in air parcels which have taken up emissions in the PBL. The initial concentrations of these species in the trajectories are set to zero, since they are not considered by TOMCAT. A small net positive CiTTyCAT  $P(O_3)$  up to 2 ppbv  $hr^{-1}$  is modelled above the PBL during flights A773 and A774, in the fresh outflow of recent ascent in the WCB system. There are also regions of net ozone destruction, with  $P(O_3)$  as low as  $\sim -1.0$  ppbv  $hr^{-1}$ , as a result of uplift of large quantities of moist air. TOMCAT shows almost exclusively net positive  $P(O_3)$  for these periods, with maximum values of just over 1.0 ppbv  $hr^{-1}$  [O'Connor *et al.*, 2004]. The small TOMCAT rates cannot be attributed to less complex NMHC chemistry, since

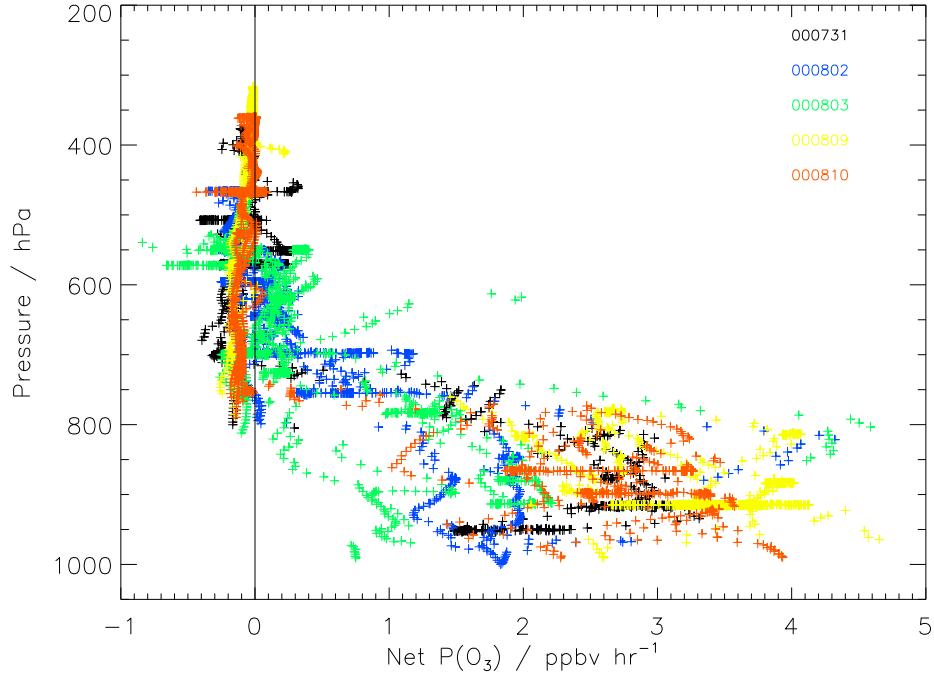


Figure 5.8: *Net modelled instantaneous ozone production rates for the EXPORT campaign coloured by day of flight. All modelled odd-oxygen producing and destroying reactions considered.*

CiTTyCAT calculated model rates are not greatly different at these altitudes for the simple and more complex NMHC schemes (Fig. 5.9). It therefore seems likely that one or more of the concentrations of  $\text{NO}_x$ ,  $\text{HO}_2$ , or the basic NMHC peroxy radicals are larger in CiTTyCAT compared with those in the TOMCAT simulation for these periods.

For the more vertically stable periods, net  $\text{P}(\text{O}_3)$  above the CiTTyCAT PBL is negative, in contrast to the TOMCAT results. Loss of  $\text{NO}_x$  to  $\text{NO}_y$  reservoirs in trajectories not influenced by emissions results in a low potential for ozone production after four days, on arrival at the flight location. Processes such as vertical transport by convection and mixing with aircraft and lightning  $\text{NO}_x$  emissions, as well as surrounding air from different locations in the TOMCAT model, allows mid/upper troposphere  $\text{NO}_x$  concentrations to be better maintained and more realistic.

The major individual photochemical production and loss terms for ozone are shown

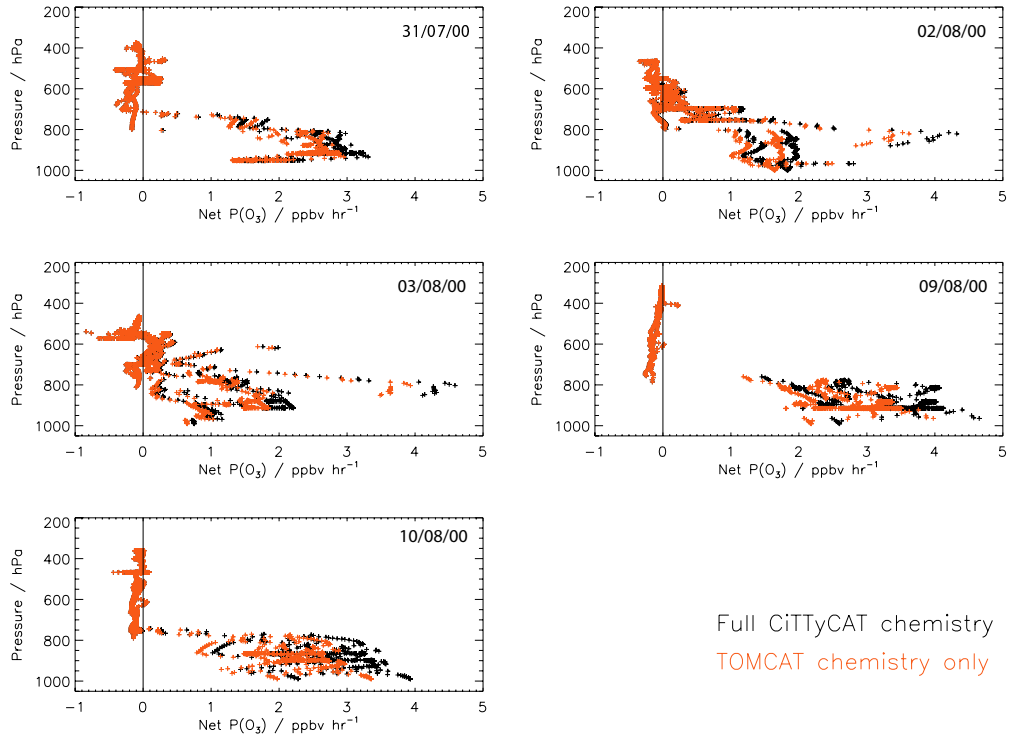


Figure 5.9: *Net CiTTyCAT modelled instantaneous ozone production rates (ppbv hr<sup>-1</sup>) for the EXPORT campaign, considering all CiTTyCAT NMHCs (black) and only NMHCs present in TOMCAT (red).*

in Figure 5.10. The largest contributor to the net rate is the reaction  $\text{HO}_2 + \text{NO}$ . In the PBL, this contributes approximately 60-70% of the ozone production rate.  $\text{MeOO} + \text{NO}$  makes a smaller contribution of between 10 and 20%. The loss term  $\text{O}(^1\text{D}) + \text{H}_2\text{O}$  is of similar magnitude to the  $\text{MeOO} + \text{NO}$  production term, and is largest in the moist PBL. This term also reaches PBL-like magnitudes in the mid troposphere in the outflow from the WCB system sampled in flight A774, and also in some of the trajectories ascending the WCB sampled during flight A773. This indicates the uplift of moisture-rich air in the modelled resolved flow. For the vertically settled conditions of flights A775 and A776, the net photochemical term is small and negative, and there is a balance between production and loss terms of magnitudes of only  $\sim 0.2 \text{ ppbv hr}^{-1}$ . This again highlights how slow the ozone photochemistry becomes in free tropospheric air masses 4 days after initialisation.

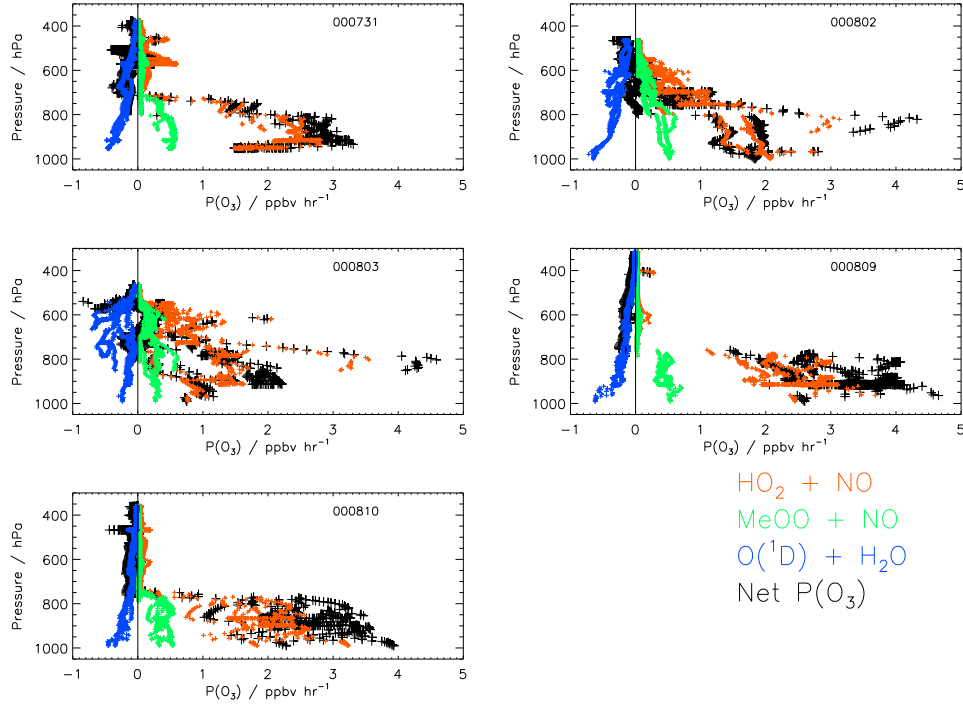


Figure 5.10: *Modelled instantaneous photochemical ozone production and loss terms ( $\text{ppbv hr}^{-1}$ ) on the flight tracks of the five EXPORT science flights.*

### 5.3.2 Net change in ozone over 4 days

As well as examining the instantaneous rates of ozone production and loss at the time and location of the aircraft, the Lagrangian model framework allows straightforward diagnosis of the net change in ozone concentration in the air masses over the course of their 4-day trajectories before arriving at the aircraft location. In effect, this provides information on the recent photochemical history of air which the aircraft has sampled.

Figure 5.11 shows the net change in ozone in the 4-day back trajectories arriving on the EXPORT flights. For some trajectories arriving in the PBL, a net production of up to 60 ppbv is modelled, equivalent to a mean production rate of  $\sim 0.6 \text{ ppbv hr}^{-1}$ . This is substantially smaller than the peak instantaneous PBL rates shown in Fig. 5.8, due to the instantaneous rates being calculated for the middle of the day, where they are largest. The net change over 4 days also includes deposition of

ozone in the PBL. Air masses advected in the free troposphere under the vertically settled conditions of August 9 and 10, show net loss due to photochemical removal, since the initial chemical state is not capable of sustaining ozone production over the four days. A net loss of between 5 and 10 ppbv over the four days is equivalent to a mean loss rate of between  $\sim 0.05$  and  $0.10$  ppbv  $\text{hr}^{-1}$ , roughly consistent with the small instantaneous net loss rates shown in the free troposphere previously. Air masses sampled in the free troposphere, in the region of outflow from the WCB on August 2 and 3 show large net production of ozone of up to 40 ppbv. Here, ascending trajectories have picked up strong ozone precursor signatures from initialisation in polluted air in the European lower troposphere, or have picked up emissions before ascending out of the PBL.

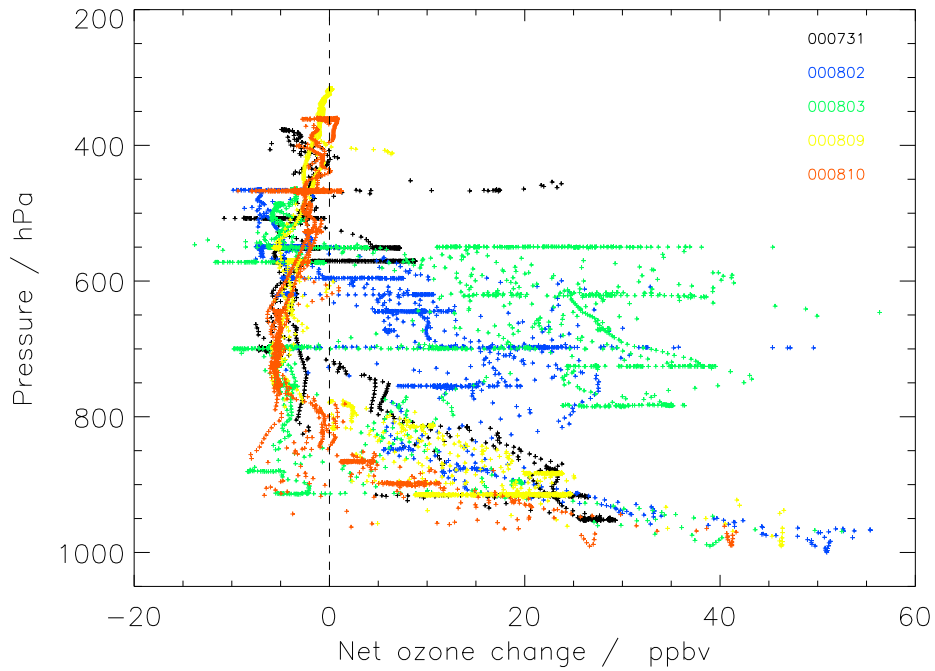


Figure 5.11: *Modelled net change in ozone along 4-day back trajectories arriving on the EXPORT flights, coloured by day of flight.*

## 5.4 Ozone budget in individual air masses

As well as looking at net changes and mean rates of change over 4-day back trajectories, the Lagrangian model allows detailed investigation of processing in the air mass as it is advected. Here, output from the CiTTyCAT model is used to examine the terms of the ozone budget as air masses are advected under different transport scenarios. Examples are taken from the four day advection of air masses sampled during EXPORT. The four example trajectories are shown in Figure 5.12, and described in Table 5.1.

Table 5.1: Details of trajectory types used for individual air mass budget studies.

	Arrival Date	Arrival Time	Description
Type A	10/08/00	09:20UT	PBL advection over North West Europe.
Type B	10/08/00	08:20UT	Westerly transport from Atlantic in free troposphere.
Type C	09/08/00	13:57UT	Advection in North Atlantic upper troposphere.
Type D	03/08/00	12:14UT	Uplift from Spanish PBL in WCB.

Figures 5.13 - 5.16 show output along the four trajectory types during their 4 day advection to the aircraft position.

### 5.4.1 Type A

Trajectory type A represents air mass transport from the Atlantic marine PBL into the Western European PBL. This air mass is therefore heavily affected by emissions. For example, CO concentrations increase from less than 100 ppbv to  $\sim 150$  ppbv over the course of advection across Europe, with  $\text{NO}_x$  concentrations reaching between 3 and 4 ppbv. Formation of  $\text{HONO}_2$  is considerable, due to rapid conversion from  $\text{NO}_x$  and lack of mixing, as outlined previously. Both oceanic and continental emissions of isoprene are evident, contributing to peak concentrations of  $\sim 150$  pptv, and rapid

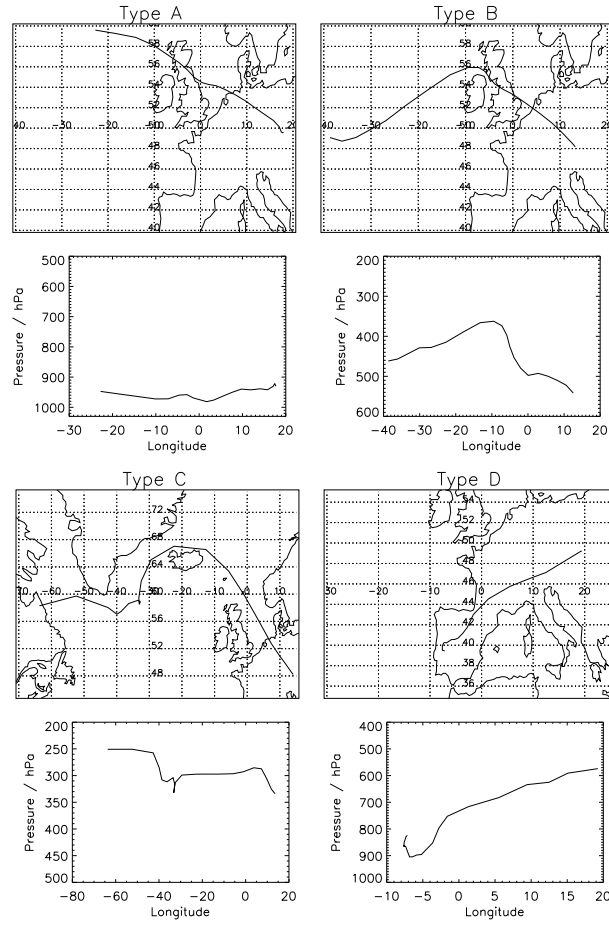


Figure 5.12: 4-day back trajectories for 4 different air mass transport regimes used in the individual air mass budget studies.

formation of PAN.

Net  $P(O_3)$  is mostly positive, with diurnal maxima between 1 and 3 ppbv  $hr^{-1}$ . Dry deposition removes between 0 and 0.4 ppbv  $hr^{-1}$  of ozone, exceeding the photochemical loss through  $O(^1D) + H_2O$ , which has a diurnal maximum rate of 0.2 ppbv  $hr^{-1}$ . Over continental Europe, NMHCs contribute up to 22 % of the diurnal maximum ozone production rate.



### 5.4.2 Type B

Trajectory type B transports air from the Atlantic into Europe in the free troposphere, away from the influence of PBL processes, such as emissions and deposition. As a result, in the isolated air mass, concentrations of CO and NMHCs decrease as they are removed chemically.  $\text{NO}_x$  concentrations are less than 30 pptv, with a slight increase as the air mass descends due to decomposition of PAN.

Net  $\text{P}(\text{O}_3)$  is slightly negative ( $\sim -0.05$  to  $-0.12$  ppbv  $\text{hr}^{-1}$ ), and is a balance between weak formation, mainly from  $\text{HO}_2 + \text{NO}$  and direct destruction of ozone by  $\text{HO}_x$  and  $\text{O}(^1\text{D}) + \text{H}_2\text{O}$ . These terms all increase in magnitude as the air mass descends. The increase to the loss routes is greater due to enhanced water vapour concentrations, leading to increased flux through the  $\text{O}(^1\text{D}) + \text{H}_2\text{O}$  channel and more efficient  $\text{HO}_x$  formation.

### 5.4.3 Type C

Air mass transport in the Atlantic upper troposphere imposes a relatively dry, low temperature and low pressure environment. In the absence of any contributions from aircraft emissions, or mixing from the surrounding air, CO and NMHCs are removed by photochemistry during advection. PAN concentrations remain approximately constant, due to the cold temperatures where PAN is stable. Formation of extra PAN during advection is not favoured due to the low abundances of peroxyacetyl-forming NMHCs, and the large  $\text{NO}/\text{NO}_2$  ratio. At UT altitudes the photolysis of  $\text{HONO}_2$  is more efficient, and this leads to a net loss of  $\text{HONO}_2$  over the course of the trajectory. Despite the release of  $\text{NO}_2$  through this photolysis,  $\text{NO}_x$  concentrations also decline, due to the sequestering of  $\text{NO}_2$  into  $\text{HO}_2\text{NO}_2$  and  $\text{MeO}_2\text{NO}_2$ , facilitated by the cold temperatures.

Ozone loss dominates, although the magnitude of the net  $\text{P}(\text{O}_3)$  is small (less than  $0.04$  ppbv  $\text{hr}^{-1}$  maximum). There is a weak production flux, mainly through  $\text{HO}_2 + \text{NO}$ , suppressed by low  $\text{NO}_x$ , and low  $\text{HO}_x$ .  $\text{MeOO} + \text{NO}$  contributes a maximum of only  $0.01$  ppbv  $\text{hr}^{-1}$ . *In situ* observations of MeOO and NO at these altitudes, described in Section 5.3.1, gave ozone production rates through this channel of up

to  $1 \text{ ppbv hr}^{-1}$ . Model values of NO concentrations at this altitude are an order of magnitude smaller than those observed. This is likely to be the major factor in the model producing such small  $P(\text{O}_3)$  rates.

#### 5.4.4 Type D

This transport regime moves an air mass out of the Spanish PBL, ascending over France and the Alps in the WCB outflow examined during flight A774 (Aug. 3 2000). The air mass spends approximately two days in the PBL, where large concentrations of isoprene (up to 300 pptv) are picked up, and CO increases. Formation of both  $\text{HONO}_2$  and PAN is very efficient, sequestering much of the freshly emitted  $\text{NO}_x$ . PAN concentrations increase rapidly as the air mass ascends to cooler temperatures, reducing ozone production efficiency through the removal of both  $\text{NO}_2$  and peroxyacetyl radicals from isoprene oxidation.

During the day, ozone production dominates, with up to 50% as a result of NMHC oxidation products. This is a reflection of the large isoprene concentrations in the model, which produce large quantities of efficient ozone producing peroxy radicals through photo-oxidation. At night, ozone loss dominates in the PBL due to deposition. After ascent from the PBL when isoprene concentrations diminish, NMHCs contribute a little over 10% to the total ozone production rate. The reduction in  $\text{NO}_x$  concentrations due to PAN formation reduces the peak diurnal  $P(\text{O}_3)$  by approximately 25%. This highlights importance of isoprene in the ozone budget, both locally near emission sources, and as a major precursor for PAN which can store  $\text{NO}_x$  for release far downwind of emission.

### 5.5 Contributions of NMHCs to PBL photochemistry

In Chapter 4, observations of NMHCs were used to infer their relative importance in the regional photochemistry of the Central European PBL. It was shown that isoprene was often the dominant OH sink in the south of the sample region, near the Hungary-Romania border. In the north, near the industrial regions of Poland

and the Czech Republic, the alkane sink for PBL OH was comparable with CO. The contribution of isoprene was generally less than that from the alkanes.

Figure 5.17 shows the contributions to the OH loss rate made by NMHCs in the PBL, in CiTTyCAT. The model output has been averaged over the same locations and times as the canister samples taken on board the C130. The general difference between the northern and southern regions inferred from the observations of NMHCs (Fig. 4.14) is reproduced, where contributions from individual species are generally smaller in the south.

Isoprene is the dominant NMHC in the south, contributing between 0.01 and 0.1  $\text{s}^{-1}$  OH loss. This is in good agreement with the observations-based study (Section 4.6). The magnitude of the contribution from the alkanes is in good agreement with observations in both regions, although in the north the contribution is slightly large and in the south, observations showed that it was often equal to the contribution from isoprene.

The dominance of isoprene in the north is not in agreement with the observation-based study. This may suggest too much model emission of isoprene in this region. The biggest non-alkane contributor in the model is toluene, accounting for  $\sim 0.01 \text{ s}^{-1}$  OH loss in the south, and up to  $\sim 0.1 \text{ s}^{-1}$  OH loss in the north. Observations of such aromatic species are not available. However, these model results suggest that it may play an important role in regional PBL photochemistry. Modelled contributions from ethene and propene are up to an order of magnitude lower than suggested by the observation-based study. This points to a deficiency in the model NMHC emissions scheme, where PBL concentrations of the alkenes are underestimated. The subsequent large underestimation in their contribution to photochemistry may be an important model deficiency, reducing the overall peroxy radical burden of the PBL.

## 5.6 Conclusions

In this Chapter, output from the CiTTyCAT Lagrangian trajectory model has been compared with trace gas observations made on board the C130 during the EXPORT

flights.

The choice of model initialisation has been shown to be critical in regions of slow photochemistry, where it is important for the final trajectory output. The 2D initialisation provided initial conditions that were too polluted over the Atlantic ocean and less polluted over Europe due to its zonally averaged fields. The zonal mean chemical treatment was also shown to give a very different  $\text{NO}_y$  partitioning from the 3D (TOMCAT) model output, with PAN being the dominant  $\text{NO}_y$  component in the 2D climatology. Initial ozone taken from the TOMCAT fields was shown to provide a good model/observation comparison after four days of advection under free tropospheric conditions, and relatively slow photochemistry.

In the free troposphere, ozone concentrations over 4-day trajectories were shown to be dominated by the initial chemical state of the air mass. Net  $\text{P}(\text{O}_3)$  rates were shown to be small and negative away from recent PBL influence, and were often less than  $0.1 \text{ ppbv hr}^{-1}$ . Observations of NO and MeOO along with results from the TOMCAT CTM [O'Connor *et al.*, 2004] suggest that the ozone production is likely to be larger in these regions, and the CiTTyCAT model underestimates  $\text{P}(\text{O}_3)$  due to its lack of mixing and rapid loss of  $\text{NO}_x$  to reservoir species.

Results from flight A773, where a WCB system was sampled, suggest that the Lagrangian advection does not capture the more rapid ascent of freshly polluted PBL air into the free troposphere. This supports the hypothesis of Purvis *et al.*, [2003] who suggested embedded convection in the WCB system was responsible for much of the PBL mass uplift.

Isoprene has been shown to dominate the photochemistry of the PBL in the model, in agreement with observations in the south of the EXPORT study region. The modelled isoprene contribution to photochemistry in the north, was too large compared with that of anthropogenic alkanes. The model suggests an important role for toluene in the photochemistry of the European PBL, although without observations it is difficult to assess the validity of this. Alkenes contributed up to an order of magnitude less to PBL peroxy radical concentrations in the model than suggested by observations.

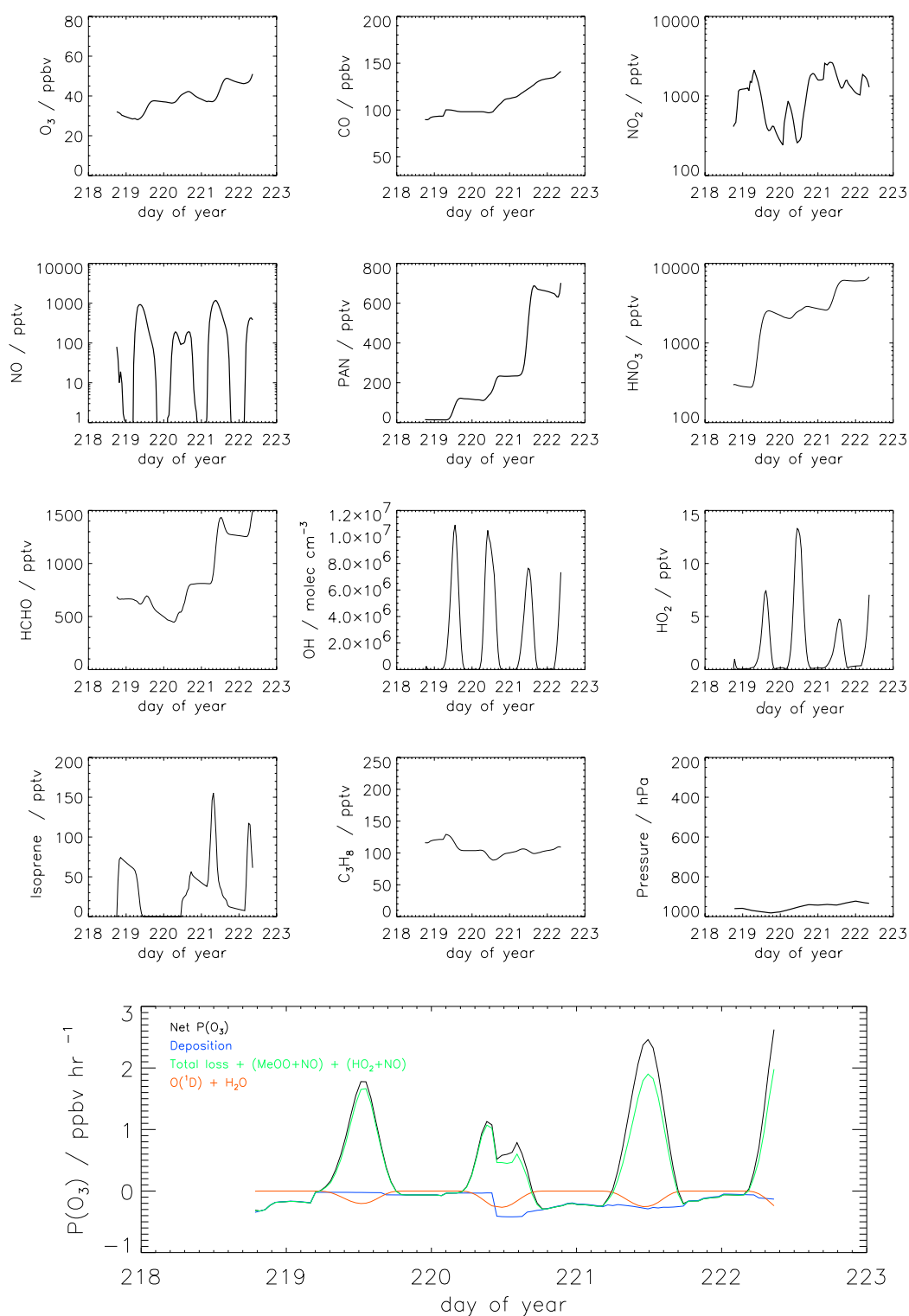


Figure 5.13: *Along-trajectory model output for air mass Type A over four days of advection.*

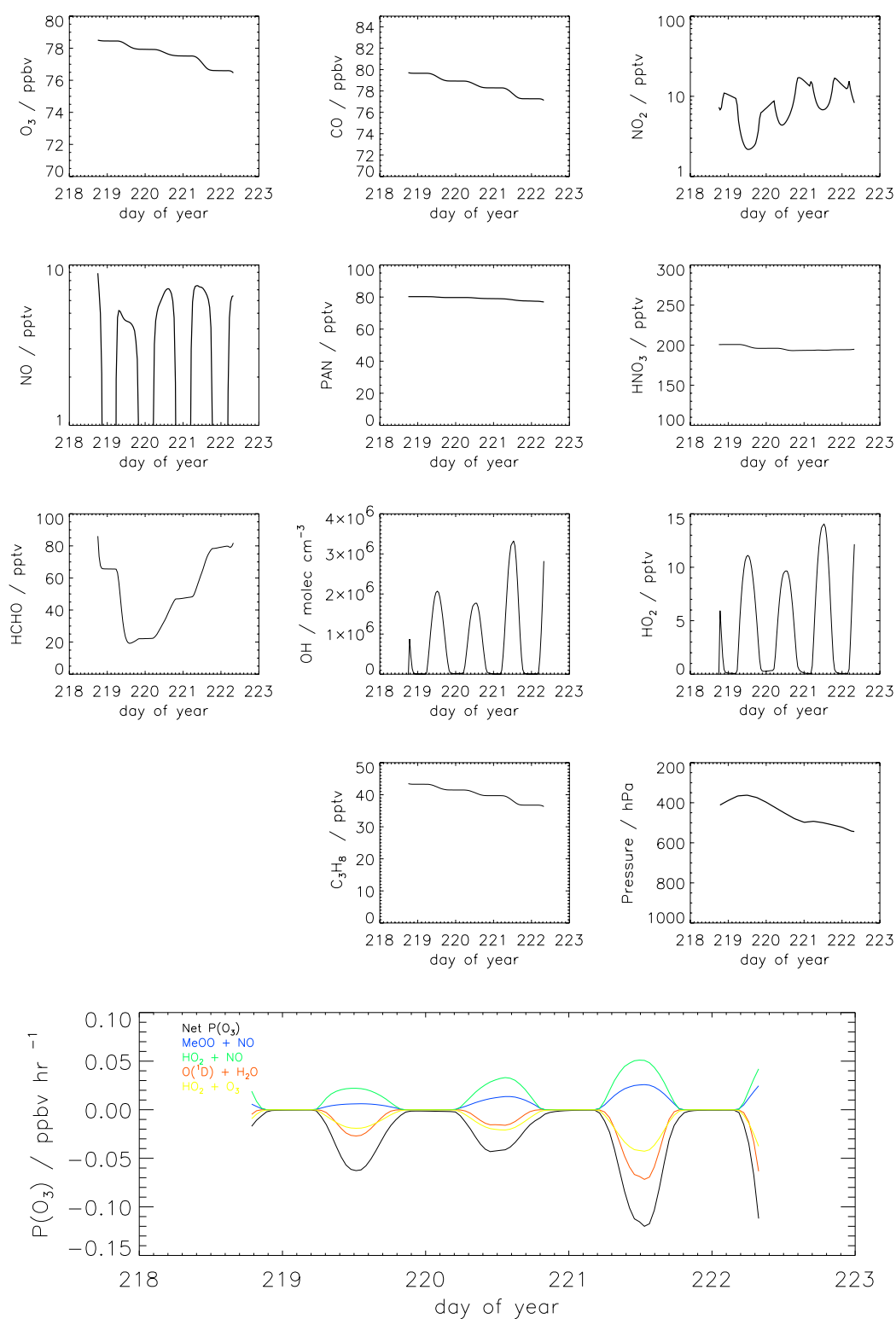


Figure 5.14: Along-trajectory model output for air mass Type B over four days of advection.

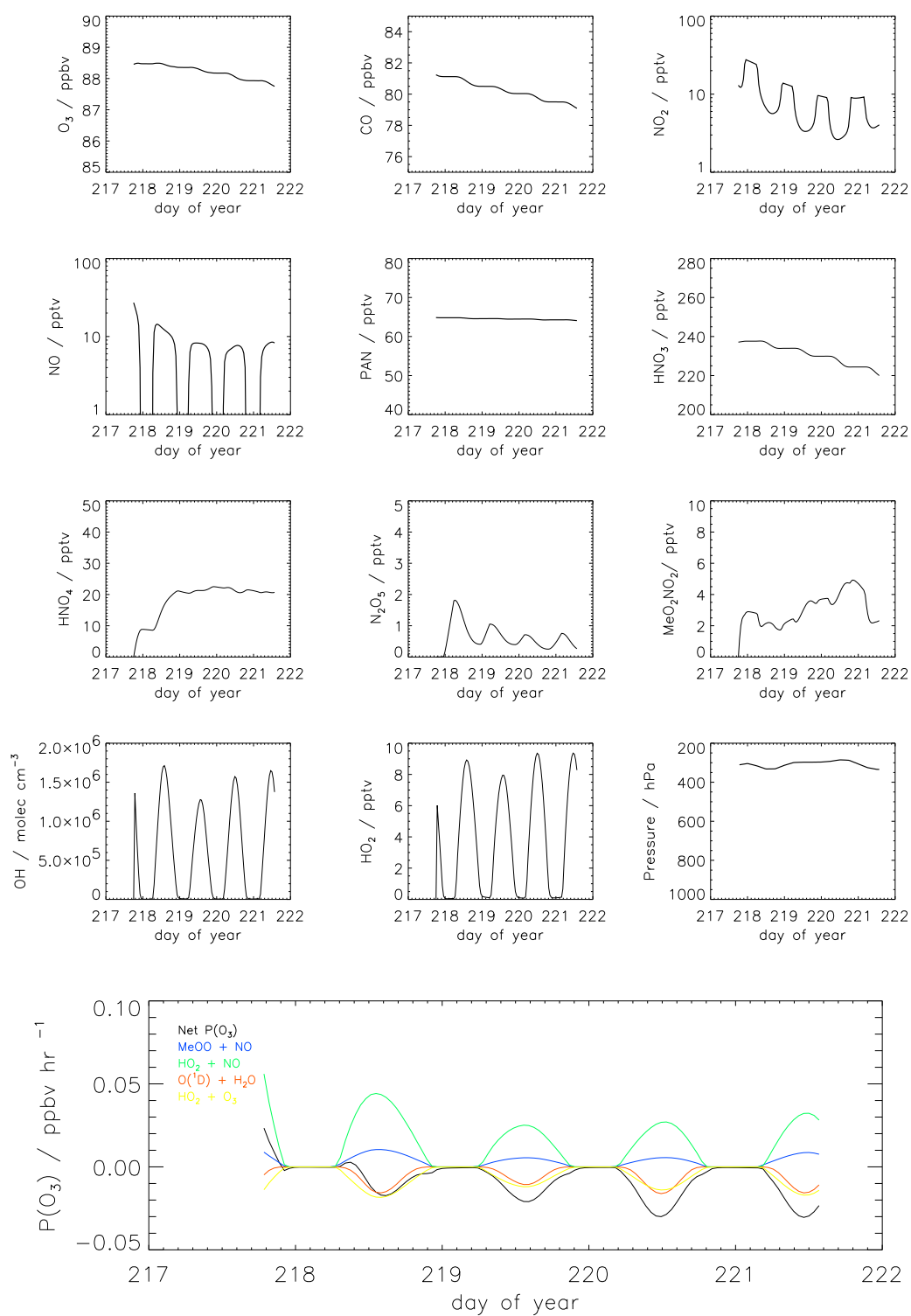


Figure 5.15: Along-trajectory model output for air mass Type C over four days of advection.

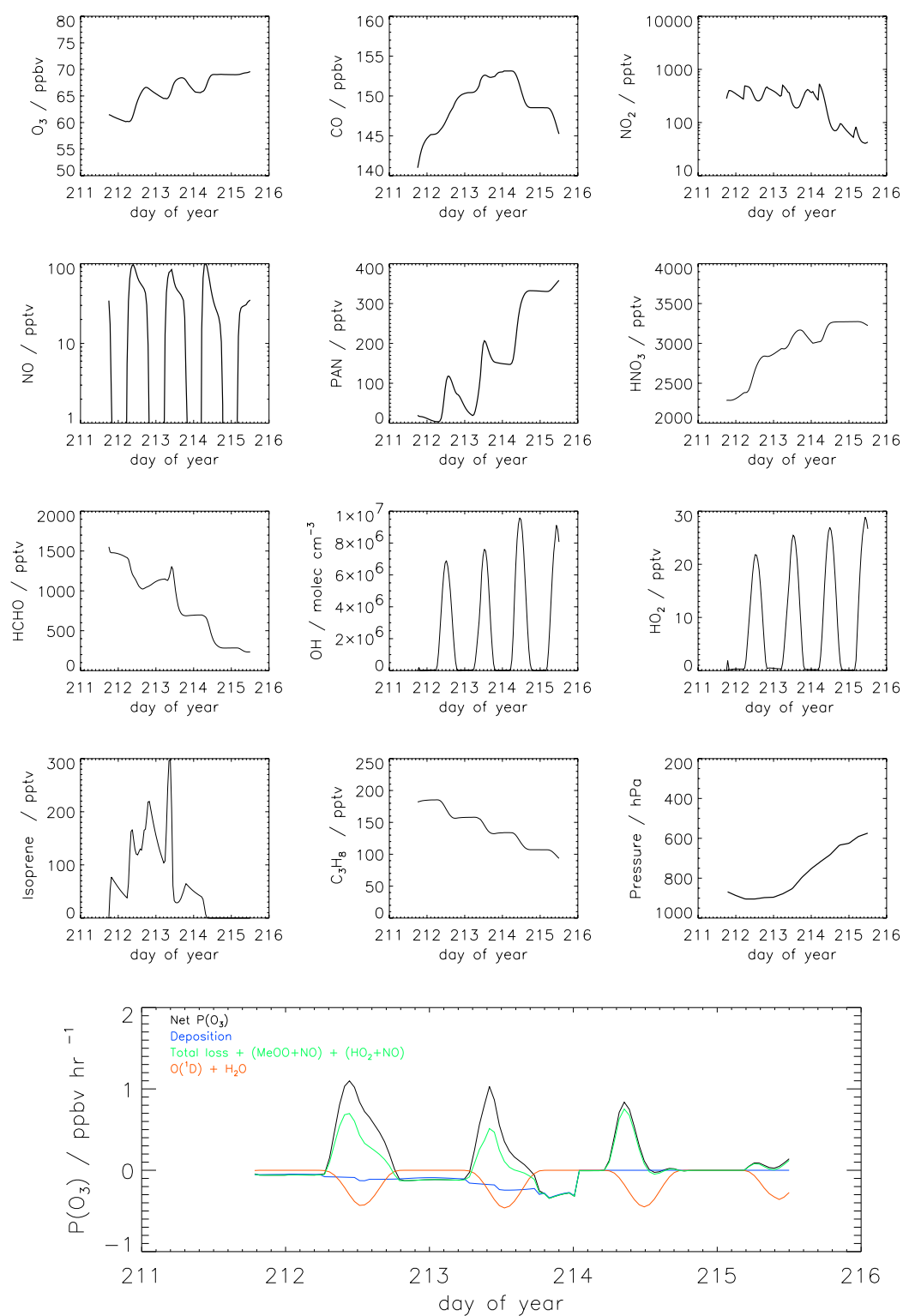


Figure 5.16: Along-trajectory model output for air mass Type D over four days of advection.



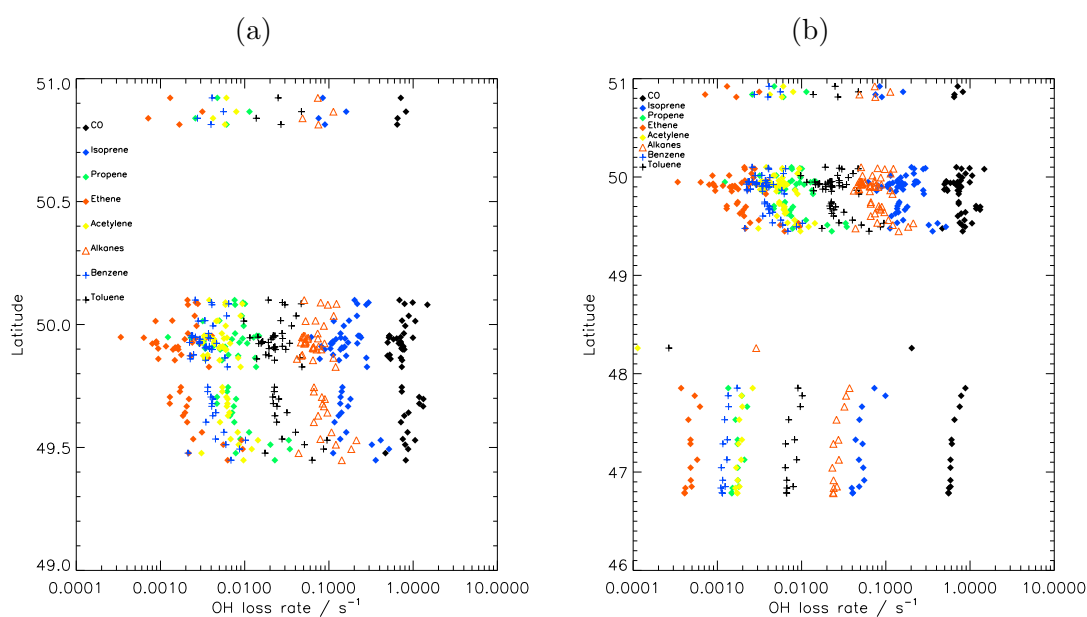


Figure 5.17: Contributions of individual model NMHC concentrations to the PBL OH loss rate over Central Europe. (a) Northern region (Czech Republic and Poland) only. (b) Entire EXPORT sampling region.

## 6. Chemistry and transport in a cold frontal region

### 6.1 Introduction

EXPORT flight A773 on August 2, 2000 sampled a warm conveyor belt (WCB) as the aircraft flew transects through a cold frontal zone over Germany. In Chapter 3, 3D RDF simulations were used to reveal the structure of the WCB and the flight path of the aircraft relative to regions of strong ascent resolved by the analysed winds. *Purvis et al.*, [2003] concluded from the freshly polluted, very young signature of air sampled in upper levels of the flight, that rapid convective transport was likely to be responsible for a great deal of the vertical pollutant transport from the European PBL, rather than slower slant-wise ascent along the WCB airstream. CiTTyCAT model calculations in Chapter 5 support this hypothesis, since enhancements to primary pollutants on the upper flight legs were very small compared with the observations. Back trajectories used in the model, derived from the large-scale winds in the ECMWF analyses did not penetrate the polluted PBL. This chapter contains a more detailed analysis of the sampled system, and includes modifications to the treatment of vertical transport in the CiTTyCAT model to investigate the relative roles of different processes in transporting pollutants.

In Section 6.2, the formation of mid-latitude cyclones is discussed and the conceptual model of Lagrangian airstreams in these systems is introduced. Section 6.3 describes the structure of the WCB sampled during EXPORT flight A773. The CiTTyCAT model is used to investigate vertical mixing in the frontal region in Section 6.4. Section 6.5 describes the use of trajectories from a mesoscale GCM to drive the CiTTyCAT model in an attempt to resolve vertical transport in the frontal region.

Conclusions are drawn in Section 6.6.

## 6.2 Mid-latitude cyclones

The particular case of August 2 will be examined in detail in the next section, but it is first useful to examine the conceptual model of airstreams in synoptic cyclones, which has been well documented [e.g. see *Browning and Monk*, 1982; *Browning*, 1995; *Cooper et al*, 2001].

Mid-latitude cyclones generally form along the polar front, which is a band around the mid-latitudes separating colder polar air masses from warm tropical air masses. They are generally the result of interaction between a horizontal temperature gradient at the surface and some forcing mechanism which encourages the cyclonic ascent of warm air.

The simple conceptual ‘Norwegian model’ of cyclogenesis [*Bjerkens and Solberg*, 1926], although superseded by recent, more detailed understandings of the forcing mechanisms of cyclogenesis, serves as a useful illustration of the formation of a mid-latitude cyclone (Fig. 6.1). In this model cyclones can be viewed as the result of an instability along an existing surface front between cold and warm regions (Fig. 6.1a-b). The horizontal temperature difference gives a large available potential energy at the surface front. As the instability disturbs the front, cyclonic rotation is set up around a deepening low pressure region (Fig. 6.1c). In a fully developed cyclone, this rotation results in a warm front moving to the northeast and a cold front moving to the southeast (Fig. 6.1c-d). Cold air rapidly runs in behind the cold front and the warm air runs over the top of the cold air towards the north-east.

It is now accepted that rather than representing instabilities on an existing surface front, cyclogenesis can result from a large-scale atmospheric response to upper atmospheric disturbances, such as an upper level trough associated with divergence around the mid-latitude jet [*Carlson*, 1991]. Over North America, the majority of cyclones are initiated in this way. It has been observed that the likely position of formation of a cyclone can be pre-determined by an existing disturbance in a region of strong temperature gradient or an existing maximum in local vorticity (e.g. in

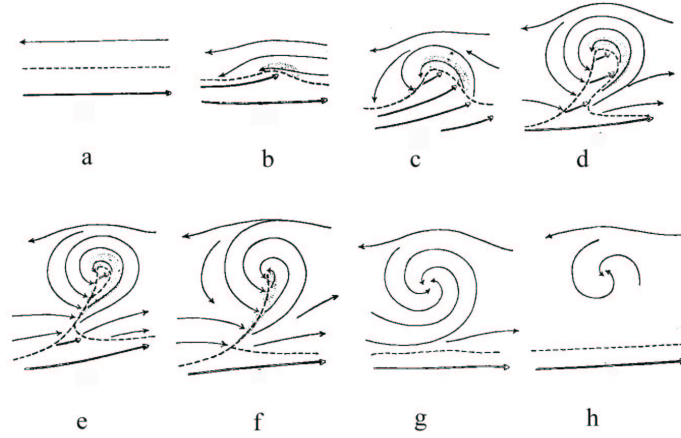


Figure 6.1: *The sequence of events in the life-cycle of a mid-latitude cyclone as shown by Bjerkens and Solberg, [1926]. Stages a-d represent the development of the cyclone from an instability along the polar front, and the maturing of the fully developed cyclone with a cold and warm front moving to the south-east and north-east respectively. Stages e-h represent occlusion, which is not discussed here. Figure adapted from Carlson, [1991].*

the lee of orographic features).

Frontal boundaries between cold and warm sectors can extend hundreds of kilometres away from the centre of the cyclone, where air masses may be drawn into the synoptic flow patterns associated with the system. Using the ‘conveyor-belt’ type description of Harrold [1973], who identified system relative flow along layers of constant wet-bulb potential temperature, distinct air-streams can be identified in a mid-latitude cyclone (Fig. 6.2). Air flow in mid-latitude cyclones is seen to be approximately adiabatic, along sloping isentropic surfaces, which cut across isobaric levels in the troposphere. In the absence of deep convection or interactions with the turbulent PBL, saturated air masses move along isentropes of constant  $\theta_e$ , in a slant-wise ascent or descent motion. This is often termed slant-wise convective transport, and leads to the classical ‘conveyor belt’ type description of air mass transport in mid-latitude cyclones. The concept has been developed extensively by Browning and co-workers since the 1970s [e.g. Browning and Monk, 1982].

The Browning-type model describes three main air streams carrying system-relative

flow around the cyclone: the warm conveyor belt (WCB), cold conveyor belt (CCB) and the dry airstream (DA) (Fig. 6.2). The WCB carries moist, warm air from near the surface in the warm sector ahead of the cold front. The air ascends isentropically polewards ahead of the cold front into the mid/upper troposphere towards the parent low pressure region. Due to the ascent of air high in humidity, the WCB can be identified as a band of cloud aligned approximately with the surface cold front. The CCB originates northwards of the surface warm front and ascends from east to west on the north side of the warm front, underneath the ascending WCB. The ascent in the CCB is somewhat shallower than in the WCB. Condensation in air ascending both the WCB and CCB leads to the characteristic ‘comma’ shaped cloud around the cyclone. Finally, the DA descends from high altitude, polewards of the parent cyclone, southwards into the mid troposphere behind the cold front. The DA primarily flows in the opposite direction to the WCB, with a secondary tongue of air which peels off towards the northeast in the same direction as the WCB, behind the cold front. The DA brings down dry, cold air from the upper troposphere and so results in a ‘dry slot’ behind the cold front, often visible as an absence of cloud in satellite imagery.

The term ‘conveyor belt’ should be interpreted with care. More recent studies have examined airflow around mid-latitude cyclones in detail using large ensembles of air mass trajectories [e.g. *Wernli, 1997*]. By imposing a range of criteria for the selection of groups of trajectories, such as their rates of ascent or moisture content, coherent ensembles of trajectories can be selected with similar histories or properties. *Wernli, [1997]* showed that rather than the three isolated airstreams carrying air from one place to another, a limited number coherent ensembles or ‘families’ of trajectories can be identified. These tend to be quasi-continuous features over the lifetime of the system as it moves relative to the surface. Such ensembles were seen to be flexible ‘tubes’ of strong ascent or descent, that can be deformed by the synoptic development, rather than the invariant conveyor belt-type air streams described in the classical Browning-type model.

The RDF simulations used in this Chapter reveal a group of trajectories with warm, moist origins strongly ascending along the axis of the position of the classical WCB. It is this ensemble of strongly ascending air masses which is henceforth referred to



Figure 6.2: *Schematic showing the relative positions of airstreams carrying system-relative flow around a mid-latitude cyclone. Each airstream carries air of distinct origin and thermodynamic characteristics into the cyclone. The three main airstream types: the warm conveyor belt (WCB), the cold conveyor belt (CCB), and dry airstream (DA) have been identified in observations of frontal systems and as coherent ensembles of air mass trajectories in model studies. Taken from Cooper et. al, contribution to IGACtivities Newsletter No. 24, Aug 2001.*

as the warm conveyor belt.

## 6.3 WCB structure

### 6.3.1 RDF trajectories and satellite data

In Chapter 3, reverse domain-filling (RDF) trajectories were used to reveal the location of the WCB airstream sampled during flight A773 (August 2, 2000). The aircraft was shown to have sampled the strongly ascending band of air masses resolved in ECMWF analyses at lower altitudes, and then to have flown above this strongly ascending airstream at higher altitudes. *Purvis et al.*, [2003] concluded that

rapid ascent of PBL air in convective events in the frontal zone was responsible for much of the vertical transport sampled, since resolved slant-wise advection along the WCB occurred on a timescale too long to explain the presence of very short-lived NMHCs at the higher altitudes. Figure 6.3 reproduces the RDF reconstruction of the WCB region from  $\theta_e$  at two-day back-trajectory origins. Sections along and perpendicular to the axis of the WCB reveal the orientation of the band of ascent relative to the position of the cold front. The band of elevated  $\theta_e$  is aligned north-eastwards, approximately along the position of the cold front, and ascends polewards towards the parent cyclone. Figure 6.3b shows that the resolved WCB is forward sloping in the direction of the frontal advance, with the large  $\theta_e$  airstream at lower altitudes to the northwest, sloping to higher altitudes in the southeast.

The path of the 12UT-relative flight-track shows that due to the polewards ascent and forward sloping nature of the WCB airstream, the north-western extreme of the flight path is somewhat remote from the WCB. In Chapter 3, the transition between Legs 4 and 5 showed a sudden drop in observed  $\theta_e$ , and chemical observations suggested more aged polluted air was sampled with a signature characteristic of background free tropospheric air. This is consistent with the simulated WCB structure, since the aircraft is furthest from the resolved WCB at this point.

As well as resolving the strongly ascending WCB airstream, the ECMWF analyses suggest appreciable condensation and mixing in the region around the WCB. This can be revealed by plotting the change in  $\theta_e$  and  $q$  interpolated from the analyses along two-day back trajectories (Fig. 6.4). A reduction in  $q$  results from condensation in the WCB. A reduction in  $\theta_e$  is likely to point towards turbulent mixing or precipitation.  $\theta_e$  is well conserved in isolated air parcels over timescales of a few days, in the absence of precipitation or strong mixing. In the WCB, a reduction in  $\theta_e$  and  $q$  can occur as a result of mixing colder, drier air from the surroundings into the WCB airstream as it ascends polewards, as noted by *Methven et al.*, [2003]. Under such circumstances it is reasonable to suggest that air uplifted in the main band of slantwise ascent would be likely to be mixed out to the surroundings, and may be responsible for some of the observed short-lived tracer enhancements above the ascending band. Increases in  $\theta_e$  occur in air masses imported into the region immediately above the band of ascent, which may point to heating by mass exchange

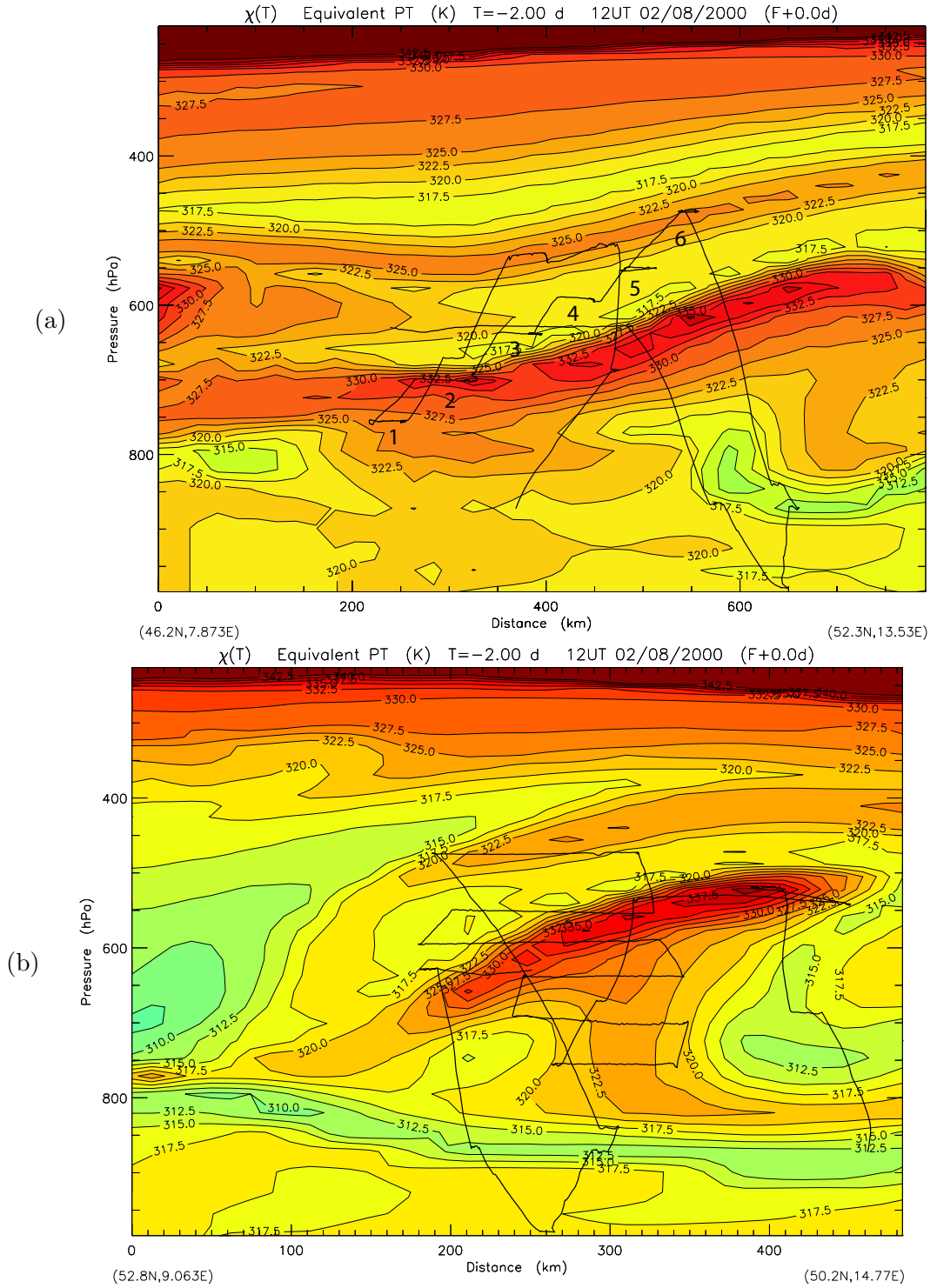


Figure 6.3:  $\theta_e$  (K) at 2-day back trajectory origins arriving on the A773 RDF grid. (a) Vertical cross-section approximately along the axis of the WCB. (b) Vertical cross-section normal to the WCB axis. The WCB appears as a strong feature of elevated  $\theta_e$ , with a forward sloping orientation in the direction of the frontal advance. The 12UT air mass relative flight track is shown as a solid line. Large numbers in panel (a) refer to horizontal legs through the WCB region, discussed in the text.



with the ascending warm stream. As noted in Chapter 3, it is likely that both this type of mixing and convection from near the surface is responsible for the observed pollutant enhancements, since mixing from the main band of ascent into the region above would release pollutants of an age given by the large-scale flow up the WCB ( $\sim 1$ -2 days). Increases in  $q$  and  $\theta_e$  are also seen in the cold dry air which descends under the head of the WCB, to the northeast of the flight path. Turbulent mixing is also likely to be strong in this region of the system.

Strong condensation in the frontal region can be seen in the IR brightness temperature satellite image (Fig. 6.5). Extensive cloud is evident in the region of the ascending WCB airstream, aligned approximately along the cold front. At the cloud head, near the north coast of Germany, the WCB ascent has reached its highest altitude and ascending air spreads out anticyclonically. The coldest brightness temperatures indicate the highest altitude cloud tops in the system. The satellite image reveals a certain amount of scatter in the positions of these areas through the system. It is likely that these are isolated, organised convective regions embedded in the WCB, giving rise to deep clouds scattered throughout the frontal region.

### 6.3.2 CTM output

The CiTTyCAT model uses three-dimensional air mass trajectories which are derived from analysed ECMWF winds at an approximate horizontal resolution of  $1.125^\circ$ . At mid latitudes this corresponds to  $\sim 60$  km. Transport processes which have a spatial scale less than this do not affect the path of trajectories, since they are calculated using only the large-scale winds from the analyses. Convective cells in the frontal system will generally have a horizontal scale of less than 10km. Rapid vertical transport of PBL emissions to higher altitudes in these cells will therefore not be captured by the standard CiTTyCAT simulation.

The standard CiTTyCAT output using 4-day ECMWF back trajectories, as shown in Section 5.2, is reproduced in Figure 6.6. Output from the TOMCAT model simulation interpolated to the time and position of the aircraft is also plotted. The amount of structure in the TOMCAT output is reduced compared with the CiTTyCAT output, due to the coarse model grid resolution ( $2.8^\circ$ ). However, during

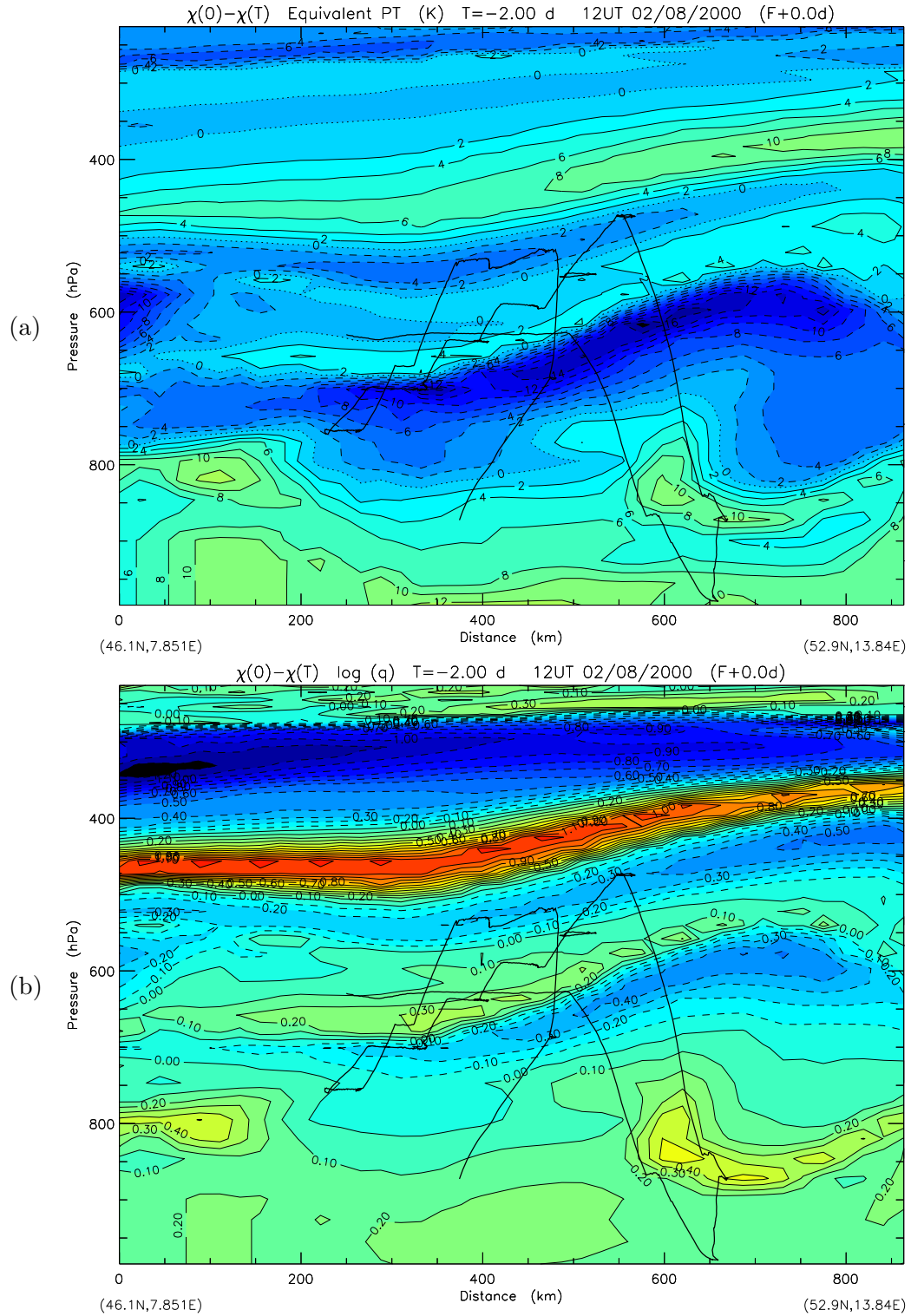


Figure 6.4: Change in (a)  $\theta_e$  (K) and (b)  $q$  ( $\text{kg kg}^{-1}$ ) along 2-day back trajectories arriving on the RDF grid shown in Figure 6.3a.

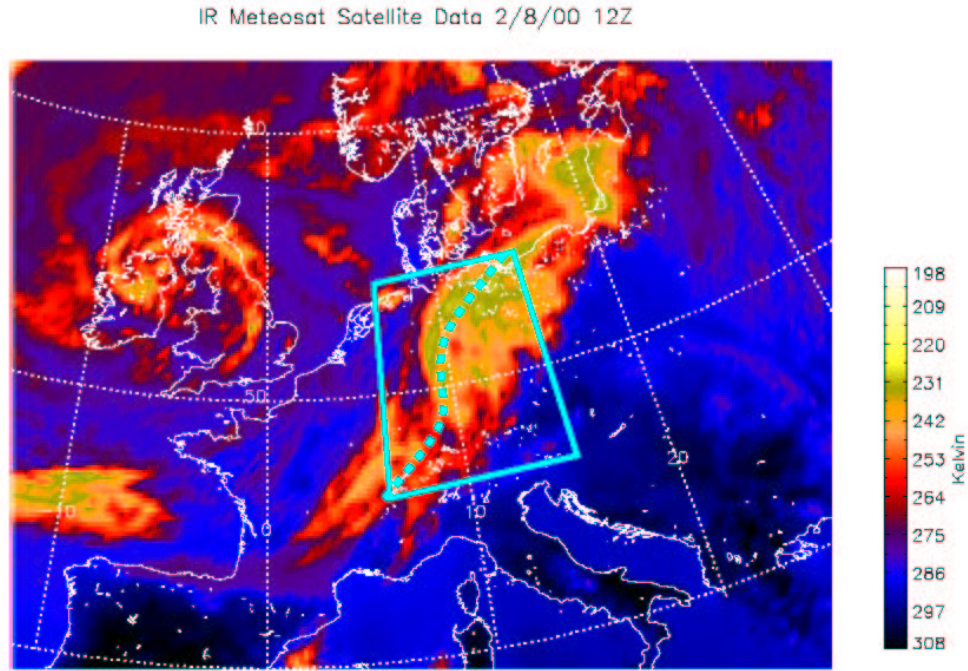


Figure 6.5: *Meteosat satellite image of IR brightness temperature (K) (12UT Aug 2, 2000) (from Purvis et al., [2003]). The dotted line indicates the approximate position of the cold front discussed in this Chapter.*

the higher altitude flight legs through the WCB region, enhancements to CO and  $\text{NO}_x$  are larger in the TOMCAT simulation. Over Legs 3-6, the range of TOMCAT simulated CO concentrations are within the range of those observed. The CiTTyCAT simulation produces much lower CO concentrations, up to 30-40% less than those observed. TOMCAT  $\text{NO}_x$  concentrations over this period lie between the periodic larger enhancements associated with crossing the WCB region itself, and the lower concentrations observed outside of the region of rapid ascent. The CiTTyCAT  $\text{NO}_x$  concentrations are much smaller, by almost an order of magnitude during Legs 4-6. Similar enhancements in HCHO concentrations in both the observations and TOMCAT reveal efficient photochemical processing of relatively fresh pollution. CiTTyCAT HCHO concentrations are underestimated during the stepped ascent of the WCB region, indicating the presence of less freshly polluted air.

The key differences in the two model simulations arise through their treatment of

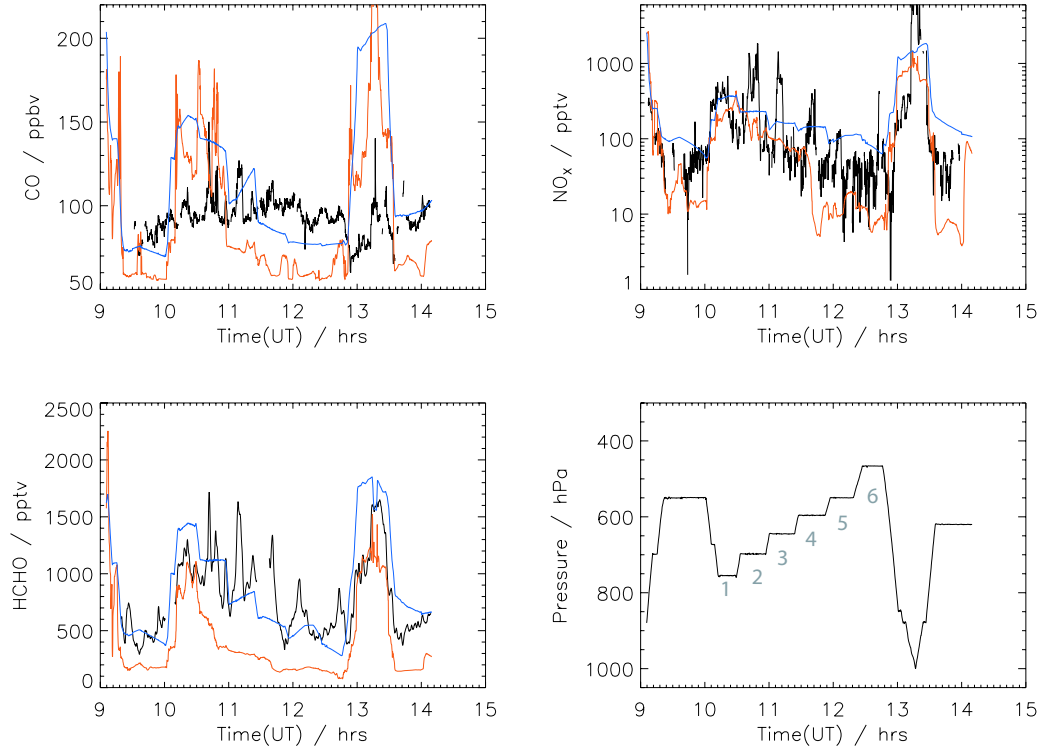


Figure 6.6: *Output from the standard CiTTyCAT model along 4-day back trajectories (red) and TOMCAT output interpolated to the aircraft time and position (blue) compared with observations (black) for EXPORT flight A773 (02/08/00). The bottom right panel shows aircraft pressure (hPa) along the flight track.*

vertical transport. The TOMCAT model parameterises turbulent PBL mixing and convective transport on a sub-grid scale, whereas CiTTyCAT does not account for such sub-grid vertical transport. The TOMCAT simulation appears to be efficient in the rapid vertical re-distribution of PBL emissions into the free troposphere, in the region of the sampled frontal system. Comparison of the CiTTyCAT and TOMCAT simulations, which use the same source of large-scale winds, suggests that the TOMCAT convection scheme is active in providing this vertical transport.

Figure 6.7a shows TOMCAT model CO output for 12UT 02/08/00 interpolated to the RDF grid arrival points in the region of the WCB for the same time. CO concentrations picked up from the 12UT 31/07/00 TOMCAT field at 2-day RDF back-trajectory origins are shown on the RDF grid in Figure 6.7b. Effectively, this allows a comparison of the CO field produced by the TOMCAT model for 12UT

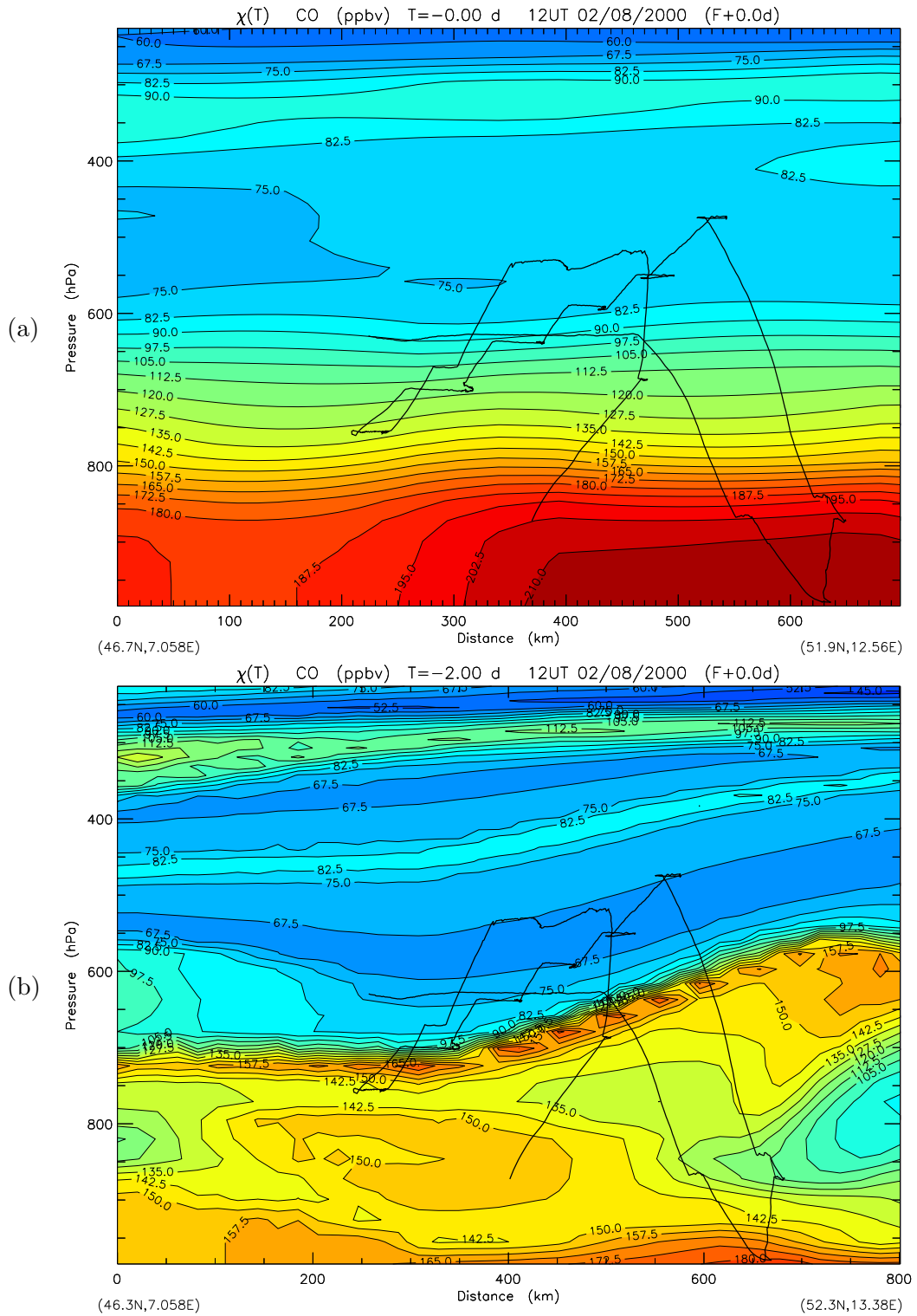


Figure 6.7: Concentrations of CO (ppbv) taken from the TOMCAT model (a) interpolated to the RDF arrival grid at 12UT 02/08/00 and (b) from 2-day back trajectory origins of trajectories arriving on the RDF grid.

02/08/00 (Fig. 6.7a) and the CO field produced on the same grid by two days of advection by the large-scale ECMWF winds only, without sub-grid transport i.e. along back trajectories (Fig. 6.7b). CO concentrations can be assumed to be approximately conserved over the 48 hour timescale.

The TOMCAT simulation gives CO concentrations in the range 75-83 ppbv for the three upper transects of the WCB region. In the RDF 2-day back-trajectory simulation, CO concentrations are up to 25% smaller in this region, in the range 60-68 ppbv. Stronger enhancements to CO in the range  $\sim 90$ -170ppbv are confined to the main band of slant-wise ascent resolved by the 2-day back-trajectories, which the aircraft mainly flies above. The TOMCAT convection scheme produces enhanced CO concentrations of as much as 80 ppbv up to an altitude of 600hPa, uniformly across the domain. Observations suggest that in the region of the sampled WCB, the TOMCAT model produces more realistic vertical transport than the resolved flow used to drive the Lagrangian advection of CiTTyCAT.

## 6.4 Vertical mixing in the frontal region

### 6.4.1 Uniform mixed layer

As a simple sensitivity test, the boundary layer height in the CiTTyCAT model has been increased to simulate a convectively mixed layer up to a height of 5 km. This is the approximate altitude to which elevated concentrations of shorter lived NMHCs were observed to persist in the region of the WCB [Purvis *et al.*, 2003]. In effect, increasing this PBL height causes surface emissions in CiTTyCAT to be instantaneously diluted across the depth of the new deep mixed layer. This allows trajectories passing within 5km of the surface to be influenced by surface emissions, crudely simulating convective vertical redistribution of emissions in the lower troposphere.

Figure 6.8 shows output from such a model run, using 2-day back trajectories arriving on the flight path of flight A773 at a 10 second frequency. Comparing this to the model using the standard PBL height data shows that the well mixed-layer

is successful in enhancing pollutant concentrations in trajectories arriving at higher altitudes. Shorter lived NMHCs such as isoprene and n-butane show substantial enhancements during the latter horizontal steps of the aircraft ascent. Modelled isoprene concentrations are comparable with those observed, in the range 3-12 pptv. Model n-butane shows enhancements comparable with the highest concentrations observed on the higher altitude steps, in the range 50-100 pptv. However, the smaller concentration observations of the order  $\sim 20$  pptv, are now overestimated by the model using the well-mixed 5km layer.

The overestimate of smaller concentration observations which were reproduced well by the standard PBL run, is also apparent in  $\text{NO}_x$ . This is due to the deep vertical mixing of fresh emissions throughout the troposphere, rather than only in the region of the frontal system. Using the 5km mixed layer, the  $\text{NO}_x$  concentration remains at several hundred pptv throughout the flight. The observations show only occasional enhancements to such concentrations, coinciding with flying across the WCB region. The standard PBL run better matches the baseline of free tropospheric type  $\text{NO}_x$  concentrations of 10-100 pptv observed outside of the regions of rapid ascent from the PBL. This is a similar result to that seen when comparing TOMCAT pollution enhancements in the frontal region to CiTTyCAT in Section 6.3.2.

With a deep mixed layer implemented, peroxide concentrations are suppressed at higher altitudes. Peroxides are formed by the reaction of  $\text{HO}_2$  with itself or  $\text{RO}_2$  radicals. In the polluted troposphere, this process will compete with the reactions of  $\text{RO}_2$  and  $\text{HO}_2$  with  $\text{NO}$  to produce  $\text{NO}_2$  and  $\text{OH}$  and with ozone to produce  $\text{OH}$ . The mixed layer to 5km greatly increases  $\text{NO}_x$  concentrations at higher altitudes. The model comparison demonstrates that this has a marked effect in suppressing peroxide formation at higher altitudes. These competing reactions also explain the increased abundance of  $\text{OH}$  relative to  $\text{HO}_2$  in these regions.

A consequence of simply increasing the height of the mixed layer in the model is that modelled pollutant enhancements in trajectories entering the lowest layers (e.g. pressure  $> 750\text{hPa}$ ) are decreased. This is due to the crude instantaneous dilution of emissions across the height of the mixing layer (see Fig. 6.9). For the same surface emission flux, this gives a reduced rate of increase of concentration, or ‘emission rate’ in the mixed layer. The model pollutant enhancements therefore

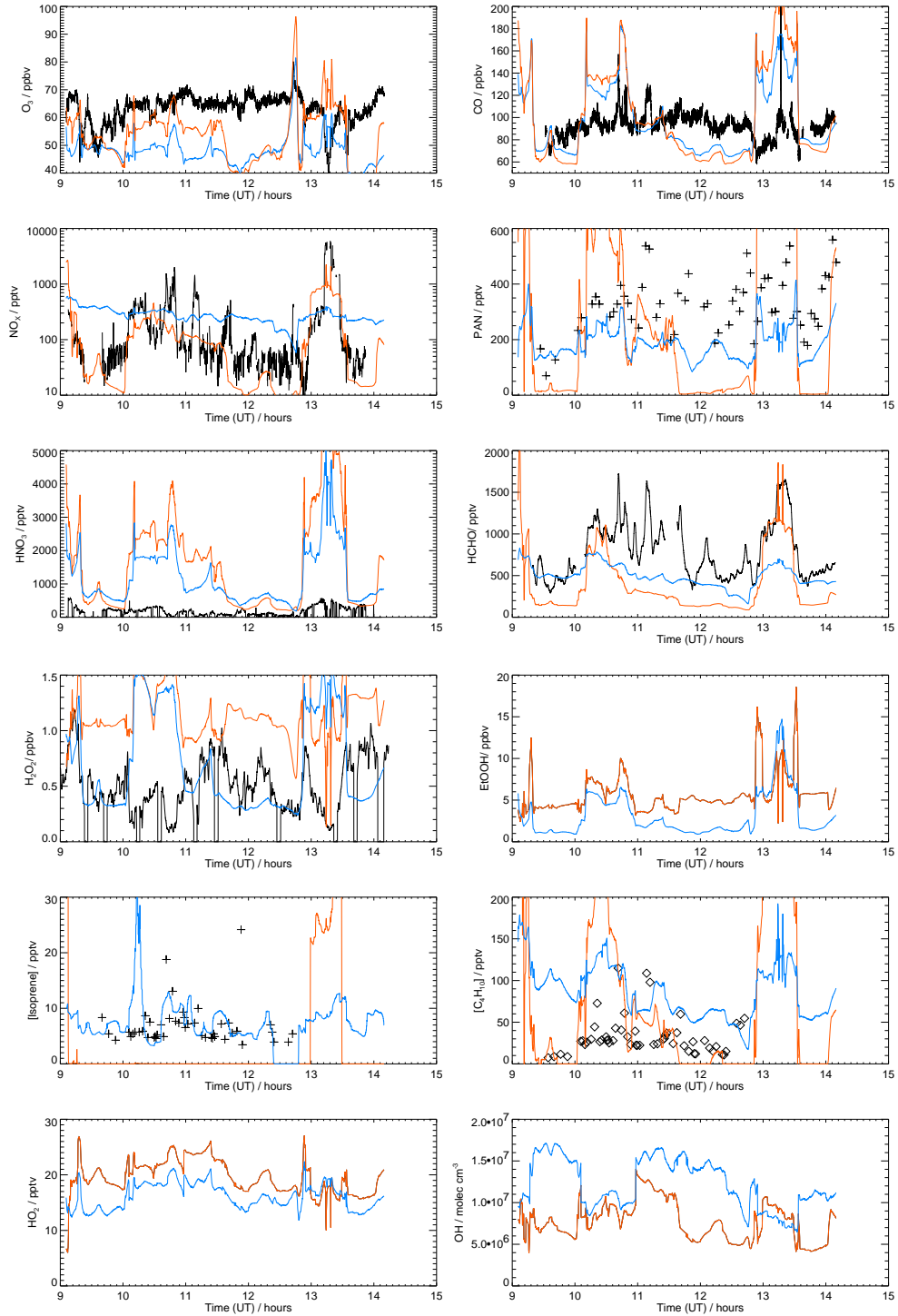


Figure 6.8: 2-day back-trajectory CiTTyCAT model results compared with observations for flight A773. Black/symbols: observations; Red: standard model PBL; Blue: artificial mixed layer to 5km.



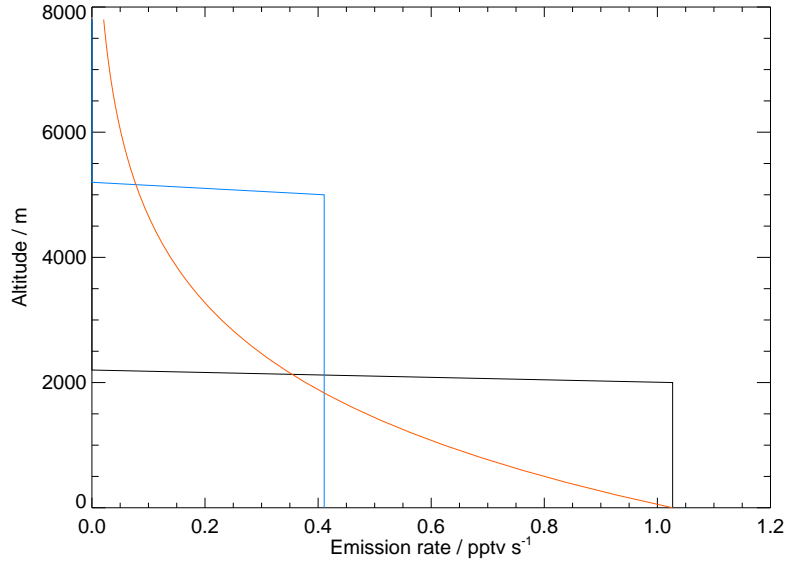


Figure 6.9: *Emission rates into the CiTTyCAT air parcel given by the three treatments of the surface mixed layer discussed in the text. The calculated emission rates are due to a surface emission of  $1 \times 10^{12}$  molecules  $\text{cm}^{-2}$  from a  $1^\circ \times 1^\circ$  grid box at mid-latitudes. Black: standard CiTTyCAT PBL with an example 2km height. Blue: Imposed uniform mixed layer to 5km altitude. Red: Exponential decay of emission rate with altitude using a scale height and a surface emission rate given by the example 2km PBL height.*

show less contrast across their profile with altitude, being reduced at lower altitudes and enhanced at higher altitudes. In the case of the WCB, this seems to better match the homogeneous, well mixed observations than the standard PBL.

#### 6.4.2 Decaying emissions profile

It is interesting to compare the basic treatment of instantaneous dilution across the mixing layer, with a PBL treatment which decays the emission rate with altitude through the mixed layer (Fig. 6.9). This crudely simulates the dispersion and chemical loss of high concentrations of emitted pollutants near the surface as they are diluted into the mixed layer above, and should be more realistic. An exponential profile of emission rates has been imposed through the depth of the troposphere in

the CiTTyCAT model, with a maximum at the surface equivalent to that using the standard PBL depth. The emission rate falls off with a scale height determined by the PBL heights of the standard model. This corresponds to an emission rate of approximately 8% of the surface rate at 5km altitude for a scale height of 2km.

Figure 6.10 shows that there are only small differences between using this type of emission profile compared with the uniformly well mixed deep layer of 5km. The fresh pollutant enhancements at higher altitudes are now reduced and compensated for by larger enhancements at the surface, equivalent to the standard model run. CO enhancements during the higher altitude horizontal ‘steps’ are now very small compared with the standard model run, and the lower altitudes show much higher CO concentrations than given by the observations. The magnitude of modelled  $\text{NO}_x$  concentrations match observations well in the later steps, however PAN concentrations are very small compared with observations, and were better modelled by the uniform mixed layer. This is linked to the vertical distribution of NMHCs which is more strongly affected by imposing the exponential profile of emission rates. This arises through the shorter lifetimes of these species. Modelled isoprene and n-butane enhancements in the later steps tend to match better the lowest observed concentrations when employing the exponentially decaying emissions profile. For the uniformly well-mixed layer, enhancements better match these NMHC observations generally and capture the magnitudes of the higher concentration observations.

Generally, the uniformly well-mixed layer to 5km tends to show better agreement with observations for this flight. This allows the model to reproduce the larger concentration observations at higher altitudes, and reduces the model overestimates of lower altitude PBL pollutant concentrations. Imposing the exponential emission rate profile with altitude better reproduces the lowest observed enhancements, and also the general magnitude of the  $\text{NO}_x$  observations. This suggests that the use of a spatially constant, well-mixed layer or an imposed emissions profile over the entire flight is not a good approximation, and rapid vertical ascent of fresh emissions cannot be treated as spatially homogeneous over the horizontal domain of the model.

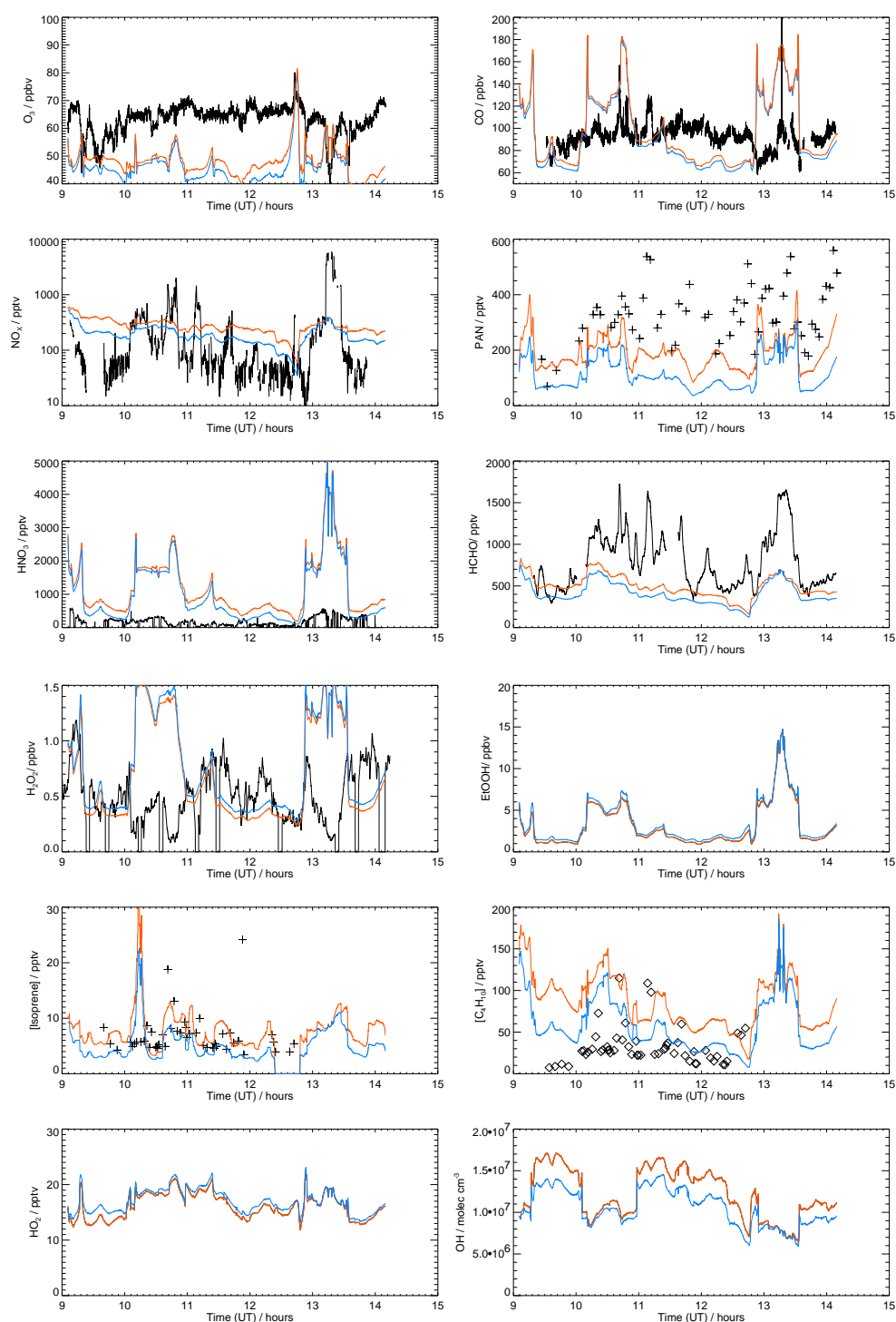


Figure 6.10: 2-day back-trajectory CiTTyCAT model results compared with observations for flight A773. Black/symbols: observations; Red: artificial mixed layer to 5km; Blue: Emissions decayed exponentially with altitude (see text).

## 6.5 Resolving vertical transport: Mesoscale trajectories

Sections 6.3 and 6.4 suggested that the resolution of the global ECMWF analyses used in the Lagrangian advection of the CiTTyCAT model ( $1.125^\circ$ ) appears to be too coarse to account for smaller scale vertical transport in the frontal region. However, the TOMCAT model, forced by the same analyses at even lower resolution, appears to be more efficient in transporting freshly polluted air to the higher altitudes sampled by the C130 aircraft. This is due to the parameterised convection and PBL turbulence in the TOMCAT model. Section 6.4 also demonstrated that the scattered locations of rapid ascent of fresh PBL air inferred from the observations cannot be approximated by assuming a vertically well-mixed layer of uniform horizontal extent.

It is possible, but problematic, to account for sub-grid convective transport in air mass trajectories calculated from global model winds. This requires output of convective mass fluxes on the global model grid, which can be used to modify the vertical advection of Lagrangian air parcels. Such approaches have been used with some success [e.g. *Freitas et al.*, 2000], however care must be taken to ensure that the convective mass fluxes are applied in a way consistent with mass exchange through the convective column. For example, if only a single trajectory passes through a grid box in which a vertical mass flux is present due to sub-grid convection, it is not obvious how the trajectory path should be modified to take this into account. Some mass which enters the bottom of the convective column may be detrained at mid levels, while some may travel all the way to the upper troposphere. Similarly, mass may enter the column at mid levels and be detrained further aloft, along with the air which originally entered at the bottom. This makes the concept of a Lagrangian ‘air parcel’ meaningless, since a single air mass trajectory cannot account for entrainment and detrainment from the column.

Some Lagrangian models account for convection by allowing mass exchange between different trajectories coming into proximity over a convective column to simulate entrainment, detrainment and mixing of contributions from the different air parcels [e.g. *Collins et al.*, 2000]. Other approaches use a large enough number of trajectories so that there can be a statistical distribution of weights given to vertical

velocities across the ensemble according to the convective mass flux, to simulate detrainment and entrainment through the column.

In the model used in this work, it is not easy to employ either of these methods, since convective mass fluxes are not routinely output in the ECMWF analyses available to us.

An alternative approach is to employ a higher resolution model to drive the Lagrangian trajectory advection. *Esler et al.*, [2003] found that a mesoscale simulation of a cold frontal region produced stronger vertical ascent than coarse resolution global analyses. Better resolution in the region of the WCB in this case should allow some of the more rapid sub-global-grid-scale vertical transport to be resolved. It can also be expected that by explicitly modelling the smaller-scale structure around the frontal system, the positions of regions of stronger vertical mixing may be accounted for in the trajectories, providing a treatment of the horizontal inhomogeneity of the system, rather than crudely assuming strong vertical mixing throughout the entire domain.

### 6.5.1 Mesoscale Unified Model

The mesoscale Unified Model (UM) is a limited-area general circulation model (GCM) which is capable of resolving dynamic features on a scale of a few kilometres. Its typical horizontal resolution is approximately 10-15km, and it has 38 vertical levels, 14 of which are in the nominal boundary layer. The model has been used in past studies of transfer of PBL mass to the free troposphere by frontal systems [*Donnell et al.*, 2001; *Esler et al.*, 2003]. These showed that the grid was fine enough for the resolved winds of the model to capture much of the transport due to frontal motions and associated slantwise convection. However, smaller-scale convection and turbulence which is parameterised as sub-grid in the mesoscale simulation, was still seen to play an important role.

The mesoscale UM version 4.5 was run over a limited domain to encompass western Europe, at a horizontal resolution of  $0.11^\circ$  ( $\sim 11\text{km}$ ). The model was initialised from global UM analyses at 12UT on July 31, and boundary conditions were obtained

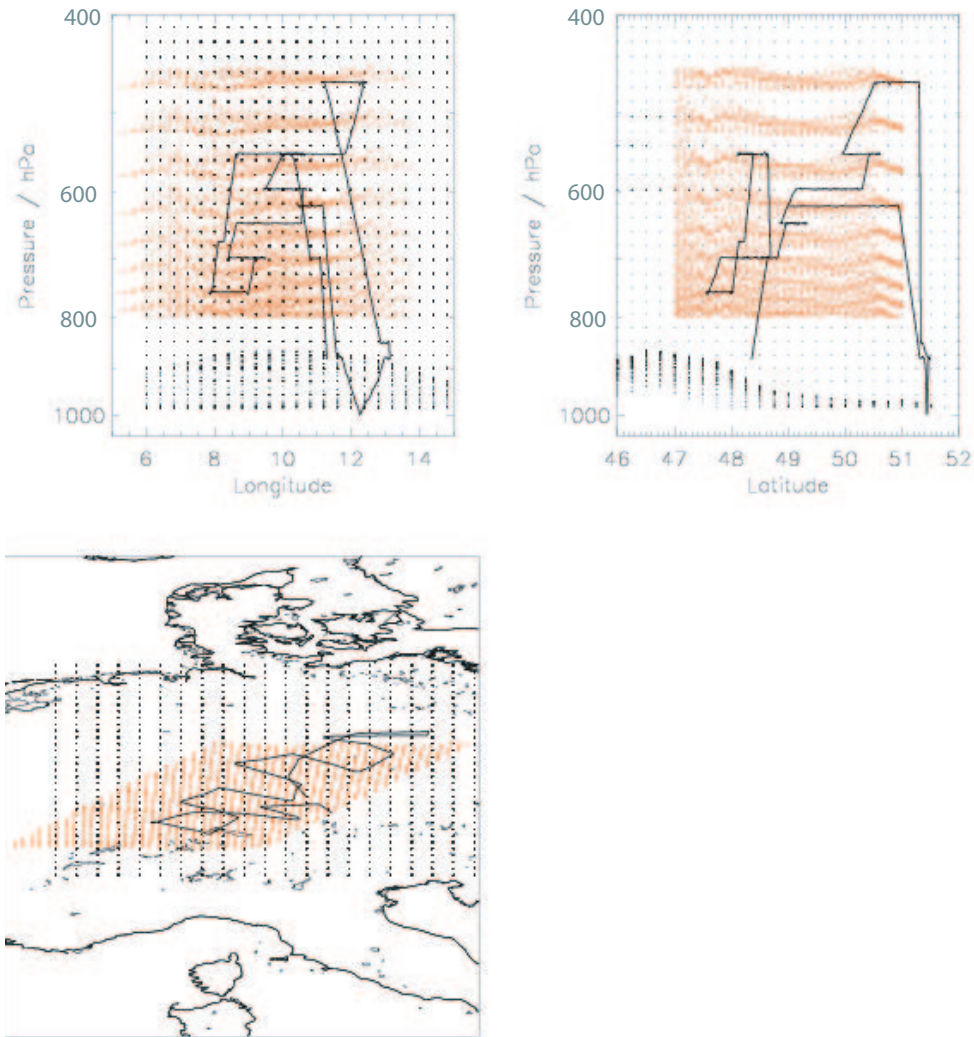


Figure 6.11: *Arrival positions for back trajectories arriving at 12UT on Aug 2. Red dots: trajectories from mesoscale Unified Model; Black dots: trajectories from global ECMWF analyses. Solid line shows the 12UT air mass relative flight track.*

from analysed output from the global model. Trajectories arriving at 12UT in the domain of the C130 flight path on August 2 were output from the resolved model winds. (Output supplied by *Sue Gray University of Reading, personal communication*, 2003). These trajectories do not include contributions from parameterised sub-grid fluxes due to convection and turbulence, and use only the winds resolved on the model grid.

Figure 6.11 shows the arrival points for the UM trajectories and those arriving on

the grid used in the RDF simulations described previously. The arrival points of the UM trajectories are very dense compared to the ECMWF trajectory grid, and the period of stepwise ascent through the mid troposphere coincides with the regions of UM trajectory arrival for all 6 horizontal steps.

### 6.5.2 Model comparison

Despite the UM trajectories not including contributions from sub-grid transport, it is expected that the model's finer horizontal resolution may allow more of the stronger vertical transport in the frontal system to be captured than in the global analyses. Some of the larger organised convective systems in the region of the front may be resolved at the 11km resolution, leading to trajectories which ascend more rapidly than those following the large-scale flow of the ECMWF analyses.

Figure 6.12 shows the paths of the UM 2-day back trajectories and the paths of the ECMWF back trajectories arriving on the coarser ECMWF arrival grid at points within the arrival domain of the UM trajectories.

The domain is centred over the main WCB region, approximately along the axis of the cold front. It is evident that air masses arriving in the domain have undergone much stronger ascent in the UM over the previous 2 days compared with those arriving within the same domain in the ECMWF model. Although there are 2625 UM trajectories arriving in the domain compared with only 1650 arriving in this domain in the RDF grid, 64% of the UM trajectories have ascended from pressures greater than 800hPa compared with only 8% of the ECMWF trajectories. The paths of the UM trajectories show much greater variability and demonstrate periods of very rapid ascent and descent. This points to intense uplift of air in resolved mesoscale features in the simulation, and may be consistent with the presence of convective systems in the frontal region. There is a larger-scale ascent in the mid troposphere over the north of the Iberian peninsula, consistent with the flow resolved in the ECMWF trajectories. However, in the south there is a much stronger ascent from lower altitudes over the western Mediterranean and Spain imposed on the larger-scale flow. It is apparent that there are mesoscale aspects of the flow around the Iberian peninsula that are resolved by the UM, but which the lower resolution ECMWF

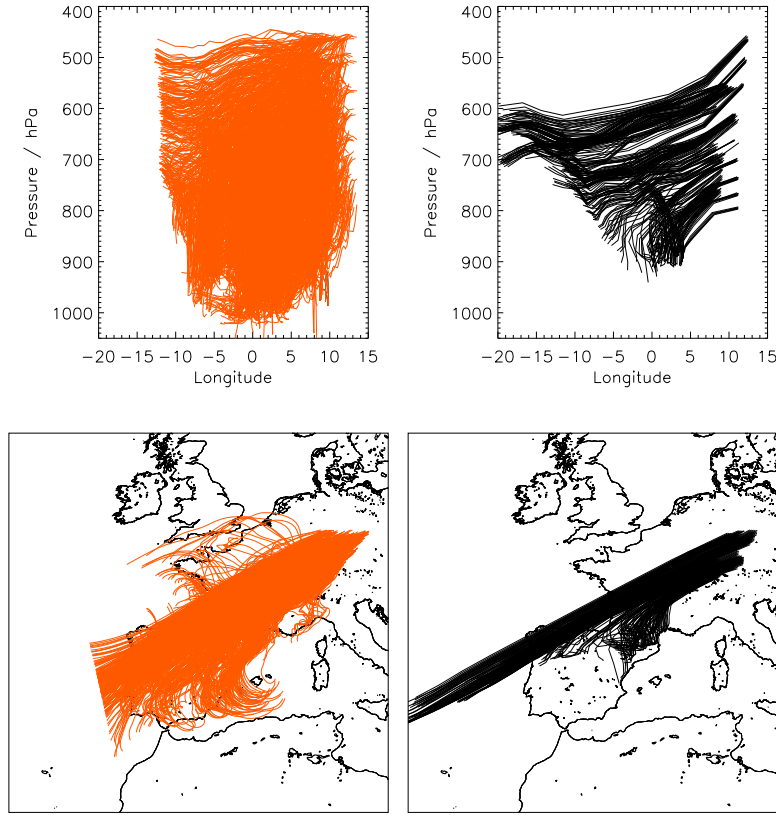


Figure 6.12: *Two-day back trajectories calculated from the Mesoscale UM (red, left) and ECMWF global analyses (black, right) arriving in the region of the WCB on grids shown in Figure 6.11. Only ECMWF trajectories arriving within the range of longitude, latitude and pressure of the UM arrival grid are shown. Every tenth UM trajectory is plotted only, for clarity.*

analyses do not capture. The anticyclonic flow near the surface, ahead of the cold front that precedes ascent along the WCB, typical of such systems, appears to be far more evident in the mesoscale trajectories.

The UM trajectories do not arrive at positions coincident with the 12UT relative flight track, so a direct model/observation comparison is not possible. However, the arrival grid is sufficiently dense that a large number of trajectories can be selected that arrive within  $0.1^\circ$  and 10hPa of the 12UT-relative flight track. ECMWF-forced back-trajectories were then run backwards from the arrival positions of these



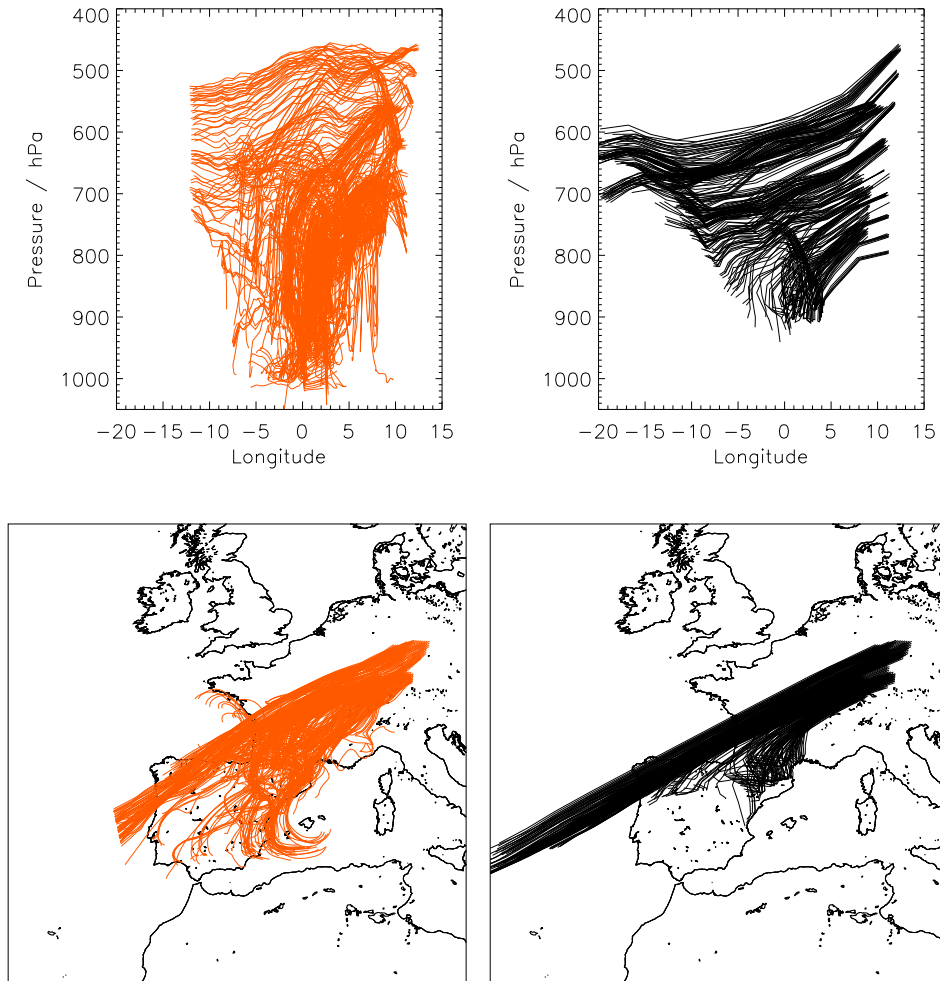


Figure 6.13: *Two-day back trajectories arriving within  $0.1^\circ$  and  $10\text{hPa}$  of the 12UT-relative flight track for flight A773 from the mesoscale UM (red, left) and ECMWF analyses (black, right).*

selected trajectories for comparison with the UM trajectories (Fig. 6.13). UM back trajectories penetrate the boundary layer more deeply, and rapid ascent from the PBL is evident on some of the higher altitude flight legs. Both trajectory sets show a large-scale westerly ascending flow along the axis of the front, but again only the 2-day UM back trajectories show the rapid ascent over the Iberian peninsula.

### 6.5.3 UM trajectories with chemistry

The CiTTyCAT model was integrated with full emissions and chemistry along the 2-day back trajectories described in Section 6.5.2. Results of these integrations are plotted against the pressure of their arrival coordinates in Figure 6.14.

The effect of rapid ascent in the UM trajectories is to produce elevated concentrations of shorter lived NMHCs (e.g. n-butane) at higher altitudes compared with the ECMWF trajectories. The use of the ratio of propane/ethane as a proxy for the amount of processing the air has seen since emission (see Chapter 4) also demonstrates rapid ascent of freshly emitted pollutants in the UM trajectories. Higher concentrations of HCHO demonstrate that the uplifted air is characteristic of photochemically active fresh pollution, compared to more aged air at higher altitudes given by the ECMWF trajectories. The scatter of model output is also greater using UM trajectories, and resembles the inhomogeneity between rapidly ascending polluted air and more aged air discussed in Section 6.4. The UM trajectories are successful in capturing the inhomogeneity between these different air mass ages, which was not given by the uniform mixed layer in Section 6.4. The ECMWF trajectories produce less scatter, since they are driven by the large scale-flow bringing in air masses in rapid westerlies from similar origins.

## 6.6 Conclusions

Model output from a 3D Lagrangian CTM (CiTTyCAT) and a global 3D CTM (TOMCAT) have been used to investigate chemistry and transport around a cold frontal zone, sampled by the C130 aircraft on August 2, 2000 over Central Europe. Results from the Lagrangian CTM demonstrate that the resolved winds from global analyses are not sufficient for capturing the rapid vertical transport revealed by chemical observations in the region of the WCB. The 3D Eulerian model better reproduces the vertical transport of fresh PBL pollution in this region through its parameterised sub-grid convection. This supports the hypothesis of *Purvis et al.*, [2003] that embedded convective cells in the frontal zone are responsible for a large quantity of the observed vertical transport of PBL air. Comparisons of RDF sim-

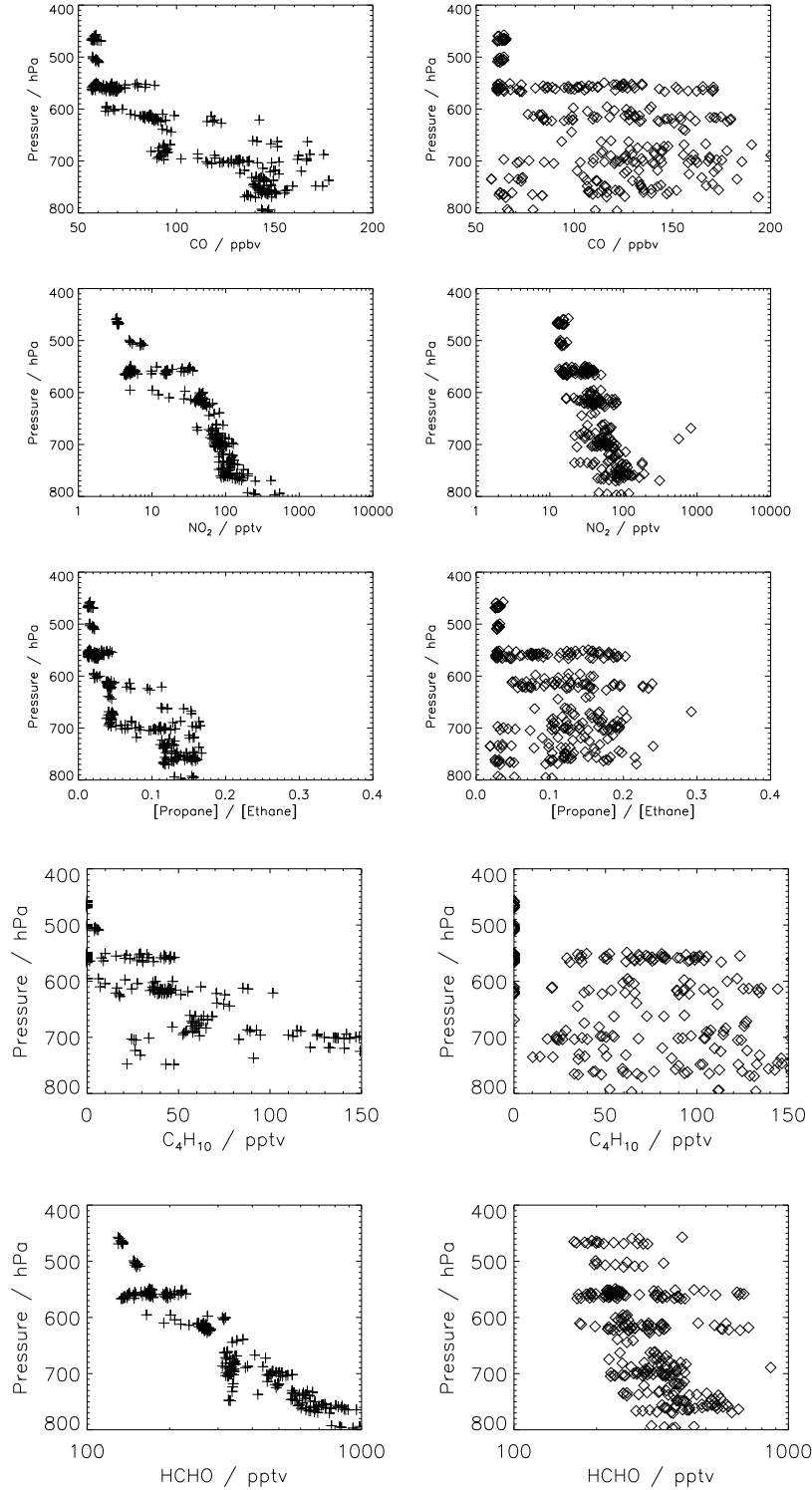


Figure 6.14: *Comparison of CiTTyCAT model output in the region of EXPORT Flight A773 (Aug. 2 2000) for model driven by trajectories derived from ECMWF global analyses (pluses, left) and mesoscale UM winds (diamonds, right).*

ulations using a CO tracer, with interpolated TOMCAT model output, reveal that using the large-scale winds alone leads to a CO mixing ratio up to 25% smaller than that given by the TOMCAT model in the region above the band of resolved ascent.

Attempts to account for the rapid vertical distribution of emissions by imposing a deep mixed layer of emissions over the region have shown limited success. A 5km uniformly mixed layer allows the CiTTyCAT model to reproduce the maximum observed enhancements in the upper flight legs. However, the smaller pollutant enhancements observed away from the WCB are then overestimated in the model. Increasing the impact of emissions over a depth of 5km, with an imposed exponential decay with altitude on the emission rate allows the smaller enhancements to NMHC concentrations in these regions to be simulated. It is not a good assumption to impose a horizontally uniform treatment for vertical transport of emissions throughout the frontal zone. The scattered nature of regions of strong ascent due to convective cells embedded in the large-scale, slower vertical motion therefore appears to be important in determining the observed tracer features.

The use of winds from a mesoscale GCM allows the trajectory paths to resolve some of this rapid ascent due to organised convective regions in the frontal system. Driving the model using such trajectories produces a scatter of large tracer enhancements due to very rapid ascent of fresh pollution, embedded in smaller enhancements from air masses undergoing slower ascent. This approach allows the best simulation of the transport of PBL pollutants in the frontal zone.

## 7. Long-range transport to Europe observed during EXPORT

### 7.1 Introduction

In Chapter 3 layers of enhanced CO, ozone and NO<sub>y</sub> were identified in the mid/upper troposphere during EXPORT flights A775 and A776 (August 9 and 10). These were attributed to long-range transport of pollution into Europe from sources west of the Atlantic Ocean. In this Chapter, the transport pathways responsible for this import are identified using meteorological analyses and trajectory calculations. The CiTTyCAT model is used to investigate processing of these air masses as they are imported across the Atlantic.

Section 7.2 gives a brief introduction to long-range pollution transport. Section 7.3 describes the observed air mass structure sampled in the upper level legs of the two flights, and compares observations with reverse domain-filling (RDF) simulations to gain a 3D picture of long-range transport air mass structure. Pathways for the trans-Atlantic transport in the observed cases are discussed in Section 7.4. Section 7.5 compares output from the CiTTyCAT and TOMCAT models with observations in order to understand the roles of mixing and chemistry in determining the air mass structure observed. Chemistry and transport of individual air mass types are examined in Section 7.6.

## 7.2 Long-range pollution transport

The European troposphere has been described as a ‘crossroads’ for global air pollution transport [Lelieveld *et al.*, 2002]. North American pollution can be imported into Europe in the middle and upper troposphere [e.g. Stohl and Trickl, 1999], as well as by low level transport in the Atlantic marine boundary layer [e.g. Li *et al.*, 2002]. There is also evidence to suggest import from very long-range westerly transport of Asian emissions in the mid-upper troposphere [Trickl *et al.*, 2003], as well as direct import from Asia in the monsoon outflow from the east into the UT over the eastern Mediterranean [Lelieveld *et al.*, 2002]. In summer, export of European pollution at low altitudes follows a northerly flow into the Mediterranean and south-eastern Europe. Westerly flow dominates in the free troposphere, exporting air masses eastwards towards Eurasia. In summer, there is also a branch of air from the mid-latitude middle-troposphere, which extends down into the lower troposphere over the Mediterranean, North Africa and south-west Asia, as a result of adiabatic descent associated with the Asian monsoon [Rodwell and Hoskins, 1996].

The transport of pollution on a global scale has been shown to have an impact on regional surface air quality [e.g. Bey *et al.*, 2001; Li *et al.*, 2002]. Much work has focused on the roles of North America and Asia as exporters of significant quantities of anthropogenic pollutants to the global troposphere, and their subsequent impact on air quality in Europe and North America respectively. Export of air from the North American PBL is generally facilitated by the action of mid latitude cyclones off the eastern seaboard. In particular, ascent in warm conveyor belt airstreams has been shown to be a major mechanism in the uplift of significant quantities of PBL mass to the mid/upper troposphere [Stohl, 2001]. Here, it can be transported eastwards in the large-scale westerly flow and rapidly in the mid latitude jet. Air masses characteristic of polluted continental outflow have been observed many hundreds of kilometres downstream, both over the Atlantic and Pacific Oceans as thin, distinct layers in the upper troposphere [e.g. Newell *et al.*, 1996].

These layers can be formed by the action of large-scale advective processes, such as those in mid latitude cyclones. As discussed in Chapter 6, these systems stir together air streams with very different origins and characteristics. As these layers are

stretched by the large-scale winds, they become narrow and their depth decreases, leading to the formation of fine-scale structures composed of interleaved narrow filaments [Methven and Hoskins, 1999]. Ultimately these filaments can become narrow enough for molecular diffusion to allow mixing of air between them. Small-scale turbulence, for example in the region of the jetstream, can encourage such mixing, which can have important chemical consequences [Esler *et al.*, 2001]. In the absence of strong mixing, filaments can persist for many days [Bithell *et al.*, 2000]. The action of mid latitude cyclones over North America and the West Atlantic, upwind of Europe, can lead to the formation and transport of these layers into the European free troposphere [e.g. Stohl and Trickl, 1999].

## 7.3 Observed air mass structure

### 7.3.1 August 9th 2000 (A775)

During the high altitude return legs of flight A775, the C130 sampled air which had been imported into the European troposphere from longitudes far west, over the North American continent. Figure 7.1 shows change in pressure along RDF trajectories arriving in the region of the upper flight legs. This reveals a sloping air mass of strong ascent, which the final east-west portion of the flight track cuts through. Trajectories indicate that this air mass has ascended strongly from the North American east coast. This relatively thin layer is surrounded by air which has shown slow westerly descent from the UT over the same time period. The upper level flight legs took place along an approximate north-east south-west section followed by a section of approximate constant latitude, denoted by A-B and B-C respectively in Figure 7.1.

Change in pressure along 5-day back trajectories arriving on the sections A-B and B-C are shown in Figure 7.2. Selected observations from the latter sections of this flight are reproduced in Figure 7.3. As the aircraft climbed to the high altitude sector, after 13.00UT, it entered relatively dry air containing correlated and moderately large concentrations of ozone and CO. Back trajectories (Fig. 7.4) trace the origins of this air to the UT over north-east US. Advection of the air is rapid, and appears to

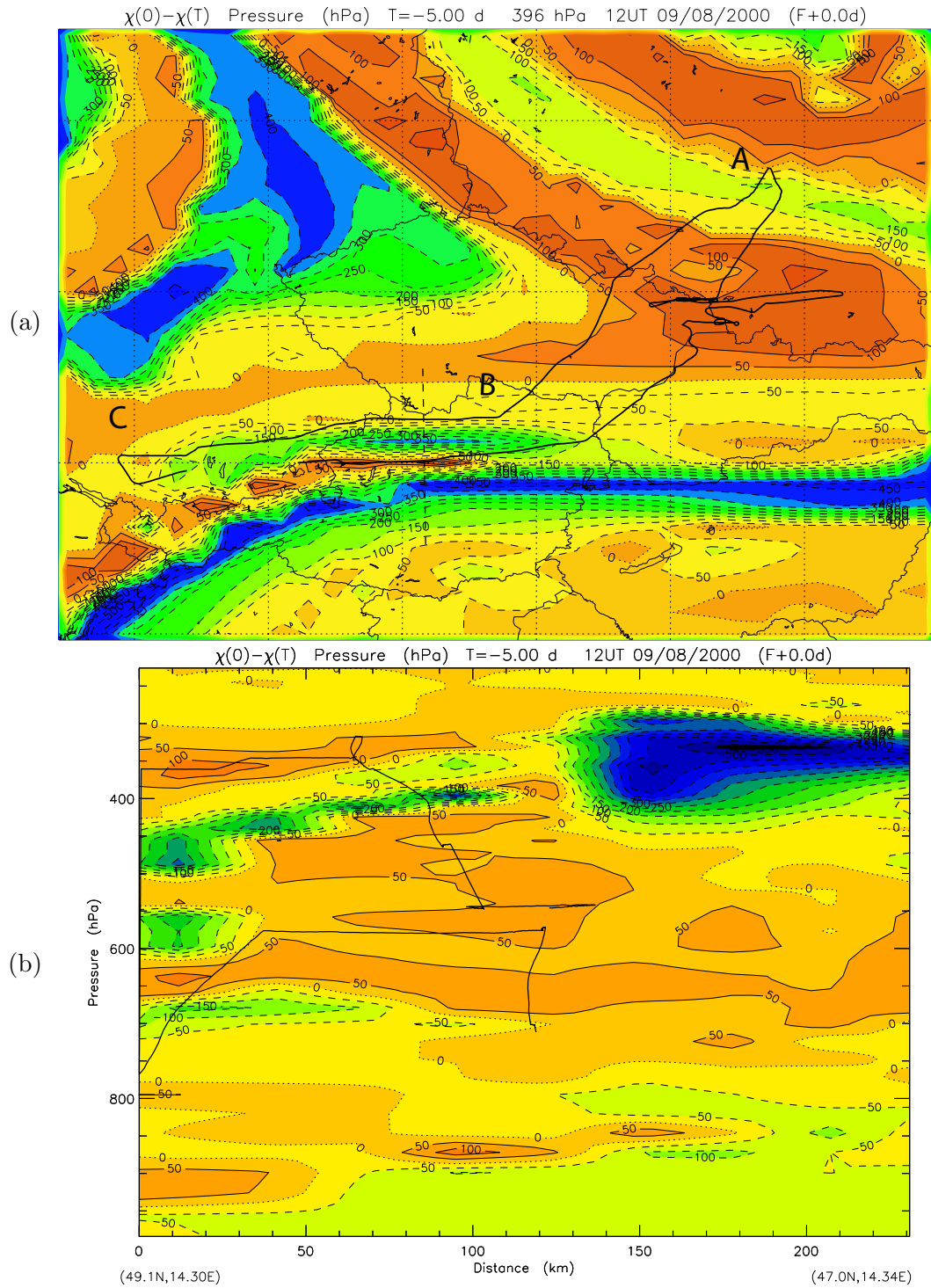


Figure 7.1: *Change in pressure (hPa) over 5-day back-trajectories arriving on (a) the 396hPa pressure surface and, (b) on the vertical section denoted by the dashed line in Panel (a), in the region of Flight A775 (Aug. 9 2000). The blue areas denote air which has ascended strongly from the North American east coast.*



follow a path consistent with the position of the mid-latitude jet. The transition of the aircraft across the point B from the first section to the second, at around, 13.5UT coincides with the onset of the ozone-CO anti-correlation noted in Chapter 3. As the aircraft turned onto the second section, and began its approximately constant latitude flight leg, it entered air close to the thin air mass of North American uplift described above, and crossed it at around 14.17UT. Trajectories show a number of 7 day origins in the lower troposphere, over the North East tip of the US, with surrounding air having UT origins over the US. The presence of an elevated feature in observed  $q$  at around 14.17-14.25 UT may indicate the crossing of this uplifted layer, although it appears to be slightly displaced from the position indicated by the back trajectories.

The origins of chlorine which may be responsible for NMHC oxidation, described in Chapter 4 are far from clear. The ozone-CO anti-correlation, where CO is high relative to the observed ozone, was seen almost immediately after the aircraft turned and began to fly along the axes of the uplifted US and North American UT filaments, brought into close proximity. However, unusual NMHC ratios were observed from about 12.4UT onwards through the rest of the flight. Air mass origins in the uplifted filament are close to the US north-east coast, and may be influenced by marine PBL air.

### 7.3.2 August 10th 2000 (A776)

During the latter part of flight A776 (August 10 2000), the C130 made more extensive sampling of a number of air masses with origins over North America. Between  $\sim 13.0$  and  $15.0$ UT, the aircraft flew on two constant pressure levels in the mid/upper troposphere, at an almost constant latitude. Figure 7.5 shows an RDF vertical section calculated along that approximate latitude highlights the air mass structure sampled. The trajectory arrival points are spaced by  $0.1^\circ$  in longitude and  $\sim 6$ hPa in pressure. Longitude and  $q$  at 5-day back trajectory origins reveal and interleaved structure of air masses originating west of the Atlantic.

By comparing  $q$  from short back trajectory origins arriving on the aircraft flight track, with observed  $q$ , the ability of the RDF simulation to resolve the positions

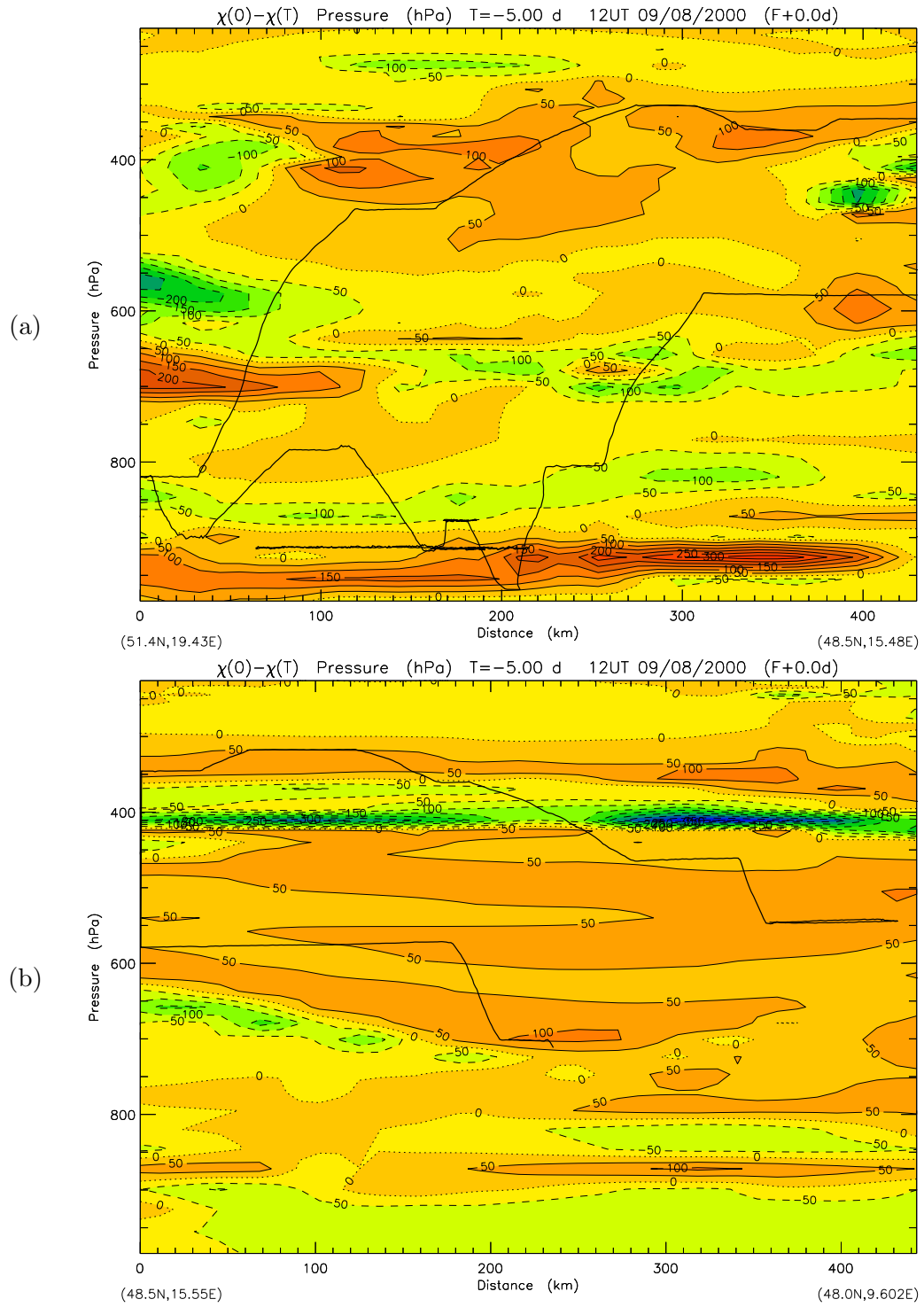


Figure 7.2: Change in pressure (hPa) over 5-day back-trajectories arriving on vertical sections along flight legs (a) A-B and (b) B-C denoted in Figure 7.1a.

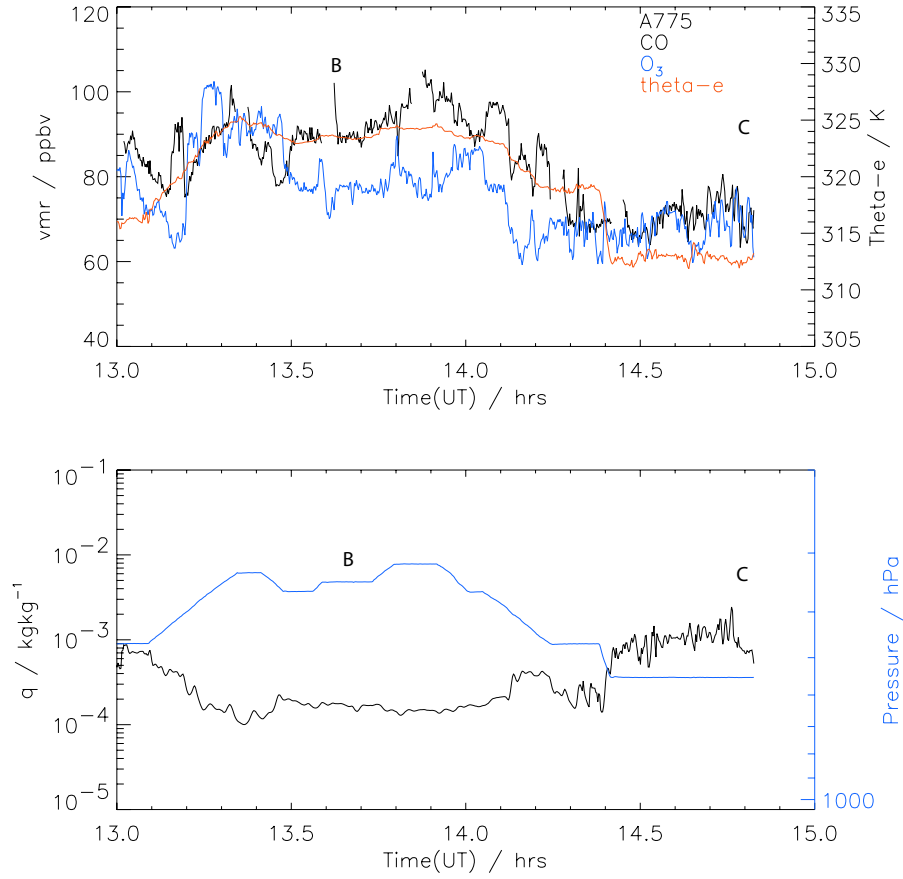


Figure 7.3: Observed CO (ppbv), ozone (ppbv),  $q$  ( $\text{kg kg}^{-1}$ ), and  $\theta_e$  (K) for the latter part of Flight A775. Letters refer to points labelled in the RDF simulation shown in Figure 7.1a.

and boundaries of the different air mass types can be evaluated. This comparison is shown in Figure 7.6 for  $q$  taken from 2 and 4-day back trajectory origins. The positions of air mass boundaries during the end part of the flight do not tie in well with those observed. This is likely to be due to a small displacement error in the trajectory calculation. Such errors occur through interpolation of the ECMWF wind fields to the trajectory position, and can result in the displacement of calculated features. Examining the RDF section suggests that the position of the flight track relative to the simulated air mass features means that the aircraft is not sampling the full range of air masses in the observations. In order to account for this offset, the position of the aircraft relative to the air mass structure has been shifted by  $0.4^\circ$

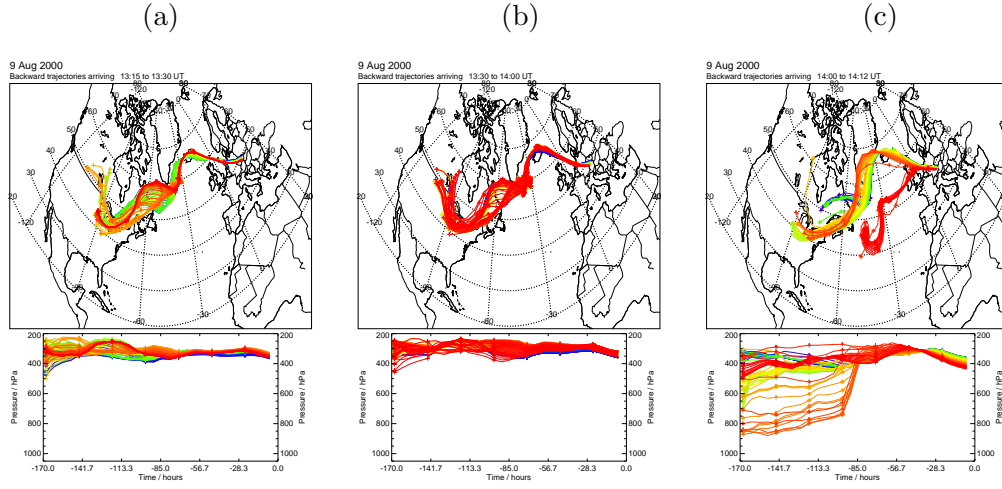


Figure 7.4: 7-day back trajectories arriving between (a) 13.0 and 13.5 UT, (b) 13.5 and 14.0 UT and (c) 14.0 and 14.2 UT on the flight track of EXPORT Flight A775 (Aug. 9 2000)

east in longitude. After employing such a shift, time series of observed  $q$  from the aircraft tie in with the position of features from the trajectories and RDF simulation far better.

Figure 7.7 shows observed ozone, CO, specific humidity ( $q$ ) and the altitude trace of the aircraft from the latter half of the flight, with position labels corresponding to locations on Figure 7.5 marked by letters. The aircraft passes between these positions, sampling a number of distinct air mass types. These are described below.

- Initially the aircraft is climbing for a short time towards point A, through air which has come from the far west North American continent, which is relatively moist, and high in CO and ozone (Air mass ‘W.Am.’). Back trajectories (Fig. 7.8) indicate that there is uncertainty regarding the origin of pollutant enhancements in the W.Am air mass, since the large-scale flow does not demonstrate any appreciable uplift from the US boundary layer. Convective ascent of fresh pollution from the American continent to the UT, or even very long range transport of pollutants from the West Pacific are possible sources for the observed enhancements to CO.

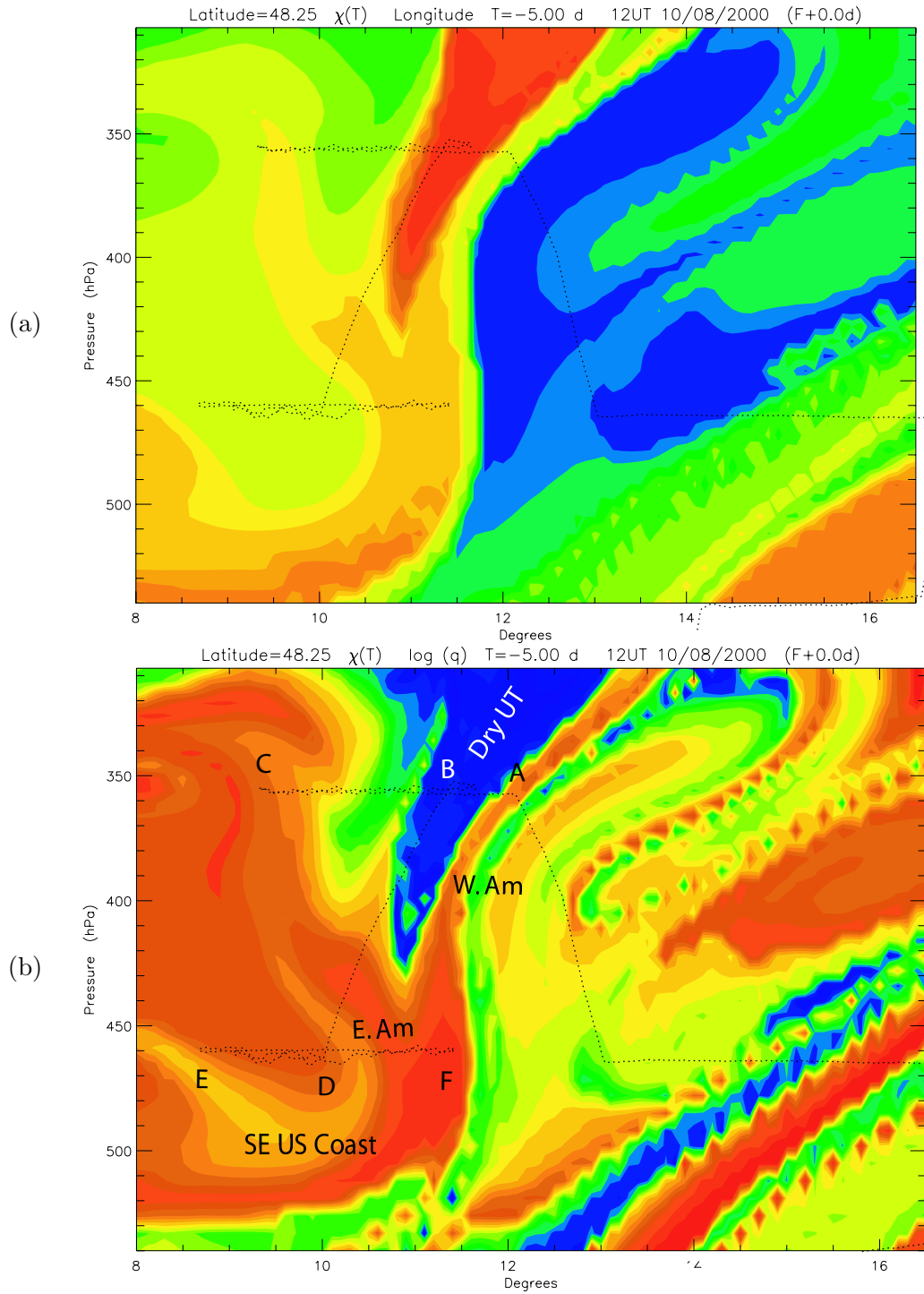


Figure 7.5: Cross section along constant latitude section of flight A776. (a) Longitude at 5-day back trajectory origins. (b)  $q$  ( $\text{kg kg}^{-1}$ ) at 5-day back trajectory origins. Layering of air masses of different origins in close proximity in the region of the flight track is evident. Labelled air mass types are discussed in the text. Letters refer to points along the 12UT-relative flight path (dotted line), discussed with reference to aircraft observations.

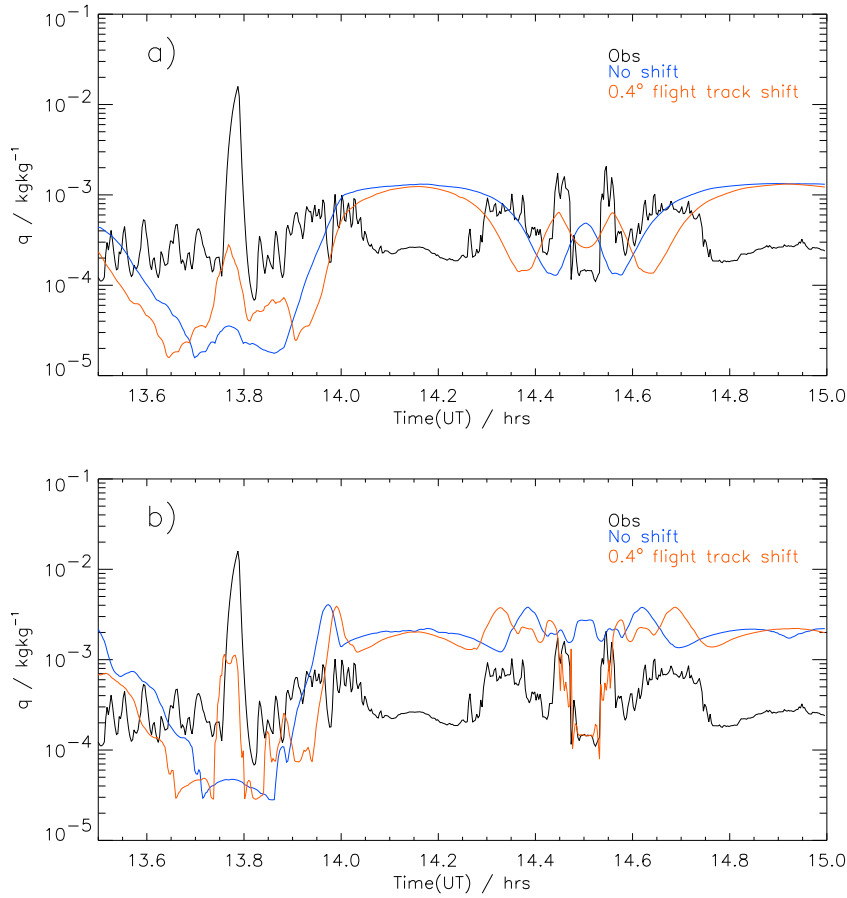


Figure 7.6: Comparisons of ECMWF specific humidity at (a) 2-day and (b) 4-day back trajectory origins arriving on the flight track of flight A776 (Aug. 10 2000) with observed specific humidity averaged over the 10-second trajectory arrival frequency. A shift in the flight track of  $0.4^\circ$  east in longitude relative to the ECMWF fields gives a better representation of the air masses sampled on the aircraft.

- **13.20UT** The aircraft leaves the W.Am. air mass (point A) and enters a relatively unpolluted, dry air mass (point B) which back trajectories indicate has descended slightly from the mid-Atlantic upper troposphere.
- **~13.40UT** The RDF simulation shows the aircraft entering a slightly more moist air mass with origins in uplift from the far west American continent as well as the North American UT.
- **13.45UT** At point C, the aircraft turns back through the same air and returns

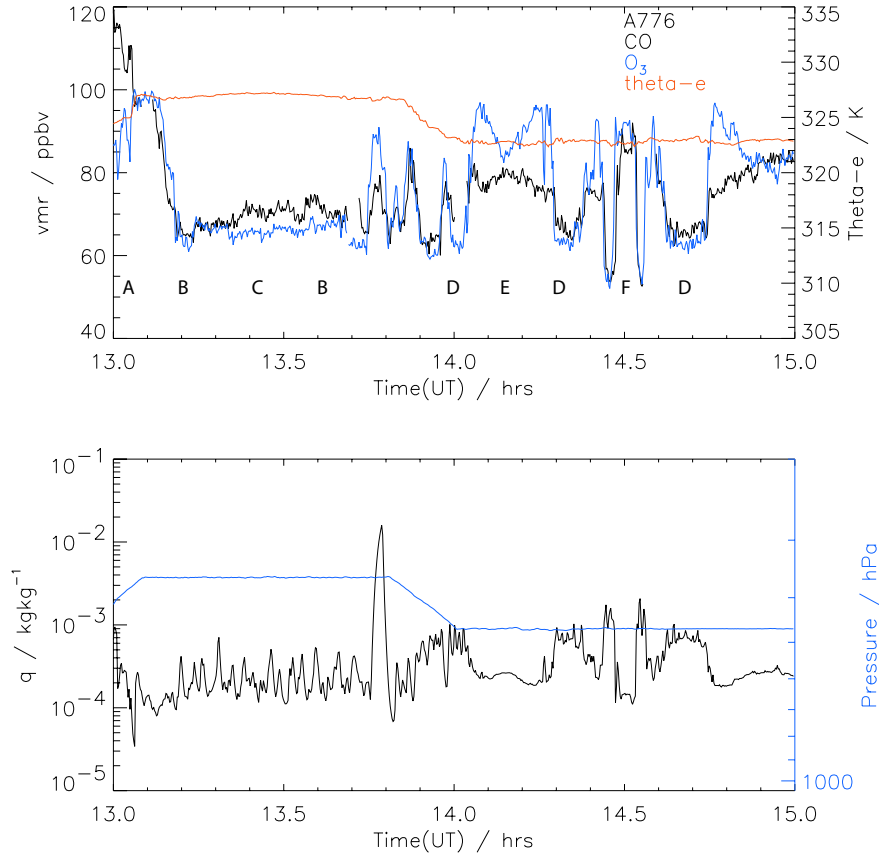


Figure 7.7: Observed CO (ppbv), ozone (ppbv),  $q$  ( $\text{kg kg}^{-1}$ ), and  $\theta_e$  (K) for the latter part of Flight A776. Letters refer to points labelled in the RDF simulation shown in Figure 7.5a.

to point B. This is a very homogeneous air mass, the observations showing little evidence of variability arising from the different distinct origin types suggested by the RDF simulation. This indicates mixing between the different air mass types as they have run together just below the tropopause for several days. (Air mass ‘NA.Mix.’)

- **13.75UT** At point B, the aircraft briefly enters a polluted air mass with origins in the mid-US lower troposphere, indicated in the observations by correlated spikes in ozone and CO, before turning back and beginning a descent.
- **~13.85UT** CO and ozone observations suggest that the W.Am air mass is briefly intercepted again. Although this is not supported conclusively by the

RDF simulation, the descent takes the aircraft very near to the simulated sloping boundary between the W.Am and dry UT air masses.

- **~13.95UT** The aircraft enters an air mass with origins in the boundary layer of eastern United States, which ozone and CO observations suggest contains signatures of photochemical pollution. (Air mass ‘E.Am.’)
  - **~14.00UT** At the bottom of the descent (point D), the aircraft goes west, leaving the E.Am polluted air mass into relatively clean air that has ascended from the Carribean Sea.
  - **14.03UT** The aircraft enters moist air which is more polluted and has origins in the Tropical Atlantic marine boundary layer, close to the coasts of Florida and North Carolina (Air mass ‘SE US Coast’).
- 14.15UT** At point E the aircraft turns back on itself, passing through the cleaner Carribean air, then again reaching point D, beyond which it continues eastwards.
- **14.4UT** The RDF simulation shows the aircraft intercepting a large, moist air mass with origins in ascent from the eastern United States, with enhancements in ozone and CO; this is a large part of the E.Am air mass sampled earlier.
  - **14.45UT** A narrow, clean, drier filament is intercepted which trajectories indicate has origins in the upper troposphere over the tropical Atlantic. Directly following this, the aircraft enters the W.Am polluted air mass again, before turning (at point F) back towards point D.

## 7.4 Transport pathways

The back trajectories shown in Section 7.3 indicate transport pathways resolved by the ECMWF analyses that bring air masses from the North American continent into Europe during August 9 and 10 2000. These trajectories generally show either rapid advection in the UT over North America and the Atlantic, along a path coincident with the position of the mid-latitude jet, or advection at low altitudes followed by



rapid ascent to the UT over the North American east coast or the Atlantic Ocean. In some cases, uplift from the lower troposphere appears to merge with more rapid advection of air masses from further west in the UT (e.g. Fig. 7.8b). In these cases, mixing may play an important role as uplifted air streams are stretched and aligned in close proximity to air streams transporting air of UT character. Proximity to the jet is also likely to lead to the air streams experiencing turbulence which will facilitate efficient mixing. Other sets of trajectories suggest more isolated transport pathways, where large groups of back trajectories are bundled tightly along a given back-trajectory pathway, with little divergence (e.g. Fig 7.8d). These suggest transport of more coherent airstreams, which may have the potential to retain their own strong tracer signatures during transport in the absence of turbulent mixing.

Figure 7.9 shows synoptic surface charts from NCEP analyses for the North American and North Atlantic regions during early August 2000. Periods of strong ascent denoted by the trajectories can be associated with warm conveyor belts, which are approximately aligned along cold fronts depicted in the analyses. A sequence of mid-latitude cyclones can be seen transversing the North American continent and the North Atlantic, with their associated cold fronts stretching down the North American east coast, and progressing eastwards out into the Atlantic.

A cyclonic system and its cold front are highlighted in green in Figure 7.9(a). This system appears to correspond well to the position of uplift depicted in the trajectories in Figure 7.4(c). This appears to be the earliest uplift from the North American coast which has contributed to the sampled air masses described in Section 7.3. The air ascends polewards and eastwards along a warm conveyor belt, until it reaches the UT. The trajectories show that this air runs in the UT close to airstreams which have ascended more slowly from the mid-troposphere over the Great Lakes region of the US. Approximately two days prior to arrival in Europe, the air masses run along in the UT close to air which has also ascended strongly along a WCB, although much later on around August 5.

The system which appears to be responsible for the later uplift can be seen in its early stages as a frontal wave over the US-Canadian border on August 2 (Fig. 7.9 (b) - highlighted red). An upper level trough is marked on the synoptic chart, which is coincident with a surface low pressure centre on the frontal wave. Divergence

around the trough forces the deepening of the surface low, and over the subsequent days the low develops into a fully mature mid latitude cyclone. On August 5 and 6, a cold front associated with this cyclone lies along the US east coast, trailing from the southern US states. The position of this system is consistent with the later uplift shown in the A775 trajectories, and also strong uplift off the US east coast shown for the E.Am, Mid US and SE US Coast air masses sampled during A776 (Fig. 7.8).

Using CO as a tracer of PBL pollution, the advection of polluted air from the North American east coast can be seen in the TOMCAT model simulation during this period (Fig. 7.10). Flow of TOMCAT CO out of the US east coast into the Atlantic region follows the position of the WCB features described above. Ascent resolved by the trajectories is reproduced well by the TOMCAT simulation, despite its degraded wind resolution ( $2.8^\circ$  compared with  $1.1^\circ$ ).

## 7.5 Modelling LRT using the CiTTyCAT model

Most past studies of intercontinental transport have employed either Lagrangian particle models using passive tracers [e.g. *Stohl and Trickl, 1999; Trickl et al., 2003*] or Eulerian global CTMs [*Jacob et al, 1999; Liu et al, 2002 Bey et al, 2001*]. Global CTMs allow an assessment of the contribution of different source regions of pollutants to the large-scale troposphere and their effects on regions many hundreds of kilometres downwind. The production of secondary pollutants such as ozone or PAN can also be treated, allowing an attempt to understand the contributions from long-range transport to the complex processes controlling downwind surface ozone. The grid resolution of such models, however, means that fine-scale layers and filaments characteristic of long-range transport cannot be resolved, and may be mixed out unrealistically quickly in the simulation leading to erroneous chemistry.

Lagrangian models will tend to preserve strong tracer gradients, and without some treatment of mixing will allow the production of increasingly small-scale structures until fields become unrealistically noisy. Nevertheless, over the timescale of a few days Lagrangian air mass advection can be used to create realistic structure of a scale less than the large-scale winds used to drive the advection [*Methven and Hoskins,*

1999; *Methven et al.*, 2003]. Lagrangian models are also useful for establishing direct source-receptor relationships, where transport of a tracer is not masked by excessive mixing in the model domain and complicated by contributions from other sources. While useful in this context, passive tracer studies do not include chemical processes and so the simulation of concentration fields of secondary pollutants such as tropospheric ozone cannot be treated completely. In addition, any contributions from mixing with the background atmosphere or additional tracer sources are generally absent unless a ‘global’ domain of sources and air parcels can be employed with a suitable mixing parameterisation (e.g. the STOCHEM model [*Stevenson et al.*, 1998]).

### 7.5.1 Basic model along 10-day back trajectories

The CiTTyCAT model has been used to re-construct the observed tropospheric tracer signatures described in Section 7.3. Figure 7.11(a) shows observations of CO and ozone for the latter part of flight A776 compared with output from the CiTTyCAT model. The model run uses 10-day back trajectories initialised from  $2.8^\circ \times 2.8^\circ$  TOMCAT fields, arriving at a 10-second frequency along the flight. The model output is noisy compared with the observations, with very large variability in the modelled tracer output. This is due to the lack of mixing in the model, and associated with very disparate origin air masses being advected into close proximity, preserving strong gradients. These gradients are eroded by mixing in the real atmosphere. Despite the lack of mixing, the model output provides a useful comparison with the observations.

The E.Am air mass, which is crossed between 14.32 and 14.45 UT and then again between 14.55 and 14.68 UT, shows very large model concentrations of CO, since the 10-day back trajectories spend an appreciable amount of time in the US PBL before travelling across the Atlantic. Due to the lack of mixing, the only loss route for CO along the trajectories is by photochemistry, and any dilution of the exported US plume into the background free troposphere over the Atlantic is not modelled.

The CO model output shows excellent agreement with the observed position of the ‘clean slot’ sampled at around 14.47 UT and 14.55 UT, which is sandwiched between

the W.Am and E.Am air masses.

The W.Am air mass itself, which is centred around 14.5 UT, and is also sampled just before 13.9 UT shows very large concentration, noisy ozone model output with lower than observed CO concentrations. Air mass trajectories arriving on the flight during these periods are advected at high altitudes near the tropopause. Initialisation from TOMCAT appears to be picking up high ozone concentrations, and this may be due to differences between the position of the tropopause in the TOMCAT model and in the real atmosphere, or the smearing out of lower stratospheric air in TOMCAT in the tropopause region. The lack of CO enhancements is due to low CO from the TOMCAT initialisation, which does not appear to contain a sufficiently polluted signature in the western US UT. This is addressed further in Section 7.6.

The very homogeneous NA.Mix. air mass sampled between 13.2 and 13.7 UT contains far more structure in the model output, due to the disparate origins of the air masses which arrive during that period of the flight. The large difference between the level of structure in the observations compared with the model output confirms the importance of strong mixing in determining the overall evolution of this air mass.

The enhanced ozone and CO sampled between 14.05 and 14.30hrs UT in the SE US Coast air mass is not captured by the model. Back trajectories arriving here indicate air uplifted from very close to the South East US coasts off Florida and North Carolina. The displacement of the trajectories from the coast means that continental emissions are not picked up by the model. The initial conditions derived from TOMCAT are also low in CO and ozone, however this is not surprising since the 10-day origins of the back trajectories are further from the continental coastal region in the Caribbean marine boundary layer. The lack of model enhancements may be due to an error in the Lagrangian advection arising from the finite resolution of the analyses which may result in small shifts in the air mass position as it is advected back in time. There may also be movement of polluted air out off the US coast in TOMCAT which is not picked up by the trajectories without a consideration of along-trajectory mixing.

### 7.5.2 Introduction of mixing

As shown in Chapter 5, 4-day back trajectories are not sufficiently long to pick up the polluted features associated with long-range transport across the Atlantic. It is necessary to employ trajectories long enough to pick up North American emissions, but as shown in Section 7.5.1, mixing of the air masses as they undergo advection must also be included to avoid noisy model output. A simple mixing treatment is employed here, where the Lagrangian air parcels use the TOMCAT global model fields as a ‘background’. Mixing with these background fields allows strong gradients to be reduced by relaxing the chemistry of the Lagrangian air masses to a tracer background which is of a coarser resolution, but consistent with the modelled chemistry and transport in the domain. Effectively, the mixing inherent in the Eulerian model advection is used to smooth the created Lagrangian tracer fields. In addition, it is hoped that any transport processes that occur on a spatial scale smaller than the scale of the winds used for the Lagrangian advection, and that are parameterised in the Eulerian model (e.g. convection) will have an influence on the chemistry of the Lagrangian air parcels through this relaxation.

The modelled concentrations in the CiTTYCAT trajectories are relaxed to the background concentrations from TOMCAT at every model timestep according to

$$\frac{d[X]}{dt} = \frac{1}{t_r}([X]_{3d} - [X]_{box}) \quad (7.1)$$

where  $t_r$  is a relaxation timescale for adjusting the box concentrations to the external 3D model fields,  $[X]_{3d}$  is the external mixing ratio from the 3D TOMCAT fields, and  $[X]_{box}$  is the CiTTYCAT box mixing ratio. Values of  $t_r$  are based on studies which have attempted to model the level of fine-scale structure in aircraft observations using various lengths of trajectory, also initialised from a  $2.8^\circ \times 2.8^\circ$  TOMCAT model simulation [Good *et al.*, 2003]. For the 10-day back trajectories used in the CiTTYCAT simulation of flight A776, values of 5.0 and 2.5 days are compared for  $t_r$ .

The inclusion of mixing successfully reduces the strong air mass gradients seen in the original model comparison (Fig. 7.11a). Despite a 2.5-day mixing timescale, the

large homogeneous air mass retains more structure than in the observations. The global TOMCAT fields interpolated to the flight track seem to best produce the amount of structure observed here, indicating rapid mixing between the air masses.

Large model ozone concentrations associated with the initial position of back trajectories for the W.Am air mass is also retained, even with 2.5-day mixing timescale. However, the ozone concentrations are reduced by both the 5 and 2.5-day mixing timescales. For the faster mixing, the ozone concentrations reduce to  $\sim 100$  ppbv.

The E.Am air mass is modelled well. Observed CO enhancements lie between the model output for  $t_r=5$  and 2.5 days. Ozone enhancements are relatively low, however. Mixing does not affect the position of the modelled ‘clean slot’ between the W.Am and E.Am air masses, but the strength of the tracer gradients between these air masses is eroded compared with the observations when using the faster mixing. This suggests quite weak mixing between these airstreams in the real atmosphere, with individual chemical characteristics of the air parcels well retained.

The SE US coast air mass remains very low in CO and ozone compared to the observations. A  $t_r$  value of 0.5 days employed in the PBL of the mixing simulations, in an attempt to incorporate any low level coastal export of pollution captured by TOMCAT.

## 7.6 Chemistry and mixing in observed air mass types

The Lagrangian model can be used to investigate the effects of chemistry and mixing on the individual air mass types sampled during the high altitude sections of flight A776. Figure 7.12 shows examples of 10-day back trajectories arriving on the A776 flight-track, representative of each air mass type.

### 7.6.1 E.Am Air Mass

The E.Am. air mass ascends strongly from the southern US PBL. Emissions of isoprene are especially large in this region [Guenther *et al*, 1995], and concentrations

reach between 3 and 4ppbv during the initial two days of advection (Fig. 7.13). PBL  $\text{NO}_x$  concentrations are between 1 and 2 ppbv, leading to efficient formation of PAN from isoprene. The abundance of peroxy radicals from isoprene oxidation also leads to efficient ozone production of up to 4 ppbv  $\text{hr}^{-1}$ .

As the air mass moves away from the continental PBL, large PAN concentrations lead to the release of  $\text{NO}_x$ , which maintain  $\text{NO}_2$  concentrations at more than 100pptv. PAN concentrations in the TOMCAT background fields are very low, due to the lack of complex hydrocarbon chemistry (e.g. isoprene). As a consequence, away from the continental PBL,  $\text{NO}_2$  falls off to as low as 10pptv in the TOMCAT background. Mixing to the TOMCAT background therefore reduces both PAN and  $\text{NO}_x$  directly, reducing the efficiency of ozone production.

After  $\sim 6$  days, the air mass reaches its maximum altitude. Here, in the non-mixed case, PAN stabilises in the cold temperatures. The results show that  $\text{NO}_x$  concentrations at this altitude are buffered by  $\text{HONO}_2$  photolysis. Under this regime, reduction of  $\text{HONO}_2$  by mixing with the lower  $\text{HONO}_2$  TOMCAT background, has a marked effect on ozone production. Mixing of  $\text{HONO}_2$  alone accounts for a  $\sim 60\%$  reduction in diurnal maximum  $\text{P}(\text{O}_3)$ .

For this air mass, mixing with TOMCAT has been shown to reduce production of ozone through loss of  $\text{NO}_y$ , which is required to buffer  $\text{NO}_x$  concentrations through decomposition of PAN at lower altitudes and photolysis of  $\text{HONO}_2$  at higher altitudes.

### 7.6.2 Mid US Air Mass

The Mid US air mass is advected rapidly across the US in the mid troposphere, ascending to the UT over the mid-Atlantic. The consequences of mixing for ozone production are small (Fig. 7.14).  $\text{NO}_x$  concentrations are between 10 and 50pptv at initialisation, and reduce further as the air mass ascends due to formation of  $\text{HO}_2\text{NO}_2$ , and to smaller degree PAN.

Once in the UT,  $\text{HONO}_2$  photolysis recovers  $\text{NO}_x$  concentrations to near their initial values. Net  $\text{P}(\text{O}_3)$  is slightly negative during advection and ascent. This is

also the case for the mixed air parcel, since background  $\text{NO}_x$  concentrations are not too different from those in the isolated air parcel. Interestingly, background PAN concentrations are up to approximately 50% larger than those in the isolated air mass. This is a reflection of the very low air parcel PAN concentration and PAN precursor concentrations taken from the TOMCAT initialisation. TOMCAT background concentrations of NMHCs (e.g. propane) remain far larger than those in the isolated parcel in the free troposphere, as mixing in the Eulerian model allows emitted propane to become well-mixed into the background atmosphere. The lack of any such mixing in CiTTyCAT means that during advection away from the continental regions, NMHC concentrations are reduced through oxidation, and cannot be maintained through mixing. This also leads to PAN formation being maintained better in the TOMCAT background than in the isolated CiTTyCAT air mass.

The most significant change to the evolution of the ozone concentration comes from mixing with larger ozone in the TOMCAT background at high altitudes. This leads to an increase in the final ozone concentration from  $\sim 50$  to  $\sim 60$  ppbv.

### 7.6.3 S.E. US Coast Air Mass

In Section 7.5.1 it was discussed that a possible explanation for the lack of model polluted signature associated with this air mass was a trajectory displacement error. This may lead to the trajectory path being offset from the continental emission sources it should have been influenced by. The TOMCAT background and emissions data in the model were shifted by one TOMCAT gridpoint to the east ( $2.8125^\circ$ ) to take account of this possibility. Figures 7.15 and 7.16 show along-trajectory model output with and without this shift respectively.

In the isolated air mass, without the shift, ozone falls off rapidly to just over 10ppbv in the marine PBL environment. Net  $\text{P}(\text{O}_3)$  remains small and negative throughout the advection, with ozone decreasing very slowly in the UT after uplift. Mixing has little effect on  $\text{P}(\text{O}_3)$ , although it does increase  $\text{NO}_x$  concentrations from less than 1 pptv to over 10 pptv. Background PAN and  $\text{HONO}_2$  concentrations also increase these concentrations in the mixed parcel.



After employing the shift to the emissions and the TOMCAT background, the evolution of ozone in both the non-mixed and mixed cases changes significantly. Emissions picked up around day 4, where the trajectory now passes over a ‘land’ signature of emissions data, result in strong ozone production of more than  $4 \text{ ppbv hr}^{-1}$ .  $\text{NO}_x$  reaches over 4ppbv, also resulting in rapid formation of PAN and  $\text{HONO}_2$ . The evolution of concentrations of CO,  $\text{NO}_x$ , NMHCs and ozone early in the trajectory are larger in the TOMCAT background than in the isolated air mass. This suggests the presence of photochemically polluted air off the US East coast, and may reflect the large grid-box size of the TOMCAT model. Mixing therefore increases ozone early in the trajectory. This is offset later, at higher altitudes where mixing reduces  $\text{P}(\text{O}_3)$ , due to lower background concentrations of  $\text{NO}_x$  and  $\text{NO}_y$  in the TOMCAT background. Interestingly, the final ozone concentrations at the end of the trajectory for the mixed and non-mixed cases, and in the TOMCAT background agree within  $\sim 7 \text{ ppbv}$ .

The shifted emissions and background resulted in a polluted signature being given to the S.E. US Coast air mass, supporting the hypothesis of the discrepancy arising through a trajectory displacement error. However, the final ozone concentration remains lower than that observed in this air mass. This may suggest mixing of ozone-rich air from the tropopause region into the air mass. Background ozone concentrations from TOMCAT along the trajectory reach up to 70ppbv in the UT, however this is still 15-30ppbv lower than the observed concentrations.

#### 7.6.4 W.Am Air Mass

The W.Am air mass is advected rapidly in the UT, across the USA and Atlantic. The net change in ozone along the trajectory is small (Fig. 7.17). Indicating the low potential for ozone production from the initial state. The initial 30-40pptv of  $\text{NO}_x$  is sufficient for over  $0.1 \text{ ppbv hr}^{-1}$  net ozone production. This is enhanced by mixing initially, due to elevated  $\text{NO}_x$  and  $\text{HONO}_2$  in the TOMCAT background, relative to the isolated air parcel. Throughout the advection, the chemical system appears to be operating very close to the  $\text{P}(\text{O}_3)$  ‘compensation point’, where small increases to  $\text{NO}_x$  due to mixing can shift the net  $\text{P}(\text{O}_3)$  regime from negative to

positive. However, the major effect on changing ozone in the mixed case, is mixing from the TOMCAT background ozone field. The net result is to decrease the final ozone from 80 to 75 ppbv relative to the non-mixed case.

Observations of CO suggest that the W.Am. air mass has a stronger polluted signature than is suggested by the CiTTyCAT model. Observed CO is between 80 and 90ppbv, whereas final CO in the model is less than 60ppbv. This may be a result of the initial conditions from TOMCAT missing some source of pollution. This could arise from convective transport of US emissions to the UT, somewhere along the trajectory path, or from aged pollution present over the Eastern pacific as a result of export of Asian pollution across the Pacific.

To address these possibilities, the trajectory was initialised using observations from the PHOBEA aircraft experiment [Kotchenruther *et al.*, 2001]. These observations provide a realistic set of concentrations in the UT, over the West Coast of the US. Ozone is approximately the same as in the original TOMCAT initialisation, and  $\text{NO}_x$  is slightly lower (Fig. 7.18). This results in small negative  $\text{P}(\text{O}_3)$  initially, compared to the positive  $\text{P}(\text{O}_3)$  from the TOMCAT initialisation. However, CO and PAN are both substantially elevated compared to the TOMCAT initial field.  $\text{P}(\text{O}_3)$  remains small and negative, until in the mixed case where the air mass descends slightly. Thermal decomposition of PAN then nudges the  $\text{NO}_x$  concentration large enough for a small amount of ozone production. The net change in ozone along the trajectory is small however, with the final ozone concentration being similar to that in the TOMCAT initialised case. Final CO concentrations are  $\sim 120$ ppbv in the non-mixed case and  $\sim 70$ ppbv in the mixed case. Given the sensitivity of this final concentration to the mixing timescale chosen, this appears to represent a better simulation of the aged polluted signature seen in the EXPORT observations for the W.Am air mass. This suggests that TOMCAT's Eastern Pacific UT conditions are not sufficiently polluted. It is not possible to ascertain here whether this is due to inadequate modelling of US convection or of trans-Pacific long-range transport.

## 7.7 Modelled ozone production in LRT layers

### 7.7.1 RDF with full chemistry

The 3D RDF grid has been shown to give a good representation of the positions of air mass features sampled in the UT during flight A776. By integrating the CiTTyCAT model along each of the back trajectories used to construct the RDF grid, ozone concentrations and tendencies in the fine-scale layers can be estimated. To achieve this, the CiTTyCAT model was integrated using full emissions and chemistry, along the 10-day RDF back trajectories using  $t_r = 5$  days in the free troposphere and  $t_r = 0.5$  days in the model PBL, as previously used for flight track trajectory arrival.

Figure 7.19 compares the distribution of ozone concentrations on the RDF section calculated in this way with ozone concentrations obtained from the  $2.8^\circ$  resolution TOMCAT integration, interpolated to the RDF arrival grid. As was evident from the flight track time-series comparisons in Figure 7.11, the TOMCAT simulation smears out much of the fine-scale air mass structure revealed in the observations. The range of TOMCAT ozone concentrations is  $\sim 55$ -70 ppbv over the 2D section, in a smooth gradient from low to high altitudes. The CiTTyCAT chemistry RDF field, however shows a great deal of structure associated with the different air mass types in the domain. The E.Am air mass shows  $\sim 70$  ppbv of ozone, with a lower  $\sim 45$  ppbv in the S.E. US Coast air mass, associated with its moist MBL origins. The ‘clean slot’ between the E.Am and W.Am air masses is resolved as a narrow segment of low ozone concentrations ( $\sim 50$  ppbv) sandwiched alongside much larger concentrations ( $> 100$  ppbv) in the W.Am air mass, due to its origins near the tropopause. Model output for the large homogeneous air mass sampled between points B and C, shows more structure than is suggested from the observations, with  $> 100$  ppbv ozone in air originating in the UT and 65-75 ppbv in air uplifted from western US lower troposphere.

A comparison can also be made of the rates of ozone production in air masses as they arrive on the section from the two models. To achieve this, the temperature and pressure of every arrival point in the grid has been used in conjunction with  $\text{HO}_2$  and  $\text{NO}$  concentrations from the models to calculate the distribution of rates of

the reaction  $\text{HO}_2 + \text{NO}$  on the section. From CiTTyCAT, the final concentrations in the air masses as they arrive on the grid have been used. Concentrations from the TOMCAT model output have been interpolated to the fine-scale RDF arrival grid. Figure 7.20 compares the distributions of these rates. They differ greatly between the two models, the CiTTyCAT output again showing more fine-scale structure associated with the different air mass types. The TOMCAT model shows strongest ozone production below  $\sim 500\text{hPa}$ , with a relatively uniform field of less than  $0.02\text{ ppbv hr}^{-1}$  over the region of the two isobaric flight legs. The CiTTyCAT model output shows a range of larger values throughout the domain, peaking at  $\sim 0.30\text{ ppbv hr}^{-1}$  in the E. Am air mass, and remaining of the order  $\sim 0.10\text{ ppbv hr}^{-1}$  in the less polluted air masses.

The mean  $\text{P}(\text{O}_3)$  rates from the  $\text{HO}_2 + \text{NO}$  reaction over the RDF section are  $0.132$  and  $0.033\text{ ppbv hr}^{-1}$  for the CiTTyCAT and TOMCAT model output respectively. This demonstrates what may be a serious limitation for large grid-scale global Eulerian CTMs, when attempting to model regions largely influenced by long-range transport of polluted air. The mix-down of fine-scale filaments of polluted air in the global model means that the mean fields of ozone precursors downwind of the pollution source produce an underestimate of the ozone production rates which occur within the individual fine-scale features. Comparisons of observations with CiTTyCAT model output in this Chapter have demonstrated that the fine-scale features modelled appear to exist in the real atmosphere. The underestimation of NO concentrations in these filaments will mean that the difference in  $\text{P}(\text{O}_3)$  between the Lagrangian and Eulerian models is likely to be an underestimate of the difference in  $\text{P}(\text{O}_3)$  between the Eulerian model and the real troposphere.

### 7.7.2 LRT ozone budget

In Section 5.3, ozone production rates in the UT from the reaction  $\text{MeOO} + \text{NO}$  were seen to be smaller than the rates based on the observed concentrations of MeOO and NO. This was attributed to lower than observed concentrations of both of these species in the UT model air masses. Figure 7.21 shows vertical profiles of NO, MeOO and the calculated net  $\text{P}(\text{O}_3)$  rate from observations, and the 10-day back trajectory

flight track calculations with and without mixing and with and without the shift in TOMCAT background and surface emissions.

The non-mixed model run gives a wide scatter of  $P(O_3)$  rates, reflecting the variety of air mass origins and the isolated nature of the air masses. In the E.Am air mass, between 470 and 460 hPa, some net production of more than  $0.5 \text{ ppbv hr}^{-1}$  is calculated, which exceeds values calculated using the 4-day back trajectories in Section 5.3. These are air masses uplifted from the US PBL, which contain NO concentrations of the order  $\sim 100\text{--}200 \text{ pptv}$  on arrival in Europe, buffered by relatively large concentrations of  $NO_y$ , as described in Section 7.6.1.

Figure 7.22 shows the dependence of the model calculated net  $P(O_3)$  rate on the model NO concentration. The wide scatter of  $P(O_3)$  in the non-mixed case is seen to be a function of the scatter in model NO concentrations. The model results demonstrate that at an NO concentration of  $\sim 20 \text{ pptv}$ , the net  $P(O_3)$  rate switches from negative to positive. This is the  $P(O_3)$  ‘compensation point’ for the model at this altitude range, and appears to be quite robust over the non-mixed and mixed cases. Mixing reduces the scatter in  $P(O_3)$ , and produces positive  $P(O_3)$  in the majority of air masses sampled, despite reducing the largest of the  $P(O_3)$  rates in the non-mixed case. The effect of mixing on the model NO concentration is critical in controlling this shift. For mixing with  $t_r=5$  days, the mean NO concentration becomes  $12.4 \text{ pptv}$ . With  $t_r=2.5$  days, the mean NO concentration becomes  $26.1 \text{ pptv}$ . The faster mixing timescale therefore shifts the mean NO concentration above the NO compensation point. More mixing also reduces the scatter in the model concentrations, so for the faster mixing timescale almost all the air masses are operating in a positive net  $P(O_3)$  regime.

Figure 7.22 shows that the faster mixing timescale also improves the correlation between observed and modelled NO. At all altitudes, MeOO concentrations are underestimated by the model. Mixing reduces these model concentrations further. This does not offset the increase to  $P(O_3)$  resulting from larger NO concentrations, suggesting that  $NO_x$  concentrations are dominant in controlling the  $P(O_3)$  rate.

Shifting the model emissions and TOMCAT background results in more positive  $P(O_3)$  rates for the S.E. US Coast air mass compared with the other model runs.

This appears to be through elevated NO concentrations relative to the non-shifted model runs. The effect on MeOO concentrations is small. At higher altitudes, shifting the emissions also increases NO concentrations to values between those from the runs using  $t_r=5$  and  $t_r=2.5$  days. This is due to shifting the TOMCAT US pollution eastwards, giving more time for trajectories to be influenced by ‘continental’ emissions in the PBL.

## 7.8 Conclusions

A detailed study has been made of air mass transport from the North American continent to Europe during the EXPORT campaign. It has been shown that pathways for this trans-Atlantic air mass transport, diagnosed from back trajectories are consistent with the positions of frontal features in meteorological analyses. This implicates a role for WCB ascent in mid latitude cyclones in the uplift of air off the eastern US coast.

Air mass structure resolved by RDF trajectory simulations in the European UT show a range of air mass types with origins in a number of environments over North America. Aircraft observations of chemical tracers in the European UT show features which tie in remarkably well with the simulated positions of these air masses.

The use of 10-day back trajectories in the CiTTyCAT model resolves the gradients between air masses, and picks up their chemical characteristics, although these are exaggerated due to lack of mixing. The introduction of a form of mixing into the CiTTyCAT simulation successfully reduces unrealistic, strong gradients and better reproduces the magnitudes of observed tracer structures.

The coarse resolution of TOMCAT means that the fine-scale features revealed by the observations and the RDF simulation are smeared out into a smooth field, with little variability in the European UT. This has been shown to have important implications for the calculated domain-average  $P(O_3)$  rates. For the reaction  $HO_2 + NO$ , the average  $P(O_3)$  rate from the TOMCAT field over the RDF domain is only 25% of that from the CiTTyCAT fields over the same domain. Observations suggest that this underestimation is likely to be more severe when compared with the real

atmosphere. This has important implications for global CTM calculations in regions dominated by fine-scale filamentary air masses imported from long-range.

UT  $P(O_3)$  has been shown to be very sensitive to mixing, where mixing rapidly adjusts the  $NO_y$  concentrations of the air mass. Mixing CiTTyCAT fields with TOMCAT narrows the range of CiTTyCAT final  $P(O_3)$  rates, due to increased homogeneity of the CiTTyCAT NO concentrations. This has been shown to reduce ozone production in air masses where large quantities of  $NO_y$  are exported from the US PBL, but to increase ozone production rates in less polluted air masses through replenishment of  $NO_x$  from the TOMCAT UT. Mixing on a timescale of 2.5 days is enough to shift the NO concentrations in almost all the air masses considered above the NO compensation point, which is  $\sim 26$  pptv in the CiTTyCAT model in the UT domain considered.

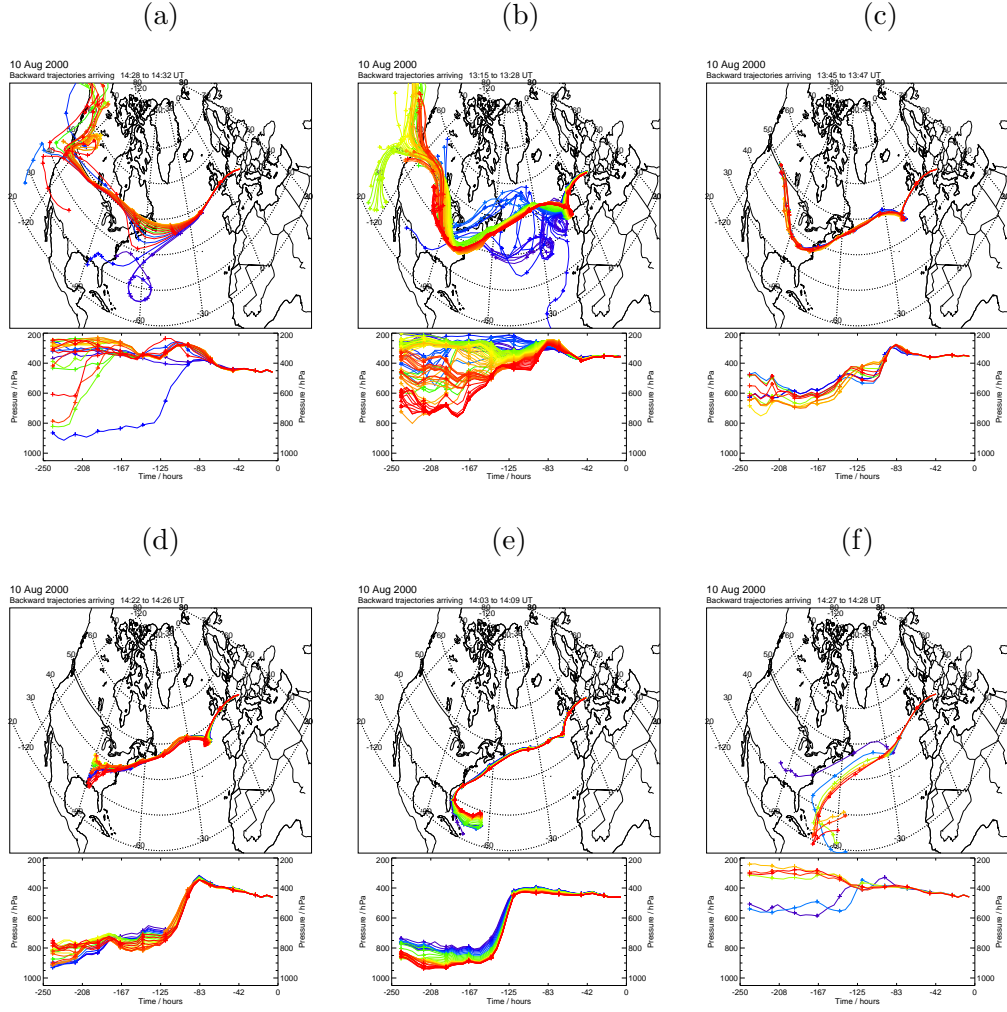


Figure 7.8: 7-day back trajectories arriving between (a) 14.47 and 14.53 UT, (b) 13.25 and 13.47 UT, (c) 13.75 and 13.78 UT, (d) 14.37 and 14.43 UT, (e) 14.05 and 14.15 UT and (f) 14.45 and 14.47 UT, on the flight track of EXPORT Flight A776 (Aug. 10 2000)



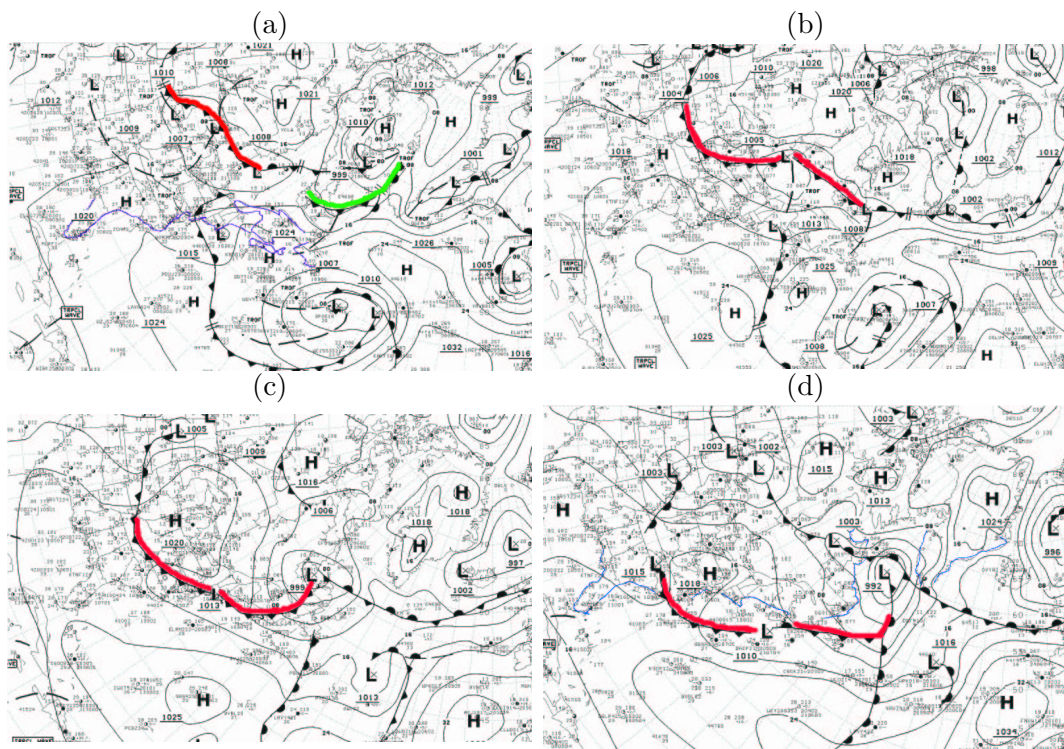


Figure 7.9: *Surface charts from NCEP analyses [http://www.wetterzentrale.de/topkarten/tkfaenwsar.htm] for August 2000. (a) Aug 2 2000, (b) Aug 3 2000, (c) Aug 5 2000, (d) Aug 6 2000. Coloured lines highlight frontal features discussed in the text.*

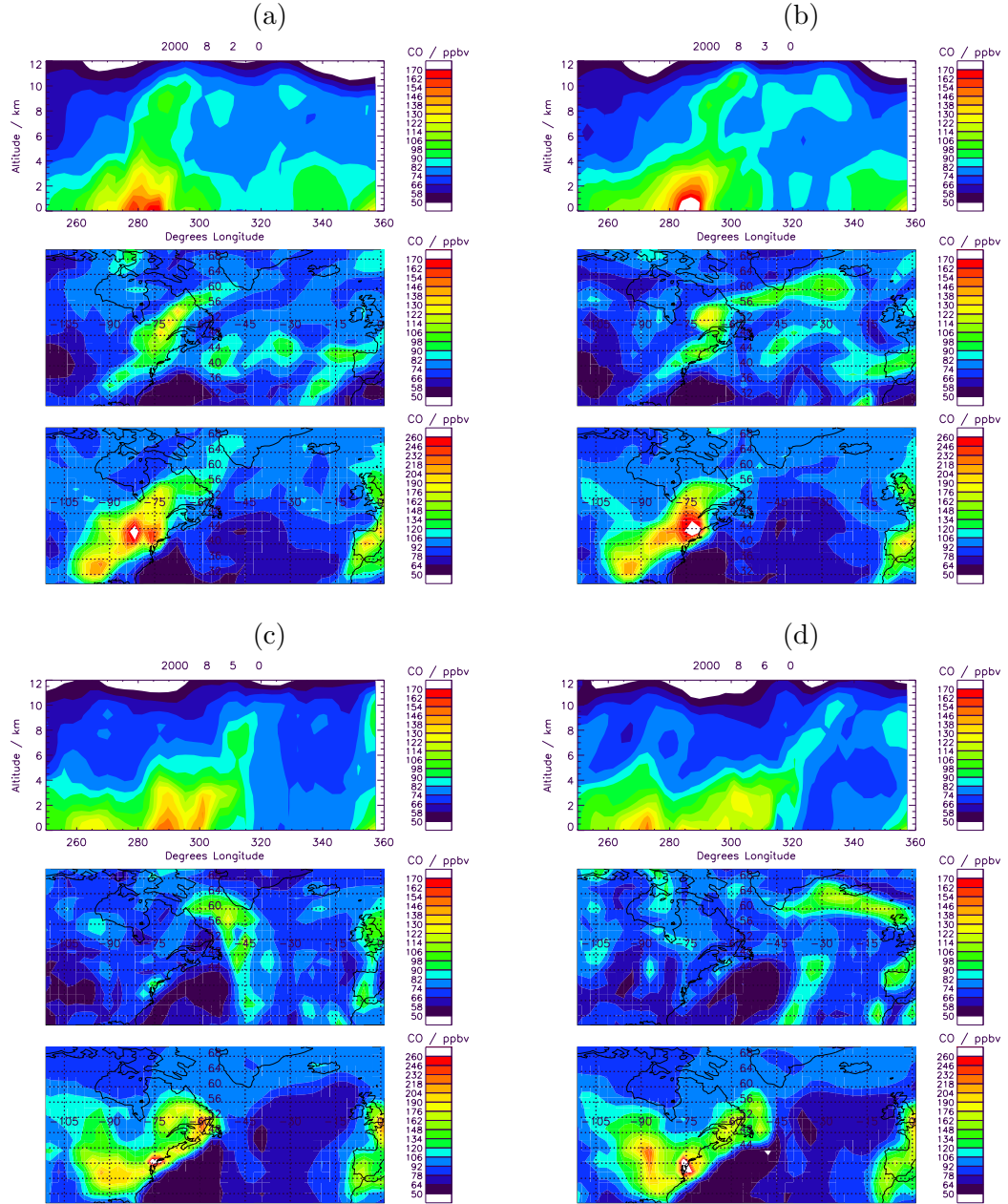


Figure 7.10: *TOMCAT CO (ppbv) in the North Atlantic region at midnight on (a) 02/08/00, (b) 03/08/00, (c) 05/08/00 and (d) 06/08/00. Upper panels show a zonal mean CO field taken between  $46^{\circ}$  and  $66^{\circ}$  latitude. Middle and lower panels show longitude-latitude plots at altitudes of  $\sim 7\text{km}$  and  $\sim 150\text{m}$ , respectively.*

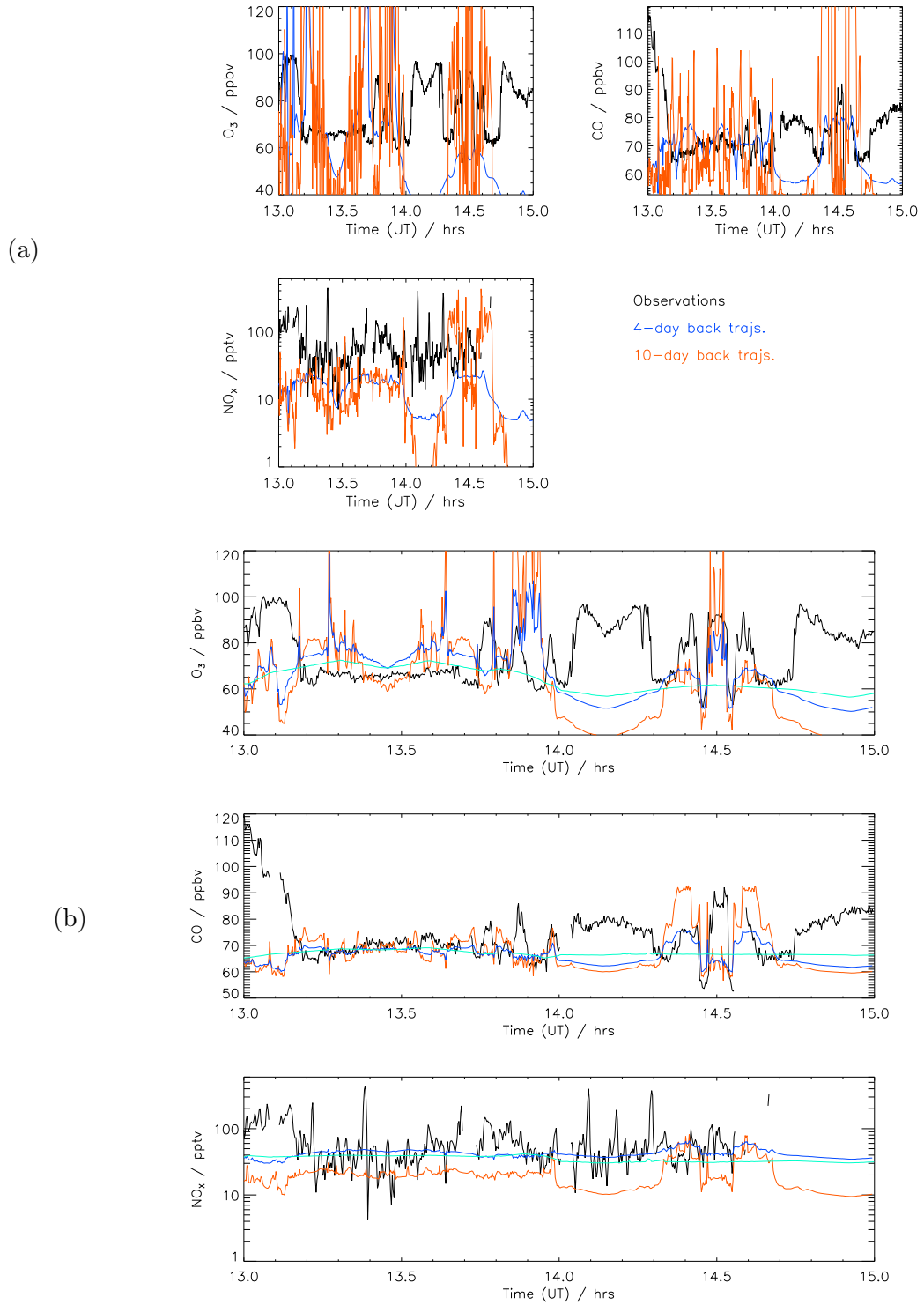


Figure 7.11: *End section of flight A776 (August 10th 2000). (a) Standard CiTTyCAT model output using 4-day (blue) and 10-day (red) back trajectories compared with observations. (b) CiTTyCAT model with mixing parameterisation using  $t_r=5$  days (red) and  $t_r=2.5$  days (blue) compared with TOMCAT model output (green) and observations (black).*

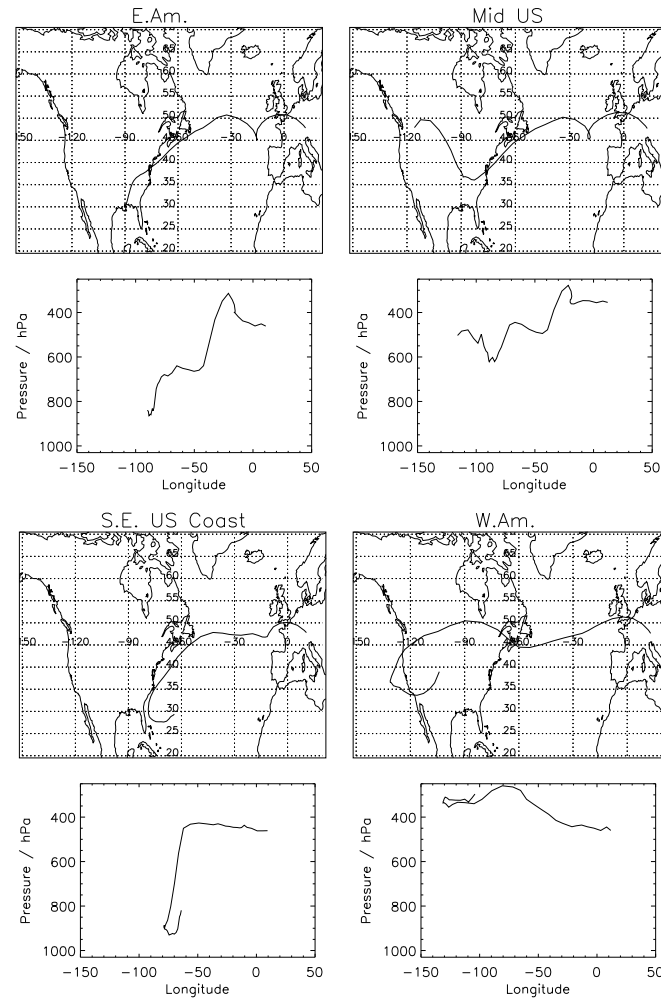


Figure 7.12: *Example 10-day back trajectories for different air mass types sampled during the high altitude legs of EXPORT flight A776 (10/08/00).*

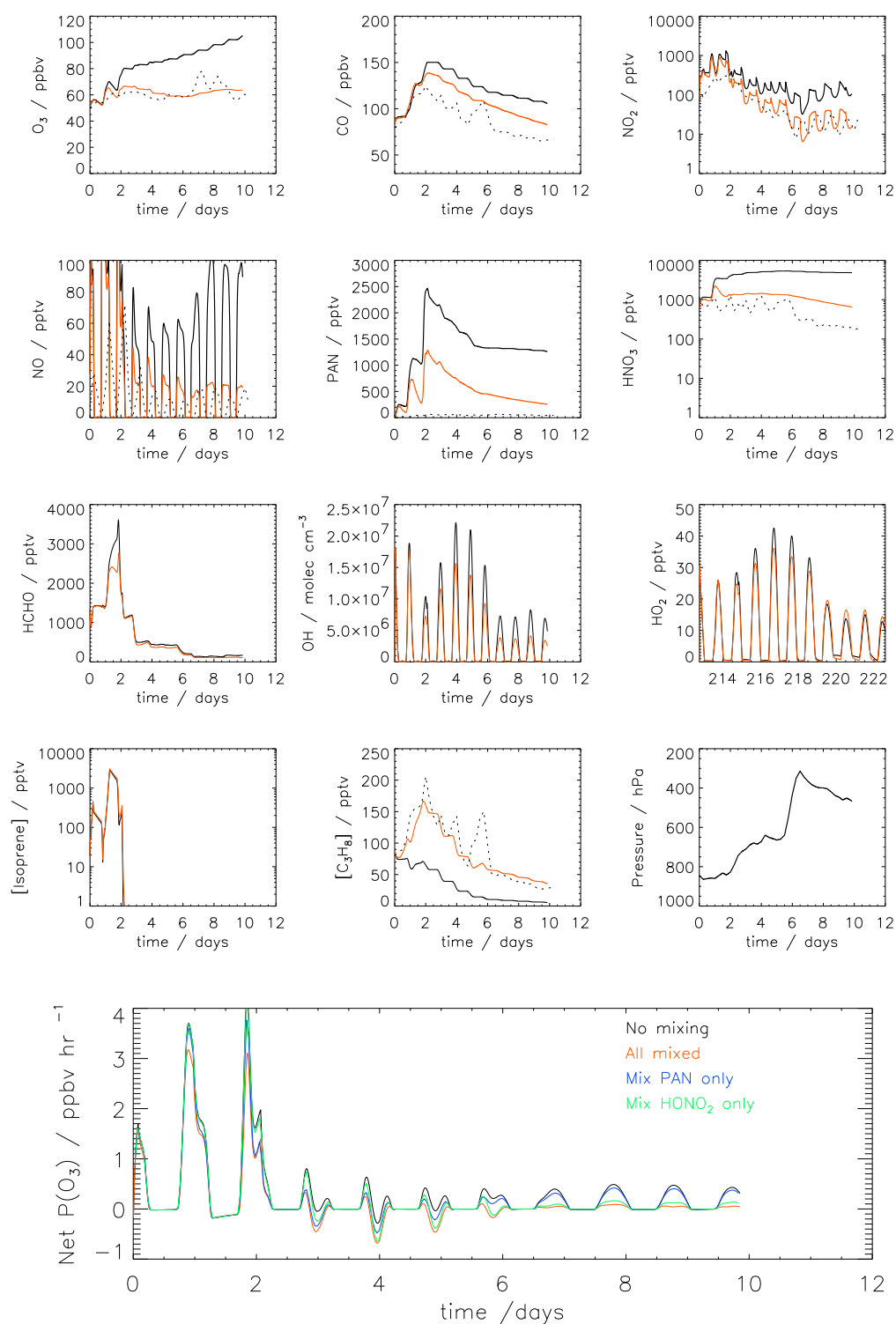


Figure 7.13: Along-trajectory output for air mass type E.Am as it is advected across the Atlantic. Small panels - Black: no mixing; Red: 5-day mixing timescale to TOMCAT; Dotted: TOMCAT background.

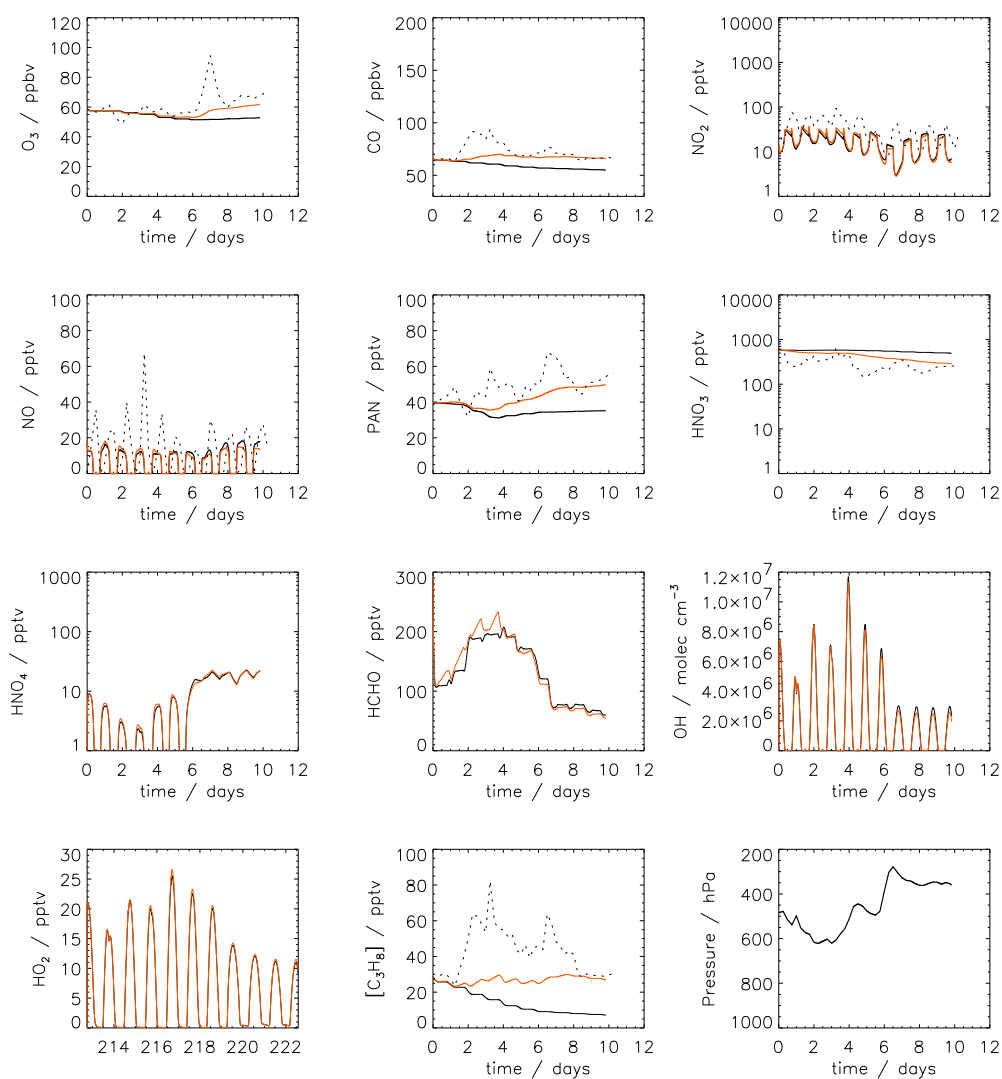


Figure 7.14: *Along-trajectory output for air mass type Mid US as it is advected across the Atlantic. Black: no mixing; Red: 5-day mixing timescale to TOMCAT; Dotted: TOMCAT background.*

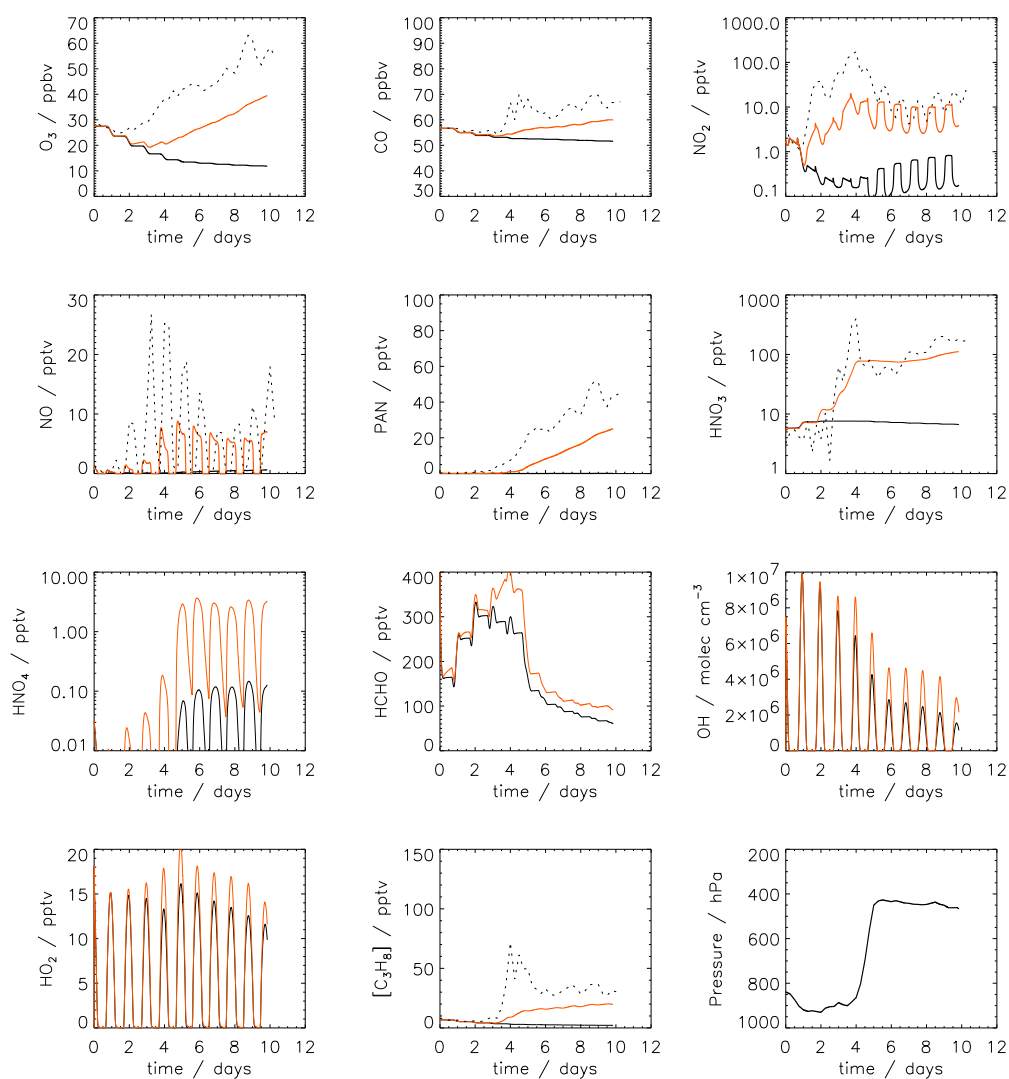


Figure 7.15: *Along-trajectory output for air mass type S.E. US Coast as it is advected across the Atlantic. Black: no mixing; Red: 5-day mixing timescale to TOMCAT; Dotted: TOMCAT background.*



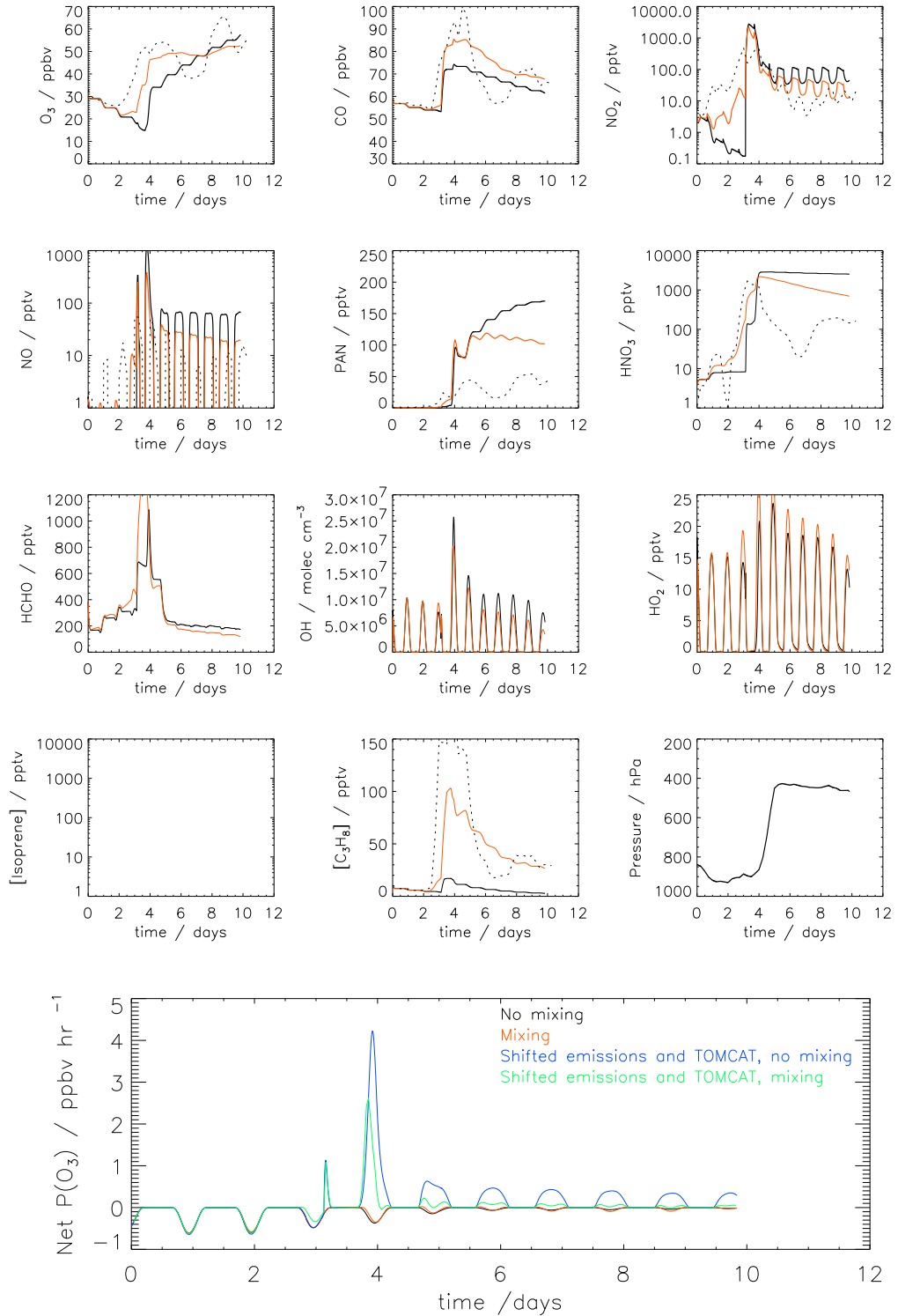


Figure 7.16: Along-trajectory output for air mass type S.E. US Coast as it is advected across the Atlantic using a 2.8125° eastwards shift in emissions and TOMCAT background. Small panels - Black: no mixing; Red: 5-day mixing timescale to TOMCAT; Dotted: TOMCAT background.



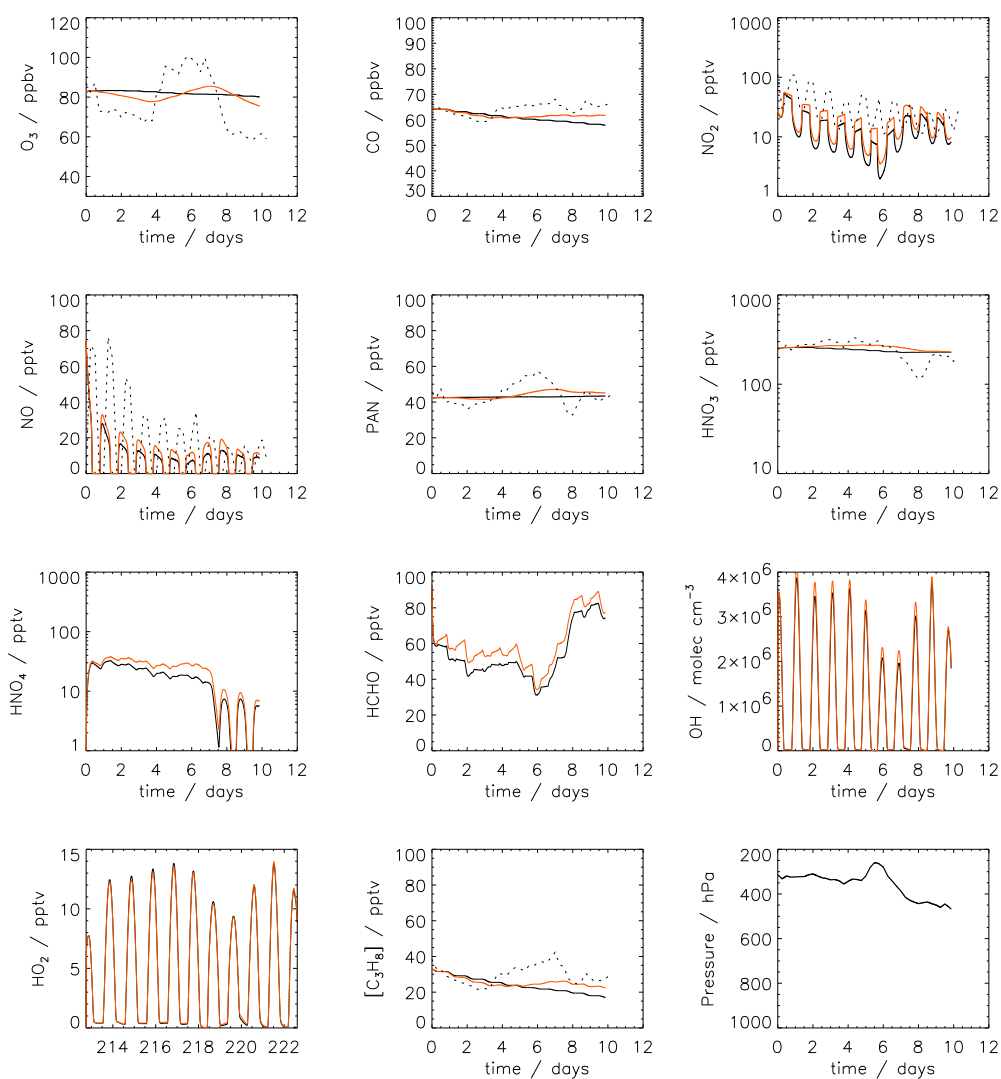


Figure 7.17: *Along-trajectory output for air mass type W.Am. as it is advected across the Atlantic. Black: no mixing; Red: 5-day mixing timescale to TOMCAT; Dotted: TOMCAT background.*

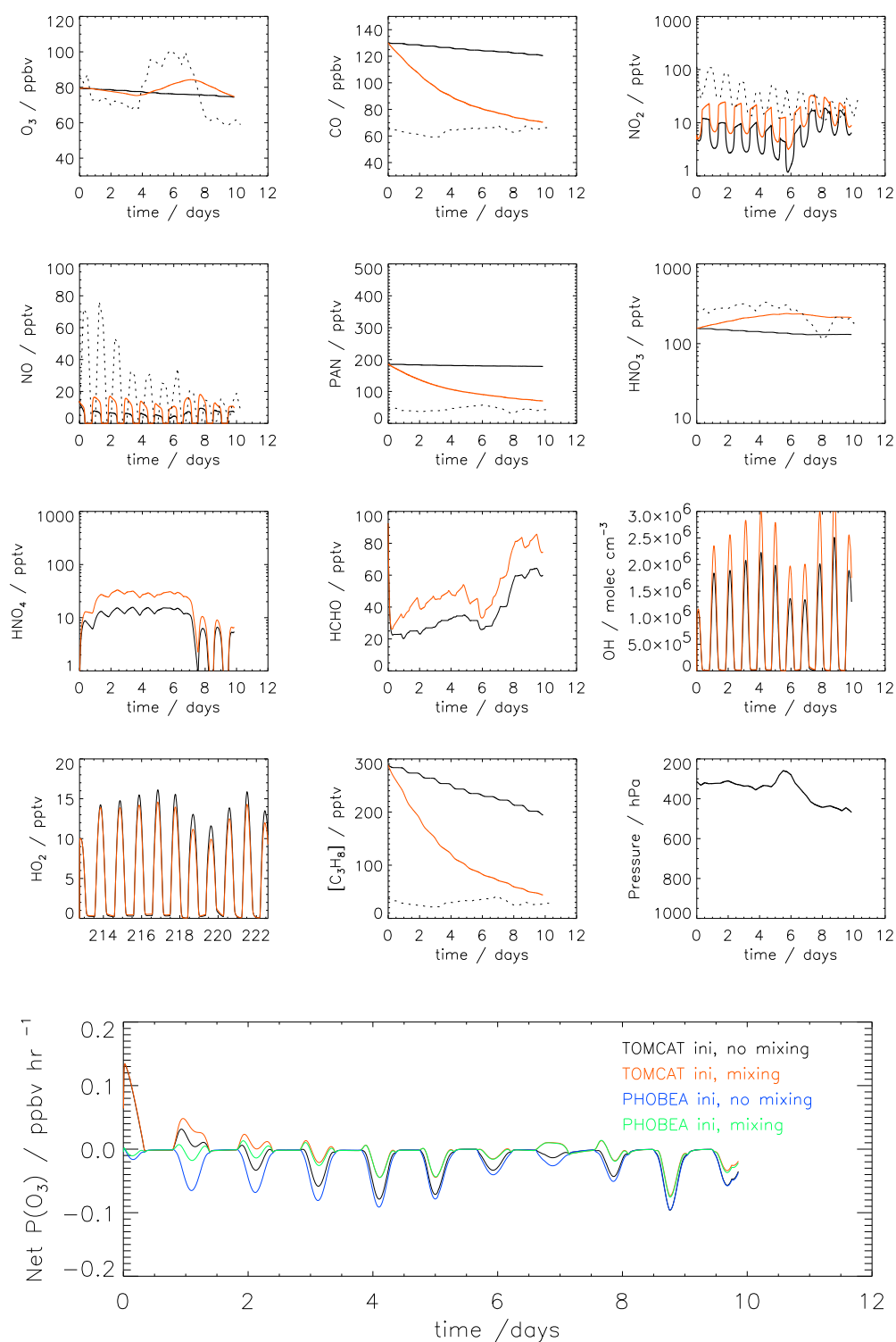


Figure 7.18: *Along-trajectory output for air mass type W.Am. as it is advected across the Atlantic, initialised from observations from the PHOBEA experiment. Small panels - Black: no mixing; Red: 5-day mixing timescale to TOMCAT; Dotted: TOMCAT background.*

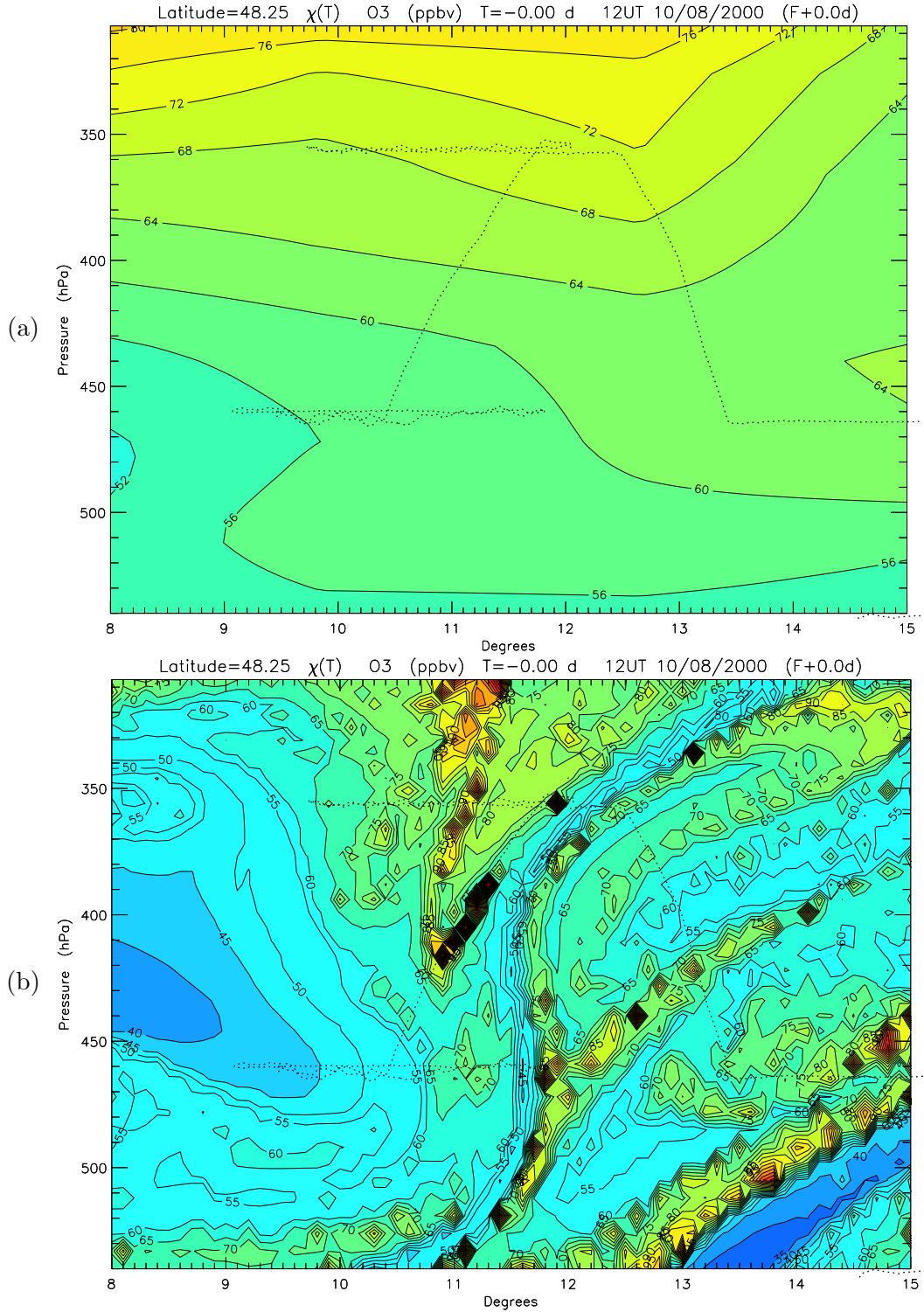


Figure 7.19: Model ozone concentrations (ppbv) on the RDF vertical section in the region of flight A776. (a) TOMCAT output interpolated to trajectory arrival positions. (b) ozone at trajectory arrival points from a full chemistry integration of CiTTYCAT along each RDF 10-day back trajectory using  $t_r=5$  days in the free troposphere and  $t_r=0.5$  in the model PBL.

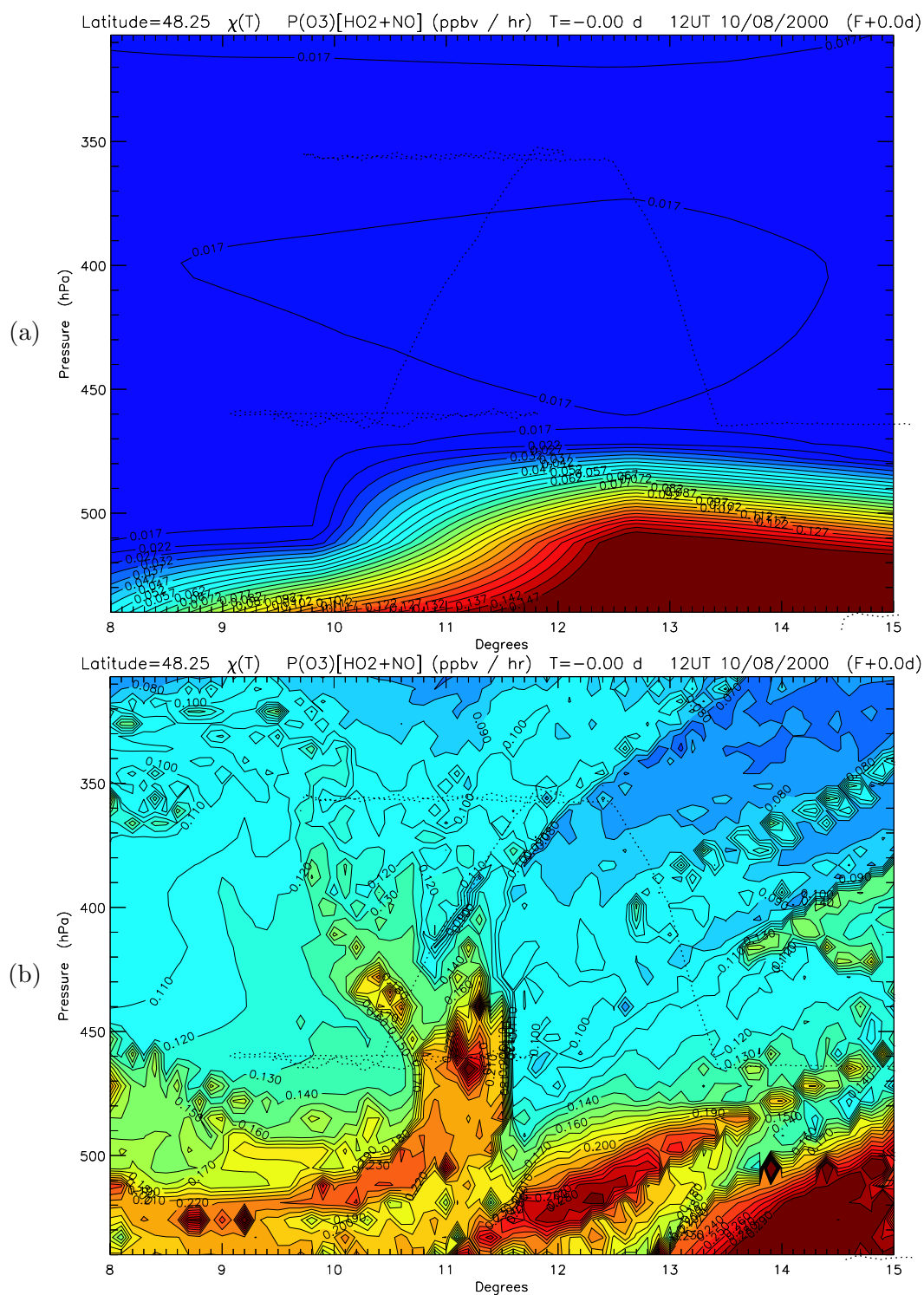


Figure 7.20: As Figure 7.19, but showing  $P(O_3)$  (ppbv hr<sup>-1</sup>) for the reaction  $HO_2 + NO$  from (a) TOMCAT model output and (b) CiTTyCAT model output.

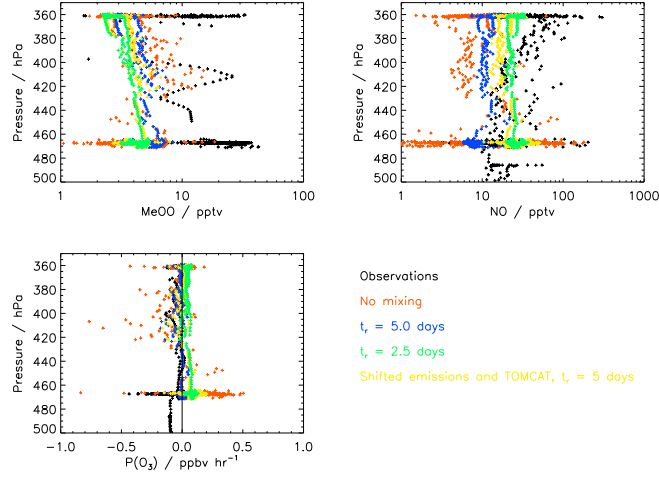


Figure 7.21: Vertical profiles of MeOO (pptv), NO (pptv) and net ozone production rate  $P(O_3)$  (ppbv  $hr^{-1}$ ) for the end of flight A776 (10/08/00). Model output is for 10-day back trajectories arriving on the flight track. Black pluses in the third panel show 4-day back trajectory net rates and not observed rates.

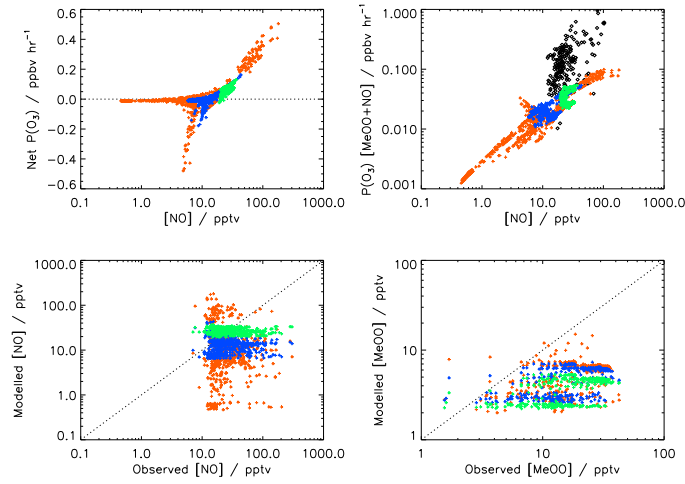


Figure 7.22: Correlations of modelled  $P(O_3)$  rates with model NO concentration (top) and correlations of observed and modelled MeOO and NO concentrations (bottom). Red: no mixing; Blue:  $t_r=5.0$  days; Green:  $t_r=2.5$  days. The correlation of  $P(O_3)$  rate calculated from observed MeOO and NO with observed NO is shown by diamonds in top right panel.

## 8. Photodissociation of acetone in the troposphere

### 8.1 Introduction

Recent laboratory measurements of the photodissociation of acetone have revealed a previously unseen temperature-dependence for the photolysis quantum yields. In this Chapter, these new data are presented and parameterised for use in atmospheric modelling. The impacts of the new quantum yield data on tropospheric chemistry are addressed.

In Section 8.2, sources, sinks and the chemistry of acetone in the troposphere are discussed. Section 8.3 presents the new quantum yield data, and its parameterisation. The implications of the new data are discussed in Section 8.4. The role of acetone in the  $\text{HO}_x$  budget of the UT over Central Europe is discussed in Section 8.5. Section 8.6 summarises the results of the chapter.

### 8.2 Atmospheric Chemistry of Acetone

Acetone ( $\text{CH}_3\text{COCH}_3$ ) is an oxygenated NMHC, which has been observed as being ubiquitous throughout the troposphere [Singh *et al.*, 1995]. Observations suggest abundances of  $\sim 400$ -600 pptv of acetone in the Northern Hemisphere background troposphere [Singh *et al.*, 2001], although free tropospheric concentrations of more than 2 ppbv have been observed [Poschl *et al.*, 2001].

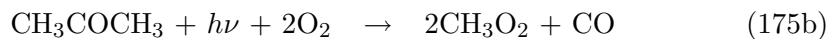
Acetone is emitted into the atmosphere directly. Sources include biomass burning

activity [Andrae and Merlet, 2001], vegetation, decaying plant matter and the oceans (see Jacob *et al.*, [2002]). Acetone is also a product of the oxidation of hydrocarbons such as propane and butanes, as well as biogenic hydrocarbons such as the monoterpenes. Sinks for acetone are photolysis, reaction with OH and deposition. Table 8.1 summarises the magnitudes of these source and sink terms from a comprehensive acetone budget study using a global CTM and observations [Jacob *et al.*, 2002]. Photolysis contributes approximately 48% of the global sink for acetone, with OH oxidation contributing  $\sim 28\%$ .

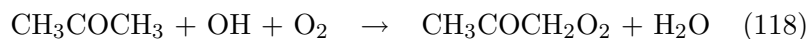
Table 8.1: Global atmospheric budget of acetone. Data from Jacob *et al.*, [2002].

Sources	Tg/yr	Sinks	Tg/yr
Anthropogenic emissions	$1.1 \pm 0.5$	OH oxidation	27
Biomass burning	$4.5 \pm 1.6$	Photolysis	46
Vegetation	$33 \pm 9$	Dry deposition	23
Plant decay	$2 \pm 5$		
Ocean	$27 \pm 6$		
Alkanes	$21 \pm 5$		
Monoterpenes	$6 \pm 3$		
Methylbutenol	$1.4 \pm 1.2$		

Photolysis of acetone occurs *via* two channels R(175a & b). In the troposphere, R(175a) dominates, since the wavelength threshold for R(175b) is 299nm. This results in the rate of R(175a) being orders of magnitude faster than R(175b), even in the UT.



Reaction of acetone with OH can be represented by:



Photolysis of acetone occurs in the wavelength range 290-320 nm in the troposphere, so the rates of R(175a) and R(175b) increase with altitude. In contrast R(118) is

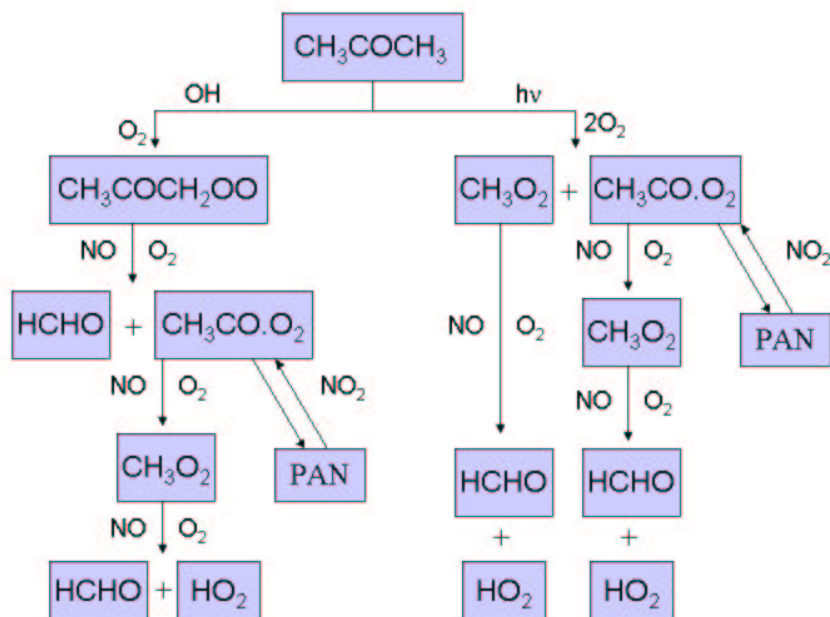


Figure 8.1: Schematic of photo-oxidation scheme for acetone used in the *CiTTyCAT* model.

more efficient in the moist lower troposphere. Assuming a yield of 0.6 extra  $\text{HO}_x$  molecules per  $\text{HCHO}$  molecule photolysed (see Chapter 1), photolysis of acetone can lead to a net production of 3.2  $\text{HO}_x$  molecules, while reaction with  $\text{OH}$  leads to a net production of up to 2  $\text{HO}_x$  molecules [Singh *et al.*, 1995], dependent on local  $\text{NO}_x$  (see Fig. 8.1). Consequently, the relative importance of the different acetone sinks as a function of altitude has implications for tropospheric chemistry.

Recent studies have indicated that acetone may play an important role in the chemistry of the UT. As well as a source of  $\text{HO}_x$ , acetone photolysis acts as a source of peroxy and alkoxy radicals which can change the partitioning of odd-nitrogen between  $\text{NO}_x$  and reservoir species such as  $\text{HONO}_2$  and peroxyacetylnitrate (PAN) [e.g. Singh *et al.*, 1995; Arnold *et al.*, 1997; McKeen *et al.*, 1997]. The photolysis of acetone and other oxygenated NMHCs has been shown to be an important contributor to the UT  $\text{HO}_x$  budget, and a way of resolving discrepancies between modelled and observed  $\text{HO}_x$  concentrations [e.g. Jaeglé *et al.*, 2000].

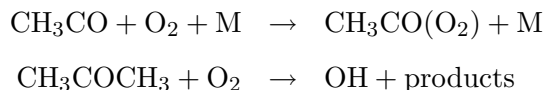


## 8.3 Temperature-dependent quantum yields for acetone photolysis

### 8.3.1 Determination of quantum yields

Recently, new laboratory measurements of the quantum yields for acetone photodissociation have been made by Mark Blitz, University of Leeds [*Blitz et al.*, 2004]. These observations showed a temperature-dependence as well as a pressure-dependence. Previous studies have shown the quantum yields to have a pressure-dependence, but to be constant with temperature [*Gierczak et al.*, 1998; *Emrich and Warneck*, 2000].

The new observations were made by monitoring the yield of  $\text{CH}_3\text{CO}$ , by using the OH product of one channel of its reaction with  $\text{O}_2$  as a marker [*Blitz et al.*, 2002]. Acetone was photolysed using a range of laser radiation wavelengths between 279 and 327.5 nm, and over a range of temperatures. Laser induced fluorescence (LIF) was used to probe the OH produced.



Quantum yields were calculated by comparing the measurements of OH yield at the wavelength of interest to the OH yield at 248nm. At this reference wavelength, all excited acetone molecules are believed to dissociate, with no quenching of the excited state.

For wavelengths less than 302nm, the dependence of the acetyl quantum yield ( $\phi_{\text{CH}_3\text{CO}}$ ) on density ( $[\text{M}]$ ), can be represented by a Stern-Volmer relationship (8.1).

$$\frac{\phi_{\text{CH}_3\text{CO},248\text{nm}}}{\phi_{\text{CH}_3\text{CO},\lambda}} = \left( \frac{\phi_{\text{CH}_3\text{CO},\lambda}}{\phi_{\text{CH}_3\text{CO},248\text{nm}}} \right)_{[\text{M}]=0} (1 + A_1[\text{M}]) \quad (8.1)$$

$A_1$  represents the ratio of rate coefficients for dissociation and quenching of the excited singlet state of acetone. At wavelengths greater than 302nm, the acetone triplet state is excited, and the Stern-Volmer relationship is modified (8.2) to take account of dissociation and quenching of the triplet state as well as the singlet state.

$$\frac{\phi_{CH_3CO,248nm}}{\phi_{CH_3CO,\lambda}} = \left( \frac{\phi_{CH_3CO,\lambda}}{\phi_{CH_3CO,248nm}} \right)_{[M]=0} (1 + A_2[M] + A_3) \frac{1 + A_4[M]}{1 + A_4[M] + A_3} \quad (8.2)$$

When  $[M]=0$ , the total acetone quantum yield follows the relationship:

$$(\phi_{total})_{[M]=0} = (\phi_{CH_3CO,\lambda})_{[M]=0} + \phi_{CO,\lambda} = 1 \quad (8.3)$$

Plots of  $\frac{\phi_{CH_3CO,248nm}}{\phi_{CH_3CO,\lambda}}$  vs  $[M]$  from Equations 8.1 and 8.2, will have an intercept  $\left( \frac{\phi_{CH_3CO,\lambda}}{\phi_{CH_3CO,248nm}} \right)_{[M]=0}$ . Since all excited acetone dissociates at a wavelength of 248nm,  $\phi_{CH_3CO,248nm} = (\phi_{CH_3CO,\lambda})_{[M]=0}$ . The CO quantum yield, which is observed to be independent of pressure, can therefore be derived from the intercept of such a plot and the relationship given by (8.3).

Stern-Volmer-type plots from observations made at the four temperatures 218, 248, 273 and 295K over the range of wavelengths were used to infer the acetyl and CO quantum yields. Figure 8.2 shows the quantum yield observations over the wavelength range 279 - 327.5 nm at the four experimental temperatures of 218, 248, 273 and 295 K. Both the acetyl and CO quantum yields show a temperature dependence. The CO yield is largest at high temperatures, where at the lowest wavelengths it contributes ~40% of the total. At the lowest temperatures, representative of the upper troposphere, the CO yield is orders of magnitude less than the acetyl yield.

### 8.3.2 Parameterisation of quantum yields as a function of wavelength, pressure and temperature

The quantum yield observations were parameterised in collaboration with Mark Blitz, University of Leeds. There was not an adequate expression to describe the

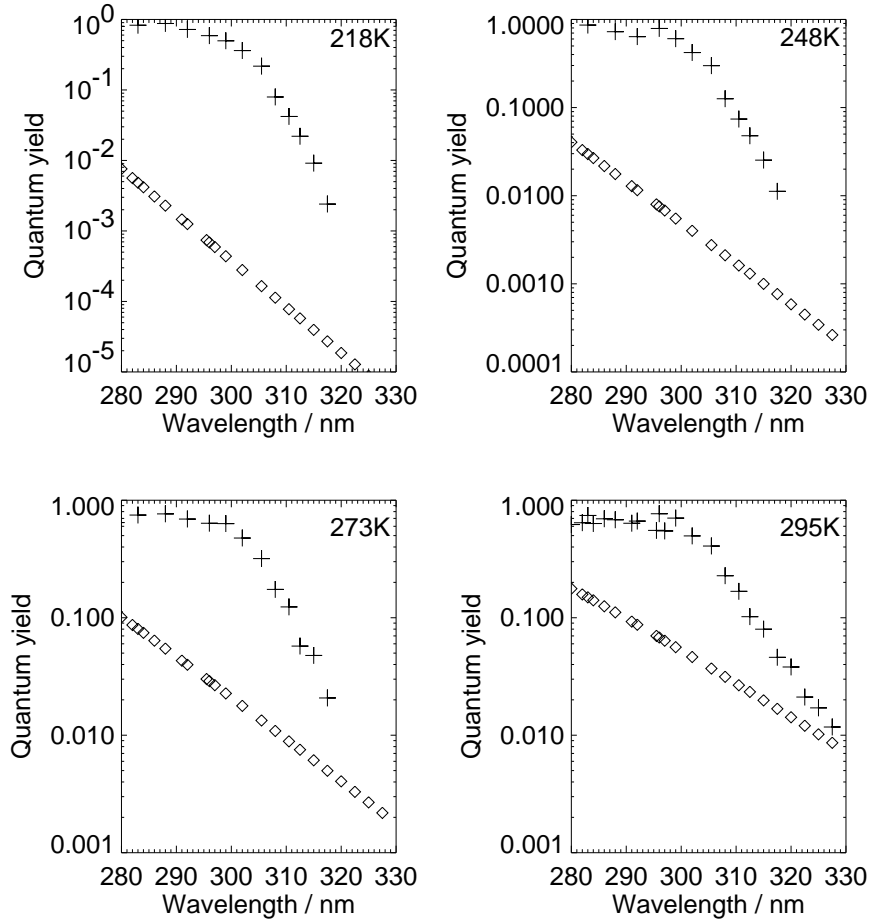


Figure 8.2: Observed quantum yields for acetone photolysis as a function of wavelength at the four experimental temperatures described by Blitz et al., [2004], at a density of  $5 \times 10^{18}$  molecules  $\text{cm}^{-3}$ . Crosses denote the quantum yields for the acetyl channel only (R175a) and diamonds denote the quantum yields for the CO channel only (R175b).

quantum yields across the entire wavelength range 279 - 327.5 nm, so two different expressions were used above and below 302nm, either side of the onset of excitation of the triplet state.

Between wavelengths of 279 and 302nm, the standard Stern-Volmer expression (8.6) was fitted globally to the observations over the four temperatures 218, 248, 273 and 295 K. Temperature and wavelength-dependent expressions for the ‘A’ coefficients

were optimised to maximise the ‘goodness of fit’, using the errors on each data point to weight the fit. Between 302 and 327.5nm, the modified Stern-Volmer expression (8.2) was fitted globally to all the observations, to optimise temperature and wavelength-dependent expressions for the ‘A’ coefficients.

The CO component of the quantum yield, obtained from intercepts of the Stern-Volmer plots, is independent of pressure, and can be represented across the entire wavelength range by:

$$\phi_{CO}(\lambda, T) = \frac{1}{1 + A_0} \quad (8.4)$$

where

$$\begin{aligned} A_0 &= \frac{a_0}{1 - a_0} \exp[b_0(\lambda - 248)] \\ a_0 &= (0.350 \pm 0.003)(T/295)^{(-1.28 \pm 0.03)} \\ b_0 &= (0.068 \pm 0.002)(T/295)^{(-2.65 \pm 0.20)} \end{aligned}$$

For  $\lambda = 279\text{-}302\text{nm}$ ,

$$\phi_{CH_3CO}(\lambda, T, [M]) = \frac{1 - \phi_{CO}(\lambda, T)}{1 + A_1[M]} \quad (8.5)$$

where

$$\begin{aligned} A_1 &= a_1 \exp[-b_1((10^7/\lambda) - 33113)] \\ a_1 &= (1.60 \pm 0.032) \times 10^{-19} (T/295)^{(-2.38 \pm 0.08)} \\ b_1 &= (0.55 \pm 0.02) \times 10^{-3} (T/295)^{(-3.19 \pm 0.13)} \end{aligned}$$

For  $\lambda = 302\text{-}327.5\text{nm}$ ,

$$\phi_{CH_3CO}(\lambda, T, [M]) = \frac{(1 + A_4[M] + A_3)}{(1 + a_2[M] + a_3)(1 + A_4[M])} (1 - \phi_{CO}(\lambda, T)) \quad (8.6)$$

where

$$A_2 = a_2 \exp[-b_1((10^7/\lambda) - 30488)]$$

$$a_2 = (1.62 \pm 0.06) \times 10^{-17} (T/295)^{(-10.03 \pm 0.20)}$$

$$b_2 = (1.79 \pm 0.02) \times 10^{-3} (T/295)^{(-1.364 \pm 0.036)}$$

$$A_3 = a_3 \exp \left[ -b_3 \left( \frac{10^7}{\lambda} - c_3 \right)^2 \right]$$

$$a_3 = (26.29 \pm 0.88) (T/295)^{(-6.59 \pm 0.23)}$$

$$b_3 = (5.72 \pm 0.20) \times 10^{-7} (T/295)^{(-2.93 \pm 0.09)}$$

$$c_3 = (30006 \pm 41) (T/295)^{(-0.064 \pm 0.0004)}$$

$$A_4 = a_4 \exp[-b_4((10^7/\lambda) - 30488)]$$

$$a_4 = (1.67 \pm 0.14) \times 10^{-15} (T/295)^{(-7.25 \pm 0.54)}$$

$$b_4 = (2.08 \pm 0.07) \times 10^{-3} (T/295)^{(-1.16 \pm 0.15)}$$

Figure 8.3 shows the observation derived data points for the total quantum yield of acetone, with the parameterised expressions for the total quantum yield and the CO channel yield. The parameterised expressions adequately describe the experimental data over the experimental wavelength and temperature range. Plots of the quantum yields at low temperature as a ratio to the quantum yields at the highest temperature reveal the strong temperature dependence, especially at longer wavelengths.

## 8.4 Atmospheric implications of temperature-dependence

### 8.4.1 Altitude dependence of photolysis rates

The temperature-dependence of the new quantum yield data is likely to have consequences for the loss rate of acetone over the depth of the troposphere, due to the

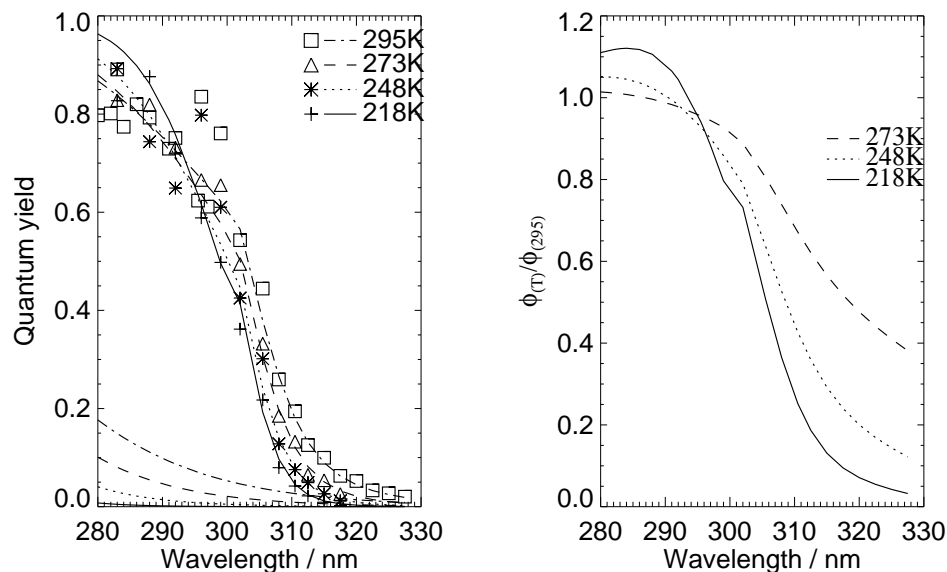


Figure 8.3: *Left panel: Parameterised expressions for the total acetone quantum yields (upper lines) and CO channel yields (lower lines) compared with observed total quantum yields (symbols). Right panel: ratio of parameterised total yields at the three lower temperatures to those at 295K.*

decrease in temperature between the surface and the tropopause. This has been investigated using the CiTTyCAT model to calculate the photolysis (J) loss rates through the depth of the troposphere over 13 levels between 1000 and 150 hPa, using the new data and using the currently recommended quantum yield data from Warneck, [2001]. Temperature was taken from the US Standard Atmosphere (1976), and  $\text{H}_2\text{O}$  was taken as the saturated vapour pressure at each model level. Ozone and methane concentrations were taken from the Cambridge 2D model climatology [Law and Pyle, 1993a,b].

Figure 8.4 shows vertical profiles of recommended and new acetone J-rates and  $\text{OH} + \text{acetone}$  loss rates for three different locations and times of year. These represent mid-winter and mid-summer at mid latitudes, and maximum insolation at the equator. The new J-rates are substantially slower in the UT compared with those derived from the recommended quantum yields. The maximum reduction is between a factor of  $\sim 3.5$  and  $\sim 10$  at mid latitudes, at a pressure of between 200

and 300 hPa. At the equator, the maximum reduction is a factor of more than 2.5 at  $\sim 200$  hPa. These reductions to the acetone J-rate are likely to have important implications for the chemistry of acetone in the UT, and our understanding of its atmospheric budget.

### 8.4.2 Chemical implications

The impact of the new yields was investigated in a series of three chemical model experiments (summarised in Table 8.4.2). These cover situations where the chemistry is constrained by observations of acetone (and other species) and situations where the model acetone is free to evolve. For these experiments, the CiTTyCAT model is used as a box model at a fixed location without transport. The constrained model experiments were run over a perpetual 24-hour period until a repeatable diurnal cycle was reached.

New yields (NQY) are included using the parameterisation given in Section 8.3.2, while the recommended yields (RQY) are taken from *Warneck* [2001], as recommended by IUPAC 2002 [*Atkinson et al.*, 2002]. Acetone absorption cross-sections are taken directly from *Gierczak et al.* [1998]. The rate constant for the reaction of acetone with OH is taken from a 2003 update to the IUPAC 2002 recommendation [<http://www.iupac-kinetic.ch.cam.ac.uk/>], which has  $k = 8.8 \times 10^{-12} \exp(-1320/T) + 1.7 \times 10^{-14} \exp(420/T)$ .

#### Experiment 1: Constrained model.

To investigate the impact of NQY on a chemical system typical of the UT, the model was constrained using observations of UT concentrations for mid-latitude (Exp. 1a) and tropical (Exp. 1b) conditions. Species were constrained to their observed concentrations (Table 8.2) every 5-minute model timestep.  $\text{NO}_y$  species were constrained every 24hrs to allow the model to diagnose chemical diurnal cycles over the course of a day.  $\text{H}_2\text{O}_2$ ,  $\text{HCHO}$ ,  $\text{HO}_2$  and  $\text{OH}$  were allowed to run freely in the simulation.

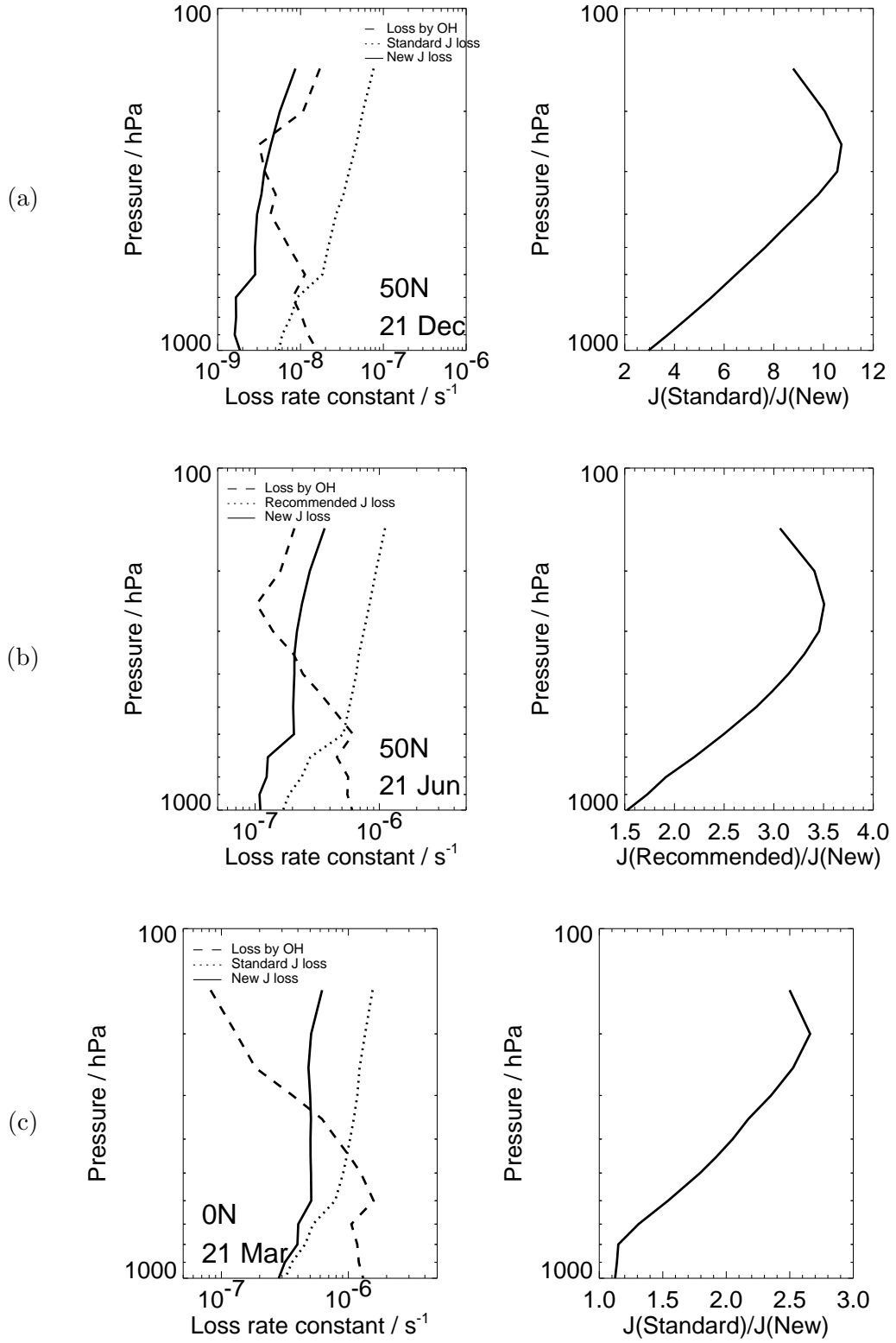


Figure 8.4: Vertical profiles of model-derived  $J$ -rates for new (solid line) and recommended (dotted line) acetone quantum yields, and OH acetone loss rates. (a) Mid-winter mid latitudes, (b) mid-summer mid latitudes and (c) maximum insolation at the equator.



Table 8.2: Prescribed chemistry and conditions for UT model experiments.

	Exp 1a	Exp 1b	Exp 2	Exp 3
Description	Constrained background		Initialised convective	Convective mixing
Latitude	50°N	0°N	50°N	0°N
Pressure/hPa	287	230	262	230
Temperature/K	222	225	220	226
H <sub>2</sub> O/kgkg <sup>-1</sup>	7.5×10 <sup>-5</sup>	9.4×10 <sup>-6</sup>	8.0×10 <sup>-5</sup>	6.25×10 <sup>-5</sup>
Acetone/pptv	510	250	560	600
NO/pptv	56	58	443	10-6000
NO <sub>2</sub> /pptv	30	-	163	-
O <sub>3</sub> /ppbv	55	36	55	20
CO/ppbv	90	60	92	60
CH <sub>4</sub> /ppmv	1.761	1.720	1.761	1.700
PAN/pptv	64	-	55	-
HONO <sub>2</sub> /pptv	120	-	130	-
HO <sub>2</sub> NO <sub>2</sub> /pptv	60	-	63	-
C <sub>2</sub> H <sub>6</sub> /pptv	670	-	720	-
C <sub>3</sub> H <sub>8</sub> /pptv	79	-	110	-
C <sub>2</sub> H <sub>2</sub> /pptv	91	-	110	-
C <sub>6</sub> H <sub>6</sub> /pptv	15	-	14	-
H <sub>2</sub> O <sub>2</sub> /pptv	-	-	-	50
CH <sub>3</sub> OOH/pptv	-	-	-	50

Experiment 1a uses mid-latitude observations from the background UT made during the SONEX experiment [Jaeglé *et al.*, 2000]. The box was situated at  $\sim 10$ km, at 50°N, on October 28 to coincide with the approximate location and median time of the observations. Table 8.3 shows the results of this experiment. Steady-state HO<sub>x</sub> concentrations calculated by the constrained model are shown as diurnal mean values. HO<sub>x</sub> increases due to acetone are significantly reduced by the slower J rate given by NQY. OH and HO<sub>2</sub> increases of approximately 35% and 45% with the introduction of acetone, are reduced to increases of about 9% and 11% respectively. The steady state lifetime of acetone in the mid-latitude background UT is significantly increased from  $\sim 75$  days to  $\sim 255$  days. The reduction in calculated HO<sub>x</sub>

Table 8.3: Steady-state day averages from box model constrained by mid-latitude UT observations (Experiment 1a).

	No acetone	RQY	NQY
OH/pptv	0.019	0.026	0.021
HO <sub>2</sub> /pptv	0.48	0.70	0.54
Acetone loss J/s <sup>-1</sup>		1.23×10 <sup>-7</sup>	1.94×10 <sup>-8</sup>
Acetone loss $k_2[\text{OH}]/\text{s}^{-1}$	1.90×10 <sup>-8</sup>	3.27×10 <sup>-8</sup>	2.62×10 <sup>-8</sup>
Propane loss $k[\text{OH}]/\text{s}^{-1}$	1.01×10 <sup>-7</sup>	1.36×10 <sup>-7</sup>	1.09×10 <sup>-7</sup>
Acetone lifetime		74 days	254 days

Table 8.4: Steady-state day averages from box model constrained by tropical UT observations (Experiment 1b).

	No acetone	RQY	NQY
OH/pptv	0.069	0.097	0.084
HO <sub>2</sub> /pptv	1.46	2.38	1.89
Acetone loss J/s <sup>-1</sup>		1.22×10 <sup>-6</sup>	4.81×10 <sup>-7</sup>
Acetone loss $k_2[\text{OH}]/\text{s}^{-1}$	6.84×10 <sup>-8</sup>	9.70×10 <sup>-8</sup>	8.34×10 <sup>-8</sup>
Propane loss $k[\text{OH}]/\text{s}^{-1}$	2.97×10 <sup>-7</sup>	4.22×10 <sup>-7</sup>	3.63×10 <sup>-7</sup>
Acetone lifetime		9 days	21 days

concentrations suggests that further contributions from HO<sub>x</sub> sources in addition to acetone are required for basic NMHC-NO<sub>x</sub>-HO<sub>x</sub> chemistry schemes to reproduce the magnitudes of tropospheric HO<sub>x</sub> abundances.

For tropical UT conditions, Experiment 1b takes values from a compilation of observations in the North and South tropical Pacific [Crawford *et al.*, 1999]. The model was run at an altitude of ~11km at the Equator. Results are presented in Table 8.4. Acetone induced OH and HO<sub>2</sub> increases of approximately 40% and 63%, are reduced to increases of about 22% and 29% respectively, with the steady-state lifetime of acetone increasing from ~9 to ~21 days. The impact of acetone on HO<sub>x</sub> is greater than for the mid-latitude SONEX conditions, due to the dry tropical UT environment where the O(<sup>1</sup>D) + H<sub>2</sub>O primary source is smaller. The NQY J rate therefore plays a significant role in reducing steady-state HO<sub>x</sub> concentrations under these conditions, despite a smaller reduction to the J rate itself than seen at

mid-latitudes.

It should be noted that the calculated changes to lifetimes and chemistry are dependent on the specific conditions and locations chosen. Nevertheless, the two contrasting latitudes used illustrate the potential impact of the NQY on tropospheric chemistry.

### **Experiment 2: Free-running model.**

To allow the chemical model to respond to an increase in acetone above background in the UT, the model was allowed to run freely after initialisation with observations of median UT concentrations from air masses with influence from continental convection intercepted during the SONEX experiment (see Table 8.2). This simulates the evolution of a freshly polluted isolated air parcel having been injected to the UT in a convective updraught. The box altitude was set with the median pressure of convectively influenced observations. Chemistry was allowed to run freely for 30 perpetual days, simulating an assumed isolation of the air mass in the UT over that period.

Results from this experiment are shown in Figure 8.5. The slower production of peroxy radicals given by the reduced NQY acetone loss rate results in a reduction in the enhancement to ozone production seen when introducing acetone to the system. The reduced acetone loss also produces a slower conversion of  $\text{NO}_x$  to PAN and  $\text{HONO}_2$ , through reductions in peroxyacetyl and  $\text{HO}_x$  formation. The result is that  $\text{NO}_x$  concentrations are maintained for longer in the fresh convective plume. As a consequence, the ozone production efficiency per molecule of acetone lost increases with the NQY. Figure 8.5 demonstrates that integrated ozone production rates for NQY and RQY are  $\sim 0.17$  ppbv and  $\sim 0.06$  ppbv ozone per pptv acetone loss respectively.

Note that this result is affected by the lack of transport in the model. Conversion of  $\text{NO}_x$  to PAN and preservation of the PAN that is formed, are facilitated by the air mass remaining at cold temperatures in the UT. However, the result highlights a shift in the speciation of  $\text{NO}_y$  and ozone production in the UT resulting from the

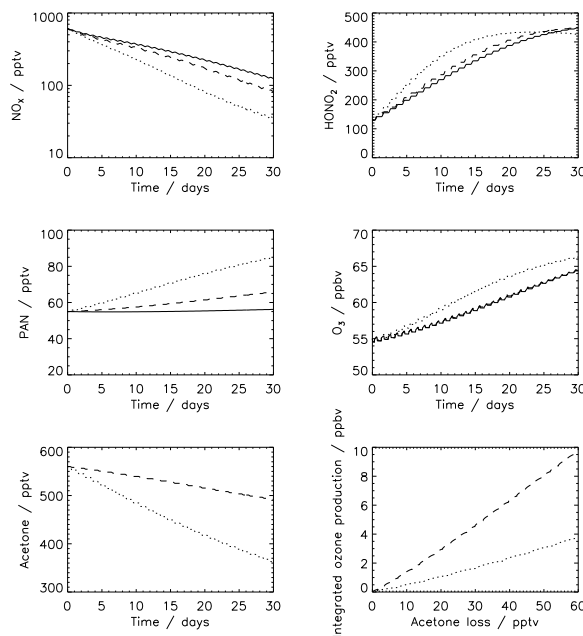


Figure 8.5: Comparison of chemical responses to the injection of a convective plume of fresh acetone into the UT for the recommended acetone quantum yields (RQY, dotted) and the new acetone quantum yields (NQY, dashed). A base run without acetone is shown by the solid curves.

NQY.

### Experiment 3: Convective outflow into UT

This model experiment is designed to give a more realistic treatment of the impact of a convective influx of freshly polluted air to the UT. We have repeated the box model experiments of *Folkins and Chatfield* [2000], using a model set up without acetone, with acetone and NQY, and with acetone and RQY. The experiment simulates the chemical response of the UT to a steady-state replacement of air in the UT by fresh convective outflow, with varying concentrations of  $\text{NO}_x$ . Table 8.2 shows the concentrations used for the incoming convective air. NO was varied between 0.01 and 6.0 ppbv. Following *Folkins and Chatfield* [2000], the box was situated

at a temperature of 226K at 230hPa in the tropical UT, and air was continuously replaced in the box by fresh ‘convective influx’ on a 15-day timescale. The model was run for each concentration of incoming  $\text{NO}_x$  and for each acetone photolysis set-up for 110 perpetual days to allow a steady state to be reached between chemistry and mixing. Note that the updated acetone + OH rate constant and the most recently recommended acetone quantum yields RQY are different from those used in the original study of *Folkins and Chatfield* [2000].

The effect of varying  $\text{NO}_x$  in the incoming convective air is shown in Figure 8.6. The fractional increase in  $\text{HO}_x$  with the introduction of acetone is seen to be greatest at high  $\text{NO}_x$ , where the photo-oxidation route of acetone is most efficiently taken to completion and has been confirmed by others [*Singh et al.*, 1995; *Folkins and Chatfield*, 2000]. However, the NQY reduce this maximum increase to approximately +55% OH and +95%  $\text{HO}_2$  from approximately +85% OH and +170%  $\text{HO}_2$ . Above 100 pptv of  $\text{NO}_x$ , ozone and  $\text{HO}_x$  are increased by the addition of acetone and PAN formation is maximised. These increases are suppressed by NQY, with a reduction in maximum PAN production of approximately 30%. The maximum increase to ozone production with the introduction of acetone occurs at around 1ppbv  $\text{NO}_x$ , where radical conversion of NO to  $\text{NO}_2$  is most efficient. At high  $\text{NO}_x$ , where  $\text{HO}_x$  production from acetone is maximised, increases in ozone production decrease due to enhanced formation of  $\text{HONO}_2$ . The NQY reduce the maximum enhancement in ozone from approximately +35% to +20%, while increases in  $\text{HONO}_2$  are reduced from about +30% to about +20%. Our range of steady-state acetone concentrations is increased from 200-230 pptv to 300-370 pptv when using the new yields. As noted previously, the NQY mean that the loss of acetone to OH and photolysis are of a more similar magnitude. This is also evident from the enhanced reduction in steady-state acetone concentration at the  $\text{NO}_x$  concentration which maximises OH.

It is interesting to compare the results of this experiment with Experiment 2. The continuous replacement of fresh  $\text{NO}_x$  in the incoming convective air means that the production of PAN is not a hindrance to enhanced ozone production from acetone. However, at very low  $\text{NO}_x$  ozone production is reduced as loss of  $\text{NO}_x$  to PAN outweighs any increase in  $\text{HO}_2$  from acetone, as observed by *Folkins and Chatfield* [2000].

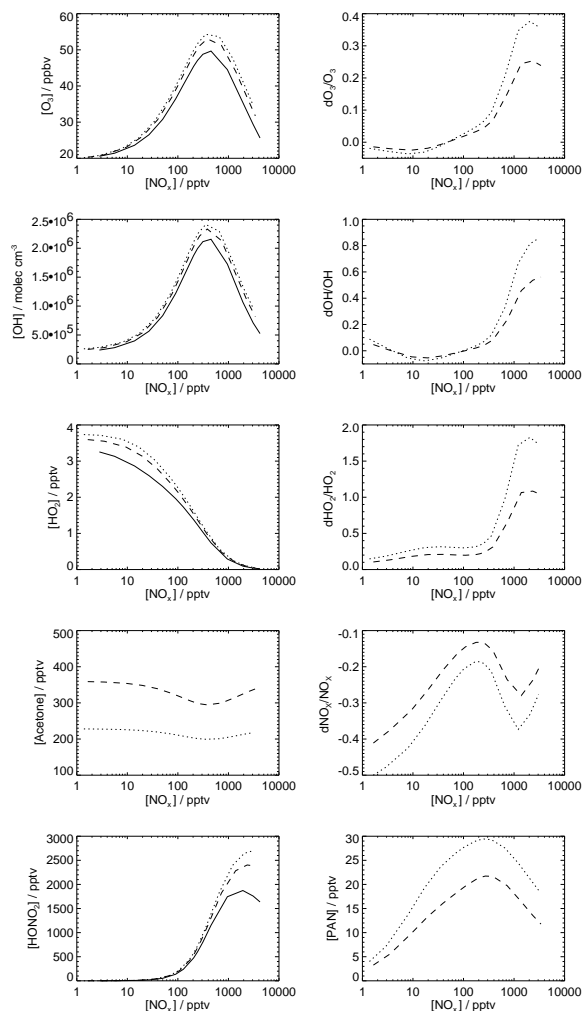


Figure 8.6: *Comparison of the UT chemical response to steady-state continuous convective outflow into the UT as a function of ambient  $\text{NO}_x$  for recommended acetone quantum yields (RQY, dotted) and the new acetone quantum yields (NQY, dashed). Solid curves show a baseline run with no acetone included.*

## 8.5 Acetone during EXPORT

Observations of acetone were not made during the EXPORT flights. However, it is possible to estimate acetone concentrations from an empirically derived correlation

between concentrations of CO and acetone. The slopes of such correlations appear relatively robust for the free troposphere, PBL and stratospheric air masses [*de Reus et al.*, 2003]. To estimate free tropospheric acetone concentrations during the EXPORT flights, a correlation derived from observations in the Mediterranean free troposphere in Summer 2000 has been used. These observations are the nearest available to the EXPORT region in both season and location. The correlation is given by *de Reus et al.*, [2003] as:

$$[\text{Acetone}(\text{pptv})] = 21.8 \times [\text{CO}(\text{ppbv})] - 762 \quad (8.7)$$

This expression has been used to derive acetone concentrations from free tropospheric CO observations made on the five EXPORT flights (Fig. 8.7) and values are in the range 500-2000pptv. These are much larger than the observed concentrations used to constrain the model experiments in Section 8.4, which were observed in the remote background UT. Largest concentrations of 1.5-2.0 ppbv are derived in the WCB uplift during flights A773/4. The range of concentrations derived are in agreement with those observed from aircraft during Summer 2000 over the Mediterranean region [*Traub et al.*, 2003].

Using observations of other species and the estimates of the acetone concentrations, the box model has been used to assess the impact of acetone on the  $\text{HO}_x$  budget of the UT during EXPORT. Median observed concentrations at altitudes above 400 hPa altitude have been used to constrain the box model for the three flights during which these altitudes were sampled (A772, A775 and A776). Pressure, temperature and humidity are taken from the median of the observed values above this altitude for each flight. Three model runs have been carried out for each flight; one set without acetone, another set using acetone and the RQY and a final set using acetone and the NQY. Acetone concentrations are derived from the CO correlation (Equation 8.7).

Table 8.5 shows the results of these experiments. For all cases the presence of acetone increases  $\text{HO}_x$  in the European UT. A maximum increase of  $\sim 14\%$  is obtained for the RQY, which is reduced to  $\sim 5\%$  for the NQY. For the three model runs, OH decreases by up to about 4% with the RQY and up to about 2% for the NQY.

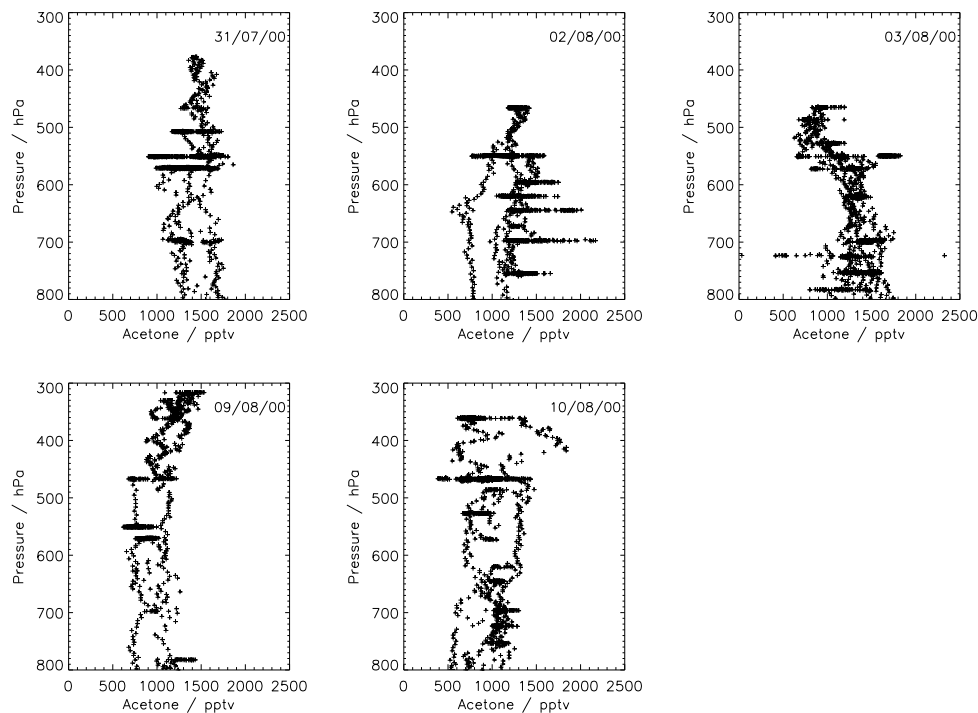


Figure 8.7: *Vertical profiles of acetone concentrations for EXPORT derived from CO observations using an empirical correlation from the Mediterranean summer free troposphere.*

The small decrease to OH is a result of a shift in the photochemical balance between OH and HO<sub>2</sub> brought about by loss of NO<sub>x</sub> to PAN formation. The altitude of the EXPORT data used in these experiments is somewhat lower than the UT background constrained runs performed in Section 8.2. The acetone loss to OH and by photolysis are of similar magnitudes at this altitude. The change to OH is therefore sensitive to the HO<sub>x</sub> yield from acetone, the efficiency of NO<sub>x</sub> loss to PAN and the OH reaction rate with acetone.

Overall, using the NQY, acetone does not appear to play a large role in the budget of total UT HO<sub>x</sub> over Central Europe in these cases at the altitudes considered. For example, the perturbations derived here are less than half the magnitude of those obtained from using the SONEX data (Section 8.2). However, the large acetone concentrations may be important for repartitioning of HO<sub>x</sub>, through perturbations to NO<sub>y</sub> at these altitudes.



Table 8.5: Steady-state day average concentrations from box model constrained with EXPORT UT observations.

	No acetone	RQY	NQY
A772			
Acetone/pptv		1473	1473
OH/molec cm <sup>-3</sup>	3.67×10 <sup>5</sup>	3.58×10 <sup>5</sup>	3.62×10 <sup>5</sup>
HO <sub>2</sub> /pptv	2.72	2.87	2.77
HO <sub>x</sub> /pptv	2.74	2.89	2.79
A775			
Acetone/pptv		1270	1270
OH/molec cm <sup>-3</sup>	6.90×10 <sup>5</sup>	6.65×10 <sup>5</sup>	6.78×10 <sup>5</sup>
HO <sub>2</sub> /pptv	2.73	3.12	2.87
HO <sub>x</sub> /pptv	2.80	3.18	2.93
A776			
Acetone/pptv		755	755
OH/molec cm <sup>-3</sup>	6.48×10 <sup>5</sup>	6.21×10 <sup>5</sup>	6.35×10 <sup>5</sup>
HO <sub>2</sub> /pptv	2.89	3.04	2.94
HO <sub>x</sub> /pptv	2.95	3.10	3.00

## 8.6 Conclusions

The new Leeds quantum yields (NQY) for acetone photolysis have been shown to make significant differences to the chemical perturbations resulting from the introduction of acetone into the UT at both mid-latitudes and in the tropics. For the specific conditions used, the steady-state lifetime of acetone diagnosed from a box model constrained with observed UT concentrations increases from about 75 to 250 days at mid-latitudes and from 9 to 21 days in the tropical UT. Increases in background HO<sub>x</sub> due to acetone are reduced by a factor of ~4 at mid-latitudes and by a factor of ~2 in the tropics. The tropical conditions used here mean that a 30% contribution by acetone to the total OH concentration is reduced to 18%. At mid-latitudes, the example constraints used suggest a reduction in the acetone contribution to OH from 25% to 8%.

With NQY, PAN formation in the model is significantly reduced, which has been shown to have implications for the efficiency of ozone production from acetone in the UT. These results suggest that an isolated injection of acetone and  $\text{NO}_x$  into the UT may result in less storage of  $\text{NO}_x$  in the reservoir species PAN, than would have been suggested by using RQY. Regular replacement of air in the UT by fresh acetone and  $\text{NO}_x$  allows efficient ozone production despite more efficient  $\text{NO}_x$  loss to PAN with RQY, since enough  $\text{NO}_x$  is replenished to maintain ozone production. Under such conditions, the enhancement to UT ozone is reduced by NQY. These issues are likely to have implications for the large-scale distribution of reactive  $\text{NO}_y$  and ozone in the troposphere.

The large increases in the acetone lifetime have been deduced under UT conditions, where the NQY show a maximum departure from RQY [Blitz *et al.*, 2004]. However, the effects of the NQY are likely to have important implications for the global troposphere. Longer transport timescales for acetone in the UT may help reconcile previously unexplained abundances of acetone in the UT remote from source regions. Acetone budget studies [e.g. Jacob *et al.*, 2002] will need to re-address the source terms required to balance a greater acetone lifetime. The reduced  $\text{HO}_x$  yield from acetone in the UT also suggests that additional  $\text{HO}_x$  sources must be sought in order to balance UT  $\text{HO}_x$  budgets [e.g. Jaeglé *et al.*, 2000].

Using acetone concentrations derived from a CO-acetone correlation, the impact of acetone on the  $\text{HO}_x$  budget of the UT during EXPORT has been evaluated. With NQY,  $\text{HO}_x$  increases of up to 5% from acetone were derived. Slight decreases of OH were calculated when introducing acetone, due to re-partitioning of  $\text{HO}_x$  as a result of loss of  $\text{NO}_x$  to increased PAN formation. These results suggest a smaller role for acetone than those obtained from the background UT experiments. However, the EXPORT observations were obtained at lower altitudes than those used for the background UT constraints.

## 9. Conclusions

### 9.1 Summary of results

This thesis has been concerned with the composition of the troposphere over Central Europe. In particular, transport and chemistry processes important in controlling ozone concentrations have been investigated using aircraft data and chemistry-transport models. Key questions set out in Chapter 1, highlighted areas for investigation. These included assessment of the chemistry in the European environment, how different transport processes control the import and export of pollution into the European troposphere, and how different modelling approaches may affect conclusions regarding ozone photochemistry.

Analysis of observed NMHC concentrations showed that quantitative estimates of air mass age from NMHC ratios are complicated by mixing effects. The relative importance of mixing and chemistry in changing a given NMHC ratio were shown to be dependent on both season (due to the abundance of OH) and the synoptic situation (due to the strength of vertical mixing). Nevertheless, a qualitative relationship was demonstrated between absolute NMHC concentrations and NMHC ratios, revealing decreasing ratios with degree of atmospheric processing. These results show that despite observations indicating some relationship between NMHC ratios and air mass age, mixing must be accounted for when estimating transport timescales.

The spatial distribution of PBL NMHC observations suggested that estimates of the at-source relationship of emitted NMHC concentrations from other studies made over Germany did not agree with inferred at-source ratios from the EXPORT data. The spatial distributions of PBL NMHC observations suggested that assumptions of fixed at-source relationships for pairs of NMHCs, even throughout the relatively

limited Central European region, may be erroneous.

Isoprene was shown to be important for photochemistry in the study region, being the dominant OH sink in the region of the Romania-Hungary border. In Poland and the Czech Republic short-lived alkenes played an important role in photochemistry, being the dominant OH sink in fresh outflow from the sampled WCB system. The CiTTyCAT model underestimated this contribution significantly. The model results also suggested that aromatic NMHCs may play an important role in polluted PBL photochemistry. However, no observations of such species were available.

The complexity of the chemical schemes used in models also have important impacts for diagnosed ozone photochemistry. The inclusion of more NMHC species in the CiTTyCAT scheme compared to TOMCAT was shown to increase PBL ozone production rates by up to  $\sim 30\%$ . Isoprene in the CiTTyCAT model results in large ozone production rates locally to the emissions, but also stores large amounts of  $\text{NO}_x$  as PAN during ascent of air from the PBL. TOMCAT produces much less PAN, due to its lack of isoprene which likely has implications for ozone photochemistry downwind.

This thesis has re-evaluated the importance of acetone for chemistry in the UT, in light of new laboratory measurements of its photolysis quantum yields. Chemical perturbations resulting from the presence of acetone in the UT are reduced in magnitude when using these new measurements of the quantum yields, compared to using the currently recommended values. A 30% contribution by acetone to the total OH concentration in the tropics is reduced to 18%. At mid-latitudes, a reduction in the acetone contribution to OH from 25% to 8% has been calculated. The increased acetone lifetime means that it is likely to play a more important role in the ozone and  $\text{NO}_y$  budgets of more remote regions than previously thought. Acetone concentrations derived from EXPORT observations using an empirical correlation with CO, are calculated to be consistent with those from the Summer Mediterranean troposphere. Contributions from acetone to  $\text{HO}_x$  in the regions of the highest altitude EXPORT observations are seen to be small ( $< 5\%$  for the updated quantum yield photolysis rates). Repartitioning of  $\text{HO}_x$  was noted, due to loss of  $\text{NO}_x$  to PAN formation.

This thesis has demonstrated that neither the Lagrangian nor Eulerian modelling approach is superior for all applications; they complement each other in their treatments of transport. While global Eulerian models are necessary for long-term, large-scale studies, the careful use of Lagrangian models for shorter-term studies of individual cases or processes can have advantages.

Vertical exchange between the PBL and the free troposphere is better treated using an Eulerian approach where sub-grid mixing processes play a key role, which are difficult to account for in a Lagrangian model. The use of the Lagrangian model in conjunction with trajectories from the mesoscale model for flight A773 represents the best attempt to use the Lagrangian approach in such a situation. The fine-scale resolution of the mesoscale grid allows some of the ‘sub-global-grid’ vertical transport to be resolved. The use of emissions coupled to a full chemical treatment in the CiTTyCAT model was able to demonstrate that the rate of ascent resolved by the large-scale flow from the ECMWF global analyses was inadequate for recreating the observed tracer enhancements above the resolved WCB air stream. The Eulerian TOMCAT model achieved this with more success due to its parameterised convection scheme. However, the heterogeneity in the locations of convective cells embedded in the frontal region meant that both TOMCAT and CiTTyCAT with a horizontally uniform mixed layer did not reproduce the scatter between freshly polluted uplift and more aged air observed. The use of trajectories from the mesoscale UM gave the best reproduction of observations, since they resolved some regions of very strong ascent in close proximity to regions which had followed the large-scale, less rapid ascent. In the future, higher resolution meteorological studies will become more routine. The ability of Lagrangian models to resolve vertical transport will therefore improve, allowing more reliable Lagrangian chemistry-transport studies of systems such as that modelled here.

In domains dominated by fine-scale layering of air masses, the novel Lagrangian RDF technique with chemistry simulates the positions of air mass gradients and characteristics remarkably well. The Eulerian TOMCAT model has been shown to mix down filaments undergoing long-range transport too quickly. This work indicates important consequences for domain-average ozone photochemistry, where the absence of observed fine-scale structure in the Eulerian model was shown to pro-

duce an underestimate of a factor 4 in ozone production from the reaction  $\text{NO} + \text{HO}_2$ . Observed tracer gradients and concentrations in the layered structure were best reproduced by parameterising mixing between the Lagrangian air masses and a background from the Eulerian model fields on a timescale of 2.5 - 5 days. This represents a hybrid of the two approaches; retaining air mass gradients using Lagrangian advection, with a controlled implementation of Eulerian mixing processes. Ozone photochemistry in air masses exported from the US across the Atlantic was shown to be sensitive to this mixing, in particular with regard to the loss or gain of  $\text{NO}_y$  species, which were key in controlling NO concentrations.

## 9.2 Future work

Studies carried out in this thesis have highlighted some areas for possible future work. Some of these issues can be addressed with further use of existing modelling tools, while others would require further model development. Other issues may be resolved through additional observations or new observation strategies.

The impacts of the new acetone quantum yields should be examined on a global scale, by incorporating the new quantum yields into a 3D Eulerian model. This will allow a full assessment of the implications of changes to  $\text{NO}_y$  partitioning,  $\text{HO}_x$  and ozone production from the new yields to be assessed in the global troposphere. Given the revised quantum yield data, future studies should also examine the roles of non-acetone oxygenated NMHCs in the  $\text{HO}_x$  budget of the troposphere.

Despite the qualitative result that some incorporation of small-scale vertical mixing in the CiTTyCAT model is required to better resolve transport around a frontal system, a more quantitative estimate of the roles of different transport processes would be useful in assessing the limitations of different modelling approaches. [Donnel *et al.*, 2001] used the mesoscale UM to examine the contributions from large-scale dynamics, PBL turbulence and parameterised convection on transfer of an inert tracer from the PBL to the free troposphere. To investigate the chemical importance of these mechanisms, NMHC- $\text{NO}_x$ -ozone photochemistry would need to be included in the mesoscale model.

The development of a more self-consistent treatment of mixing between filaments undergoing long-range transport in a Lagrangian model, rather than with a large-scale ‘background’, may allow a more realistic estimate of the role of mixing processes during such transport. Better estimates of the interaction between Lagrangian-type isolated transport of filaments undergoing long-range transport and Eulerian mixing processes acting on those filaments could also be made from observations, in order to quantify limitations of the different modelling approaches. This may be made possible with pseudo-Lagrangian aircraft experiments. In such experiments, chemical observations made by one aircraft are compared to those made in the same air mass, by a second aircraft at some location downwind. By using relationships between observed tracers (e.g. NMHCs) the departure of the relationship from ideal isolated, Lagrangian-type transport can be used to infer the role of mixing over the time period of transport between the two aircraft.

Studies concerning the chemistry of the European PBL have also highlighted the need for more detailed NMHC observations. These should include a better quantification of at-source NMHC relationships. This model study has also highlighted the possible importance of aromatic NMHCs for polluted PBL photochemistry, as well as uncertainties regarding the extent of the role of isoprene. More detailed observations of these species would reduce these uncertainties. The reduced role for acetone deduced from the revised quantum yield data suggests that other oxygenated NMHCs may play more important roles in tropospheric chemistry than previously believed. Future observations and modelling studies focused on these species are therefore desirable.

# Appendix A

Reactions and rate coefficients used in the CiTTyCAT chemistry scheme are given in the tables below.

## Bimolecular reactions

Bimolecular reactions are parameterised in the Arrhenius form. The rate constant,  $k$ , has units  $\text{molecules}^{-1} \text{cm}^3 \text{s}^{-1}$ .

				k
1	$\text{CH}_3 + \text{O}_2$	$\rightarrow \text{HCHO} + \text{OH}$		$3.00 \times 10^{-16}$
2	$\text{CH}_3 + \text{O}_3$	$\rightarrow$		$5.10 \times 10^{-12} \exp(-210.0/T)$
3a	$\text{EtOO} + \text{EtOO}$	$\rightarrow \text{EtOH} + \text{MeCHO} + \text{O}_2$		$2.05 \times 10^{-14}$
3b	$\text{EtOO} + \text{EtOO}$	$\rightarrow \text{EtO} + \text{EtO} + \text{O}_2$		$3.97 \times 10^{-14}$
3c	$\text{EtOO} + \text{EtOO}$	$\rightarrow \text{EtOOEt} + \text{O}_2$		$3.84 \times 10^{-15}$
4a	$\text{H} + \text{HO}_2$	$\rightarrow \text{H}_2 + \text{O}_2$		$5.60 \times 10^{-12}$
4b	$\text{H} + \text{HO}_2$	$\rightarrow \text{OH} + \text{OH}$		$7.20 \times 10^{-11}$
4c	$\text{H} + \text{HO}_2$	$\rightarrow \text{H}_2\text{O} + \text{O}$		$2.40 \times 10^{-12}$
5	$\text{H} + \text{NO}_2$	$\rightarrow \text{OH} + \text{NO}$		$4.00 \times 10^{-10} \exp(-340.0/T)$
6	$\text{H} + \text{O}_3$	$\rightarrow \text{OH} + \text{O}_2$		$1.40 \times 10^{-10} \exp(-470.0/T)$
7	$\text{HCO} + \text{O}_2$	$\rightarrow \text{CO} + \text{HO}_2$		$5.20 \times 10^{-12}$
8	$\text{HO}_2 + \text{HCHO}$	$\rightarrow$		$9.70 \times 10^{-15} \exp(625.0/T)$
9	$\text{HO}_2 + \text{HO}_2$	$\rightarrow \text{H}_2\text{O}_2 + \text{O}_2$		$2.20 \times 10^{-13} \exp(600.0/T)$
10	$\text{HO}_2 + \text{MeOO}$	$\rightarrow \text{O}_2 + \text{MeOOH}$		$3.80 \times 10^{-13} \exp(780.0/T)$
11	$\text{HO}_2 + \text{NO}$	$\rightarrow \text{OH} + \text{NO}_2$		$3.60 \times 10^{-12} \exp(270.0/T)$
12	$\text{HO}_2 + \text{NO}_3$	$\rightarrow \text{O}_2 + \text{HONO}_2$		$2.00 \times 10^{-12}$
13	$\text{HO}_2 + \text{NO}_3$	$\rightarrow \text{OH} + \text{NO}_2 + \text{O}_2$		$2.00 \times 10^{-12}$
14	$\text{HO}_2 + \text{O}_3$	$\rightarrow \text{OH} + \text{O}_2 + \text{O}_2$		$2.03 \times 10^{-16} (T/300)^{4.57} \exp(693.0/T)$
15a	$2 \text{HOCH}_2\text{CH}_2\text{OO}$	$\rightarrow \text{HOCH}_2\text{CH}_2\text{OH} + \text{HOCH}_2\text{CHO} + \text{O}_2$		$3.90 \times 10^{-14} \exp(1000.0/T)$
15b	$2 \text{HOCH}_2\text{CH}_2\text{OO}$	$\rightarrow \text{HOCH}_2\text{CH}_2\text{O} + \text{HOCH}_2\text{CH}_2\text{O} + \text{O}_2$		$3.90 \times 10^{-14} \exp(1000.0/T)$
16	$\text{MeO} + \text{NO}$	$\rightarrow \text{HCHO} + \text{HNO}$		$8.00 \times 10^{-12}$
17	$\text{MeO} + \text{O}_2$	$\rightarrow \text{HCHO} + \text{HO}_2$		$7.20 \times 10^{-14} \exp(-1080.0/T)$
18a	$\text{MeOO} + \text{MeOO}$	$\rightarrow \text{MeOH} + \text{HCHO} + \text{O}_2$		$6.49 \times 10^{-14} \exp(365.0/T)$
18b	$\text{MeOO} + \text{MeOO}$	$\rightarrow \text{MeO} + \text{MeO} + \text{O}_2$		$3.81 \times 10^{-14} \exp(365.0/T)$
19	$\text{MeOO} + \text{NO}$	$\rightarrow \text{MeO} + \text{NO}_2$		$2.95 \times 10^{-12} \exp(285.0/T)$
20	$\text{MeOO} + \text{O}_3$	$\rightarrow$		$2.90 \times 10^{-16} \exp(-1000.0/T)$
21	$\text{N}_2\text{O}_5 + \text{H}_2\text{O}$	$\rightarrow \text{HONO}_2 + \text{HONO}_2$		$2.50 \times 10^{-22}$
22	$\text{NO} + \text{NO}_3$	$\rightarrow \text{NO}_2 + \text{NO}_2$		$1.80 \times 10^{-11} \exp(110.0/T)$
23	$\text{NO} + \text{O}_3$	$\rightarrow \text{NO}_2 + \text{O}_2$		$1.40 \times 10^{-12} \exp(-1310.0/T)$
24	$\text{NO}_2 + \text{NO}_3$	$\rightarrow \text{NO} + \text{NO}_2 + \text{O}_2$		$4.50 \times 10^{-14} \exp(-1260.0/T)$
25	$\text{NO}_2 + \text{O}_3$	$\rightarrow \text{NO}_3 + \text{O}_2$		$1.40 \times 10^{-13} \exp(-2470.0/T)$
26	$\text{NO}_3 + \text{C}_2\text{H}_2$	$\rightarrow$		$1.00 \times 10^{-16}$
27	$\text{NO}_3 + \text{C}_2\text{H}_4$	$\rightarrow$		$3.30 \times 10^{-12} \exp(-2880.0/T)$
28	$\text{NO}_3 + \text{C}_3\text{H}_6$	$\rightarrow$		$4.60 \times 10^{-13} \exp(-1155.0/T)$
29	$\text{NO}_3 + \text{CO}$	$\rightarrow \text{NO}_2 + \text{CO}_2$		$4.00 \times 10^{-19}$
30	$\text{NO}_3 + \text{HCHO}$	$\rightarrow \text{HONO}_2 + \text{HCO}$		$5.60 \times 10^{-16}$
31a	$\text{O} + \text{C}_2\text{H}_2$	$\rightarrow \text{C}_2\text{HO} + \text{H}$		$1.50 \times 10^{-11} \exp(-1600.0/T)$
31b	$\text{O} + \text{C}_2\text{H}_2$	$\rightarrow \text{CH}_2 + \text{CO}$		$1.50 \times 10^{-11} \exp(-1600.0/T)$
32	$\text{O} + \text{CH}_3$	$\rightarrow \text{HCHO} + \text{H}$		$1.30 \times 10^{-10}$
33	$\text{O} + \text{H}_2\text{O}_2$	$\rightarrow \text{OH} + \text{HO}_2$		$1.40 \times 10^{-12} \exp(-2000.0/T)$
34	$\text{O} + \text{HCHO}$	$\rightarrow \text{OH} + \text{HCO}$		$3.40 \times 10^{-11} \exp(1600.0/T)$
35	$\text{O} + \text{HO}_2$	$\rightarrow \text{OH} + \text{O}_2$		$2.70 \times 10^{-11} \exp(224.0/T)$
36	$\text{O} + \text{HO}_2\text{NO}_2$	$\rightarrow$		$7.80 \times 10^{-11} \exp(-3400.0/T)$
37	$\text{O} + \text{HONO}_2$	$\rightarrow \text{OH} + \text{NO}_3$		$3.00 \times 10^{-17}$
38	$\text{O} + \text{MeCHO}$	$\rightarrow \text{MeCO} + \text{OH}$		$1.80 \times 10^{-11} \exp(-1100.0/T)$
39	$\text{O} + \text{N}_2\text{O}_5$	$\rightarrow$		$3.00 \times 10^{-16}$
40	$\text{O} + \text{NO}_2$	$\rightarrow \text{O}_2 + \text{NO}$		$5.50 \times 10^{-12} \exp(188.0/T)$
41	$\text{O} + \text{NO}_3$	$\rightarrow \text{O}_2 + \text{NO}_2$		$1.70 \times 10^{-11}$
42	$\text{O} + \text{O}_3$	$\rightarrow \text{O}_2 + \text{O}_2$		$8.00 \times 10^{-12} \exp(-2060.0/T)$
43	$\text{O} + \text{OH}$	$\rightarrow \text{O}_2 + \text{H}$		$2.40 \times 10^{-11} \exp(110.0/T)$
44a	$\text{O}(^1\text{D}) + \text{CH}_4$	$\rightarrow \text{OH} + \text{CH}_3$		$1.42 \times 10^{-10}$
44b	$\text{O}(^1\text{D}) + \text{CH}_4$	$\rightarrow \text{HCHO} + \text{H}_2$		$8.00 \times 10^{-12}$
45	$\text{O}(^1\text{D}) + \text{H}_2\text{O}$	$\rightarrow \text{OH} + \text{OH}$		$2.20 \times 10^{-10}$
46	$\text{O}(^1\text{D}) + \text{N}_2$	$\rightarrow \text{O} + \text{N}_2$		$1.80 \times 10^{-11} \exp(107.0/T)$
47	$\text{O}(^1\text{D}) + \text{O}_2$	$\rightarrow \text{O} + \text{O}_2$		$3.20 \times 10^{-11} \exp(67.0/T)$



			k
48a	$O(^1D) + O_3$	$\rightarrow O_2 + O + O$	$1.20 \times 10^{-10}$
48b	$O(^1D) + O_3$	$\rightarrow O_2 + O_2$	$1.20 \times 10^{-10}$
49	$O_3 + C_2H_2$	$\rightarrow$	$1.00 \times 10^{-20}$
50	$OH + CH_4$	$\rightarrow H_2O + CH_3$	$1.85 \times 10^{-12}$ exp(-1690.0/T)
51	$OH + CO$	$\rightarrow H + CO_2$	$1.30 \times 10^{-13}$
52	$OH + H_2O_2$	$\rightarrow H_2O + HO_2$	$2.90 \times 10^{-12}$ exp(-160.0/T)
53	$OH + HCHO$	$\rightarrow H_2O + HCO$	$8.20 \times 10^{-12}$ exp(40.0/T)
54	$OH + HO_2$	$\rightarrow H_2O + O_2$	$4.80 \times 10^{-11}$ exp(250.0/T)
55	$OH + HO_2NO_2$	$\rightarrow$	$1.90 \times 10^{-12}$ exp(270.0/T)
56	$OH + HONO_2$	$\rightarrow H_2O + NO_3$	$1.50 \times 10^{-13}$
57a	$OH + MeOOH$	$\rightarrow H_2O + HCHO + OH$	$1.00 \times 10^{-12}$ exp(190.0/T)
57b	$OH + MeOOH$	$\rightarrow H_2O + MeOO$	$1.90 \times 10^{-12}$ exp(190.0/T)
58	$OH + NO_3$	$\rightarrow HO_2 + NO_2$	$2.00 \times 10^{-11}$
59	$OH + O_3$	$\rightarrow HO_2 + O_2$	$1.70 \times 10^{-12}$ exp(-940.0/T)
60	$OH + OH$	$\rightarrow H_2O + O$	$6.31 \times 10^{-14}$ (T/300) <sup>2.60</sup> exp(945.0/T)
61	$C_2H_6 + OH$	$\rightarrow EtOO$	$6.90 \times 10^{-12}$ exp(-1000.0/T)
62	$C_3H_8 + OH$	$\rightarrow 0.585 BuOO + 0.330 EtOO$	$7.60 \times 10^{-12}$ exp(-585.0/T)
63	$C_4H_{10} + OH$	$\rightarrow 0.28 EtOO + 0.59 BuOO + 0.18 HxOO$	$9.10 \times 10^{-12}$ exp(-405.0/T)
64	$C_5H_{12} + OH$	$\rightarrow 0.25 EtOO + 0.663 BuOO + 0.38 HxOO$	$2.20 \times 10^{-12}$ exp(183.0/T)
65	$C_6H_{14} + OH$	$\rightarrow 0.24 EtOO + 0.705 BuOO + 0.45 HxOO$	$1.38 \times 10^{-12}$ exp(414.0/T)
66	$EtOO + NO$	$\rightarrow 0.985 MeCHO + 0.985 HO_2 + NO_2$	$2.60 \times 10^{-12}$ exp(380.0/T)
67	$MeCHO + OH$	$\rightarrow MeCO_3$	$4.40 \times 10^{-12}$ exp(365.0/T)
68	$MeCHO + NO_3$	$\rightarrow MeCO_3 + HONO_2$	$1.40 \times 10^{-12}$ exp(-1860.0/T)
69	$PAN + OH$	$\rightarrow HCHO + NO_2$	$9.50 \times 10^{-13}$ exp(-650.0/T)
70	$MeCO_3 + NO$	$\rightarrow MeOO + NO_2$	$7.50 \times 10^{-12}$ exp(290.0/T)
71	$BuOO + NO$	$\rightarrow 0.91 EtCOMe + 0.91 HO_2 + NO_2$	$2.54 \times 10^{-12}$ exp(360.0/T)
72	$EtCOMe + OH$	$\rightarrow MeCOOHCOMe$	$1.30 \times 10^{-12}$ exp(-25.0/T)
73	$MeCOOHCOMe + NO$	$\rightarrow 0.92 MeCHO + 0.92 MeCO_3 + NO_2$	$2.54 \times 10^{-12}$ exp(360.0/T)
74	$HxOO + NO$	$\rightarrow 0.96 EtOO + 0.96 EtCOMe + NO_2$	$2.54 \times 10^{-12}$ exp(360.0/T)
75	$HOCH_2CH_2OO + NO$	$\rightarrow HO_2 + NO_2 + HCHO + MeCHO$	$2.54 \times 10^{-12}$ exp(360.0/T)
76	$C_2H_4 + O_3$	$\rightarrow HCHO + 0.42 CO + 0.12 H_2 + 0.12 HO_2$	$9.10 \times 10^{-15}$ exp(-2580.0/T)
77	$HOPriOO + NO$	$\rightarrow MeCHO + HCHO + HO_2 + NO_2$	$2.54 \times 10^{-12}$ exp(360.0/T)
78	$C_3H_6 + O_3$	$\rightarrow 0.525 HCHO + 0.5 MeCHO + 0.06 CH_4$ $+ 0.33 CO + 0.23 HO_2 + 0.095 OH$ $+ 0.215 MeOO + 0.06 H_2$	$5.50 \times 10^{-15}$ exp(-1880.0/T)
79	$C_6H_6 + OH$	$\rightarrow 0.64 ArOO$	$2.33 \times 10^{-12}$ exp(-193.0/T)
80	$C_7H_8 + OH$	$\rightarrow 0.76 ArOO$	$1.81 \times 10^{-12}$ exp(338.0/T)
81	$ArOO + NO$	$\rightarrow MeCOCHO + HCOCHCHCHO + HO_2 + NO_2$	$2.54 \times 10^{-12}$ exp(360.0/T)
82	$HCOCHCHCHO + OH$	$\rightarrow HCOCHCHCO_3$	$5.20 \times 10^{-11}$
83	$HCOCHCHCO_3 + NO$	$\rightarrow HCOCHO + CO + HO_2 + 3 NO_2 - 2 NO$	$2.54 \times 10^{-12}$ exp(360.0/T)
84	$HCOCHO + OH$	$\rightarrow CO + CO + HO_2$	$1.10 \times 10^{-11}$
85	$MeCOCHO + OH$	$\rightarrow MeCO_3 + CO$	$1.50 \times 10^{-11}$
86	$EtOO + HO_2$	$\rightarrow EtOOH$	$3.80 \times 10^{-13}$ exp(900.0/T)
87	$BuOO + HO_2$	$\rightarrow BuOOH$	$1.82 \times 10^{-13}$ exp(1300.0/T)
88	$HxOO + HO_2$	$\rightarrow HxOOH$	$1.82 \times 10^{-13}$ exp(1300.0/T)
89	$MeCO_3 + HO_2$	$\rightarrow MeCO_3H$	$5.20 \times 10^{-13}$ exp(983.0/T)
90	$MeCOOHCOMe + HO_2$	$\rightarrow MeCHO + MeCO_3 + OH$	$1.82 \times 10^{-13}$ exp(1300.0/T)
91	$HOCH_2CH_2OO + HO_2$	$\rightarrow HO_2 + MeCHO + HCHO + OH$	$2.00 \times 10^{-13}$ exp(1250.0/T)
92	$HOPriOO + HO_2$	$\rightarrow HO_2 + MeCHO + HCHO + OH$	$1.51 \times 10^{-13}$ exp(1300.0/T)
93	$ArOO + HO_2$	$\rightarrow$	$2.39 \times 10^{-13}$ exp(1300.0/T)
94	$HCOCHCHCO_3 + HO_2$	$\rightarrow$	$4.30 \times 10^{-13}$ exp(1040.0/T)
95	$MeOO + MeCO_3$	$\rightarrow HCHO + 0.5 MeOO + 0.5 HO_2$	$2.00 \times 10^{-12}$ exp(500.0/T)
96	$MeCO_3 + MeCO_3$	$\rightarrow MeOO + MeOO$	$2.90 \times 10^{-12}$ exp(500.0/T)
97	$EtOOH + OH$	$\rightarrow 0.75 MeCHO + 0.75 OH + 0.25 EtOO$	$1.20 \times 10^{-11}$
98	$BuOOH + OH$	$\rightarrow EtCOMe + OH$	$2.15 \times 10^{-11}$
99	$HxOOH + OH$	$\rightarrow HxOO$	$1.90 \times 10^{-12}$ exp(190.0/T)
100	$MeCO_3H + OH$	$\rightarrow MeCO_3$	$3.70 \times 10^{-12}$
101	$MVK + OH$	$\rightarrow MVKOO$	$4.13 \times 10^{-12}$ exp(452.0/T)
102	$MVKOO + NO$	$\rightarrow NO_2$	$2.54 \times 10^{-12}$ exp(360.0/T)
103	$MVKOO + HO_2$	$\rightarrow 0.6 MeCO_3 + 0.6 MeCHO + 0.3 MeCOCHO$ $+ 0.3 HCHO + 0.3 HO_2 + 1.8 CO + 0.6 H_2$	$1.82 \times 10^{-13}$ exp(1300.0/T)
104	$MVK + O_3$	$\rightarrow 0.5 MeCOCHO + 0.5 HCHO + 0.15 MeCO_3$ $+ 0.15 MeCHO + 0.21 HO_2 + 0.2 CO + 0.06 H_2$	$7.51 \times 10^{-16}$ exp(-1521.0/T)
105	$MACR + OH$	$\rightarrow MACROO$	$1.86 \times 10^{-11}$ exp(175.0/T)
106	$MACROO + NO$	$\rightarrow NO_2 + 0.9 MeCOCHO + 0.9 HO_2 + 0.9 HCHO$	$2.54 \times 10^{-12}$ exp(360.0/T)
107	$MACROO + HO_2$	$\rightarrow 2.2 CO + 0.6 H_2$	$1.82 \times 10^{-13}$ exp(1300.0/T)
108	$MACR + O_3$	$\rightarrow 0.65 HCHO + 0.36 HO_2 + 0.36 H_2 + 0.35 CO$ $+ 0.5 MeCOCHO + 0.15 NO_2 - 0.15 NO$	$1.36 \times 10^{-15}$ exp(-2112.0/T)
109	$ISOPRENE + OH$	$\rightarrow ISOPROO$	$2.70 \times 10^{-11}$ exp(390.0/T)
110	$ISOPROO + NO$	$\rightarrow 0.9 HCHO + 0.9 HO_2 + 0.45 MVK$ $+ 0.45 MACR + NO_2$	$2.54 \times 10^{-12}$ exp(360.0/T)

			k
111	ISOPROO + HO <sub>2</sub>	→ 2.75 CO + 0.9 H <sub>2</sub>	$2.05 \times 10^{-13} \exp(1300.0/T)$
112	ISOPRENE + O <sub>3</sub>	→ 0.5 HCHO + 0.2 MVK + 0.2 CO + 0.3 MACR + 0.06 HO <sub>2</sub> + 0.06 H <sub>2</sub>	$7.86 \times 10^{-15} \exp(-1913.0/T)$
113	O <sub>3</sub> + HONO	→ O <sub>2</sub> + HONO <sub>2</sub>	$5.00 \times 10^{-19}$
114	OH + HONO	→ H <sub>2</sub> O + NO <sub>2</sub>	$2.50 \times 10^{-12} \exp(260.0/T)$
115	MeOO + NO <sub>3</sub>	→ MeO + NO <sub>2</sub> + O <sub>2</sub>	$1.00 \times 10^{-12}$
116	MeCO <sub>3</sub> + NO <sub>3</sub>	→ MeOO + CO <sub>2</sub> + NO <sub>2</sub>	$4.00 \times 10^{-12}$
117a	EtOH + OH	→ MeCHO + HO <sub>2</sub>	$2.94 \times 10^{-12} \exp(-70.0/T)$
117b	EtOH + OH	→ HOCH <sub>2</sub> CH <sub>2</sub> OO	$1.62 \times 10^{-13} \exp(-70.0/T)$
118	Me <sub>2</sub> CO + OH	→ MeCOCH <sub>2</sub> O <sub>2</sub>	$8.80 \times 10^{-12} \exp(-1320.0/T)$ $+1.70 \times 10^{-14} \exp(420.0/T)$
119	MeCOCH <sub>2</sub> O <sub>2</sub> + NO	→ HCHO + MeCO <sub>3</sub> + NO <sub>2</sub>	$2.54 \times 10^{-12} \exp(360.0/T)$

## Termolecular reactions

Termolecular rates are parameterised according to:

$$k_t = \left( \frac{k_0[M]}{1 + \frac{k_0[M]}{k_\infty}} \right) F \left( 1 + \log \left[ \frac{k_0[M]}{k_\infty} \right]^2 \right)^{-1}$$

			F	k <sub>0</sub>	k <sub>∞</sub>
121	CH <sub>3</sub> + O <sub>2</sub> + M	→ MeOO + M	0.27	1.00×10 <sup>-30</sup> (T/300) <sup>-3.30</sup>	1.80×10 <sup>-12</sup> (T/300) <sup>1.10</sup>
122	EtOO + NO + M	→ EtONO <sub>2</sub> + M	0.00	0.00	1.30×10 <sup>-13</sup>
123	EtOO + NO <sub>2</sub> + M	→ EtO <sub>2</sub> NO <sub>2</sub> + M	0.31	1.30×10 <sup>-29</sup> (T/300) <sup>-6.20</sup>	8.80×10 <sup>-12</sup>
124	H + O <sub>2</sub> + M	→ HO <sub>2</sub> + M	0.50	5.40×10 <sup>-32</sup> (T/300) <sup>-1.80</sup>	9.50×10 <sup>-11</sup> (T/300) <sup>0.44</sup>
125	HO <sub>2</sub> + HCHO + M	→ HOCH <sub>2</sub> OO + M	0.00		9.70×10 <sup>-15</sup> exp(-625.0/T)
126	HO <sub>2</sub> + HO <sub>2</sub> + M	→ H <sub>2</sub> O <sub>2</sub> + O <sub>2</sub> + M	0.00	1.90×10 <sup>-33</sup> exp(-980.0/T)	
127	HO <sub>2</sub> + NO <sub>2</sub> + M	→ HO <sub>2</sub> NO <sub>2</sub> + M	0.60	1.80×10 <sup>-31</sup> (T/300) <sup>-3.20</sup>	4.70×10 <sup>-12</sup>
128	HO <sub>2</sub> NO <sub>2</sub> + M	→ HO <sub>2</sub> + NO <sub>2</sub> + M	0.60	4.10×10 <sup>-5</sup> exp(10650.0)	4.80×10 <sup>15</sup> exp(11170.0/T)
129	MeO + NO + M	→ MeONO + M	0.60	1.60×10 <sup>-29</sup> (T/300) <sup>-3.50</sup>	3.60×10 <sup>-11</sup> (T/300) <sup>-0.60</sup>
130	MeO + NO <sub>2</sub> + M	→ MeONO <sub>2</sub> + M	0.44	9.00×10 <sup>-29</sup> (T/300) <sup>-4.50</sup>	1.90×10 <sup>-11</sup>
131	N <sub>2</sub> O <sub>5</sub> + M	→ NO <sub>2</sub> + NO <sub>3</sub> + M	0.35	1.30×10 <sup>-3</sup> (T/300) <sup>-3.50</sup> exp(11000.0/T)	9.70×10 <sup>14</sup> (T/300) <sup>0.10</sup> exp(11080.0/T)
132	NO + NO + M	→ NO <sub>2</sub> + NO <sub>2</sub> + M	0.00	3.30×10 <sup>-39</sup> exp(-530.0/T)	
133	NO <sub>2</sub> + NO <sub>3</sub> + M	→ N <sub>2</sub> O <sub>5</sub> + M	0.35	3.60×10 <sup>-30</sup> (T/300) <sup>-4.10</sup>	1.90×10 <sup>-12</sup> (T/300) <sup>0.20</sup>
134	O + NO + M	→ NO <sub>2</sub> + M	0.85	1.00×10 <sup>-31</sup> (T/300) <sup>-1.60</sup>	3.00×10 <sup>-11</sup> (T/300) <sup>0.30</sup>
135	O + NO <sub>2</sub> + M	→ NO <sub>3</sub> + M	0.60	2.50×10 <sup>-31</sup> (T/300) <sup>-1.80</sup>	2.20×10 <sup>-11</sup> (T/300) <sup>-0.70</sup>
136	O + O <sub>2</sub> + M	→ O <sub>3</sub> + M	0.00	6.00×10 <sup>-34</sup> (T/300) <sup>-2.40</sup>	
137	O( <sup>1</sup> D) + N <sub>2</sub> + M	→ N <sub>2</sub> O + M	0.00	3.50×10 <sup>-37</sup> (T/300) <sup>-0.60</sup>	
138	OH + NO + M	→ HONO + M	1420	7.40×10 <sup>-31</sup> (T/300) <sup>-2.40</sup>	3.30×10 <sup>-11</sup> (T/300) <sup>-0.30</sup>
139	OH + NO <sub>2</sub> + M	→ HONO <sub>2</sub> + M	0.40	3.30×10 <sup>-30</sup> (T/300) <sup>-3.00</sup>	4.10×10 <sup>-11</sup>
140	OH + OH + M	→ H <sub>2</sub> O <sub>2</sub> + M	0.50	6.90×10 <sup>-31</sup> (T/300) <sup>-0.80</sup>	2.60×10 <sup>-11</sup>
141	MeCO <sub>3</sub> + NO <sub>2</sub> + M	→ PAN + M	0.30	2.70×10 <sup>-28</sup> (T/300) <sup>-7.10</sup>	1.20×10 <sup>-11</sup> (T/300) <sup>-0.90</sup>
142	PAN + M	→ MeCO <sub>3</sub> + NO <sub>2</sub> + M	0.30	4.90×10 <sup>-3</sup> exp(12100.0/T)	5.40×10 <sup>16</sup> exp(13830.0/T)
143	C <sub>2</sub> H <sub>4</sub> + OH + M	→ HOCH <sub>2</sub> CH <sub>2</sub> OO + M	0.48	7.00×10 <sup>-29</sup> (T/300) <sup>-3.10</sup>	9.00×10 <sup>-12</sup>
144	C <sub>3</sub> H <sub>6</sub> + OH + M	→ HOPriOO + M	0.50	8.00×10 <sup>-27</sup> (T/300) <sup>-3.50</sup>	3.00×10 <sup>-11</sup>
145	C <sub>2</sub> H <sub>2</sub> + OH + M	→ HCOCHO + OH + M	0.60	5.50×10 <sup>-30</sup>	8.30×10 <sup>-13</sup> (T/300) <sup>2.00</sup>
146	MeO <sub>2</sub> NO <sub>2</sub> + M	→ MeOO + NO <sub>2</sub> + M	0.36	9.00×10 <sup>-5</sup> exp(9690.0/T)	1.10×10 <sup>16</sup> exp(10560.0/T)
147	MeOO + NO <sub>2</sub> + M	→ MeO <sub>2</sub> NO <sub>2</sub> + M	0.36	2.50×10 <sup>-30</sup> (T/300) <sup>-5.50</sup>	7.50×10 <sup>-12</sup>

## Photolysis reactions

Photolysis rates are calculated on-line in the model photolysis code, dependent on solar zenith angle, time of year, cloud scattering, temperature and pressure. Photolysis reactions considered are given below.

148	$\text{CH}_4 + h\nu$	$\rightarrow$
149	$\text{CO} + h\nu$	$\rightarrow \text{C} + \text{O}$
150	$\text{H}_2\text{O} + h\nu$	$\rightarrow \text{OH} + \text{H}$
151	$\text{H}_2\text{O}_2 + h\nu$	$\rightarrow \text{OH} + \text{OH}$
152	$\text{HO}_2 + h\nu$	$\rightarrow \text{OH} + \text{O}$
153a	$\text{HO}_2\text{NO}_2 + h\nu$	$\rightarrow \text{OH} + \text{NO}_3$
153b	$\text{HO}_2\text{NO}_2 + h\nu$	$\rightarrow \text{HO}_2 + \text{NO}_2$
154	$\text{HONO}_2 + h\nu$	$\rightarrow \text{OH} + \text{NO}_2$
155a	$\text{MeOOH} + h\nu$	$\rightarrow \text{MeO} + \text{OH}$
155b	$\text{MeOOH} + h\nu$	$\rightarrow \text{MeO} + \text{O} + \text{H}$
156a	$\text{N}_2\text{O}_5 + h\nu$	$\rightarrow \text{NO}_3 + \text{NO}_2$
156b	$\text{N}_2\text{O}_5 + h\nu$	$\rightarrow \text{NO}_3 + \text{NO} + \text{O}$
157	$\text{NO} + h\nu$	$\rightarrow \text{N} + \text{O}$
158	$\text{NO}_2 + h\nu$	$\rightarrow \text{NO} + \text{O}$
159a	$\text{NO}_3 + h\nu$	$\rightarrow \text{NO} + \text{O}_2$
159b	$\text{NO}_3 + h\nu$	$\rightarrow \text{NO}_2 + \text{O}$
160	$\text{O}_2 + h\nu$	$\rightarrow \text{O} + \text{O}$
161a	$\text{O}_3 + h\nu$	$\rightarrow \text{O}_2 + \text{O}$
161b	$\text{O}_3 + h\nu$	$\rightarrow \text{O}_2 + \text{O}(1\text{D})$
162a	$\text{HCHO} + h\nu$	$\rightarrow \text{CO} + \text{HO}_2 + \text{HO}_2$
162b	$\text{HCHO} + h\nu$	$\rightarrow \text{CO} + \text{H}_2$
163a	$\text{MeCHO} + h\nu$	$\rightarrow \text{MeOO} + \text{HO}_2 + \text{CO}$
163b	$\text{MeCHO} + h\nu$	$\rightarrow \text{CH}_4 + \text{CO}$
164	$\text{EtCOMe} + h\nu$	$\rightarrow \text{EtOO} + \text{MeCO}_3$
165	$\text{HCOCHO} + h\nu$	$\rightarrow$
166	$\text{MeCOCHO} + h\nu$	$\rightarrow \text{MeCO}_3 + \text{HO}_2 + \text{CO}$
167	$\text{EtOOH} + h\nu$	$\rightarrow \text{MeCHO} + \text{HO}_2 + \text{OH}$
168	$\text{BuOOH} + h\nu$	$\rightarrow \text{EtCOMe} + \text{HO}_2 + \text{OH}$
169	$\text{HxOOH} + h\nu$	$\rightarrow \text{EtCOMe} + \text{EtOO} + \text{OH}$
170	$\text{MeCO}_3\text{H} + h\nu$	$\rightarrow \text{MeOO} + \text{OH}$
171	$\text{PAN} + h\nu$	$\rightarrow \text{MeCOO} + \text{NO}_2$
172	$\text{HCOCHCHCHO} + h\nu$	$\rightarrow \text{HCOCHCHCO}_3 + \text{HO}_2$
173	$\text{MeO}_2\text{NO}_2 + h\nu$	$\rightarrow \text{MeOO} + \text{NO}_2$
174	$\text{HONO} + h\nu$	$\rightarrow \text{OH} + \text{NO}$
175a	$\text{Me}_2\text{CO} + h\nu$	$\rightarrow \text{MeCO}_3 + \text{MeOO}$
175b	$\text{Me}_2\text{CO} + h\nu$	$\rightarrow \text{MeOO} + \text{MeOO} + \text{CO}$

## References

- Andrae, M.O., and P.J. Crutzen, Atmospheric aerosols: Biogeochemical sources and role in atmospheric chemistry, *Science*, *276*, 1052-1058, 1997.
- Andrae, M.O., and P. Merlet, Emission of trace gases and aerosols from biomass burning, *Global Biogeochem. Cycles*, *15*, 955-966, 2001.
- Ariya P.A., R. Sander, and P.J. Crutzen, Significance of  $\text{HO}_x$  and peroxides production due to alkene ozonolysis during fall and winter: A modeling study, *J. Geophys. Res.*, *105* (D14): 17721-17738, 2000.
- Arnold, F., V. Burger, B. Droste-Fanke, F. Grimm, A. Krieger, J. Schneider, and T. Stilp, Acetone in the upper troposphere and lower stratosphere: Impact on trace gases and aerosols, *Geophys. Res. Lett.*, *24*, 3017-3020, 1997.
- Arnold, S.R., M.P. Chipperfield, M.A. Blitz, D.E. Heard, and M.J. Pilling, Photodissociation of acetone: Atmospheric implications of temperature-dependent quantum yields. *Geophys. Res. Lett.*, *31*, L07110, doi:10.1029/2003GL019099, 2004.
- Atkinson, R., D.L. Baulch, R.A. Cox, R.F. Hampson, J.A. Kerr, M.J. Rossi, and J. Troe, Evaluated kinetic, photochemical and heterogeneous data for atmospheric chemistry: Supplement V - IUPAC Subcommittee on Gas Kinetic Data Evaluation for Atmospheric Chemistry, *J. Phys. Chem. Ref. Data*, *26*, 521-1011, 1997.
- Atkinson, R., D.L. Baulch, R.A. Cox, R.F. Hampson, J.A. Kerr, M.J. Rossi, and J. Troe, Summary of evaluated kinetic and photochemical data for atmospheric chemistry, Data Sheet P7, Int. Union of Pure and Appl. Phys., London, 2002.
- Atlas, E.L., B.A. Ridley, and C. Cantrell, The Tropospheric Ozone Production about the Spring Equinox (TOPSE) Experiment: Introduction, *J. Geophys. Res.*, *108*, 8353, doi:10.1029/2002JD003172, 2003.
- Barrie, L.A., J.W. Bottenheim, R.C. Schnell, P.J. Crutzen, and R.A. Rasmussen, Ozone destruction and photochemical reactions at Polar Sunrise in the lower Arctic atmosphere, *Nature*, *334*, 134-141, 1988.
- Bey, I., D.J. Jacob, J.A. Logan, and R.M. Yantosca, Asian chemical outflow to the Pacific: Origins, pathways and budgets, *J. Geophys. Res.*, *106*, 23097-23112, 2001.
- Bithell, M., G. Vaughan, and L.J. Gray, Persistence of stratospheric ozone layers in the troposphere, *Atmos. Env.* *34*, 2563-2570, 2000.
- Bjerknes, J. and H. Solberg, Life cycle of cyclones and the polar front theory of atmospheric circulation, *Geofys. Publ.* *3*, 1-18, 1926.

- Blitz, M.A., D.E. Heard, and M.J. Pilling, OH formation from  $\text{CH}_3\text{CO} + \text{O}_2$  : A convenient experimental marker for the acetyl radical, *Chem. Phys. Lett.*, *365*, 374-379, 2002.
- Blitz, M.A., D.E. Heard, M.J. Pilling, S.R. Arnold, and M.P. Chipperfield, Pressure and temperature-dependent quantum yields for the photodissociation of acetone between 279 and 327.5 nm, *Geophys. Res. Lett.*, *31*, L06111, doi:10.1029/2003GL018793, 2004.
- Bolton, D., The computation of equivalent potential temperature, *Mon. Weather Rev.*, *108*, 1046-1053, 1980.
- Braslau, N. and J.V. Dave, Effects of aerosol on the transfer of solar energy through realistic model atmospheres. 1. Non-absorbing aerosols, *J. Appl. Meteorol.*, *12*, 601, 1973.
- Brasseur G.P., J.T Kiehl, J.F. Muller, T. Schneider, C. Granier, X. Tie, and D. Hauglustaine, Past and future changes in global tropospheric ozone: Impact on radiative forcing, *Geophys. Res. Lett.*, *29*: 20 , p. 3807, 1998.
- Brough, N., C.E. Reeves, S.A. Penkett, D.J. Stewart, K. Dewey, J. Kent, H. Barjat, P.S. Monks, H. Ziereis, P. Stock, H. Huntrieser, and H. Schlager, Intercomparison of aircraft instruments on board the C-130 and Falcon 20 over southern Germany during EXPORT 2000, *Atmos. Chem. Phys.*, *3*, 2127-2138, 2003.
- Browning, K.A, Mesoscale aspects of extratropical cyclones: an observational perspective, Internal Report 44, Joint Centre for Mesoscale Meteorology, University of Reading, 1995.
- Browning, K.A., and G.A. Monk, A simple model for the synoptic analysis of cold fronts, *Quart. J. Roy. Meteor. Soc.*, *120*, 235-257, 1982.
- Brune, W.H., D. Tan, I.F. Faloona, L. Jaeglé, D.J. Jacob, B.G. Heikes, J. Snow, Y. Kondo, R. Shetter, G.W. Schae, B. Anderson, G.L. Gergory, S. Vay, H.B. Singh, D.D. Davis, J.H. Crawford, and D.R. Blake, OH and HO<sub>2</sub> chemistry in the North Atlantic free troposphere, *J. Geophys. Res.*, *26*, 3077-3080, 1999.
- Carlson, T.N., Mid-latitude weather systems, Harper Collins Academic, ISBN 0-415-10930-2, 1991.
- Carslaw, N., D.J. Creasey, D.E. Heard, A.C. Lewis, J.B. McQuaid, M.J. Pilling, P.S. Monks, B.J. Bandy, and S.A. Penkett, Modeling OH, HO<sub>2</sub>, and RO<sub>2</sub> radicals in the marine boundary layer - 1. Model construction and comparison with field measurements, *J. Geophys. Res.*, *104*, 30241-30255, 1999.

- Carver, G.D., P.D. Brown, and O. Wild, The ASAD atmospheric chemistry integration package and chemical reaction database, *Comput. Phys. Comms.*, *105*, 197-215, 1997.
- Carver, G.D., and P.A. Stott, IMPACT: an implicit time integration scheme for chemical species and families, *Ann. Geophys.*, *18*, 337-346, 2000.
- Chamiedes, W.L. and A.W. Stelson, Aqueous phase chemical processes in deliquescent sea-salt aerosols: A mechanism that couples the atmospheric cycles of S and sea salt, *J. Geophys. Res.*, *97*, 20565-20580, 1992.
- Chameides, W.L. and J.C.G. Walker, A photochemical theory for tropospheric ozone, *J. Geophys. Res.*, *78*, 8751-8760, 1973.
- Chipperfield, M.P., Multiannual Simulations with a Three-Dimensional Chemical Transport Model, *J. Geophys. Res.*, *104*, 1781-1805, 1999.
- Chipperfield, M.P., D. Cariolle, P. Simon, R. Ramarson, and D.J. Lary, A 3-dimensional modeling study of trace species in the Arctic lower stratosphere during winter 1989-1990, *J. Geophys. Res.*, *98*, 7199-7218, 1993.
- Collins, W.J., D.S. Stevenson, C.E. Johnson, and R.G. Derwent, The European regional ozone distribution and its links with the global scale for the years 1992 and 2015, *Atmos. Env.* *34*, 255-267, 2000.
- Cooper, O.R., J.L. Moody, D.D. Parrish, M. Trainer, T.B. Ryerson, J.S. Holloway, G. Hubler, F.C. Fehsenfeld, S.J. Oltmans, and M.J. Evans, Trace gas signatures of the airstreams within North Atlantic cyclones: Case studies from the North Atlantic Regional Experiment (NARE 97) aircraft intensive, *J. Geophys. Res.*, *106*, 5437-5456, 2001.
- Crawford J., D. Davis, J. Olson, G. Chen, S. Liu, G. Gregory, J. Barrick, G. Sachse, S. Sandholm, B. Heikes, H. Singh, and D. Blake, Assessment of upper tropospheric HO<sub>x</sub> sources over the tropical Pacific based on NASA GTE/PEM data: Net effect on HO<sub>x</sub> and other photochemical parameters, *J. Geophys. Res.*, *104*, 16255-16273, 1999.
- Crutzen, P.J., A discussion of the chemistry of some minor constituents in the stratosphere and troposphere, *Pure Appl. Geophys.*, *106*, 1385-1399, 1973.
- Crutzen P.J., Geology of mankind, *Nature*, *415*, 23-23, 2002.
- Crutzen P.J. and W. Steffen, How long have we been in the Anthropocene era? Comment., *Climatic Change*, *61*, 251-257, 2003.
- DeMore, W.B., S.P. Sander, C.J. Howard, A.R. Ravishankara, D.M. Golden, C.E.

- Kolb, R.F. Hampson, M.J. Kurylo, and M.J. Molina, Chemical kinetics and photochemical data for use in stratospheric modelling: Evaluation number 12, *JPL Publ.*, 97-4, 14-143, 1997.
- Derwent, R.G., T.J. Davies, M. Delaney, G.J. Dollard, R.A. Field, P. Dumitrescu, P.D. Nason, B.M.R. Jones, and S.A. Pepler, Analysis and interpretation of the continuous hourly monitoring data for 26 C<sub>2</sub>-C<sub>8</sub> hydrocarbons at 12 United Kingdom sites during 1996, *Atmos. Env.*, 34, 297-312, 2000.
- Dockery, D.W., An association between air pollution and mortality in six US cities, *New Eng. J. Med.*, 329, 1753-1759, 1993.
- Donnell, E.A., D.J. Fish, and E.M. Dicks, Mechanisms for pollutant transport between the boundary layer and the free troposphere, *J. Geophys. Res.*, 106, 7847-7856, 2001.
- Eisele, F.L., G.H. Mount, D. Tanner, A. Jefferson, R. Shetter, J.W. Harder, and E.J. Williams, Understanding the production and interconversion of the hydroxyl radical during the Tropospheric OH Photochemistry Experiment, *J. Geophys. Res.* 102, 6457, 1997.
- Emrich, M., and P. Warneck, Photodissociation of acetone in air: Dependence on pressure and wavelength. Behavior of the excited singlet state, *J. Phys. Chem. A*, 104, 9436-9442, 2000.
- Esler, J.G., D.G.H. Tan, P.H. Haynes, M.J. Evans, K.S. Law, P.H. Plantévin, and J.A. Pyle, Stratosphere-troposphere exchange: Chemical sensitivity to mixing, *J. Geophys. Res.*, 106, 4717-4731, 2001.
- Esler, J.G., P.H. Haynes, K.S. Law, H. Barjat, K. Dewey, J. Kent, S. Schmitgen, and N. Brough, Transport and mixing between airmasses in cold frontal regions during Dynamics and Chemistry of Frontal Zones (DCFZ), *J. Geophys. Res.* 108, art. no. 4142, 2003.
- European Environment Agency, CORINAIR, Office for official publications of the European Communities, ISBN 92-826-9058-X, 1994.
- Evans, M.J., *PhD Thesis*, University of Cambridge, May 1999.
- Evans, M.J., D.E. Shallcross, K.S. Law, J.O.F. Wild, P.G. Simmonds, T.G. Spain, P. Berrisford, J. Methven, A.C. Lewis, J.B. McQuaid, M.J. Pilling, B.J. Bandy, S.A. Penkett, and J.A. Pyle, Evaluation of a Lagrangian box model using field measurements from EASE (Eastern Atlantic Summer Experiment) 1996, *Atmos. Env.* 34, 3843-3863, 2000.

- Flatoy, F., and O. Hov, Three-dimensional model studies of the effect of  $\text{NO}_x$  emissions from aircraft on ozone in the upper troposphere over Europe and the North Atlantic, *J. Geophys. Res.*, *101*, 1401-1422, 1996.
- Folkins, I., and R. Chatfield, Impact of acetone on ozone production and OH in the upper troposphere at high  $\text{NO}_x$ , *J. Geophys. Res.*, *105*, 11585-11599, 2000.
- Freitas, S.R., M.A.F Silva Dias, P.L. Silva Dias, K.M. Longo, P. Artaxo, M.O. Andreae, and H. Fischer, A convective kinematic trajectory technique for low-resolution atmospheric models, *J. Geophys. Res.*, *105*, 24375-24386, 2000.
- Gelencser, A., K. Siszler, and J. Hlavay, Toluene-benzene concentration ratio as a tool for characterizing the distance from vehicular emission sources, *Env. Sci. Tech.* *31*, 2869-2872, 1997.
- Gerbig, C., S. Schmitgen, D. Kley, A. Volz-Thomas, K. Dewey, and D. Haaks, An improved fast-response vacuum-UV resonance fluorescence CO instrument, *J. Geophys. Res.*, *104*, 1699-1704, 1999.
- Giannakopoulos, C., M.P. Chipperfield, K.S. Law, and J.A. Pyle, Validation and intercomparison of wet and dry deposition schemes using Pb-210 in a global three-dimensional off-line chemical transport model, *J. Geophys. Res.*, *104*, 23761-23784, 1999.
- Gierczak, T., J.B. Burkholder, S. Bauerle, and A.R. Ravishankara, Photochemistry of acetone under tropospheric conditions, *Chem. Phys.*, *231*, 229-244, 1998.
- Goldan, P.D., D.D. Parrish, W.C. Kuster, M. Trainer, S.A. McKeen, J. Holloway, B.T. Jobson, D.T. Sueper, and F.C. Fehsenfeld, Airborne measurements of isoprene, CO, and anthropogenic hydrocarbons and their implications, *J. Geophys. Res.*, *105*, 9091-9105, 2000.
- Good, P., C. Giannakopoulos, F.M. O'Connor, S.R. Arnold, M. de Reus, and H. Schlager, Constraining tropospheric mixing timescales using airborne observations and numerical models, *Atmos. Chem Phys.*, *3* 1023-1035, 2003.
- Guenther, A., C.N. Hewitt, D. Erickson, R. Fall, C. Geron, T. Graedel, P. Harley, L. Klinger, M. Lerdau, W.A. McKay, T. Pierce, B. Scholes, R. Steinbrecher, R. Tallamraju, J. Taylor, and P. Zimmerman, A global model of natural volatile organic compound emissions, *J. Geophys. Res.*, *100*, 8873-8892, 1995.
- Green, T.J., C.E. Reeves, N. Brough, G.D. Edwards, P.S. Monks, and S.A. Penkett, Airborne measurements of peroxy radicals using the PERCA technique, *J. Environ. Monit.*, *5*, 75-83, 2003.
- Harries, J.E., H.E. Brindley, P.J. Sagoo, and R.J. Bantges, Increases in greenhouse



forcing inferred from the outgoing longwave radiation spectra of the Earth in 1970 and 1997, *Nature*, *410*, 355-357, 2001.

Harrold, T.W., Mechanisms influencing the distribution of precipitation within baroclinic disturbances, *Quart. J. Roy. Meteor. Soc.*, *99*, 232-251, 1973.

Holstag, A.A.M, and B.A. Boville, Local versus non-local boundary-layer diffusion in a global climate model, *J. Clim.*, *6*, 1825-1842, 1993.

Hough A.M., The calculation of photolysis rates for use in global tropospheric modelling studies, AERE Report R-13259, HMSO, London [ISBN 0-7058-1259-6], 1988.

Hough, A.M., Development of a two-dimensional global tropospheric model: model chemistry, *J. Geophys. Res.*, *96*, 7325, 1991.

Hov, O., F. Flatoy, S. Solberg, N. Schmidbauer, C. Dye, J.S. Foot, K. Dewey, J. Kent, H. Richter, A. Kaye, D. Kley, S. Schmitgen, S.A. Penkett, C. Reeves, B. Bandy, N. Brough, T. Green, G. Mills, K. Law, P-H. Plantevin, N. Savage, S. Arnold, M. Cobb, M. Evans, F. O'Connor, J. Pyle, M. Beekmann, J. Kowol-Santen, E. Dugault, P.S. Monks, G.D. Edwards, and J. McQuaid, Maximum Oxidation Rates in the Free Troposphere (MAXOX), Final Report, ENV4-CT97-0525, 2000.

Inverarity, G., Correcting airborne temperature data for lags introduced by instruments with two-time-constant responses, *J. Atmos. Oceanic Technol.*, *17*, 176-184, 1999.

Isaken, I.S.A., O. Hov, S.A. Penkett, and A. Semb, Model analysis for the measured concentration of organic gases in the Norwegian Arctic, *J. Atmos. Chem.*, *3*, 3-27, 1985.

Jacob, D.J., J.A. Logan, and P. Murti, Effect of rising Asian emissions on surface ozone in the United States, *Geophys. Res. Lett.*, *26*, 2175-2178, 1999.

Jacob, D.J., B.D. Field, E.M. Jin, I. Bey, Q. Li, J.A. Logan, R.M. Yantosca, and H.B. Singh, Atmospheric budget of acetone, *J. Geophys. Res.*, *107*, 4100, doi:10.1029/2001JD000694, 2002.

Jaeglé, L., D.J. Jacob, P.O. Wennberg, C.M. Spivakovsky, T.F. Hanisco, E.J. Lanzendorf, E.J. Hinst, D.W. Fahey, E.R. Keim, M.H. Proffitt, E.L. Atlas, F. Flocke, S. Schaubler, C.T. McElroy, C. Midwinter, L. Pfister, and J.C. Wilson, Observed OH and HO<sub>2</sub> in the upper troposphere suggest a major source from convective injection of peroxides, *Geophys. Res. Lett.*, *24*, 3181-3184, 1997.

Jaeglé, L., D.J. Jacob, Y. Wang, A.J. Weinheimer, B.A. Ridley, T.L. Campos, G.W. Sachse, and D.E. Hagen, Sources and chemistry of NO<sub>x</sub> in the upper troposphere over the United States, *Geophys. Res. Lett.*, *25*, 1705-1708, 1998.

Jaeglé, L., D.J. Jacob, W.H. Brune, I. Faloon, D. Tan, B.G. Heikes, Y. Kondo, G.W. Sachse, B. Anderson, G.L. Gregory, H.B. Singh, R. Poeschel, G. Ferry, D.R. Blake, and R.E. Shetter, Photochemistry of HO<sub>x</sub> in the upper troposphere at Northern Midlatitudes, *J. Geophys. Res.*, *105*, 3877-3892, 2000.

Jaeglé, L., D.J. Jacob, W.H. Brune, and P.O. Wennberg, Chemistry of HO<sub>x</sub> radicals in the upper troposphere, *Atmos. Env.*, *35*, 469-489, 2001.

JPL, Chemical Kinetics and Photochemical Data for Use in Stratospheric Modeling, Evaluation Number 14, JPL Publication 02-25, Jet Propulsion Laboratory, California Institute of Technology, Pasadena CA, 2003.

Kanakidou, M., and P.J. Crutzen, Scale problems in global tropospheric chemistry modelling - comparison of results obtained with a 3-dimensional model, adopting longitudinally uniform and varying emissions of NO<sub>x</sub> and NMHC, *Chemosphere*, *26*, 787-801, 1993.

Klemp, D., K. Mannschreck, H.W. Patz, M. Habram, P. Matuska, and F. Slemr, Determination of anthropogenic emission ratios in the Auerberg area from concentration ratios: results from long-term measurements, *Atmos. Env.*, *36*, S61-S80, 2002.

Köhler, I., R. Sausen, and R. Reinberger, Contributions of aircraft to the atmospheric NO<sub>x</sub> content, *Atmos. Env.*, *31*, 1801-1818, 1997.

Kotchenruther, R.A., D.A. Jaffe, and L. Jaeglé, Ozone photochemistry and the role of peroxyacetyl nitrate in the springtime northeastern Pacific troposphere: Results from the Photochemical Ozone Budget of the Eastern North Pacific Atmosphere (PHOBEA) campaign, *J. Geophys. Res.*, *106*, 28731-28742, 2001.

Lamb, B., H. Westberg, and G. Allwine, Isoprene emission fluxes determined by an atmospheric tracer technique, *Atmos. Env.*, *20*, 1-8, 1986.

Langford, A.O., Stratosphere-troposphere exchange at the subtropical jet: contribution to the tropospheric ozone budget at midlatitudes, *Geophys. Res. Lett.*, *26*, 2449-2452, 1999.

Law, K.S., and J.A. Pyle, Modelling trace gas budgets in the troposphere. 1. Ozone and odd nitrogen, *J. Geophys. Res.*, *98*, 18377, 1993a.

Law, K.S., and J.A. Pyle, Modelling trace gas budgets in the troposphere. 2. CH<sub>4</sub> and CO, *J. Geophys. Res.*, *98*, 18401, 1993b.

Law, K.S., and E.G. Nisbet, Sensitivity of the methane growth-rate to changes in methane emissions from natural-gas and coal, *J. Geophys. Res.*, *101*, 14387, 1996.

- Lawrence M.G., P.J. Crutzen, P.J. Rasch, B.E. Eaton, and N.M. Mahowald, A model for studies of tropospheric photochemistry: Description, global distributions, and evaluation, *J. Geophys. Res.*, *104* 26245-26277, 1999.
- Lelieveld, J., A. Bregman, H.A. Scheeren, J. Strom, K.S. Carslaw, H. Fischer, P.C. Siegmund, and F. Arnold, Chlorine activation and ozone destruction in the northern lowermost stratosphere, *J. Geophys. Res.*, *104*, 8201-8213, 1999.
- Lelieveld, J., H. Berresheim, S. Borrmann, P.J. Crutzen, F.J. Dentener, H. Fischer, J. Feichter, P.J. Flatau, J. Heland, R. Holzinger, R. Korrman, M.G. Lawrence, Z. Levin, K.M. Markowicz, N. Mihalopoulos, A. Minikin, V. Ramanathan, M. de Reus, G.J. Roelofs, H.A. Scheeren, J. Sciare, H. Schlager, M. Schultz, P. Siegmund, B. Steil, E.G. Stephanou, P. Stier, M. Traub, C. Warneke, J. Williams, and H. Ziereis, Global air pollution crossroads over the Mediterranean, *Science*, *298*, 794-799, 2002.
- Li, Q.B., D.J. Jacob, I. Bey, P.I. Palmer, B.N. Duncan, B.D. Field, R.V. Martin, A.M. Fiore, R.M. Yantosca, D.D. Parrish, P.G. Simmonds, and S.J. Oltmans, Transatlantic transport of pollution and its effects on surface ozone in Europe and North America, *J. Geophys. Res.*, *107*, art. no. 4166, 2002.
- Liu, H., D.J. Jacob, L.Y. Chan, S.J. Oltmans, I. Bey, R.M. Yantosca, J.M. Harris, B.N. Duncan, and R.V. Martin, Sources of tropospheric ozone along the Asian Pacific Rim: An analysis of ozonesonde observations, *J. Geophys. Res.*, *107*, 4573, doi:10.1029/2001JD002005, 2002.
- McKeen, S.A., and S.C. Liu, Hydrocarbon ratios and photochemical history of air masses, *Geophys. Res. Lett.*, *20*, 2363-2366, 1993.
- McKeen, S.A., T. Gierczak, J.B. Burkholder, P.O. Wennberg, T.F. Hanisco, E.R. Keim, R.S. Gao, S.C. Liu, A.R. Ravishankara, and D.W. Fahey, The photochemistry of acetone in the upper troposphere: A source of odd-hydrogen radicals, *Geophys. Res. Lett.*, *24*, 3177-3180, 1997.
- McKenna D.S., P. Konopka, J.U. Grooss, G. Gunther, R. Muller, R. Spang, D. Offermann, and Y. Orsolini, A new Chemical Lagrangian Model of the Stratosphere (CLaMS) - 1. Formulation of advection and mixing, *J. Geophys. Res.*, *107*, art. no. 4309, 2002.
- Madronich, S., Photodissociation in the atmosphere. 1. Actinic flux and the effects of ground reflections and clouds, *J. Geophys. Res.*, *92*, 9740, 1987.
- Matthews, E., Global vegetation and land use: new high resolution database for climate studies, *J. Clim. Appl. Meteor.*, *33*, 474, 1983.
- Methven, J., Offline trajectories: Calculation and accuracy, *Tech. Rep.* 44, U.K.

Univ. Global Atmos. Model. Programme, Dep. of Meteorol., Univ. of Reading, Reading, UK, 1997.

Methven, J., and B. Hoskins, The advection of high resolution tracers by low resolution winds, *J. Atmos. Sci.*, *56*, 3262-3285, 1999.

Methven, J., S.R. Arnold, F.M. O'Connor, H. Barjat, K. Dewey, J. Kent, and N. Brough, Estimating photochemically produced ozone throughout a domain using flight data and a Lagrangian model, *J. Geophys. Res.*, *107*, 4271, 2003.

Newell, R., Z.X. Wu, Y. Zhu, W. Hu, E.V. Browell, G.L. Gregory, G.W. Sachse, J.E. Collins Jr., K.K. Kelly, and S.C. Liu, Vertical fine-scale atmospheric structure measured from NASA DC-8 during PEM-West A, *J. Geophys. Res.*, *98*, 8751-8773, 1993.

Nicholls, S., J. Leighton, and R. Barker, A new fast response instrument for measuring total water, *J. Atmos. Oceanic Technol.*, *7*, 706-718, 1990.

O'Connor, F.M., T. Green, K. Dewey, N. Brough, H. Barjat, K.S. Law, J.A. Pyle, J. Kent, and G. Phillips, Tropospheric ozone budget: regional and global calculations, *Atmos. Chem. Phys. Disc.*, *4*, 991-1036, 11-2-200420042, 2004.

Parrish, D.D., C.J. Hahn, E.J. Williams, R.B. Norton, and F.C. Fehsenfeld, Indications of photochemical histories of air masses from measurements of atmospheric trace species at Point Arena, California, *J. Geophys. Res.*, *97*, 15883-15901, 1992.

Paulson S.E., and J.J. Orlando, The reactions of ozone with alkenes: An important source of HO<sub>x</sub> in the boundary layer, *J. Geophys. Res.*, *98*, 3727-3730, 1996.

Photochemical Oxidants Review Group (PORG), Ozone in the United Kingdom - Fourth Report of the Photochemical Oxidants Review Group, DETR, ISBN: 0-870393-30-9, 1997.

Poschl, U., J. Williams, P. Hoor, H. Fischer, P.J. Crutzen, C. Warnecke, R. Holzinger, A. Hansel, A. Jordan, W. Lindinger, H.A. Scheeren, W. Peters, and J. Lelieveld, High concentrations throughout the 0-12km altitude range over the tropical rainforest, *J. Atm. Chem.*, *38*, 115-132, 2001.

Prather, M.J., Numerical advection by conservation of 2nd-order moments, *J. Geophys. Res.*, *91*, 6671-6681, 1986.

Purvis, R.M., A.C. Lewis, R.A. Carney, J.B. McQuaid, S.R. Arnold, J. Methven, H. Barjat, K. Dewey, J. Kent, P.S. Monks, L.J. Carpenter, N. Brough, S.A. Penkett, C.E. Reeves, Rapid uplift of nonmethane hydrocarbons in a cold front over central Europe., *J. Geophys. Res.* *108*, doi:10.1029/2002JD002521 15 April 2003.

- Reeves, C.E., S.A. Penkett, S. Baguitte, K.S. Law, M.J. Evans, B.J. Bandy, P.S. Monks, G.D. Edwards, G. Phillips, H. Barjat, J. Kent, K. Dewey, S. Schmitgen, and D. Kley, Potential for photochemical ozone formation in the troposphere over the North Atlantic as derived from aircraft observations during ACSOE, *J. Geophys. Res.*, *107*, 4707, doi:10.1029/2002JD002415, 2002.
- Rodwell, M.J., and B.J. Hoskins, Monsoons and the dynamics of deserts, *Quart. J. Roy. Meteor. Soc.*, *122*, 1385-1404, 1996.
- Roehl C.M., S.A. Nizkorodov, H. Zhang, G.A. Blake, and P.O. Wennberg, Photodissociation of peroxyxynitric acid in the near-IR, *Journal of Physical Chemistry A*, *106* (15): 3766-3772, 2002.
- Rudolph, J., B.R. Fu, A. Thompson, K. Anlauf, and J. Bottenheim, Halogen atom concentrations in the Arctic troposphere derived from hydrocarbon measurements: Impact on the budget of formaldehyde, *Geophys. Res. Lett.*, *26*, 2941-2944, 1999.
- Salawitch, R.J., P.O. Wennberg, G.C. Toon, B. Sen, and J.F. Blavier, Near IR photolysis of HO<sub>2</sub>NO<sub>2</sub>: Implications for HO<sub>x</sub>, *Geophys. Res. Lett.*, *29*(16): art. no. 1762, 2002.
- Saliba N.A., H. Yang, and B.J. Finlayson-Pitts, Reaction of gaseous nitric oxide with nitric acid on silica surfaces in the presence of water at room temperature, *Journal of Physical Chemistry A*, *105* (45): 10339-10346, 2001.
- Schubert, S.D., R.B. Rood, and J. Pfaendtner, An assimilated dataset for Earth science applications, *Bul. Amer. Meteor. Soc.*, *74*, No. 12, Dec 1993.
- Shindell, D.T., G. Faluvegi, and N. Bell, Preindustrial-to-present-day radiative forcing by tropospheric ozone from improved simulations with the GISS chemistry-climate GCM, *Atmos. Chem. Phys.*, *3*, 1675-1702, 2003.
- Singh, H. B., M. Kanakidou, P.J. Crutzen, and D.J. Jacob, High concentration and photochemical fate of oxygenated hydrocarbons in the global troposphere, *Nature*, *378*, 50-54, 1995.
- Singh, H.B., D. Herlth, R. Kolyer, R. Chatfield, W. Viezee, L.J. Salas, Y. Chen, J.D. Bradshaw, S.T. Sandholm, R. Talbot, G.L. Gregory, B. Anderson, G.W. Sachse, E. Browell, A.S. Bachmeier, D.R. Blake, B. Heikes, D. Jacob, and H.E. Fuelberg, Impact of biomass burning emissions on the composition of the South Atlantic troposphere: Reactive nitrogen and ozone, *J. Geophys. Res.*, *101*, 24203-24219, 1996.
- Singh, H., Y. Chen, A. Staudt, D. Jacob, D. Blake, B. Heikes, and J. Snow, Evidence from the Pacific troposphere for large global sources of oxygenated organic compounds, *Nature*, *410*, 1078-1081, 2001.

- Staehelin J., J. Thudium, R. Buehler, A. Volz-Thomas and W. Graber, Trends in surface ozone concentrations at Arosa (Switzerland), *Atmos. Env.*, *28*, 75-87, 1994.
- Stevenson D.S., C.E. Johnson, W.J. Collins, R.G. Derwent, K.P. Shine, and J.M. Edwards, Evolution of tropospheric ozone radiative forcing, *Geophys. Res. Lett.*, *25* (20): 3819-3822, 1998.
- Stockwell, D.Z., C. Giannakopoulos, P.H. Plantevin, G.D. Carver, M.P. Chipperfield, K.S. Law, J.A. Pyle, D.E. Shallcross, and K.Y. Wang, Modelling  $\text{NO}_x$  from lightning and its impact on global chemical fields, *Atmos. Env.* *33*, 4477-4493, 1999.
- Stockwell D.Z., and M.P. Chipperfield, A tropospheric chemical-transport model: Development and validation of the model transport schemes, *Quart. J. of the Royal Meteorological Society*, *125* (557): 1747-1783 Part A, 1999.
- Stohl, A., A 1-year Lagrangian ‘climatology’ of airstreams in the Northern Hemisphere troposphere and lowermost stratosphere, *J. Geophys. Res.*, *106*, 7263-7279, 2001.
- Stohl, A. and T. Trickl, A textbook example of long-range transport: Simultaneous observation of ozone maxima of stratospheric and North American origin in the free troposphere over Europe, *J. Geophys. Res.*, *104*, 30445-30462, 1999.
- Stull, R.B., An introduction to Boundary Layer Meteorology, Kluwer, 1991.
- Sutton, R.T., H. Maclean, R. Swinbank, A. O'Neill, and F.W. Taylor, High-resolution stratospheric tracer fields estimated from satellite observations using Lagrangian trajectory calculations, *J. Atmos. Sci.* *51*, 2995-3005, 1994.
- Tiedtke, M., A comprehensive mass flux scheme for cumulus parameterization in large-scale models, *Mon. Wea. Review*, *117*, 1779-1800, 1989.
- Traub, M., H. Fischer, M. de Reus, R. Kormann, J. Heland, H. Ziereis, H. Schlager, R. Holzinger, J. Williams, C. Warneke, J. de Gouw, and J. Lelieveld, Chemical characteristics assigned to trajectory clusters during the MINOS campaign, *Atmos. Chem. Phys.*, *3*, 459-468, 2003.
- Trickl, T. O.R. Cooper, H. Eisele, P. James, R. Mucke, and A. Stohl, Intercontinental transport and its influence on the ozone concentrations over central Europe: Three case studies, *J. Geophys. Res.*, *108*, art. no. 8530, 2003.
- Tulet, P., A. Maalej, V. Grassier, and R. Rosset, An episode of photooxidant plume pollution over the Paris region, *Atmos. Env.* *33*, 1651-1662, 1999.
- Wang, K.Y., J.A. Pyle, M.G. Sanderson, and C. Bridgeman, Implementation of a convective atmospheric boundary layer scheme in a tropospheric chemistry transport

model, *J. Geophys. Res.*, *104*, 23729-23745, 1999.

Wang Y.H., J.A. Logan, D.J. Jacob, Global simulation of tropospheric O<sub>3</sub>-NO<sub>x</sub>-hydrocarbon chemistry. 2. Model evaluation and global ozone budget, *J. Geophys. Res.*, *103*, 10727-10755, 1998.

Warneck, P., Photodissociation of acetone in the troposphere: An algorithm for the quantum yield, *Atmos. Environ.*, *35*, 5773-5777, 2001.

Wernli, H., A Lagrangian-based analysis of extra-tropical cyclones. II: A detailed case study, *Quart. J. Roy. Meteor. Soc.*, *123*, 1677-1706, 1997.

Wilson, M.F., and A. Hendershon-Sellers, A global archive of land cover and soil data for use in general circulation models, *J. Climatol.* *5*, 119, 1985.

Winkler, J., P. Blank, K. Glaser, J.A.G. Gomes, M. Habram, C. Jambert, W. Jaeschke, S. Konrad, R. Kurtenbach, P. Lenschow, J.C. Lorzer, P.E. Perros, M. Pesch, H.J. Prumke, B. Rappengluck, T.H. Schmitz, F. Slemr, A. Volz-Thomas, and B. Wickert, Ground-based and airborne measurements of nonmethane hydrocarbons in BERLIOZ: Analysis and selected results, *J. Atmos. Chem.*, *42*, 465-492, 2002.

Wingenter, O.W., M.K. Kubo, N.J. Blake, T.W. Smith Jr., D.R. Blake, and F.S. Rowland, Hydrocarbon and halocarbon measurements as photochemical and dynamical indicators of atmospheric hydroxyl, atomic chlorine, and vertical mixing obtained during Lagrangian flights, *J. Geophys. Res.*, *101*, 4331-4340, 1996.

World Health Organisation, Air quality guidelines for Europe, Second edition (WHO regional publications. European series No.91), Copenhagen, ISBN 92 890 1358 3.

World Meteorological Organization, Atmospheric Ozone 1985: Assessment of our understanding and processes controlling its present distribution and change, global ozone research and monitoring project, Report 16, 1985.